MODELLING TRAILING VORTICES FROM A SLENDER SHIP HULL FOR MANOEUVRING CALCULATIONS

Modelling Trailing Vortices from a Slender Ship Hull for Manoeuvring Calculations

by

Jong Jin Park

A Thesis submitted for the degree of
Doctor of Philosophy

Department of Marine Technology
The University of Newcastle upon Tyne

2001

Abstract

A particular problem that has been encountered in modelling the forces and moment acting on a manoeuvring ship, has been the correct estimation of the distribution of side force along its length. If traditional slender body theory is used, reasonable agreement can be obtained between theoretical and experimental result over the forebody of the ship. However, moving aft, the two increasingly diverge until there are significant differences at the stern. For this reason manoeuvring coefficients cannot be accurately predicted by this approach. In a number of studies, the reason for the discrepancies has been attributed to the influence of trailing vortices that develop along the hull. The conclusion is consistent with sensitivity analyses carried out with augmented slender body theory incorporating vortices of specified location and strength along the ship.

The present thesis is concerned with modelling trailing vortices along a ship in drift motion so that they can be used in the calculation of the associated distribution of forces and manoeuvring coefficients. A numerical model based on the Discrete Vortex Method has been developed for the analysis of vortex flow around the ship which is represented by slender body approximation. The trailing vortices are modelled by a series of transverse two-dimensional multi-vortex solutions marching longitudinally down the hull.

Results are presented for six different hull types; a flat plate, the Wigley hull, a block hull, a Series 60 hull, the British Bombardier and the British Bombardier with a pram stern. The effects of varying drift angles are also investigated for each hull types. Good qualitative agreement is shown between the predicted velocity and vorticity fields and results from experimental studies. The distribution of side forces and yaw moments along the hull is also well predicted. The results explain manoeuvring phenomena occurring for the hull forms considered that have been observed experimentally and at full scale.

Acknowledgements

I would like to express my sincere gratitude to my supervisor Dr. Martin Downie for his continual supervision and encouragement throughout this research. His kind guidance and expertise in fluid dynamics are greatly appreciated. I also like to thank Prof. Michael Graham for his invaluable advice in the early stage of this study, and to Dr. David Clarke for the benefit of his experience in ship manoeuvrability.

I would also like to thank Prof. Seung-Hee Lee, Prof. Young-Gill Lee and Prof. Sung-Wan Hong, who have been the source of inspiration of my research.

I am highly indebted to Inha University and the Samsung Heavy Industry for the financial support to carry out this research.

Thanks are also expressed to Wasis Dwi Aryawan, Alan Dobson, Jamie Grimwade and Mohan Anantharaman, for their friendship and nice years spent together in the same office, and to Jangho Kim for helping me to make happy memories in Newcastle.

Finally, I would like to say thanks to my parents, my wife Hea-Joung Kim and my sun Jin-Won Park for their continuous moral support and patience over the past five years.

Contents

List of Figures

Nomenclature

A_p	After perpendicular of ship.
A_r	Aspect ratio, T/L.
a_n	Coefficient in Laurent series.
B	Body force or breadth of ship.
C	Closed curve in contour integration.
C_B	Hull block coefficient.
C_p	Pressure coefficient.
C_H	Horizontal added mass coefficient at zero frequency.
F_p	Forward perpendicular of ship.
F_n	Froude number, $U_\infty / \sqrt{gL}$.
g	Acceleration due to gravity.
I_H	Vortex influence coefficient.
i	Imaginary number, $\sqrt{-1}$.
L	Ship Length between perpendiculars.
m	Source strength.
N	Hydrodynamic yawing moment.
N_a	Hydrodynamic yawing moment contributed by attached flow.
N_s	Hydrodynamic yawing moment contributed by flow separation.
N'	Dimensionless hydrodynamic yawing moment.
N'_r	Partial yaw velocity derivative $\partial N' / \partial r'$.
N'_v	Partial velocity derivative $\partial N' / \partial v'$.
n	Normal vector of a point.
p	Pressure of fluid.
R	Periodic length.
R_n	Reynolds number, $U_\infty L / \nu$.
r	Radius of circle or angular velocity about z-axis.

Nomenclature

S	Complex position in S-plane.
S_n	Normal velocity in S-plane.
S_s	Body surface point in S-plane.
S_v	Complex vortex position in S-plane.
S_p	Separation point in S-plane.
$S1$	Complex position in $S1$-plane.
T	Draft of ship.
t	Time.
U_∞	Uniform velocity of ship.
U_v	Complex vortex velocity in Z-plane.
u	Velocity along x-axis.
V	Complex velocity.
V_n	Normal velocity on sectional hull surface.
v	Velocity along y-axis.
W	Complex potential.
w	Velocity along z-axis.
X	Distance from forward perpendicular.
x	Longitudinal axis.
x'	Dimensionless distance from midship position.
Y	Hydrodynamic side force along y-axis.
Y_a	Hydrodynamic side force contributed by attached flow.
Y_s	Hydrodynamic side force contributed by flow separation.
Y'	Dimensionless hydrodynamic side force.
Y'_r	Partial yaw velocity derivative $\partial Y' / \partial r'$.
Y'_v	Partial velocity derivative $\partial Y' / \partial v'$.
y	Lateral axis in Z-plane.
Z	Complex position in Z-plane.
Z_F	Hydrodynamic lift force along z-axis.
Z_p	Separation point in Z-plane.
Z_v	Complex vortex position in Z-plane.
z	Vertical axis in Z-plane.

β	Ship drift angle.
Γ	Circulation.
ζ	Vertical axis in *S*-plane.
η	Lateral axis in *S*-plane.
θ	Angular co-ordinate.
ν	Kinematic viscosity.
ρ	Fluid density.
ϕ	Velocity potential.
φ	Stream function.
ω	Vorticity.
$\mathfrak{Re}$	Real part of complex number.
$\mathfrak{Im}$	Image part of complex number.

Chapter I

INTRODUCTION

The assessment of the manoeuvrability of a ship is an essential part of the design process. Research in this area has a long history but interest in it has been heightened over recent years because of the introduction of new IMO design criteria (IMO 1993). Also there has been an evolution of hull forms with good resistance and propulsion characteristics, but whose manoeuvring performance has not been well predicted or understood. For these reasons it has become particularly important to assess ship manoeuvrability at an early stage in the design cycle.

Captive model testing, coupled with simulation techniques now allows very accurate prediction of ship behaviour in the most complex manoeuvring situations. However, it is questionable whether this is a suitable tool for use at the early design stage, mainly due to the costs and the time involved and the fact that the hull geometry may not be sufficiently determined at that stage to allow models to be constructed and tested.

A variety of semi-empirical models exist which have been in use for a number of years and which are a practical alternative for the prediction of derivatives in preliminary design. One such set of regression equations (Clarke et al 1983) for acceleration and velocity derivatives was based on the mathematical form of the slender body theory. Clarke and Horn (1997) improved upon the performance of these equations, by developing new predictors derived from the enhanced understanding of effects of trailing vortices upon the flow along the after part of a ship. This was one outcome of a series of studies carried out over a number of years by Clarke and co-workers (Clarke 1972, Clarke 1992, Hearn et al 1994 and Clarke and Horn 1997).

Recent developments in hull design have given rise to what has been called the pram stern. These buttock flow sterns have proved to be more efficient in terms of resistance and propulsion performances but have exhibited a tendency towards directional instability. Part of the reason for this behaviour was explained by Clarke (1992), who showed that the side force generated by a skeg attached to a rectangular section, characteristic of pram sterns, was less than that generated by a skeg attached to a triangular section, more characteristic of conventional stern design. Subsequently, Clarke and Horn (1997) developed a generalised slender body theoretical analysis that included the effects of vortices on the linear hydrodynamic derivatives. They found that the vortex influence coefficients augment the side force calculated using zero-frequency horizontal added mass for conventional hull forms as if a fictitious fin was being added at the stern. They also postulated that a pram stern generates a vortex pair which has a much lower circulation, and which possibly rotate in the opposite sense, than those shed from a conventional stern. In this case the side force generated by the pram stern is less than that for the conventional stern and if the direction of rotation of the trailing vortices is reversed the side force generated by the stern sections is actually diminished. For the pram stern, this effect further reduces the effectiveness of the skeg and may explain some of the problems reported from ships with this type of stern.

The work of Clarke et al (Clarke et al 1997 and Hearn and Clarke et al 1994), although capable of further generalisation, has been based on the presence of a vortex pair at the stern about whose strength, sense and location certain assumptions need to be made. To develop it further, it is desirable to develop a method of determining the velocity distribution at the stern of any hull form of interest, preferably by modelling the flow around the hull.

The complete and accurate solution of flow about a ship hull is computationally extremely intensive and, until very recently, has been considered beyond the constraints imposed by available computer hardware. For example, Patel et al (1990) modelled the viscous flow past a ship in a cross current by solving the Reynolds-averaged Navier-Stokes equations using a $k-\varepsilon$ turbulence model for a Reynolds

number of $5x10^6$. In order to enhance the resolution of the computational mesh within the constraints of available computational resources, they used a computational domain that enclosed only the stern half of the ship. The initial upstream conditions did not include the trailing vortices generated over the ship's forebody.

One approach to simplifying the problem that has proved fruitful is the development of potential flow models, together with the application of slender body theory, to the flow around hulls whose lateral dimensions are much smaller than their length. The problem of such a slender body moving forward with constant speed whilst undergoing small lateral motion, as in yaw, can be shown to reduce to one that can be described by a two-dimensional velocity potential that varies very slowly along the body length, as described by Newman (1977) amongst others. This approach has found application, for example, in the development of the strip theory of ship motions in waves and in manoeuvring problems.

1.1 Objectives of Study

A main objective of this thesis has been to develop a relatively simple and reliable numerical model for predicting the flow around a ship subject to drift motion. The numerical model is based on slender body theory and includes trailing vortices modelled by the discrete vortex method. The discrete vortex method provides an effective way to account for the effects of vortex shedding in the potential flow calculations. Consistent with slender body theory, the hull is represented as a series of two-dimensional strips. Each two-dimensional section is modelled by using a potential comprising a component representing the longitudinal change of the body and another representing the lateral motions. In addition, the numerical method includes a third potential modelling flow separation and vortex shedding from two-dimensional strips representing the hull. The development of trailing vortices is then computed through a time marching procedure. The free surface is modelled with a low frequency (mirror image) boundary condition. A generalised transformation is employed so that simple hull sections and other more ship like sections can be treated.

A second objective of the thesis has been to carry out comprehensive studies concerning separated flows around hulls at various drift motions. To understand the relationship between hull forms and flow phenomena, including bilge separation and cross-flow separation, a numerical model has been implemented for the case of various hull forms. The vortex calculations were carried out in two different ways, depending on the hull forms involved. For hulls with defined separation points, as for the Wigley Hull or the Block hull, single vortices were introduced at the separation points so as to satisfy the Kutta condition at each time step. In the case of hulls with continuous surfaces with no well–defined separation point, such as the British Bombardier, the British Bombardier with a pram stern and the Series 60 hull, a continuous layer of discrete vortices were distributed around the section so as to satisfy a no-slip condition at collocation points.

A third important objective of this thesis has been to calculate related manoeuvring coefficients, particularly side force and yaw moment coefficients, subject to various drift angles. The computed results have been compared with experimental data and the numerical results of other researchers to validate the model developed.

In addition, the influence of stern shapes on the ship manoeuvring derivatives has also been studied. The results obtained for British Bombardier and the British Bombardier with a pram stern have been computed and compared in order to understand the influence of stern shape on the formation of the wake pattern and the related manoeuvring derivatives.

1.1 Chapter Layout

In the following chapter, a review of the flow phenomena and previous studies related to the prediction of manoeuvring derivatives is presented. In Chapter 3, a brief description of the theoretical background, related to the development of the present numerical method is given. In Chapter 4, the detailed numerical procedure for the

present model is described. The chapter deals mainly with the numerical method applicable to hulls with defined separation points.

In Chapters 5 to 6, the application of the method to a number of different hull types is described and the results are presented. The hull types are; a flat plate hull, the Wigley hull and the Block hull, which have defined separation points. In Chapter 6, the commercial numerical code called CFX, based on a Navier-Stokes solution, is also used to calculate the block hull in straight motion for the purpose of comparing with the present numerical method.

In Chapter 7, the detailed numerical method appropriate to real ship shaped hulls is described. The chapter is mainly devoted to a description of a generalised conformal transformation and the application of a pointwise no-slip condition on the hull surface. In Chapter 8, the application of the numerical model to real shaped hulls is described. These hulls are the British Bombardier, the British Bombardier with a pram stern, and a Series 60 hull. The influence of pram sterns on the wake pattern and manoeuvring derivatives is discussed in the context of the results produced by numerical method.

Finally, in Chapter 9, the work is summarised and the main findings of the present study are discussed. Suggestions for future work and possible further applications of the numerical method developed are discussed.

Chapter II

A REVIEW OF RELEVANT LITERATURE

2.1 The Flow around Manoeuvring Ships

It is well known that the flow around a ship is very complicated even in the straight ahead motion with no drift. Many different flow phenomena can be observed around a ship including bilge separation, bow-bottom-separation, bow-wave breaking, stern-wave breaking and bow-necklace separation as shown in Figure 2.1. One of the most prominent aspects is bilge separation. Bilge vortices mainly affect the formation of wake flows around the stern, which is important for propeller design and ship manoeuvring. If the ship is moving with a drift angle, cross-flow separation will be inevitable. The sway force and yaw moment is closely related to the strength and location of the vortices.

The estimation of the manoeuvrability of a ship requires information about hydrodynamic forces and moments acting on the hull. These can be obtained in three different ways; experimentally, by semi-empirical methods that are based on analyses of experimental data, or by using numerical methods that use either viscous or inviscid flow models.

Since all these methods have their own merit and are closely related to each other, they have been developed in parallel. Previous studies of these different approaches will be described in more detail in the following sections.

2.2 Experimental Studies

The side force, Y, and yaw moment, N, on model ships can be measured using conventional towing tank, wind tunnel and water channel experiments. The slope at the origin of the force and moment plotted against drift angle gives an experimental value of the velocity derivatives Y_v and N_v respectively. The yaw velocity derivatives Y_r and N_r are not easily measured by conventional towing tests. A rotating arm facility in which a model is towed along circular paths, can be used to find the angular velocity derivatives (Burcher 1972, Inoue at al 1981). The rotating arm test needs a specific facility and can not be used to measure acceleration derivatives. The planar motion mechanism system (PMM) pioneered by Gertler (1959) and Goodman (1960) can be installed in a conventional towing tank or water channel to measure both velocity derivatives and acceleration derivatives (Gill and Price 1977)

For the determination of the longitudinal distribution of velocity derivatives, the segmented model test has been used. Beukelman (1989) used a segmented model test in a towing tank to find the longitudinal distribution of velocity derivatives related to speed and drift angles. Clarke (1972) and Burcher (1972) performed rotating arm tests with a segmented tanker model to find the longitudinal distribution of both velocity and angular velocity derivatives.

Experimental studies including bilge separation (Maruo and Ikehata 1966, Tagori 1966 and Matheson and Joubert 1973) and cross-flow separation (Bradbury 1983, Tanaka et al 1983, Chan et al 1993 and Nonaka et al 1996) have been carried out to understand the development of trailing vortices and their effect on various hull types.

Tagori (1966) observed flow separation around block hull and tanker models at zero drift motion. From the block hull model experiment, he observed that the down flow along the wall side separates at the bilge and a set of conical vortices is generated at the fore bottom. At the afterbody, the flow runs out from the bottom and separates at the bilge, and a new set of large vortices is produced at the side of model. Figure 2.2 shows a schematic view of the separation flow around the block hull. These types

of flow separation are common on three-dimensional bodies but are quite different from the normal two-dimensional separation customarily considered.

Matheson and Joubert (1973) also showed the existence of two pairs of longitudinal vortices by wind tunnel experiments carried out on a tanker model. A pair of trailing vortices, one on either side of the model, was generated as the fluid flowed around the bilge at the bow of the model. These vortices extended to the stern along the bottom of the model adjacent to the bilge radius. The second pair of vortices was found at the stern of the model. They were similar to those found by Tagory (1966), only they were in a slightly different position on the model surface. Figure 2.3 shows the position of these vortices over the aft region of the model.

Bradbury (1983) investigated different types of block hulls with varying drift angles. Flow visualisation made it clear that asymmetric vortices associated with the cross flow become important for drifting motion. At low drift angles the asymmetric flow is barely apparent, but it becomes increasingly dominant over much of the hull's length as the angle increases. He also studied the influence of draft and showed that increased draft increased both the vortex strength and the side force.

Chan et al (1993) measured the flow patterns and side force and yaw moment of a Mariner hull model at various drift angles. They discussed the correlation of flow circulation obtained by direct vorticity measurements and estimated circulation based on pressure measurements. They also suggested that the circulation of the stern vortex might be approximately calculated by side force, which may complement the slender body model used in the non-lifting potential theory.

More recently, Longo and Stern (1996) carried out detailed experimental research on yaw effects for a Series 60 model with a block coefficient of 0.6. With detailed mean-velocity and pressure fields for eight stations from bow to stern, they showed that strong cross-flow effects, including forebody and afterbody keel and bilge vortices, are dominated with increasing yaw angle. The side force and yaw moment was also shown to increase significantly with increasing yaw angle. In addition they

provided detailed wave profiles along the hull for both a range of Froude numbers and yaw angles.

Experimental investigation carried out by Kuiper (1994) considered the velocity distribution in the wake behind three different stern shapes in straight ahead motion. The direction of rotation of the vortices shed from a conventional U shape stern is in good agreement with those measured by Matheson and Joubert (1973). However, the direction of shedding vortices from a pram stern showed the opposite sense of rotation compared to conventional stern. The optimised stern form, which was a combined form of a *U* shaped stern and a pram stern, showed no wake circulation. The vortex patterns are illustrated in simplified form in Figure 2.4. Kuiper's work was mainly concerned with the resistance and propulsion of ships and therefore the optimum form was considered to be one giving a minimum of circulation in the wake.

To investigate the effects of changes in stern shapes on ship manoeuvring, Nonaka et al (1996) carried out model tests on three different VLCC model ships. The ships have the same bows but different stern shapes, namely a *U* shape, a *V* shape and a medium shaped stern. By flow visualisation of the various sterns, they showed the clear difference in the distribution of vortices and consequently the wake flow. Their measured total circulation did not show clear differences but the vorticity of the *V* shape stern tended to be concentrated, whereas the vorticity of the *U* shape sterns was distributed widely. Since there were no big differences of total circulation between the three ships, the total sway forces and yaw moments were similar, but they showed big differences in the position of the centres of their sway forces.

More detailed experiments about the influence of different stern shapes on ship manoeuvring have been carried out by Horn (2000). He was concerned with the effect of trailing vortices on the hull forces on a variety of ship shapes, which he investigated by testing a set of seven hull forms with same fore body but variously shaped segmented stern regions. Five models were based on the British Bombardier with a variety of conventional and pram stern configurations, and the remaining models were variations on a simple elliptic hull form. His segmented model tests provided detailed

data relating to the longitudinal distribution of sway force and yaw moments of the stern regions of these models.

Experimental results for various kinds of ships may be used to build up generalised semi-empirical equations for manoeuvring derivatives. They may also be used for comparison with numerical result for the validation of numerical methods.

2.3 Semi-Empirical Method

Experimental methods allow very accurate prediction of ship behaviour in the most complex of manoeuvring situations. However, it is questionable whether this approach is suitable at an early design stage because of the cost and time involved, and the fact that the hull geometry may not be sufficiently determined at that stage to allow appropriate models to be constructed and tested.

A variety of semi-empirical methods exist which have been in use for a number of years and which are a practical alternative for the prediction of hydrodynamic derivatives for preliminary design. These methods have used existing theoretical frameworks to guide the formulation of predictors, which are then used in regression analysis to derive equations for the hydrodynamic derivatives. The predictors are based on combinations of the primary ship geometric parameters of length, draft, breadth and block coefficient.

The simplest way to calculate manoeuvring derivatives is to consider a ship to be a low aspect ratio wing turned on its side. In this treatment it is usual for the free surface to be assumed flat and level. Using the appropriate low aspect ratio wing theory (Jones 1946), expressions for the non-dimensional form of the velocity derivatives for a flat plate can be deduced to be

$$Y_v' = -\pi\left(\frac{T}{L}\right)^2 \qquad Y_r' = -\pi\left(\frac{T}{L}\right)^2\left(-\frac{1}{2}\right)$$
$$N_v' = -\pi\left(\frac{T}{L}\right)^2\left(\frac{1}{2}\right) \qquad N_r' = -\pi\left(\frac{T}{L}\right)^2\left(\frac{1}{4}\right) \tag{2-1}$$

where L and T of the flat plate can be assumed to be the ship draught and the length between perpendiculars respectively. These equations are often used as basis for semi-empirical formulae.

Wagner-Smitt (1970, 1971) presented simple formulae for ship manoeuvring derivatives by fitting the Jones formulae to experimental data.

Inoue at al (1981) carried out a series of model tests to investigate the hydrodynamic forces acting on ships in level and trimmed conditions. They attempted to find the relationship between ship dimensions and load conditions and the hydrodynamic forces. They obtained semi-empirical formulae for the velocity derivatives in terms of the principal dimensions and form factor, C_B, by using the rotating arm test and oblique towing test for various kinds of hull form. Their semi-empirical formulae are

$$Y_v' = -\pi\left(\frac{T}{L}\right)^2\left[1+\frac{1.4}{\pi}C_B\frac{B}{T}\right] \qquad Y_r' = -\pi\left(\frac{T}{L}\right)^2\left(-\frac{1}{2}\right)$$
$$N_v' = -\pi\left(\frac{T}{L}\right)^2\left(\frac{2.0}{\pi}\right) \qquad N_r' = -\pi\left(\frac{T}{L}\right)^2\left(\frac{1.04}{4}-\frac{4.0}{\pi}\frac{T}{L}\right) \tag{2-2}$$

where B is the breadth of a ship.

Clarke et al (1983) examined empirical formulae from a number of authors. They suggested that differences between formulae might be attributed to the authors using different sets of data covering different ranges of hull geometry, as well as inter-tank differences due to variations in tank and model dimensions and the type of measurement system used. They carried out multiple regression analysis to find empirical formulae from a database containing 72 observations of velocity derivatives

and 36 of acceleration derivatives measured in many different establishments, and gathered from the open literature. Their formulae for the velocity derivatives are as follows;

$$Y_v' = -\pi\left(\frac{T}{L}\right)^2\left[1+0.40C_B\frac{B}{T}\right] \qquad Y_r' = -\pi\left(\frac{T}{L}\right)^2\left(-\frac{1}{2}+2.2\frac{B}{L}-0.080\frac{B}{T}\right)$$

$$N_v' = -\pi\left(\frac{T}{L}\right)^2\left(\frac{1}{2}+0.24\frac{T}{L}\right) \qquad N_r' = -\pi\left(\frac{T}{L}\right)^2\left(\frac{1}{4}+0.039\frac{B}{T}-0.56\frac{B}{L}\right) \tag{2-3}$$

The equations approach the Jones result, equation (2-1), as B approaches zero.

Apart from semi-experimental method, Clarke (1972) has calculated lengthwise distributions of the velocity derivatives from a simple two-dimensional strip theory using values of the horizontal added mass, C_H, at zero frequency. The expressions for the derivatives were as follows:

$$\begin{aligned}
Y_v' &= \pi\left(\frac{T}{L}\right)^2\left[C_H\right]_{Stern}^{Bow} \\
N_v' &= \pi\left(\frac{T}{L}\right)^2\left\langle\left[(C_H)x'\right]_{Stern}^{Bow} - \int_{Stern}^{Bow}(C_H)dx'\right\rangle \\
Y_r' &= \pi\left(\frac{T}{L}\right)^2\left[(C_H)x'\right]_{Stern}^{Bow} \\
N_r' &= \pi\left(\frac{T}{L}\right)^2\left\langle\left[(C_H)x'^2\right]_{Stern}^{Bow} - \int_{Stern}^{Bow}(C_H)x'dx'\right\rangle
\end{aligned} \tag{2-4}$$

where x' is the non-dimensional distance x/L from midships. Although the overall results were fairly good, there is a disagreement between segmented experiment and theory near the stern of the hull.

Later Hearn at al (1994) pointed out that the errors come from ignoring the presence of trailing vortices at the stern. They included the influence of the vortices in the previous slender body predictions of the hull derivatives and showed the

calculated lateral forces agree well with the measurements of segmented model tests. The expressions for the linear derivatives were as follows:

$$Y_v' = \pi\left(\frac{T}{L}\right)^2 \left[C_H + I_H\right]_{Stern}^{Bow}$$

$$N_v' = \pi\left(\frac{T}{L}\right)^2 \left\langle \left[(C_H + I_H)x'\right]_{Stern}^{Bow} - \int_{Stern}^{Bow} (C_H + I_H)dx' \right\rangle \qquad (2\text{-}5)$$

$$Y_r' = \pi\left(\frac{T}{L}\right)^2 \left[(C_H + I_H)x'\right]_{Stern}^{Bow}$$

$$N_r' = \pi\left(\frac{T}{L}\right)^2 \left\langle \left[(C_H + I_H)x'^2\right]_{Stern}^{Bow} - \int_{Stern}^{Bow} (C_H + I_H)x'dx' \right\rangle$$

where I_H is a vortex influence coefficient. Since the vortex magnitude and positions used for these calculations were based on measurement, they suggested the desirability of a simple method of modelling the vortices along ship hulls.

The generalised slender body theory is also supported by a recent experiment carried out by Horn (2000). With experimental results for various stern shape hull forms, including pram sterns, he supported the hypothesis that the inclusion of the effects of stern vortices within the slender-body theory properly accounts for the difference in manoeuvring characteristics of conventional and pram stern hull forms. However, he also pointed out that the generalised slender body theory could not be a complete description of the flow phenomena around strongly up-swept sterns where boundary layer growth significantly affects the theoretical predictions.

2.4 Navier-Stokes Method

Computational Fluid Dynamics (CFD) applications in fluid flows have been increasingly developed by researchers as the power of computers has grown. CFD may include all computational methods for fluid flow, but the term is usually applied

to Navier-Stokes solvers. The governing equations for the Navier- Stokes methods are the continuity equation (2-6) and Navier-Stokes equations (2-7).

$$\frac{\partial \rho}{\partial t} + \nabla \cdot (\rho \mathbf{u}) = 0 \tag{2-6}$$

$$\frac{\partial \mathbf{u}}{\partial t} + (\mathbf{u} \cdot \nabla)\mathbf{u} = \nu \nabla \cdot (\nabla \mathbf{u} + \nabla \mathbf{u}^T) - \frac{1}{\rho}\nabla p + \mathbf{B} \tag{2-7}$$

where p is the acting pressure. $\mathbf{u}$ is the velocity vector and $\mathbf{B}$ is the body force. $\nabla \mathbf{u}^T$ denotes the transpose of matrix/tensor $\nabla \mathbf{u}$. The kinematic viscosity ν is defined as the dynamic viscosity μ divided by the fluid density ρ.

In principle, the Navier-Stokes equations can be applied to both laminar and turbulent flow, because the turbulent flows are just very complex unsteady laminar flows. Turbulent flows at high Reynolds number are extremely time-dependent flows with very high gradients in all flow parameters. Turbulent flows contain elements that are much smaller than the characteristic length scale of the problem, typically of the order of 10^{-3} times smaller or less. To resolve the motion of these elements in a numerical procedure, the mesh size of the numerical grid would have to be even smaller; therefore at least 10^9 meshes would typically be necessary to cover the flow domain in three dimensions. This requires such a large memory capacity to store the flow variables at the mesh points, and such a large number of numerical operations that the computing time would be prohibitive. As a consequence, it is not feasible to solve such problems to the required accuracy using the unmodified equations and the current technology, except for low Reynolds numbers and simple geometry.

The RANS methods, which consider Reynolds Averaged Navier-Stokes equations, may be applied to high Reynolds number flow with turbulence modelling and are becoming a popular method for ship hydrodynamics with recent advances in computer software and hardware. The RANS equation can be written as (see Fletcher 1991)

$$\frac{\partial \mathbf{u}}{\partial t}+(\mathbf{u}\cdot\nabla)\mathbf{u}=\frac{1}{\rho}\nabla\cdot\left(\mu\nabla\mathbf{u}+\mu\nabla\mathbf{u}^{T}-\overline{\mathbf{uu}}\right)-\frac{1}{\rho}\nabla p+\mathbf{B} \tag{2-8}$$

where $-\overline{\mathbf{uu}}$ is called the Reynolds stress. The Reynolds stress introduces a closure problem in which there are more unknowns than equations. The extra equations are provided by modelling the turbulence processes that generate them.

Turbulence models can be classified as simple algebraic eddy viscosity models, two equation eddy viscosity models and second order closure models. Even though the two equation $k-\varepsilon$ eddy viscosity models are commonly used, robust turbulence models have not yet been established. Detailed descriptions of the $k-\varepsilon$ model and other turbulence models can be found from Rodi (1980) and Bradshaw et al (1981).

RANS methods in ship design are mainly applied to qualitative calculations of resistance and wake distributions (CFD Workshop Tokyo 1994 and Deng and Visonneau 1996), which can be used for the improvement of afterbodies of ships and their propellers. In the CFD Workshop 1994, various researchers calculated the wake distribution and resistance of a double body HSVA tanker and a Mystery tanker, and compared the predicted results with each other and with experimental results. There was much discussion about the turbulence models, numerical schemes and grid systems seeking to find the reasons for the failure of the models to produce to the "hook" shape in the wake distribution at the propeller plane. Their discussions suggested that improvement of the turbulence models might capture the "hook" shape, but they also proposed the necessity of more research in the future to settle this question.

Even though the RANS method has been applied to wave related calculations (Tahara et al 1990), panel methods are still the established way of computing the wave pattern and the improvement of the fore body shape based on the generated waves and the pressure distribution (Jensen et al 1986 and Bruzzone 1994).

2.4.1 Applications of RANS Methods to Ship Manoeuvring

Until now, only a few researchers have carried out RANS calculations applied to ship manoeuvring problems.

Patel et al (1990) modelled the viscous flow around an HSVA tanker and a SR107 bulk carrier in a cross current by solving the RANS equations using a $k-\varepsilon$ turbulence model for high Reynolds numbers. In order to enhance the resolution of the computational mesh within the constraints of the available computational resources, they used a computational domain that enclosed only the stern half of the ship. The initial upstream conditions did not include the trailing vortices generated over the ship's forebody. Their results indicated a need for better initial conditions and suggested the desirability of calculations carried out for the complete ship.

The computation of a complete Wigley hull advancing with a drift angle was carried out by Campana et al (1994). Viscous effects were taken into account in the vicinity of the ship surface and wake region by using the RANS method and the external flow was modelled by potential methods to save computing resources.

More recently, Miyazaki et al (2000) carried out a numerical calculation around a container ship and a tanker, with and without a rudder, in a drift motion by the RANS method, and compared the results with experimental data.

Even though there are growing RANS method applications in ship hydrodynamics, these methods are still considered to be future applications in terms of ship manoeuvring problems, as mentioned by Larsson (1997), since RANS methods require considerable computing resource and time to implement.

2.5 The Discrete Vortex Method

The discrete vortex method is a well known and simple way to model the rotational flow phenomena in a real flow. Rotational activity develops in the regions adjacent to the body surfaces and in the rear wake region in the case of bluff bodies. Flow separation also occurs from sharp corners, as for a flat plate held normal to the mainstream direction. The discrete vortex method attempts to model these flows by discretisation of the distributed vorticity or separated shear layers into finite numbers of small discrete vortex elements.

The first attempt to use the discrete vortex method was by Rosenhead (1931) who studied the Kelvin-Helmholtz instability of vortex sheets. The main feature of the Kelvin-Helmholtz instability is the dramatic self-convective activity, which follows spontaneously from only a small perturbation of the sheet. Birkhoff and Fisher (1959) repeated Rosenhead's work with finer discretisation and concluded that the progressive growth of an initial disturbance, periodic along the length of a vortex sheet, tends towards the concentration of the vortivity into a series of vorticity cores or clouds. Abernathy and Kronauer (1962) extended the discrete vortex model of Rosenhead to examine the stability of a parallel pair of infinite vortex sheets. It was found that the development and interaction of two vortex layers was seen to give rise to the familiar von Karman type vortex street pattern.

Sarpkaya (1975) studied two-dimensional vortex shedding behind an inclined flat plate through the use of the discrete vortex method. The Kutta-condition was applied to the edges of the plate to determine vortex strength and the Joukowsky transformation was used to transform the flat plate to a circle. The calculated vortex shedding process and the Strouhal number was well predicted compared to experiment. The calculated normal forces using the generalized Blasius theorem were 20-25% higher than those measured.

Naylor (1982) also investigated a normal flat plate in planar oscillatory and unidirectional flow. The result for unidirectional flow showed the development of a Karman street pattern. Naylor calculated oscillatory flows in the Keulegan-Carpenter number range of 0.5 to 40 and found it necessary to use a circulation decay

mechanism to the shed vortices to get better results. The calculated forces showed good agreement with experimental results.

In the case of bluff bodies with smooth surfaces such as circular cylinders, it is not straightforward to find the separation points and the trajectory of the separated shear layer. Stansby (1977) modelled a circular cylinder flow by using fixed separation points estimated from experiment. But in reality, separation positions are changing with time according to the flow conditions. Sarpkaya and Shoaff (1979) determined the position of mobile separation points through boundary-layer calculations and the strength and position of the nascent vortices through the use of the no-slip condition at the separation points. They used the method of rediscretization of the vortex sheets for the evolution of the wake. This method was suggested by Fink and Soh (1974) to reduce initiation of instabilities leading to randomness or chaotic motion of the vortices. Ikeda and Himeno (1981) used a similar method to Sapkaya and Soaff (1979) to study flow around other body shapes as well as a circular cylinder. They used the Lewis transformation formula (Lewis 1929) to generate several ship-like sections. They presented calculated flow fields with good qualitative agreement with the flow visualisation results from experiment.

Downie (1981) avoided the definition of separation points on a circular cylinder by distributing a number of vortices around the cylinder. The strengths of vortices were calculated by satisfying the no-slip condition at points on the cylinder surface. Murray (1992) also used the same vortex distribution method as Downie (1981) to calculate both a cylinder and anode shape. A cylinder was transformed to an anode bearing cylinder by conformal mapping (Downie at al 1989). Murray employed a Cloud-in-Cell method to reduce computation time and used the Random Walk and Finite Difference models to incorporate viscous diffusion into the discrete vortex method. Further applications of vortex cloud method were made by Wardhana (1995) who modelled interaction flows between cylinders in close proximity to one another, and between cylinders and walls, with overlapping grid systems.

More detailed reviews of the discrete vortex method can be found from Fink and Soh (1974), Downie (1981), Sarpkaya (1989) and Murray (1992).

2.5.1 Applications of Vortex Methods to Ship Manoeuvring

One approach to simplifying the problem that has proved fruitful is the development of potential flow methods together with the application of the slender body assumption to the flow around hulls whose lateral dimensions are much smaller than their length. The problem of such a slender body moving forward with constant speed whilst undergoing small lateral motion can be described by a two-dimensional velocity potential.

This slender body assumption was first made by Munk (1924) in the field of aerodynamics to predict the stability characteristics of airships. Jones (1946) applied the slender body assumption to determine the lift of a delta wing by considering an inviscid flow with no separation at sharp leading edges.

The flow incident to a slender delta wing with a sharp leading edge usually separates along the edge. The vortex layer rolls up above and inboard of the leading edge to form a region of high vorticity, which strongly influences the flow pattern. Mangler and Smith (1959) and Smith (1968) included leading-edge separation from a delta wing within the framework of the slender body assumption by replacing the vortex layer with a vortex sheet of spiral form.

Wardlaw (1974) modelled the flow about a slender cylindrical body at a high angle of attack. His method was applicable to bodies of revolution and modelled the flow using the impulsive flow analogy with viscous effects being simulated using point vortices.

Bradbury (1983, 1987) developed a slender-body line vortex potential method to model the flow past a wall sided flat-bottomed vessel with a waterplane area similar to

that of a Mariner hull with a drift motion. He modelled each rolled up vortex sheet as a single concentrated line vortex together with force-carrying mathematical discontinuities in the velocity potential connecting the line vortex to the bilge. His results reproduced the important qualitative feature of the real flows, but the calculated side force showed unrealistic fluctuations in its distribution. He assumed these fluctuations resulted from spurious results modelled in the vortex behaviour.

Later Al-Hukail (1992) also calculated the same block hull type as Bradbury (1983). He followed a conventional slender body approach by using a potential comprising a component representing the longitudinal motion of the body and another representing the lateral motion. In addition he included a third potential modelling flow separation. The vortex calculations were carried out using single Brown and Micheal (1954) vortices or a sequence of point vortices, introduced into the flow at defined separation points. The calculated lateral forces were in good agreement with those measured by Bradbury(1983).

Wong and Calisal (1996) included a simple vortex shedding model in their wave–maker model to calculate a Wigley hull travelling at an angle of incidence. Their method indicated that although vortex shedding contributes significantly to the forces and moments acting over the hull, its interaction with the free surface is negligible.

Wellicome at al (1995, 1997) developed a slender body model in which at each time-step a vortex was introduced into the flow according to a relation proposed by Fage and Johanson (1928) at assumed separation points on the two dimensional strips. Since there were no defined separation points in a real ship, they assumed a nascent vortex separates from hull segments at the place where the cross flow reaches maximum speed.

Xiong and Kose (1996) compared various separation models in a numerical method based on slender body theory, and concluded that more sophisticated vortex methods can give better results, and a proper vortex model is an important factor in

the prediction of the forces and moments acting over the hull. They also tried to improve their results by replacing the numerical solution in the bow area by a theoretical solution for an ellipsoid representing the bow sections.

More recently, Nakadake et al (1998) applied a simple surface panel method to three VLCC models. Their method used source distributions (Hess and Smith type) on the hull surface and discrete vortex distributions arranged on the centre plane of the hull. Their results showed fairly good agreement with experiment, but they suggested the need of improvement of their trailing vortex method in the future.

2.6 Conclusions

In summary, a number of researchers have proposed methods of computing the flow about ships advancing with a drift angle. Both CFD methods and models based on slender body theory have shown promise but the former are prohibitively computationally expensive, and the latter need further refinement. The following chapters discuss the potential flow methods in more detail and proposes an improved method for calculating these flows.

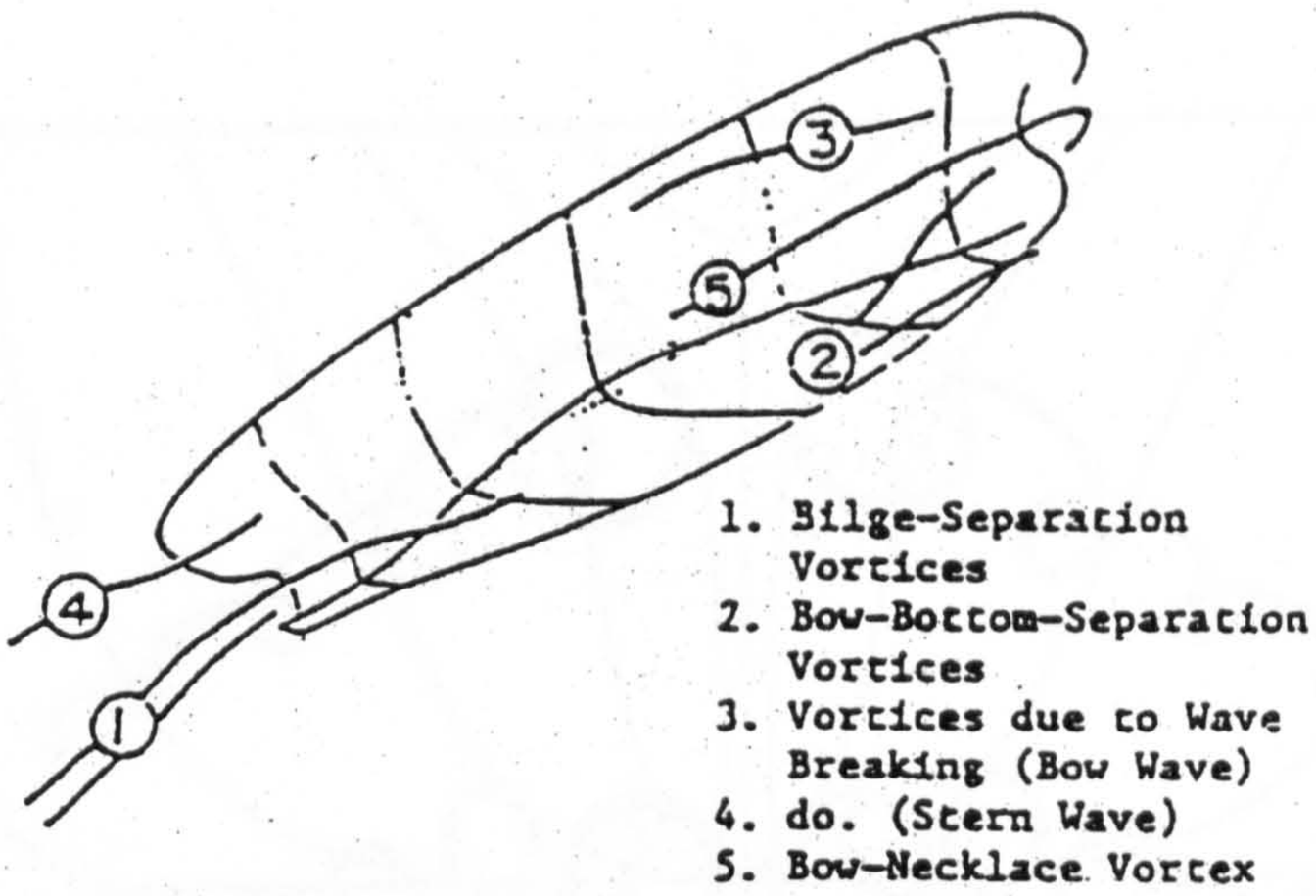

Figure 2.1: Sketch of flow separation (Chan et al 1993).

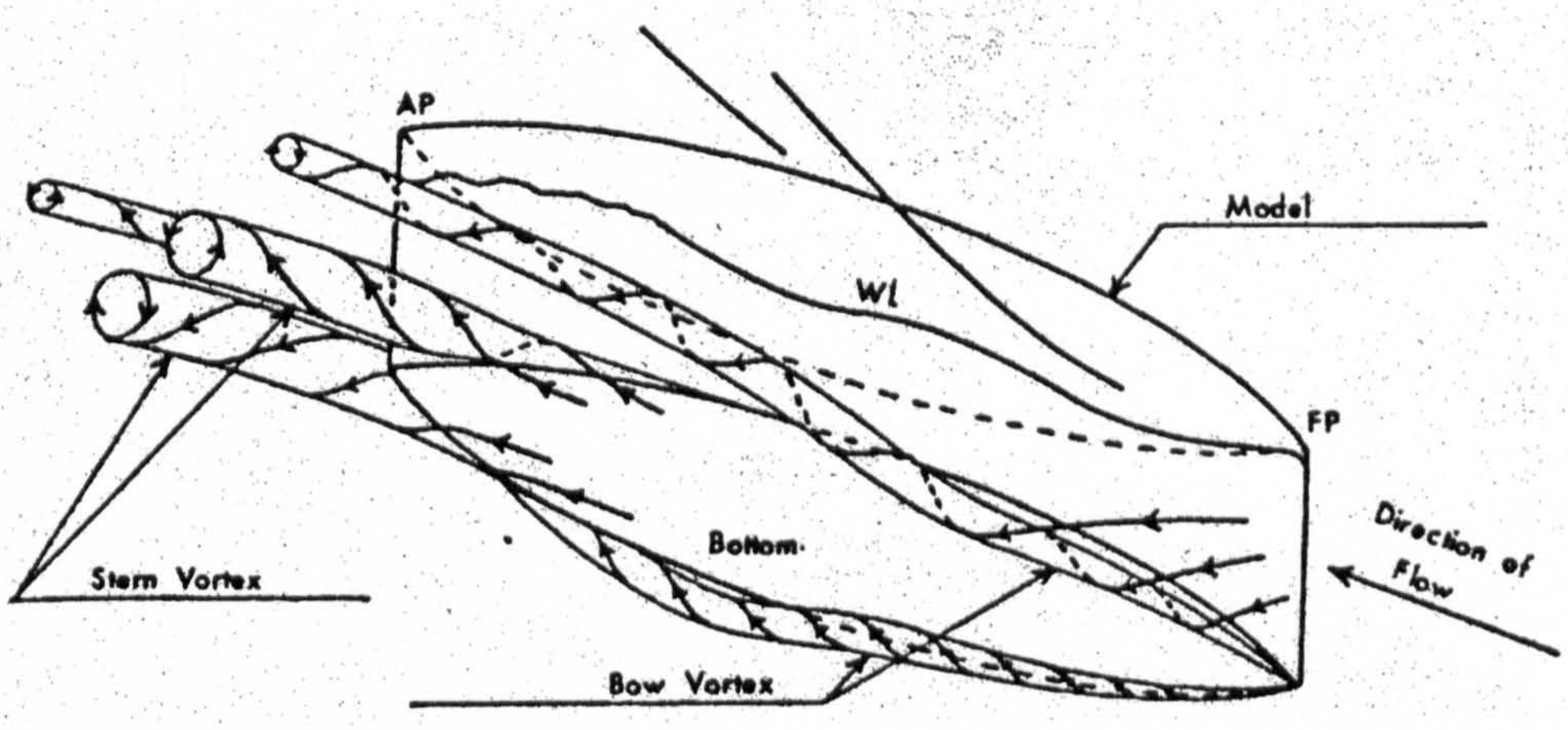

Figure 2.2: Flow around a block hull model (Tagori 1966).

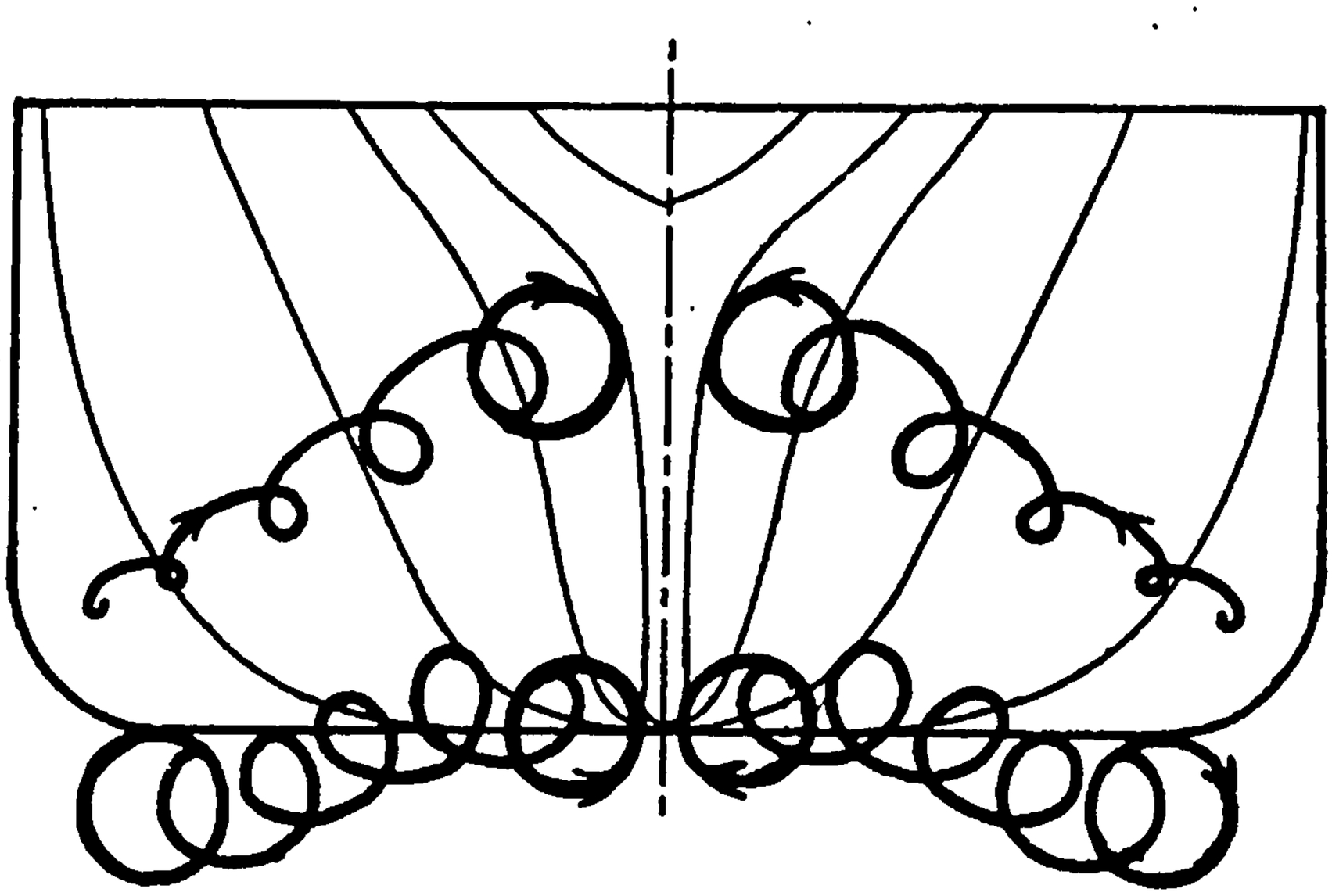

Figure 2.3: The two sets of trailing vortices over the stern of the model (Matheson and Joubert 1973).

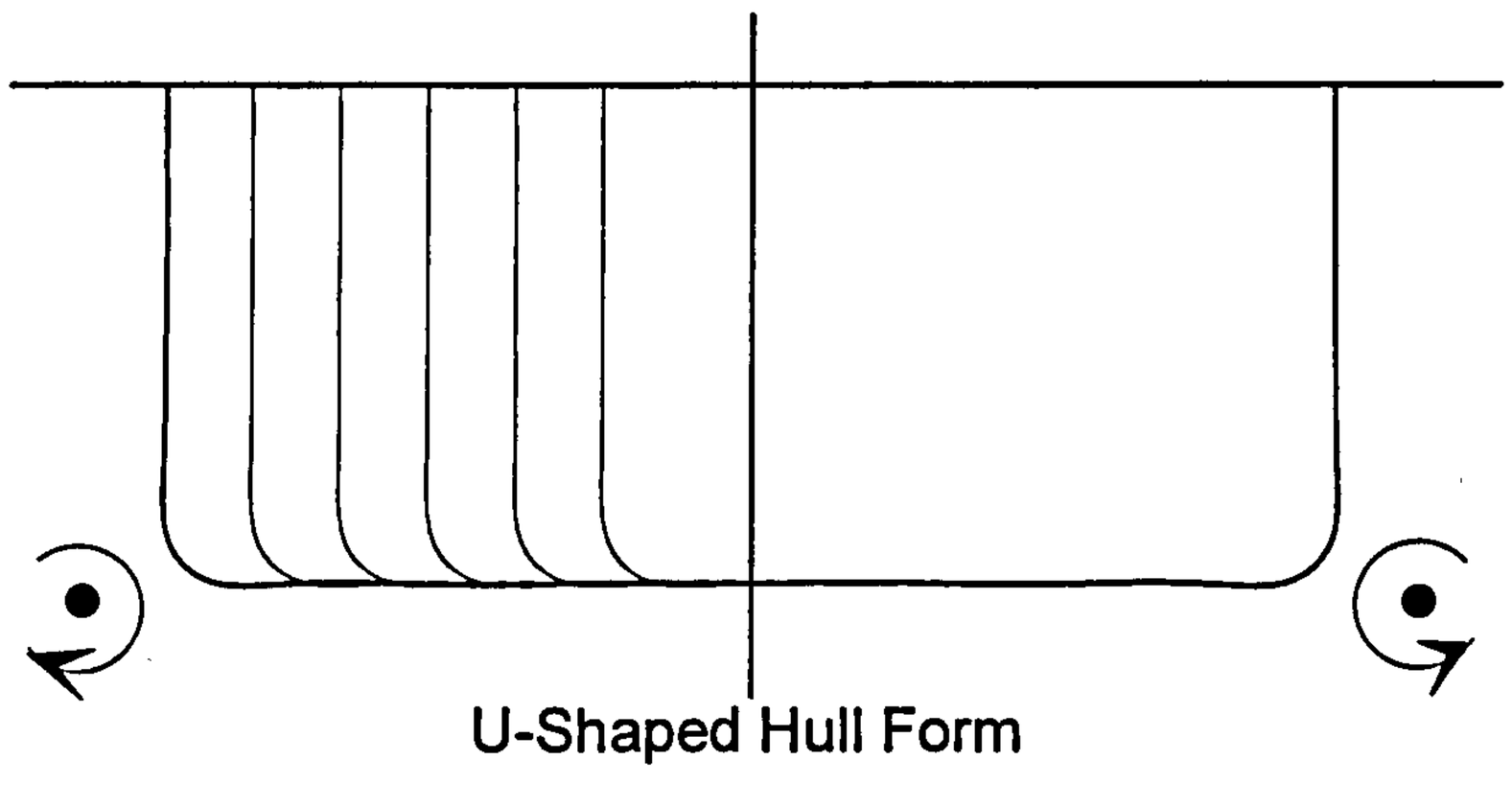

U-Shaped Hull Form

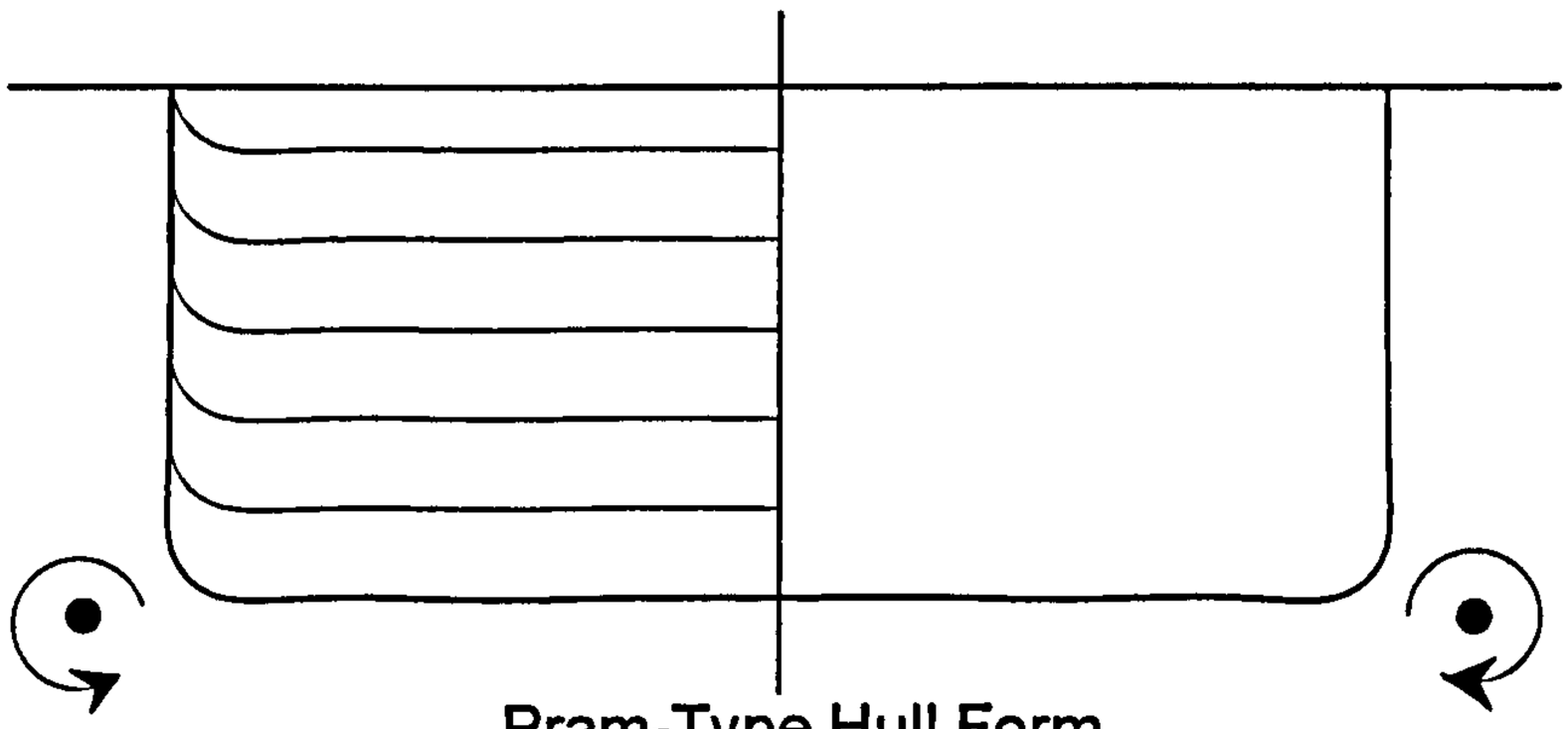

Pram-Type Hull Form

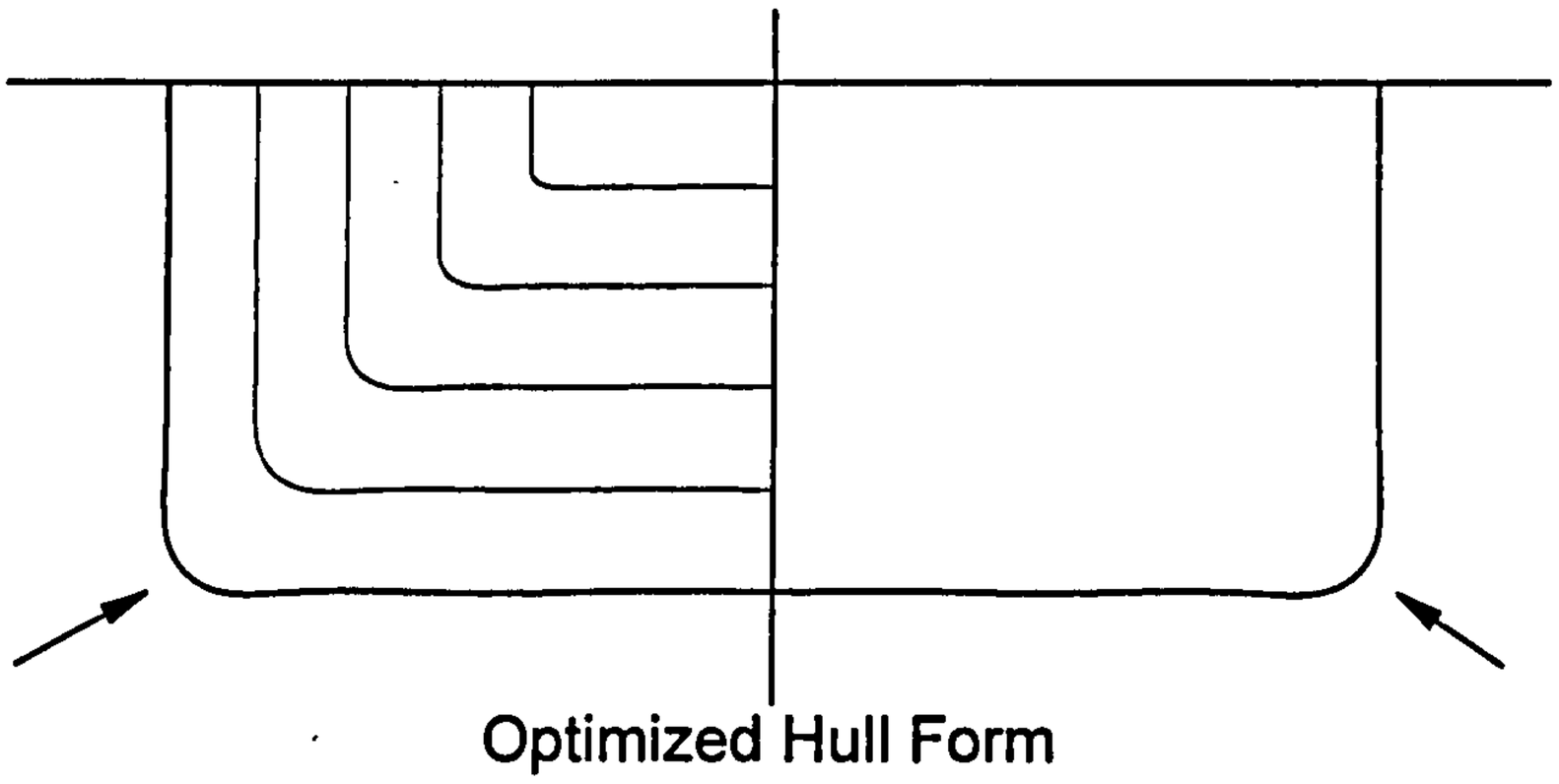

Optimized Hull Form

Figure 2.4: The representation of vortex generation from three different stern shapes as measured by Kuiper (1994).

Chapter III

THE THEORETICAL BACKGROUND

3.1 Background Theory

As described in section 2.4, the governing equations for the motion of a Newtonian fluid are the continuity equation (3-1) and the Navier-Stokes equations (3-2).

$$\frac{\partial \rho}{\partial t} + \nabla \cdot (\rho \mathbf{u}) = 0 \tag{3-1}$$

$$\frac{\partial \mathbf{u}}{\partial t} + (\mathbf{u} \cdot \nabla)\mathbf{u} = \nu \nabla \cdot (\nabla \mathbf{u} + \nabla \mathbf{u}^T) - \frac{1}{\rho}\nabla p + \mathbf{B} \tag{3-2}$$

The first and second term of the left hand side of the Navier-Stokes equations represent the local changing rate of a fluid velocity at a certain point and the convective rate of change due to the transport of an element to a different position respectively. The rate of change of momentum of a fluid element is related to the force due to viscosity, to the negative pressure gradient and to the body forces acting on the fluid element, which are represented in the right hand side of the Navier–Stokes equations.

The continuity equation (3-1) is derived from conservation of mass by the application of Gauss' Theorem. In most flow calculations related to ship hydrodynamics, the fluid is assumed to be incompressible, which means its density remains constant. This statement can be written as

$$\frac{D\rho}{Dt} = 0 \tag{3-3}$$

where the total derivative D/Dt is known as a Lagrangian type of derivative. The continuity equation (3-1) can be expanded by use of a vector identity, $\nabla \cdot (\rho \mathbf{u}) = \rho \nabla \cdot \mathbf{u} + \mathbf{u} \cdot \nabla \rho$, as

$$\frac{\partial \rho}{\partial t} + \mathbf{u} \cdot \nabla \rho + \rho \nabla \cdot \mathbf{u} = 0 \tag{3-4}$$

The first and second terms in this form of the continuity equation will be recognised as being the Eulerian form of the equation (3-3). The alternative form of the continuity equation (3-1) is

$$\frac{D\rho}{Dt} + \rho \nabla \cdot \mathbf{u} = 0 \tag{3-5}$$

with $D\rho / Dt = 0$, the equation (3-5) shows that the continuity equation is $\rho \nabla \cdot \mathbf{u} = 0$.

Since ρ cannot be zero, the continuity equation for an incompressible fluid becomes

$$\nabla \cdot \mathbf{u} = 0 \tag{3-6}$$

The circulation, $\Gamma(C)$ is defined as the line integral of the tangential velocity along a closed circuit C taken in a specified direction. That is defined as

$$\Gamma(C) = \oint_C \mathbf{u} \cdot dl \tag{3-7}$$

where dl is an element of the contour.

The vorticity of an element of fluid is defined as the curl of its velocity vector

$$\boldsymbol{\omega} = \nabla \times \mathbf{u} \tag{3-8}$$

The vorticity contained in a fluid element is related to the circulation around the element. This relationship can be obtained from the Stoke's theorem.

$$\begin{aligned}\Gamma(C) &= \oint_C \mathbf{u}\cdot dl \\ &= \int_A (\nabla\times\mathbf{u})\cdot\mathbf{n}dA\end{aligned} \tag{3-9}$$

where A is the area defined by closed contour C and $\mathbf{n}$ is the unit normal to the surface. From the definition of the vorticity vector (3-8), the circulation may be expressed as

$$\Gamma(C) = \int_A \boldsymbol{\omega}\cdot\mathbf{n}dA \tag{3-10}$$

Flows in which $\boldsymbol{\omega}=0$ are called irrotational. For an irrotational flow, there exists a well-defined scalar function ϕ called the velocity potential, such that

$$\mathbf{u} = \nabla\phi \tag{3-11}$$

Therefore the equation of continuity (3-6) for an irrotational, incompressible flow becomes,

$$\nabla^2\phi = 0 \tag{3-12}$$

Equation (3-12) is known as the Laplace equation. From the above equations, it is clear that a fluid cannot move according to an arbitrarily assigned law of distribution of velocity. For the motion to be possible it is necessary that the equation of continuity should be satisfied. For irrotational motion of a fluid, the velocity potential ϕ shall satisfy the Laplace equation. Functions satisfying this equation, usually termed as Harmonic functions, have been well studied and can easily be solved numerically.

The Navier-Stokes equations (3.2) are derived on the basis of conservation of momentum. Suppose that the body force **B** is conservative. Then there exists a body

force potential, Ω, such that $\mathbf{B} = \nabla\Omega$. And if fluid is assumed to be incompressible, the Navier-Stokes equations may be re-written as follows;

$$\frac{\partial \mathbf{u}}{\partial t} + (\mathbf{u}\cdot\nabla)\mathbf{u} = \nu\nabla^2\mathbf{u} + -\nabla\left(\frac{p}{\rho} - \Omega\right) \tag{3-13}$$

since $\nabla\cdot(\nabla\mathbf{u} + \nabla\mathbf{u}^T) = \nabla^2\mathbf{u} + \nabla\cdot(\nabla\mathbf{u}^T) = \nabla^2\mathbf{u}$. Taking the curl of this equation and noting that the curl of the gradient of any scalar is zero, we can derive the vorticity transport equation;

$$\frac{\partial \boldsymbol{\omega}}{\partial t} + (\mathbf{u}\cdot\nabla)\boldsymbol{\omega} = (\boldsymbol{\omega}\cdot\nabla)\mathbf{u} + \nu\nabla^2\boldsymbol{\omega} \tag{3-14}$$

For two-dimensional flows, the vorticity vector $\boldsymbol{\omega}$ will be perpendicular to the plane of the flow, so that the first term on the right hand side will be zero. Then

$$\frac{\partial \boldsymbol{\omega}}{\partial t} + (\mathbf{u}\cdot\nabla)\boldsymbol{\omega} = \nu\nabla^2\boldsymbol{\omega} \tag{3-15}$$

This vorticity equation, in either the general form or a two-dimensional form, is used a great deal in discrete vortex methods and is used as a basis for most schemes modelling fluid vorticity.

If a fluid has no viscosity, $\nu = 0$, it is termed inviscid and the Navier-Stokes equations (3-13) reduce to a form of Eulers equation;

$$\frac{\partial \mathbf{u}}{\partial t} + (\mathbf{u}\cdot\nabla)\mathbf{u} = -\nabla(\frac{1}{\rho}p - \Omega) \tag{3-16}$$

Further simplification of equation (3-16) using the vector identity, $1/2\nabla(\mathbf{u}\cdot\mathbf{u}) = (\mathbf{u}\cdot\nabla)\mathbf{u} + \mathbf{u}\times(\nabla\times\mathbf{u}) = (\mathbf{u}\cdot\nabla)\mathbf{u}$, and equation (3-11) leads to

$$\nabla\left(\frac{\partial\phi}{\partial t}+\frac{1}{\rho}p-\Omega+\frac{1}{2}|\nabla\phi|^2\right)=0 \tag{3-17}$$

Integration of this equation gives the unsteady Bernoulli equation which may be written as follows

$$\frac{\partial\phi}{\partial t}+\frac{1}{\rho}p-\Omega+\frac{1}{2}|\nabla\phi|^2=f(t) \tag{3-18}$$

where *f(t)* is some function of time, *t*, which may be added after integration. For steady flow, the first term on the left side of the equation will be zero and *f(t)* will be constant along each streamline. This may be written as

$$\frac{1}{\rho}p-\Omega+\frac{1}{2}|\nabla\phi|^2=\text{constant} \tag{3-19}$$

If the velocity potential is determined, the pressure can be calculated directly from the Bernoulli equation.

3.2 Slender Body Approximation

Slender body approximation originated in the field of aerodynamics by Munk (1924) to predict the stability characteristics of airships. Jones (1946) applied the slender body assumption to determine the lift of a delta wing by considering an inviscid flow with no separation at sharp leading edges. Since then this method has been utilised for a variety problems in aerodynamics and ship hydrodynamics.

If the fluid is assumed to be steady, incompressible and inviscid, the governing equation of a disturbance velocity potential should be the three-dimensional Laplace equation (3-12), expressed in terms of a cartesian co-ordinate system as,

$$\frac{\partial^2\phi}{\partial x^2}+\frac{\partial^2\phi}{\partial y^2}+\frac{\partial^2\phi}{\partial z^2}=0 \tag{3-20}$$

If the flow is about a slender body, with the x directional length much bigger than dimensions in the other y and z directions, and lying closely parallel to the x-axis, the x directional streamwise derivative term $\partial^2\phi/\partial x^2$ can be neglected. Then the equation of motion reduces to the two dimensional Laplace equation in the cross-flow plane.

$$\frac{\partial^2\phi}{\partial y^2}+\frac{\partial^2\phi}{\partial z^2}=0 \tag{3-21}$$

And ϕ can be replaced by a two-dimensional potential in the y-z plane, as

$$\phi=\varphi(y,z:x) \tag{3-22}$$

Here x appears to emphasise that this potential will vary slowly along the body length, as a result of the change in the geometry of cross section and lateral motion.

3.3 The Complex Velocity

With the slender body approximation, it has been shown that the three-dimensional Laplace equation for flow around slender ships can be simplified to the two-dimensional Laplace equation. At this point it is advantageous to use the complex plane and to define a complex potential of the motion such that

$$W(Z)=\phi(Z)+i\psi(Z) \tag{3-23}$$

where ψ is the stream function of two dimensional incompressible flow and the complex variable $Z = y + iz$ is an arbitrary point in the two-dimensional plane. From the complex potential,

$$\frac{dW}{dZ}=\frac{dW}{dy}=\frac{\partial\phi}{\partial y}+i\frac{\partial\psi}{\partial y} \tag{3-24}$$

and since the velocity components v and w can be expressed in terms of either the velocity potential or the stream function, it follows that

$$v=\frac{\partial\phi}{\partial y}=\frac{\partial\psi}{\partial z}\quad,\quad w=\frac{\partial\phi}{\partial z}=-\frac{\partial\psi}{\partial y} \tag{3-25}$$

The complex potential therefore satisfies the Cauchy-Riemann equation and is an analytic function. Its derivative is

$$\frac{dW(Z)}{dZ}=\overline{V}(Z)=v(Z)-iw(Z) \tag{3-26}$$

where $\overline{V}$ is the conjugate of the complex velocity V. Thus, if complex potential is known, the complex velocity can be obtained directly from complex potential at any point as shown in equation (3-26)

3.4 The Complex Potential of Sources and Vortices

Using the slender body assumption, the flow around a ship can be modelled as a series of two-dimensional flows around transverse sections of the ship distributed along its length.

The flow fields of each hull section can then be modelled by superposition using source and vortex potentials. The drift motion of the ship and each hull section's growing and shrinking can be represented by arrays of sources. The complex potential for a source of strength m located at the point $Z = Z_v$ will be

$$W(Z)=\frac{m}{2\pi}\ln(Z-Z_v) \tag{3-27}$$

and a sink can be obtained by replacing m by $-m$ in the equation. From equation (3-23), the velocity potential and stream function can be written as

$$\phi = \frac{m}{2\pi}\ln(r) \quad and \quad \psi = \frac{m}{2\pi}\theta \tag{3-28}$$

where r and θ are the cylindrical co-ordinates, relative to the centre of the source. The complex velocity induced by a source is given by

$$\frac{dW}{dZ} = v - iw = \frac{m}{2\pi}(Z - Z_v)^{-1} \tag{3-29}$$

The point Z_v is a singular point at which the velocity is infinite, and as fluid flows radially outwards, the velocity decreases according to equation (3-29).

The flow separating from the surface of the ship can be modelled by arrays of discrete vortices embedded in an otherwise irrotational flow. The complex potential for a positive (counterclockwise) vortex of strength Γ at $Z = Z_v$ is

$$W(Z) = -i\frac{\Gamma}{2\pi}\ln(Z - Z_v) \tag{3-30}$$

where Γ takes the opposite sign for a negative vortex. From equation (3-23), the velocity potential and stream function can be written as

$$\phi = \frac{\Gamma}{2\pi}\theta \quad and \quad \psi = -\frac{\Gamma}{2\pi}\ln(r) \tag{3-31}$$

where r and θ are the cylindrical co-ordinates, relative to the centre of the source. The complex velocity induced by the vortex is given by

$$\frac{dW}{dZ} = v - iw = -i\frac{\Gamma}{2\pi}(Z - Z_v)^{-1} \tag{3-32}$$

This flow corresponds to a so-called free vortex. That means, for any closed contour which does not include the singularity, the circulation will be zero and the flow will be irrotational. All the circulation and vorticity associated with this type of vortex is concentrated at the singularity (Curry 1993).

3.5 The Infinite Row of Sources and Vortices

The complex potential due to an infinite row of equally spaced sources, each of strength m, at the points $(0, 0), (\pm a, 0), (\pm 2a, 0), \cdots, (\pm na, 0), \cdots$ is given by the formula (see Milne-Thomson 1960)

$$\begin{aligned} W(Z) &= \frac{m}{2\pi}\{\ln Z + \ln(Z-a) + \ln(Z+a) + \ln(Z-2a) + \ln(Z+2a)\cdots \\ &\qquad \cdots + \ln(Z-na) + \ln(Z+na) + \cdots\} \\ &= \frac{m}{2\pi}\ln\{Z(Z^2-a^2)(Z^2-2^2a^2)\cdots(Z^2-n^2a^2)\cdots\} \\ &= \frac{m}{2\pi}\ln\left\{\frac{\pi Z}{a}\left(1-\frac{Z^2}{a^2}\right)\left(1-\frac{Z^2}{2^2a^2}\right)\cdots\left(1-\frac{Z^2}{n^2a^2}\right)\cdots\right\} \\ &\quad + \frac{m}{2\pi}\ln\left\{\frac{a}{\pi}\cdot a^2\cdot 2^2a^2\cdots n^2a^2\cdots\right\} \end{aligned} \tag{3-33}$$

The constant term of equation (3-33) may be omitted, so that it can be written as

$$W(Z) = \frac{m}{2\pi}\ln\left\{\frac{\pi Z}{a}\left(1-\frac{Z^2}{a^2}\right)\left(1-\frac{Z^2}{2^2a^2}\right)\cdots\left(1-\frac{Z^2}{n^2a^2}\right)\cdots\right\} \tag{3-34}$$

Now, *sin(x)* can be expressed as an infinite product in the form

$$\sin(x) = x\left(1-\frac{x^2}{\pi^2}\right)\left(1-\frac{x^2}{2^2\pi^2}\right)\cdots\left(1-\frac{x^2}{n^2\pi^2}\right)\cdots \tag{3-35}$$

With equation (3-34) and (3-35), the complex potential for an infinite row of sources can be simplified as

$$W(Z) = \frac{m}{2\pi} \ln\left(\sin\frac{\pi Z}{a}\right) \tag{3-36}$$

The complex velocity at the point Z can then be written as

$$\frac{dW}{dZ} = v - iw = \frac{m}{2a}\cot\frac{\pi Z}{a} \tag{3-37}$$

Similarly, the complex potential due to an infinite row of point vortices of strength Γ, whose co-ordinates are, $(0, 0), (\pm a, 0), (\pm 2a, 0), \cdots$ is given by (see Milne-Thomson 1960)

$$W(Z) = -i\frac{\Gamma}{2\pi} \ln\left(\sin\frac{\pi Z}{a}\right) \tag{3-38}$$

The complex velocity at the point Z is then

$$\frac{dW}{dZ} = v - iw = -i\frac{\Gamma}{2a}\cot\frac{\pi Z}{a} \tag{3-39}$$

and the velocity v and w in y-z plane are

$$v = -\frac{\Gamma}{2a}\frac{\sinh(2\pi z/a)}{\cosh(2\pi z/a) - \cos(2\pi y/a)} \tag{3-40}$$

$$w = \frac{\Gamma}{2a}\frac{\sin(2\pi y/a)}{\cosh(2\pi z/a) - \cos(2\pi y/a)}$$

These line sources and vortices are very useful in the construction of the discrete vortex flow model in this study because the transformed rectangular domain has a periodic representation of the real domain. This will be explained in more detail in the construction of the proposed discrete vortex method given in Chapter 4.

3.6 Blasius' Theorem for Forces

The main purpose of a discrete vortex model is the determination of the forces acting on a body. The obvious way to find the force is to establish the velocity components from the complex potential and then determine the pressure distribution around the body using Bernoulli's equation. The force acting on the body can then be obtained by integrating the pressure over the body surface.

Alternatively, there is a simpler way to calculate the forces directly from the complex potential without finding pressure distribution around a body. This can be achieved on manipulation of Bernoulli's equation. The forces, Y and Z_F, in the y-z plane can be related to the pressure, p, via;

$$\begin{aligned} Y - iZ_F &= -\int_C p dz - i\int_C p dy \\ &= -i\int_C p(dy - i dz) \end{aligned} \tag{3-41}$$

where C is the body surface. The pressure may be eliminated from the equation by use of the Bernoulli equation (3-18). Then, using equation (3-26) and the fact that $\int_C \Omega dz = 0$ for any constant Ω around any closed contour C, the expressions for Y and Z_F becomes

$$Y - iZ_F = i\rho\int_C \left(\frac{\partial \phi}{\partial t} + \frac{1}{2}\frac{dW}{dZ}\overline{\frac{dW}{dZ}}\right)\overline{dZ} \tag{3-42}$$

Since the stream function is zero along the body surface and $\overline{(dW/dZ)dZ}$ is real and equal to its complex conjugate, which is $(dW/dZ)dZ$. It follows that we can write

$$Y - iZ_F = \frac{1}{2}i\rho\int_C \left(\frac{dW}{dZ}\right)^2 dZ + i\rho\frac{\partial}{\partial t}\oint_C \overline{W}d\overline{Z} \tag{3-43}$$

This is known as Blasius' theorem and refers to integrals round the contour of the body. The equation is very useful since if the complex potential for the flow around a body is known, then it is possible to evaluate the forces acting on the body by means of simple contour integrals. The contour integral in this equation is usually evaluated by use of the residue theorem.

3.7 The Complex Potential of a Circular Cylinder

A complex potential of a circular cylinder introduced into the flow field *f(Z)* can be described as

$$W(Z) = f(Z) + \overline{f}\left(\frac{r^2}{Z}\right) \tag{3-44}$$

where *r* is a radius of the circular cylinder. The complex point *Z* is outside the cylinder and r^2/Z is inside the cylinder. Equation (3-44) is called the circle theorem and satisfies all the boundary conditions for inviscid flow (Milne-Thomson 1960).

From the circle theorem (3-44), the complex potential for a circular cylinder placed in the stream V_∞ becomes

$$W(Z) = \left(Z + \frac{r^2}{Z}\right)V_\infty \tag{3-45}$$

As shown in Figure 3.1, if there are a number of vortices of strength Γ_v at the points Z_v in the exterior flow, the complex potential according to the circle theorem becomes

$$W(Z) = \left(Z + \frac{r^2}{Z}\right)V_\infty - \frac{i}{2\pi}\sum_v \Gamma_v \ln(Z - Z_v) + \frac{i}{2\pi}\sum_v \Gamma_v \ln(Z - Z_v^*) \tag{3-46}$$

where Z_v^* signifies the position of image vortices inside the cylinder at the locations

$$Z_v^* = r^2 / \overline{Z}_v \tag{3-47}$$

The second term on the right hand side of equation (3-46) is the contribution from vortices themselves, and the third term is the contribution from the image vortices inside the body that satisfy the boundary conditions on its surface as given by the circle theorem. For certain flows there may also be a vortex at the centre of the cylinder. In the present study the flows are started from rest and so there is no initial circulation on the body or vortex required at its centre. The complex potential for the circular cylinder has been adopted by various researchers (Sarpkaya 1968, Downie 1981 and Murray 1992).

The force on a circular cylinder subjected to a flow of velocity V_∞ may be calculated using a generalised Blasius' theorem together with knowledge of the location and circulation of the vortices in the flow, which can be found from the complex potential (3-46). Substitution of equation 3.46 into equation 3.43 leads to an expression for the complex force (Murray 1992),

$$Y - iZ_F = \rho\left\{2\pi r^2 \frac{\partial V_\infty}{\partial t} - i\sum_v \left(U_v - U_v^*\right)\Gamma_v + i\sum_v \left(Z_v^* + r\right)\frac{\partial \Gamma_v}{\partial t}\right\} \tag{3-48}$$

where U_v denotes the complex velocity of the vortex at Z_v and U_v^* is the complex velocity of the image vortex at Z_v^*. The first term on the right hand side of the equation is associated with the added mass of the cylinder. The second term represents the drag force due to the motion of the vortices and the last term represents the force due to the change of vortex strength.

Since different shapes may be transformed to a circular cylinder by conformal mapping, the Blasius' equation of a circular cylinder may be used to find the forces of each of a series of two-dimensional sections representing a ship.

The following chapter describes how these basic elements are used to construct a model for two-dimensional incompressible separated flows about bluff bodies. This discrete vortex model is then itself incorporated into a slender body model of a ship travelling with an angle of drift.

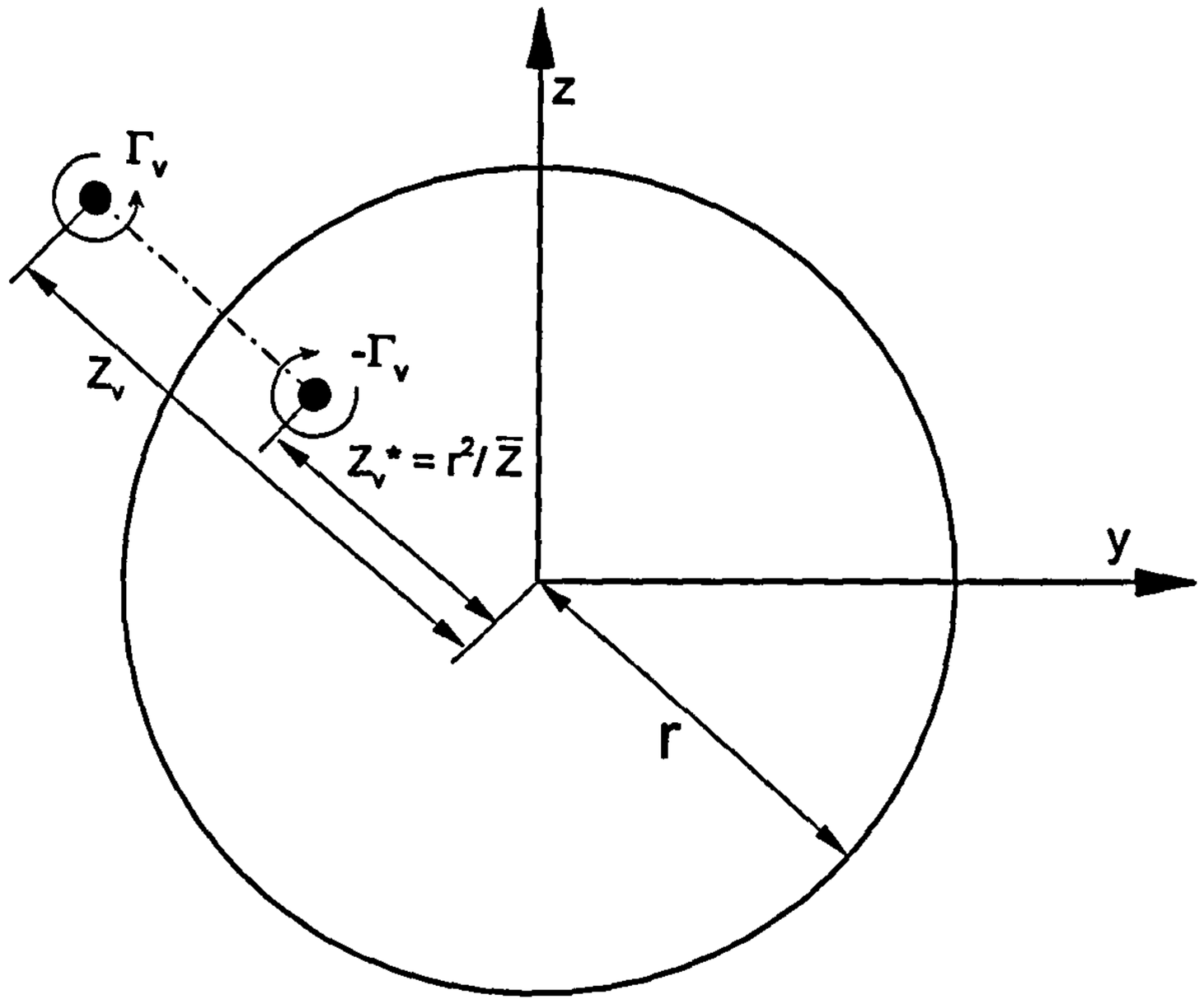

Figure 3.1: The representation of a vortex and an image vortex in a circular cylinder.

Chapter IV

THE PROPOSED DISCRETE VORTEX MODEL

4.1 Introduction

In this chapter the numerical model adopted for studying the flow around a drifting ship is described. The basic idea is that the ship is assumed to be a thin body so that the slender body approximation can be applied for an inviscid flow in which viscous effects are included and modelled by a vortex based method. The calculation is carried out on a grid based fluid domain and the velocity of each section is calculated at the grid nodes using the Biot-Savart law.

4.2 Slender Body Approximation

The flow around a ship is characterised as steady, incompressible and inviscid. Flow separation is represented by vortex sheets, which are modelled by the discrete vortex method. In this case, the governing equation for the disturbance velocity potential is the three-dimensional Laplace equation which can be written using a cartesian co-ordinate system as

$$\frac{\partial^2 \phi}{\partial x^2}+\frac{\partial^2 \phi}{\partial y^2}+\frac{\partial^2 \phi}{\partial z^2}=0 \qquad (4\text{-}1)$$

The co-ordinate system used for this study is shown in Figure 4.1. The x-axis is forward along the ship centreline, the y-axis is directed to the starboard side of the ship and the z-axis is vertically upward. The origin of the reference frame is located at

the intersection of the ship centre line plane and the waterline plane. The free surface is assumed to be level and flat, therefore the hull is modelled as a double body.

If the flow is about a slender body, for which the x directional length is much larger than its dimensions in the other y and z directions, and lying obliquely inclined to the x axis, the equation of motion reduces to the two-dimensional Laplace equation in the cross-flow plane.

$$\frac{\partial^2 \phi}{\partial y^2} + \frac{\partial^2 \phi}{\partial z^2} = 0 \tag{4-2}$$

Consistent with slender body theory, the hull is represented as a series of two-dimensional strips. Figure 4.2 shows the segmented upper sections of a double body model. The flow calculation for the ship is carried out on the upper part of a double body hull since both upper and lower parts are symmetric. The problem of the ship moving forward in the x-direction with velocity, $U_\infty \cos\beta$, at a drift angle β, is converted into a series of two-dimensional problems in which the strips experience both dilation and translation as the time marching procedure progresses from bow to stern.

On this basis, the problem in hand can be represented as a series of two-dimensional unsteady flows. The apparent time in the two-dimensional unsteady solutions may be related to the three-dimensional steady flow (Moore and Saffman 1973) by,

$$\frac{d}{dt} = U_\infty \cos\beta \frac{d}{dx} \tag{4-3}$$

4.3 General Description of the Method

For each strip, as the solution progresses along the ship, the section dilation, as shown in Figure 4.3 and 4.4, is modelled by a distribution of sources on the hull surface together with a second array of sources representing the section translation if hull is travelling with a drift angle. Figure 4.5 shows the normal velocity components of drift motion on the hull surface. Figure 4.3 and 4.4 show a normal velocity distribution for the growing and shrinking hull sections respectively as the solution progresses from bow to stern. The total source distribution, as shown in Figure 4.6, is found by the superposition of the two layers of sources.

Vortices are introduced into the flow to represent flow separation. If a hull has well defined shedding edges, such as the Wigley hull or the Block hull, single vortices and their reflected images below the free surface, together with their images internal to the cross section, are introduced at the points corresponding to the shedding edges, as shown in Figure 4.7. The positions and strengths of the vortices are simultaneously defined so as to satisfy the Kutta condition at each time step. The image vortices and their positions internal to the cross section are defined to satisfy boundary conditions on the body surface. The reflected image hull and image vortices are also introduced to satisfy a flat free surface condition.

In the case of the sections with continuous curvature, with no well-defined separation points, a continuous layer of discrete vortices is distributed around the section so as to satisfy a pointwise no-slip condition in the two-dimensional plane, and no separation point is specified. This approach is not intended to be a detailed model of the boundary layer separation, or of the boundary layer itself, but has been found to reproduce the gross features of the flow reasonably well in two-dimensional bluff body flow (Downie et al 1989).

This chapter mainly describes how the hull is modelled with well-defined separation points. The detailed numerical method for a hull without well-defined separation points, such as for the British Bombardier, the British Bombardier with a pram stern and the Series 60 hull, will be presented in Chapter 7.

As shown in Figures 4.7 and 4.8, each two-dimensional hull section and associated computational mesh in the real domain, the *Z*-plane, is mapped into the computational domain, the *S*-plane, by conformal transformation. The transformed computational domain has the advantage of being simple and invariant for all of the two-dimensional sections along the hull. Every calculation is carried out in the computational domain in which each vortex has a reflected and periodic image. The sources lie on the real axis of the computational plane and are also periodic. The transformed source distribution and vortices in the S-plane, corresponding to the *Z*-plan, are shown in Figure 4.8.

The solution proceeds by an apparent time-marching solution along the hull in which the cross-flow velocity at each time-step is computed from the two-dimensional flow at the corresponding section as shown in Figure 4.9. At each time step the vortices are carried along the hull by the axial flow field using equation (4-3) and convected away from it in the transverse direction by a cross flow computed from the complex velocity in the *S*-plane. The complex velocity is calculated on each grid node by the Biot-Savart law and distributed to neighbouring vortices using bi-linear interpolation.

Figure 4.10 shows the basic flow chart of the algorithm for the discrete vortex method. The detailed description of the method will be explained in the following sections.

4.4 Boundary Conditions in the Real Plane

The complex potential function at each cross-flow plane in the *Z*-plane, Figure 4-7, must satisfy following boundary conditions.

(1). Body boundary condition

The hull surface is impermeable so all normal velocities on the body must be equal to normal component of the hull surface movement. The normal

components of the velocities are represented by a source distribution around each sectional hull surface.

(2). Free surface boundary condition

The free surface is regarded as flat so the hull is modelled as a double body. The normal velocity along the free surface is assumed to be zero. A study by Wong and Calisal (1996), has shown that the free surface has very little influence on the trailing vortices.

(3). Outer boundary condition

The flow is undisturbed at infinity. The disturbance velocity at infinity is zero.

(4). Separation condition.

In the case of the hull with well-defined shedding edges, the Kutta condition has been applied. This means that infinite velocities do not occur at shedding edges, or equivalently, the flow separates smoothly from the edges.

(5). Zero net force condition

The force acting on each combined feeding sheet and concentrated vortex must have zero net force, since only the ship can sustain forces.

The zero net force condition can be expressed by the Brown and Michael equation (Brown and Michael 1955) as

$$\frac{dZ_v}{dt} = V(Z_v) - \frac{(Z_v - Z_p)}{\Gamma_v}\frac{d\Gamma_v}{dt} \tag{4-4}$$

where Γ_v is the strength of a vortex located at Z_v and Z_p is a separation point on the hull surface. However, for shed vortices, $d\Gamma_v / dt = 0$, thus`

$$\frac{dZ_v}{dt} = V(Z_v) \tag{4-5}$$

where $V(Z_v)$ is the appropriate solution to the Laplace equation in the cross-flow plane given by

$$V(Z_v) = v(Z_v) + iw(Z_v) = \left(\overline{\frac{dW(Z_v)}{dZ}}\right) \tag{4-6}$$

and an overbar represents a complex conjugate. The vortex at Z_v will be convected away to the next section by the cross flow $V(Z_v)$ in equation (4-5). The detailed procedure is described in section 4.10.

4.5 Hull Transformation

In the case of a two-dimensional flow calculation for an arbitrary body, a well-known and frequently used conformal mapping is that which takes an arbitrary body into a circular cylinder. The circular cylinder has the advantage that for the potential flow calculation it is easily modelled. Ikeda and Himeno (1981) used the Lewis transformation for mapping ship-like sections to a circular cylinder. Murray (1992) and Naylor (1982) have investigated an anode flow and a bluff body flow, respectively, from a transformed circular cylinder calculation.

However, in the case of the varying shape of hull sections occurring in the time marching solutions of the present study, the transformed cylinder radius also changes with each hull section. For this reason, each hull section and associated mesh in the Z-plane is mapped into a further simpler rectangular working plane, the S-plane, through intermediate transformations depending on the hull type.

For the Wigley hull, the hull section in the Z-plane, ($Z = y + iz$) is mapped into the rectangular grid in the S-plane, ($S = \eta + i\zeta$) by a two stage conformal transformation as shown in Figure 4.11.

$$Z = iS1 + i\frac{(k^2-1)}{3}\frac{r^2}{S1} + \cdots\cdots$$
$$S1 = r \cdot \exp\left(i\frac{\delta\theta}{2}\right) \cdot \exp(i\alpha S) \tag{4-7}$$

where r = the radius of a cylinder, $\delta\theta = \pi/(nk\text{-}1)$, k = draft/r in the $S1$-plane, and $\alpha = 2\pi/R$ in the S-plane. The computational mesh in the S-plane is rectangular and periodic and of length R. The line $\eta = 0$ represents the hull surface, and R is the width of the sectional body surface when represented in the S-plane. The η-axis in S-plane contains repeated representations of the surface of the hull sections, and a similar property holds for each line parallel to it, as displayed in Figure 4.11.

The rectangular working plane has the advantage of being both rectangular and invariant for all of the two-dimensional hull sections. This grid can be used to incorporate a finite difference method for a diffusion calculation to the proposed discrete vortex method later. A finite difference calculation is more easily performed in a cartesian rectangular grid, since other grid systems, such as a radially expanding polar grid system ($S1$-plane) lead to very complicated finite difference formulae (Murray 1992).

The detailed calculation and transformation of other hull types will be explained in the following chapters.

4.6 Boundary Conditions in the Transformed Plane

Following the conformal transformation, the boundary conditions in the Z-plane should be transformed to give the corresponding boundary conditions in the transformed S-plane as shown in Figure 4.8. These boundary conditions in the S-plane can be written as

(1). Body boundary condition

The hull surface in the Z-plane is transformed into $\zeta = 0$ in the S-plane. All normal components of velocity in the real η-axis are equal to the normal component of the transformed hull surface movement, which are represented by a source distribution around each sectional hull surface.

(2). Free surface boundary condition

The free surface in the Z-plane, which is regarded as flat, is transformed into the image ζ-axis, where the normal component of velocity in the corresponding ζ-axis is zero. This means there is no η directional velocity on the corresponding free surface line of the ζ-axis.

(3). Outer boundary condition

The flow is undisturbed at infinity. The disturbance velocity at infinity of the ζ-axis is zero.

(4). Separation condition.

The separation points in the Z-plane are transformed into the corresponding points in the S-plane. The Kutta condition is applied at the separation point in the S-plane and this condition means the velocities at the separation points are zero.

(5). Zero net force condition

The force acting on each combined feeding sheet and concentrated vortex must have zero, since only the ship can sustain forces.

The zero force condition also has to be satisfied in the transformed S-plane. The hull section in the Z-plane varies along the x-axis. It is therefore necessary for the transformed equation to be a function of the x-axis, which is the function of time t from equation (4-3), as well as of the position of the S-plane. That is

$$\frac{dZ}{dt} = \frac{\partial Z}{\partial S}\frac{dS}{dt} + \frac{\partial Z}{\partial t} \tag{4-8}$$

which can be rearranged as

$$\frac{dS}{dt} = \left(\frac{dZ}{dt} - \frac{\partial Z}{\partial t}\right)\frac{\partial S}{\partial Z} \tag{4-9}$$

from which the zero force condition for each vortex system, located at S_v, becomes;

$$\frac{dS_v}{dt} = V(S_v) = \left(\frac{dZ_v}{dt} - \left.\frac{\partial Z_v}{\partial t}\right|_{S_v}\right)\frac{\partial S_v}{\partial Z_v} \tag{4-10}$$

The new vortex position at the next time step in the S-plane is found using this vortex velocity equation (4-10).

4.7 Calculation of Source Strengths

From the body boundary condition, the dilation of the hull surface and drift motion of a ship section can be represented by a distribution of sources. The normal velocity on the body in each of the two-dimensional Z-planes is due to the rate of the change of body sections and the drift motion as the time marching process progresses. The normal velocities, V_n, on the hull surface at each cross section can be defined as follows,

$$V_n = \frac{-U_\infty}{\sqrt{1+(dy/dz)^2}}\left(\frac{dy}{dx}\cos\beta \pm \sin\beta\right) \tag{4-11}$$

with $y(x,z)$ defining the sectional hull shape (Wong 1994). The first term of the right hand side represents the sectional hull dilation, and the second term represents the sectional translation subject to drift motion. The positive direction of the normal velocity is taken as pointing out of the hull surface.

The normal velocity, V_n, in the Z-plane can be related to the source distribution laid on the η-axis in the computational plane as

$$S_n = \overline{\left(\frac{im(\eta)}{2}\right)}$$

$$V_n = \left(\frac{im(\eta)}{2}\frac{dS}{dZ}\right) \tag{4-12}$$

$$m(\eta) = -i2\overline{(V_n)}\frac{dZ}{dS}$$

where S_n represents the normal velocity component induced by the source distribution in the S-plane. $m(\eta)$ is the source strength distributed on the η-axis in the computational domain. Sources have been distributed on both grid nodes and at the centres of the grid nodes to get a better representation of the body movement.

With the combination of source and vortex potentials, which have already been described in section 3.4, the complex potential in the computational plane is given by

$$W(S) = \sum_{\nu=1}^{N_\nu} \frac{-i\Gamma_\nu}{2\pi} \ln\left(\frac{S - S_\nu}{S - \bar{S}_\nu}\right) + \int_{-\infty}^{\infty} \frac{m(\eta)}{2\pi} \ln(S - \eta) d\eta \tag{4-13}$$

where the first term on the right hand side of the equation refers to an array of N_ν discrete vortices of strength Γ_ν, and their images located at S_ν and $\bar{S}_\nu$ respectively. The image vortices in the computational plane are also defined so as to satisfy the boundary condition on the body surface, which lies on the η-axis of the S-plane. The second term on the right refers to the source distribution of strength $m(\eta)$. The reason for the infinite integral associated with the source distribution is that the transformed computational domain is periodic.

4.8 Introduction of Discrete Vortices into the Flow

After the potential flow analysis at each time step, new nascent vortices are introduced near each of the separation edges. The nascent vortex location and strength can be found by satisfying the Kutta condition at each separation point. The Kutta condition is satisfied when the flow velocities at the separation points on the real hull section are finite. Since the singularity in the transformation occurs at the separation points, the velocities at the corresponding separation points in the computational domain must be zero, as shown below,

$$\left.\frac{dW(S)}{dS}\right|_{S=S_p} = 0 \tag{4-14}$$

where, S_p is a separation point in the S-Plane and there may be one or more of these points, depending on the hull type.

To satisfy the Kutta condition, a parameter must be used to determine where the nascent vortex point should be introduced. The location of the nascent vortex relative to the shedding edge depends on time step size, shedding edge angle, free stream velocity and the location of all the other vortices already in the flow field. There are various approaches for implementing the Kutta condition for a body with a previously defined separation point, and these can be classified in two ways.

1. The position of the nascent vortex is fixed in advance and its strength chosen so that the Kutta condition, equation (4-14), is maintained.

2. The strength of the nascent vortex is calculated in advance from

$$\Gamma_v = \frac{1}{2} V_s^2 t \tag{4-15}$$

and its position is determined so as to satisfy the Kutta condition (Fage and Johansen 1927, 1928). V_s is the velocity at some defined point near to the separation point.

In both approaches, there is only one parameter to be determined.

Clement (1973) used introduction method (2) to model vortex flow behind a square-based section. V_s is determined at the outer edge of the boundary layer above the separation points and this velocity determined the rate of vortex shedding into the shear layers through the equation (4-15). He introduced a parameter, the distance between the separation point and the introduction point, and studied the effect of varying the parameter. The calculated Strouhal numbers were relatively insensitive to changes of the parameter and agreed well with experimental results presented by Bearman (1965). Sarpkaya (1975) also studied the flow over an inclined flat plate using introduction method (2). The V_s term for equation (4-15) was calculated by averaging the velocities of four previous vortices shed, and the position at which a new vortex appears was allowed to vary with time. The method predicted fairly well the Strouhal numbers and the kinematic features of the flow. The calculated normal-force coefficients were 20% larger than those obtained experimentally by Fage and Johanson (1927).

Kiya and Arie (1977) used introduction method (1) to investigate vortex shedding behind an inclined flat plate. They studied the effect of changing the distance between the positions of the nascent vortices and the edges of the plate, and showed that the varying distance did not affect either the Strouhal number or the nature of vortex-cluster formation, but did affect the time-averaged drag coefficient.

Method (1) is adopted in the present study and the initial location of the nascent vortex was fixed according to the hull types. In the case of a flat plate hull, the nascent vortex point is fixed along the hull and located a small distance above the separation point. The methods adopted for other hull types will be described in succeeding chapters.

4.9 Distribution of Vortex Circulation to Grid Nodes

After their introduction into the flow, all vortices are appropriately distributed over the surrounding grid nodes. Since the nodal velocities are to be calculated, the nodal circulation distribution is necessary. This method is known as the vortex-in-cell or cloud-in-cell method and has been used by many researchers. It has the advantage of reducing computing time for calculations involving large vortex distributions (Christiansen 1973, Meng and Thomson 1978, Baker 1979, Rottman et al 1987 and Murray 1992). This method also has the advantage of avoiding vortex singularities during the Biot-Savart velocity calculation, since the inter nodal distances (vortices distances) are fixed and always finite.

Since Γ_v, located at S_v, is not in reality a discrete vortex but only a simplified representation of the local distributed vorticity, the vortex strength Γ_v can be distributed to its four surrounding grid nodes. A bi-linear interpolation (area weighting) scheme, based on the relative distance of each vortex from its surrounding nodes, is used for the distribution. As illustrated in Figure 4.12, the surrounding nodes are identified as

$$N_1 = S_{j,k}, \quad N_2 = S_{j,k+1}, \quad N_3 = S_{j-1,k}, \quad N_4 = S_{j-1,k+1} \tag{4-16}$$

The parameters, with grid scale dimensions h,

$$\begin{aligned} \lambda_v &= \Re e(S_v - N_1)/h \\ \mu_v &= \Im m(S_v - N_1)/h \end{aligned} \tag{4-17}$$

represent the ratio of the vortex real, $\Re e$, and image, $\Im m$, positions relative to the node, $S_{j,k}$ and to the sides of the grid element respectively. The total area of any grid element is given by

$$A_t(v) = A_1 + A_2 + A_3 + A_4 = h^2 \tag{4-18}$$

The areas of the element's sub-regions, shown in Figure 4.12, are given by,

$$\begin{aligned} A_1(v) &= (1-\lambda_v)(1-\mu_v)h^2 \\ A_2(v) &= \lambda_v(1-\mu_v)h^2 \\ A_3(v) &= (1-\lambda_v)\mu_v h^2 \\ A_4(v) &= \lambda_v\mu_v h^2 \end{aligned} \tag{4-19}$$

These equations act as the weighting functions for distributing the vortex strength and a measure of the relative closeness of a vortex to each of its surrounding nodes. The proportion of the total circulation assigned to each node is given as follows:

$$\begin{aligned} P_1(v) &= A_1(v)/A_t(v) = (1-\lambda_v)(1-\mu_v) \\ P_2(v) &= A_2(v)/A_t(v) = \lambda_v(1-\mu_v) \\ P_3(v) &= A_3(v)/A_t(v) = (1-\lambda_v)\mu_v \\ P_4(v) &= A_4(v)/A_t(v) = \lambda_v\mu_v \end{aligned} \tag{4-20}$$

Using the above area ratio equations, the distributed vortex strength at the surrounding grid nodes may be expressed as

$$\begin{aligned} \Gamma_{j,k}(v) &= P_1(v)\Gamma_v \\ \Gamma_{j,k+1}(v) &= P_2(v)\Gamma_v \\ \Gamma_{j-1,k}(v) &= P_3(v)\Gamma_v \\ \Gamma_{j-1,k+1}(v) &= P_4(v)\Gamma_v \end{aligned} \tag{4-21}$$

where $P_1(v)+P_2(v)+P_3(v)+P_4(v)=1$. This equation ensures that the nearer the vortex position to the grid node the larger the portion of vortex strength to be distributed on it.

4.10 Calculation of Velocities

After distributing the vortices onto the neighbouring grid nodes, it is necessary to calculate complex velocity at each grid node. As explained in section 3.3, the

complex velocity at any point can be easily calculated from the complex potential at the point. Since the calculation of velocity will be carried out at the grid nodes, the circulation of each vortex is distributed at each relevant grid node as described in previous section. The velocity potential $W(S)$ described in equation (4-13) can be rewritten for the grid nodes as

$$W(S)=\frac{-i}{2\pi}\left[\sum_{S_{j,k}\neq S}\Gamma_{j,k}\ln\left(S-S_{j,k}\right)-\sum_{S_{j,k}}\Gamma_{j,k}\ln\left(S-\overline{S}_{j,k}\right)\right] + \int_{-\infty}^{\infty}\frac{m(\eta)}{2\pi}\ln(S-\eta)d\eta \tag{4-22}$$

and complex velocity at the grid point S is given by

$$\frac{dW(S)}{dS}=\frac{-i}{2\pi}\left[\sum_{S_{j,k}\neq S}\Gamma_{j,k}\left(S-S_{k,j}\right)^{-1}-\sum_{S_{j,k}}\Gamma_{j,k}\left(S-\overline{S}_{k,j}\right)^{-1}\right] + \int_{-\infty}^{\infty}\frac{m(\eta)}{2\pi(S-\eta)}d\eta \tag{4-23}$$

As shown in Figures 4.8 and 4.11, the transformed domain is a periodic representation of the Z-plane. In other words, the η-axis contains repeated representations of the body surface, occurring with a period R, and a similar property holds for each line parallel to it.

The velocity calculation in hand is not easy by the reason of the infinite periodic representation of the transformed domain. However the velocity potential can be treated as infinite row of equidistant vortices and sources, which have been described in section 3.5. From the complex potential equations (3-36) and (3-38) of infinite line sources and vortices, the disturbance velocity potential (4-22) may be written as

$$W(S)=\frac{-i}{2\pi}\left[\sum_{S_{j,k}\neq S}\Gamma_{j,k}\ln\sin\frac{\pi(S-S_{j,k})}{R}-\sum_{S_{j,k}}\Gamma_{j,k}\ln\sin\frac{\pi(S-\overline{S}_{j,k})}{R}\right] \qquad (4\text{-}24)$$
$$+\int_{S_{1,1}}^{S_{1,2nk-1}}\frac{m(\eta)}{2\pi}\ln\sin\frac{\pi(S-\eta)}{R}d\eta$$

and the complex velocities at the grid node S are

$$\frac{dW(S)}{dS}=\frac{-i}{2\pi}\left[\sum_{S_{j,k}\neq S}\Gamma_{j,k}\left(\cot\frac{\pi(S-S_{j,k})}{R}\right)-\sum_{S_{j,k}}\Gamma_{j,k}\left(\cot\frac{\pi(S-\overline{S}_{j,k})}{R}\right)\right] \qquad (4\text{-}25)$$
$$+\int_{S_{1,1}}^{S_{1,2nk-1}}\frac{m(\eta)}{2\pi}\cot\frac{\pi(S-\eta)}{R}d\eta$$

In the Z-plane, vortices are convected to the next section according to the vortex velocity $V(Z_v)$ described in section 4.4. Since the transformed S-plane is a function of both the time and the position of the Z-plane, as described in section 4.6, the vortex movement to the next time step in the S-plane can be described from equation (4-10) as

$$\frac{dS_v}{dt}=V(S_v)=\left(\frac{dZ_v}{dt}-\left.\frac{\partial Z_v}{\partial t}\right|_{S_v}\right)\frac{\partial S_v}{\partial Z_v} \qquad (4\text{-}26)$$

Since the complex velocity calculation is carried out at the grid nodes, the vortex velocity $V(S_v)$ should be calculated at the grid nodes so equation (4-26) can be written as

$$\frac{dS_{j,k}}{dt}=\left(\frac{dZ_{j,k}}{dt}-\left.\frac{\partial Z_{j,k}}{\partial t}\right|_{S_{j,k}}\right)\frac{\partial S_{j,k}}{\partial Z_{j,k}} \qquad (4\text{-}27)$$

The first term on the right can be found from equations (4-5), (4-6) and (4-25) by

$$\frac{dZ_{j,k}}{dt} = \overline{\frac{dW(Z_{j,k})}{dZ}} = \overline{\left(\frac{dW(S_{j,k})}{dS}\right)\frac{dS}{dZ}} \tag{4-28}$$

The second term on the right in equation (4-27) is the required apparent rate of change in $Z_{j,k}$, over a time step with reference to a point $S_{j,k}$. Since the grid point $S_{j,k}$ in the S-plane does not change with time, this term can be found by the simple equation,

$$\left.\frac{\partial Z_{j,k}}{\partial t}\right|_{S_{j,k}} = \frac{Z_{j,k}^{n+1} - Z_{j,k}^{n}}{\Delta t} \tag{4-29}$$

where $Z_{j,k}^{n+1}$ is the grid node for the following time step in the Z-plane corresponding to the same grid point $S_{j,k}$. Δt is the size of the time step used and can be written, from equation (4-3), as

$$\Delta t = \frac{\Delta x}{U_\infty \cos\beta} \tag{4-30}$$

The vortex velocity at the grid node is calculated from equation (4-27). For the motion of the actual vortices, the vortex velocity at S_v is required and it may be found through re-application of the bi-linear interpolation.

$$V(S_v) = P_1(v)V(N_1) + P_2(v)V(N_2) + P_3(v)V(N_3) + P_4V(N_4) \tag{4-31}$$

where the area ratios, P, are those defined by equation (4-20) and the grid node points are those surrounding the vortex, as depicted in Figure 4.12.

With the calculation of all the vortex velocities, the vortex movement over the next hull section can be calculated using a first order forward difference scheme in apparent time. The new vortex position at the next time step can be found by

$$S_v^{n+1} = S_v^n + V(S_v)\Delta t \tag{4-32}$$

where Δt is the size of time step used. The preceding operations represent a complete time step (except for the force calculation) and this process may be repeated until the final hull section is reached as shown in Figure 4.10.

4.11 Calculation of Forces

When the flow field is known, the dynamic surface pressure p on the hull surface can be calculated from the Bernoulli equation;

$$p = P - P_\infty = \frac{1}{2}\rho U_\infty^2 - \frac{1}{2}\rho U_t^2 \tag{4-33}$$

and

$$U_\infty^2 = (U_\infty \cos\beta)^2 + (U_\infty \sin\beta)^2$$

$$U_t^2 = \left(U_\infty \cos\beta + \frac{\partial\phi}{\partial x}\right)^2 + \left(\frac{\partial\phi}{\partial y}\right)^2 + \left(\frac{\partial\phi}{\partial z}\right)^2 \tag{4-34}$$

where ϕ is the velocity potential and the pressure coefficient Cp is

$$Cp = \frac{p}{1/2\rho U_\infty^2} \tag{4-35}$$

Noting that

$$\frac{dW}{dZ}\frac{\overline{dW}}{dZ} = \left(\frac{\partial\phi}{\partial y}\right)^2 + \left(\frac{\partial\phi}{\partial z}\right)^2 \tag{4-36}$$

And with the slender body assumption Cp can be reduced to

$$Cp = -\frac{1}{U_\infty^2}\left[\left(2U_\infty \cos\beta \frac{\partial\phi}{\partial x}\right) - (U_\infty \sin\beta)^2 + \left(\frac{dW}{dZ}\frac{\overline{dW}}{dZ}\right)\right] \tag{4-37}$$

or

$$Cp = -\frac{1}{U_\infty^2}\left[\left(2U_\infty \cos\beta \frac{\partial\phi}{\partial x}\right) - (U_\infty \sin\beta)^2 + \left(\frac{dW}{dS}\frac{\overline{dW}}{dS}\right)\left(\frac{dS}{dZ}\frac{\overline{dS}}{dZ}\right)\right] \tag{4-38}$$

The first term on the right represents the linear thin wing approximation and the subsequent terms represent the contribution from two dimensional cross flow.

The hydrodynamic lateral force Y of any given two-dimensional hull section can be calculated by integrating Cp over its girth (S_B)

$$Y(x) = \frac{1}{2}\rho U_\infty^2 \int_{S_B} Cp n_y dS \tag{4-39}$$

As explained in section 3.6, the lateral force on each two-dimensional hull section can be obtained by direct integration of the pressure on the hull surface (4-39) or by the application of the Blasius' equation (3-43). The latter is generally preferred because, providing complex potential is known, it is possible to calculate the force directly from the complex potential. The former is useful for checking Blasius' theorem or for finding pressure distributions around the surface.

As shown by Sarpkaya (1975) and Murray (1992), the force on a two-dimensional body of any shape can be calculated using the transformed circular cylinder. The generalised Blasius' equation for the transformed circular cylinder in the $S1$-plane can be expressed, from equation (3-48), as

$$Y - iZ_F = \rho\left[4\pi r^2 C_M \frac{\partial V_\infty}{\partial t} - i\sum_{\nu=1}^{N_\nu}\left(U1_\nu - U1_\nu^*\right)\Gamma_\nu + i\sum_{\nu=1}^{N_\nu}\left(S1_\nu^* + r\right)\frac{\partial\Gamma_\nu}{\partial t}\right] \tag{4-40}$$

where $U1_\nu$ represents the complex velocity of the vortex located at $S1_\nu$ and $U1_\nu^*$ is the complex velocity of its image at $S1_\nu^*$ in the $S1$-plane. The image vortex position $S1_\nu^*$

inside the cylinder, given by equation (3-47), is defined as $S1_v^* = r^2 / \overline{S1}_v$. C_M is the potential flow value of the inertia coefficient in an unbounded flow, which depends on the motion and the shape of the body, and is 1.0 for an infinitely thin flat plate in an in-line flow.

The first term on the right side of equation (4-40) is associated with the added mass of the body. The second term represents the force due to the motion of vortices and the last term represents the force due to the changing strength of the vortices with time. The last term is only applicable to the newly introduced nascent vortices (Sarpkaya 1968) because their strength grows from 0 to Γ over the first time step. All other vortices in the flow are considered to have an unchanging strength Γ. Since the first term is only applied to time dependent flow, the expression for the uniform flow can be simplified as

$$Y - iZ_F = \rho\left[-i\sum_{v=1}^{N_v}\left(U1_v - U1_v^*\right)\Gamma_v + i\sum_{v=1}^{N_v}\left(S1_v^* + r\right)\frac{\partial\Gamma_v}{\partial t}\right] \tag{4-41}$$

All of the two-dimensional lateral forces at each section in this study are calculated using Blasius' equation (4-41) for a circular cylinder in the transformed $S1$-plane. The lift force Z_F in the present model is zero because the hull is assumed to be a double body and consequently the flow is symmetric along the free surface.

The hydrodynamic lateral force Y_s and yaw moment N_s on a ship can be calculated by integrating the sectional force Y along the hull's length (L):

$$\begin{aligned} Y_s &= \int_{L/2}^{L/2} Y(x)dx \\ N_s &= \int_{L/2}^{L/2} Y(x)\cdot x dx \end{aligned} \tag{4-42}$$

The non-dimensional form of the lateral force and yaw moment coefficients can then be written as

$$Y_s' = \frac{Y_s}{1/2\rho U_\infty^2 LT}$$
$$N_s' = \frac{N_s}{1/2\rho U_\infty^2 L^2 T} \tag{4-43}$$

where T is the hull draft. The calculated lateral force and yaw moment in equation (4-43) are induced by flow separation and are equal to zero if there is no separation along the hull.

To find the total lateral force and yaw moment, the forces contributed by the attached flow (with no flow separation) should be added to the forces associated with the trailing vortices.

In the case of a flat plate hull, the non-dimensional form of the attached flow lateral force Y_a' and yaw moment N_a' can be calculated by the direct application of the low aspect ratio-lifting surface theory, which can be expressed (see Newman 1977) as

$$Y_a' = \pi\beta A_r$$
$$N_a' = 1/2\pi\beta A_r \tag{4-44}$$

where β is the angle of the drift motion and A_r is the aspect ratio ($A_r = T/L$).

In the case of the Wigley hull and the block hull, the attached lateral forces are the same as a flat plate even though the distributions of forces along the length are different. The attached lateral forces are entirely dependent upon the stern shapes, which are the same as a flat plate for both hulls. The attached yaw moments of the hulls cannot be found straightforwardly by reason of the different force distributions along the hulls. The force distributions can be calculated by the slender-body strip method, which is based on the horizontal zero-frequency-added mass coefficient C_H for each section along the hull (Clarke 1972). The added mass of the two-dimensional section can be calculated directly from the transformation of a circular cylinder. The detailed method for general hull forms will be described in the following chapters.

By adding a contribution associated with the trailing vortex, equation (4-43), and a contribution from attached flow, equation (4-44), the non-dimensional form of total lateral force Y' and yaw moment N' acting on the hull can be found by

$$Y' = Y'_s + Y'_a$$
$$N' = N'_s + N'_a \tag{4-45}$$

The following chapter describes the development of a discrete vortex method applied, as a preliminary calculation to a simple flat plate, and to a Wigley hull moving with a drift motion. The calculated results will be compared with existing data obtained from the calculations and experiments of other researchers for the validation of the method developed. The draft and the length of the flat plate is the same as that of the Wigley hull, so that the thickness effects of the Wigley hull on the lateral force and yaw moment will be studied by comparing the results obtained from both hulls.

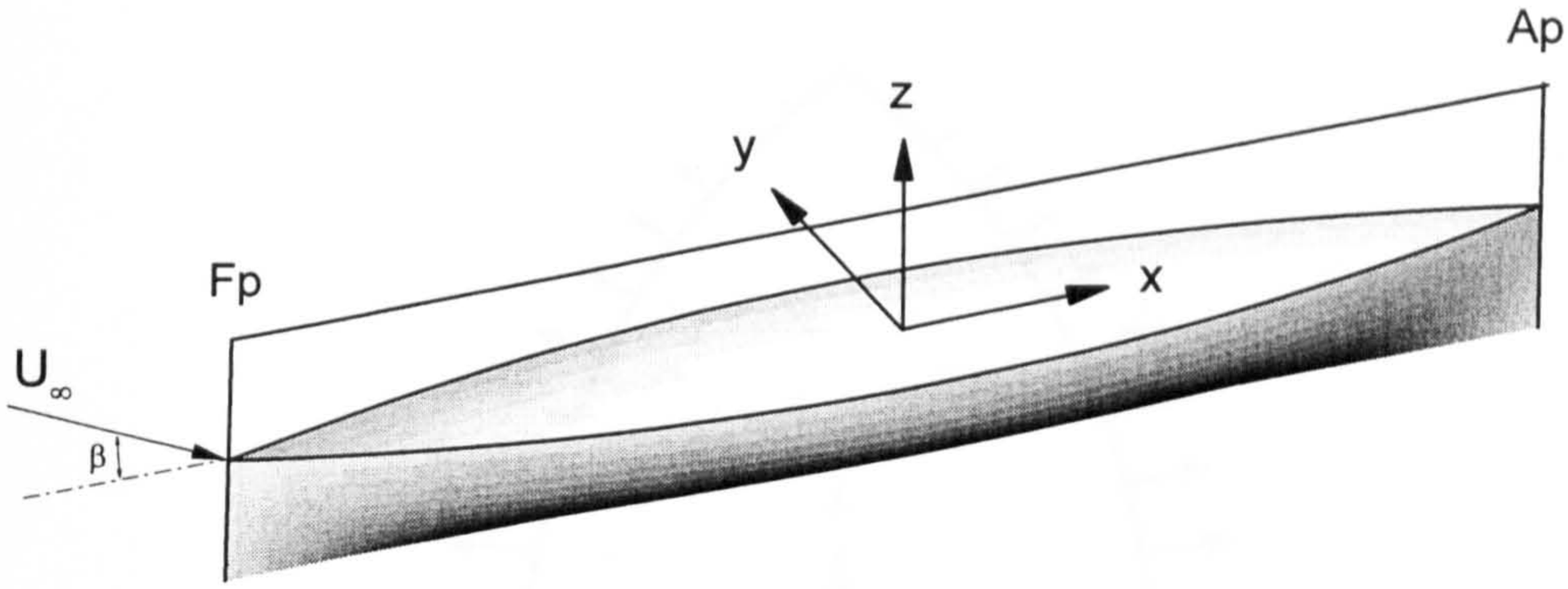

Figure 4.1: Co-ordinate system of a double body hull.

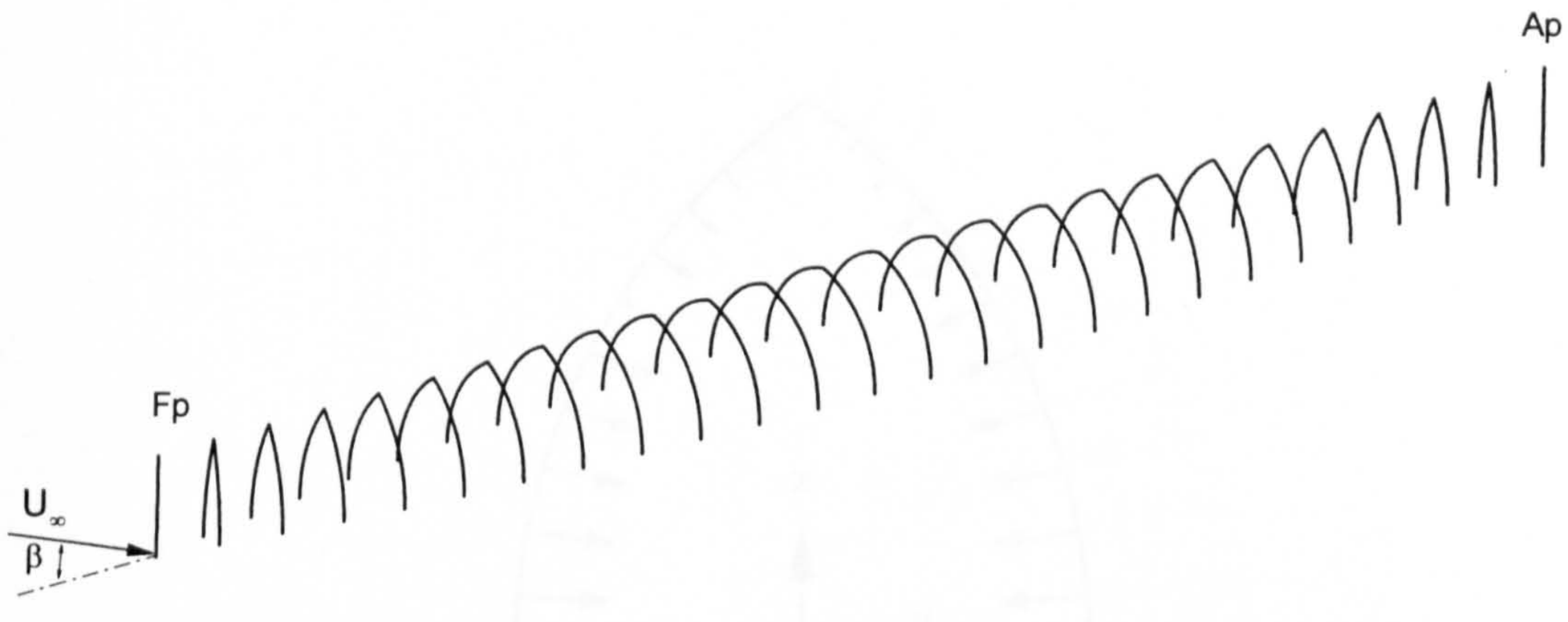

Figure 4.2: The divided two-dimensional hull sections.

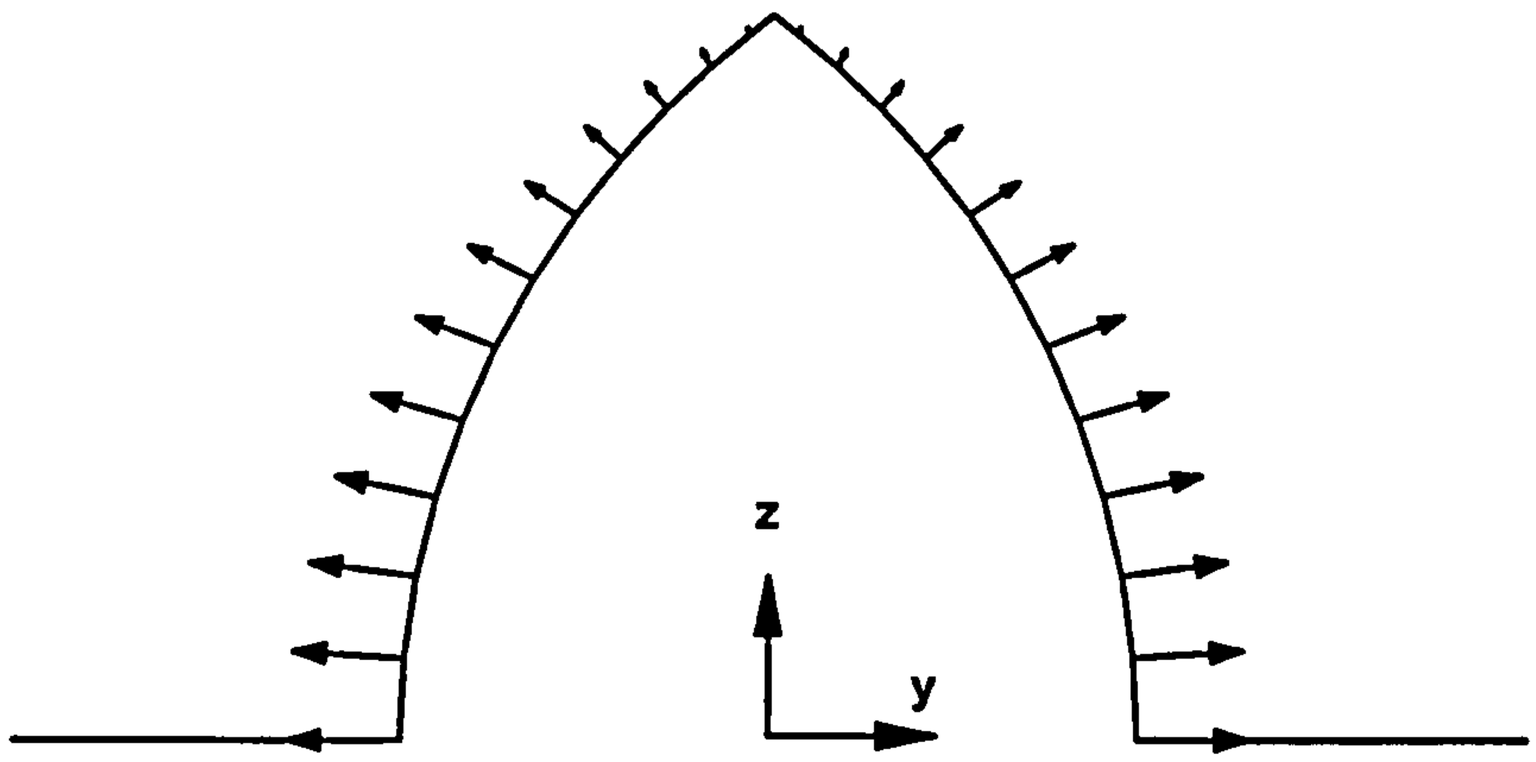

Figure 4.3: Normal velocity distribution on the growing hull surface.

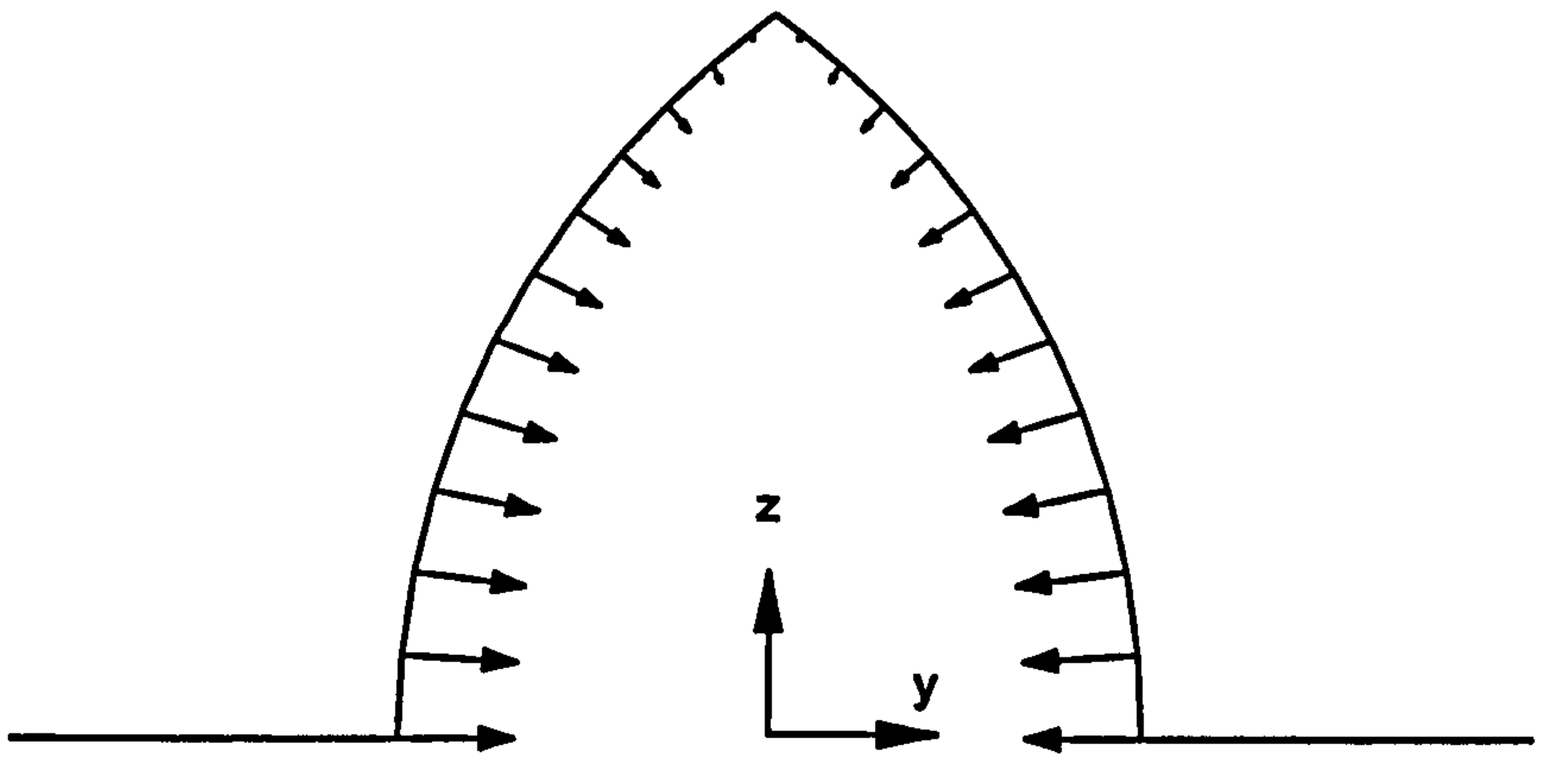

Figure 4.4: Normal velocity distribution on the shrinking hull surface.

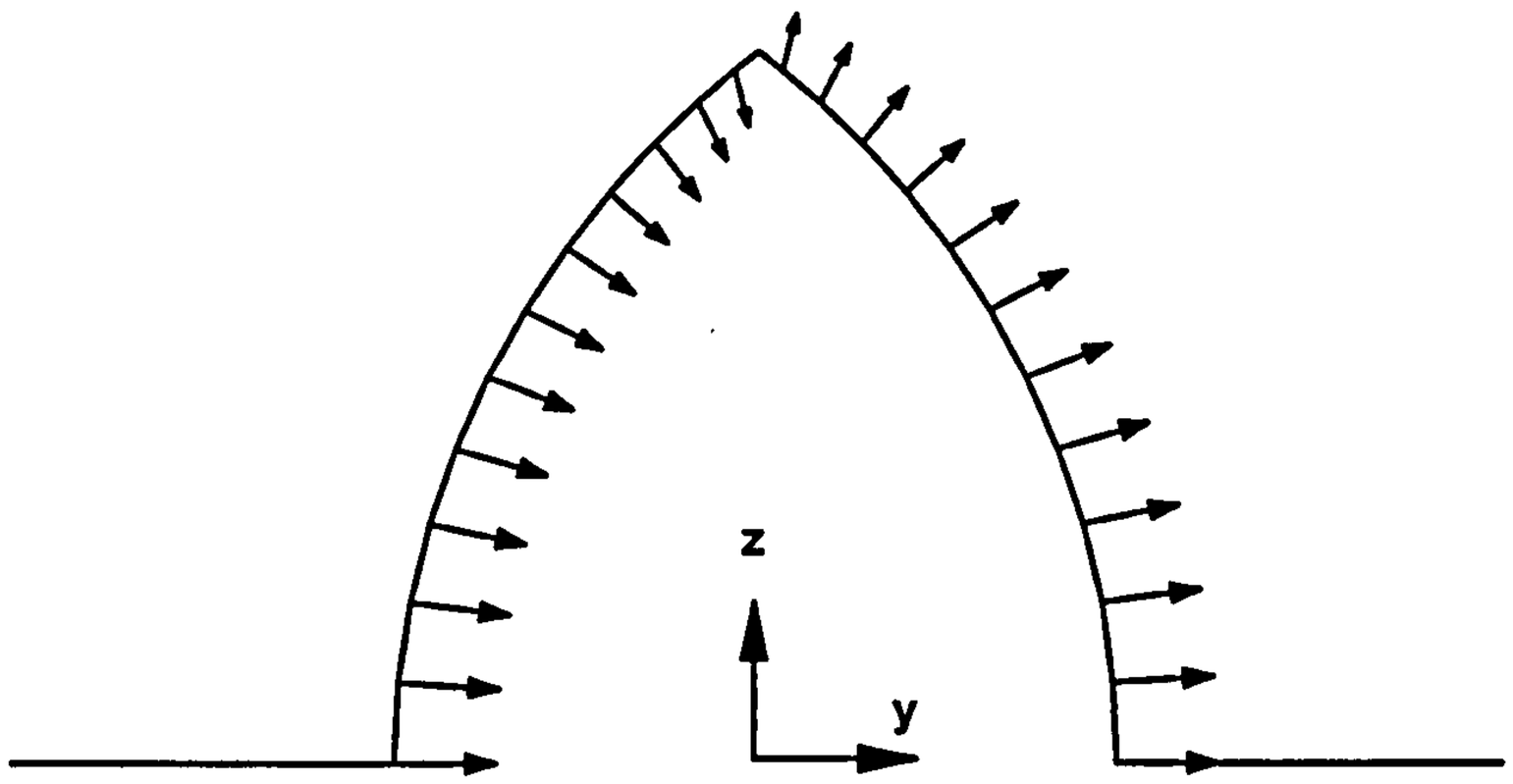

Figure 4.5: Normal velocity distribution on the hull surface due to the drift motion.

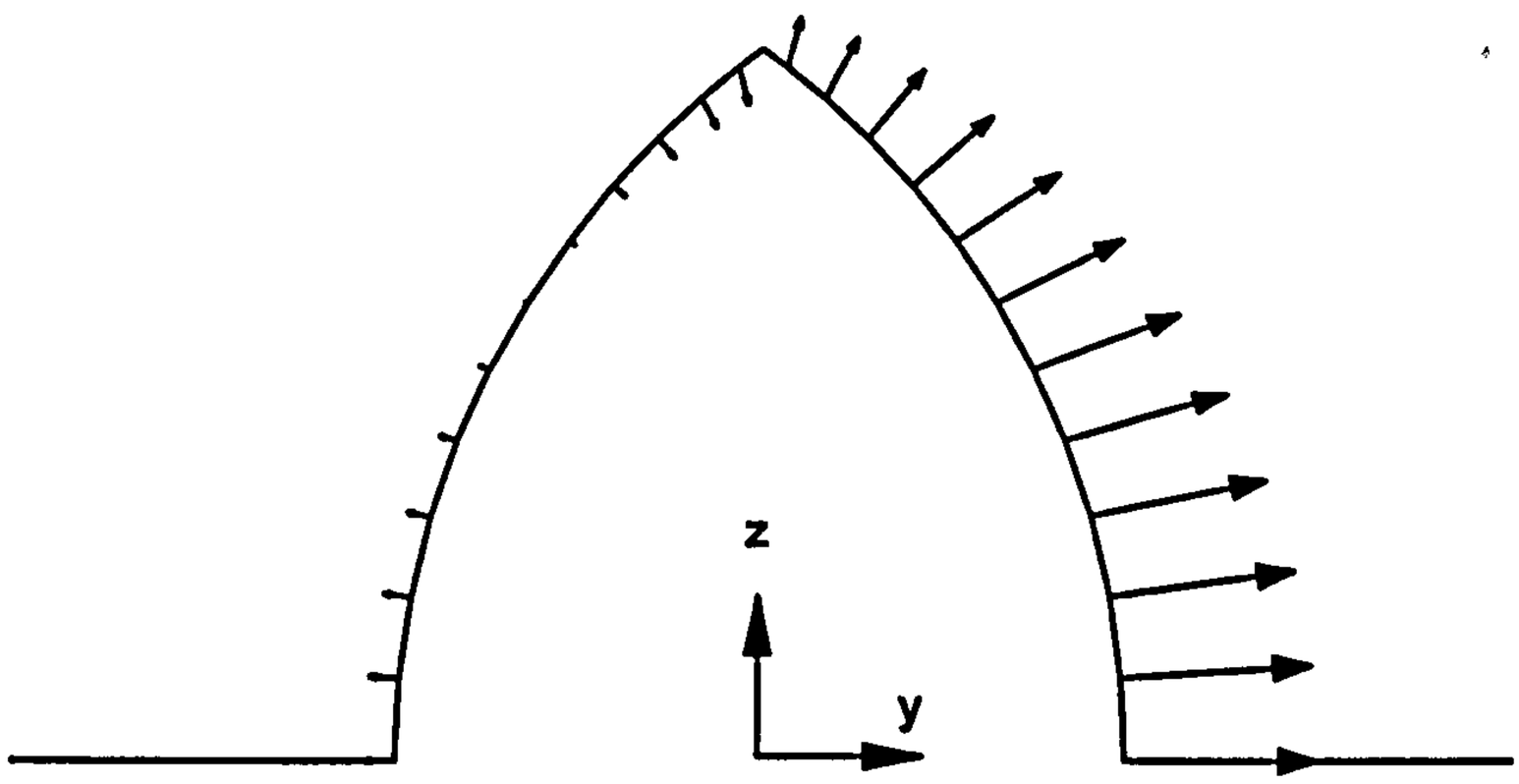

Figure 4.6: Total normal velocity distribution on the hull surface due to the growing hull section with the drift motion.

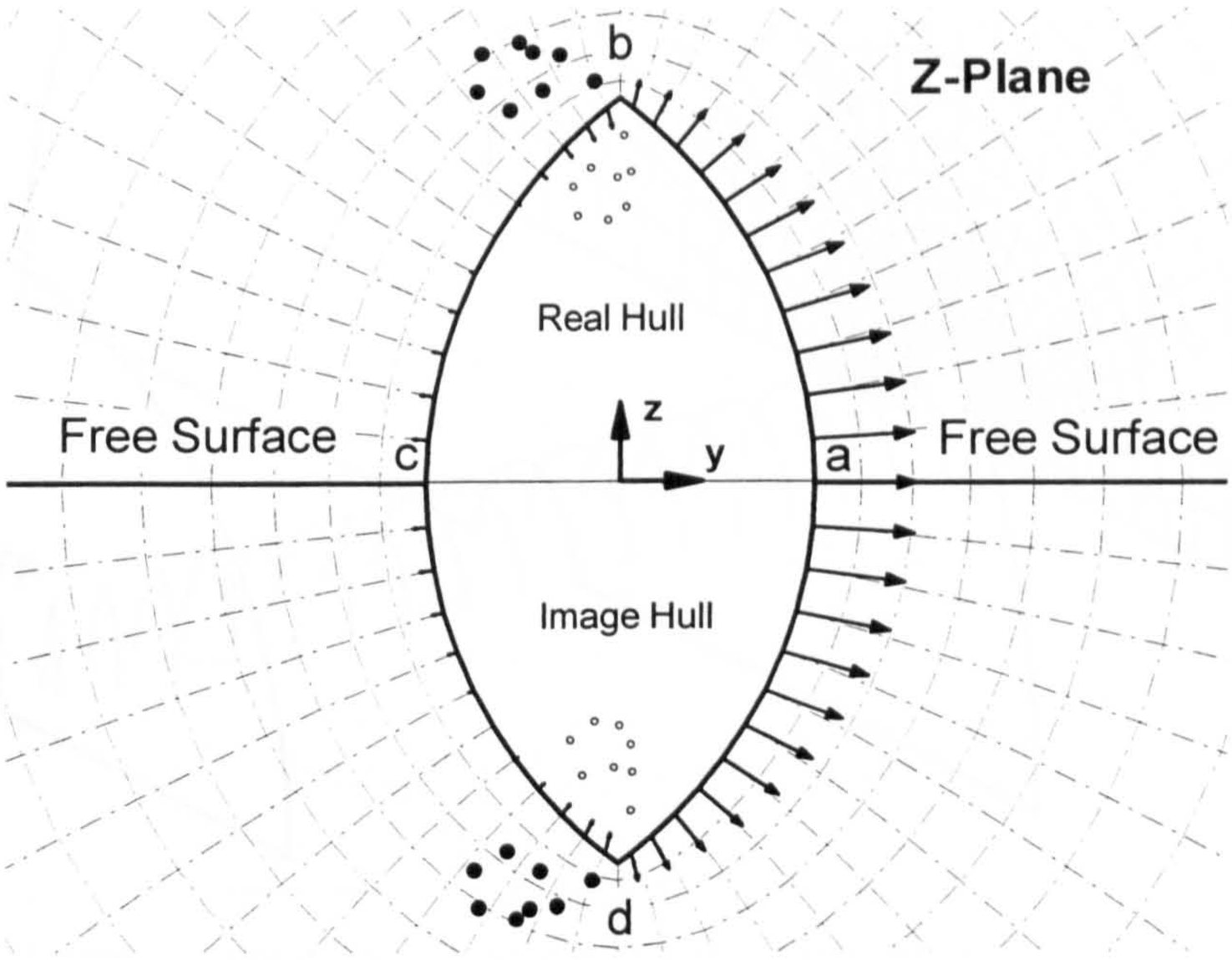

Figure 4.7: The representation of flow field of growing hull section with the drift motion.

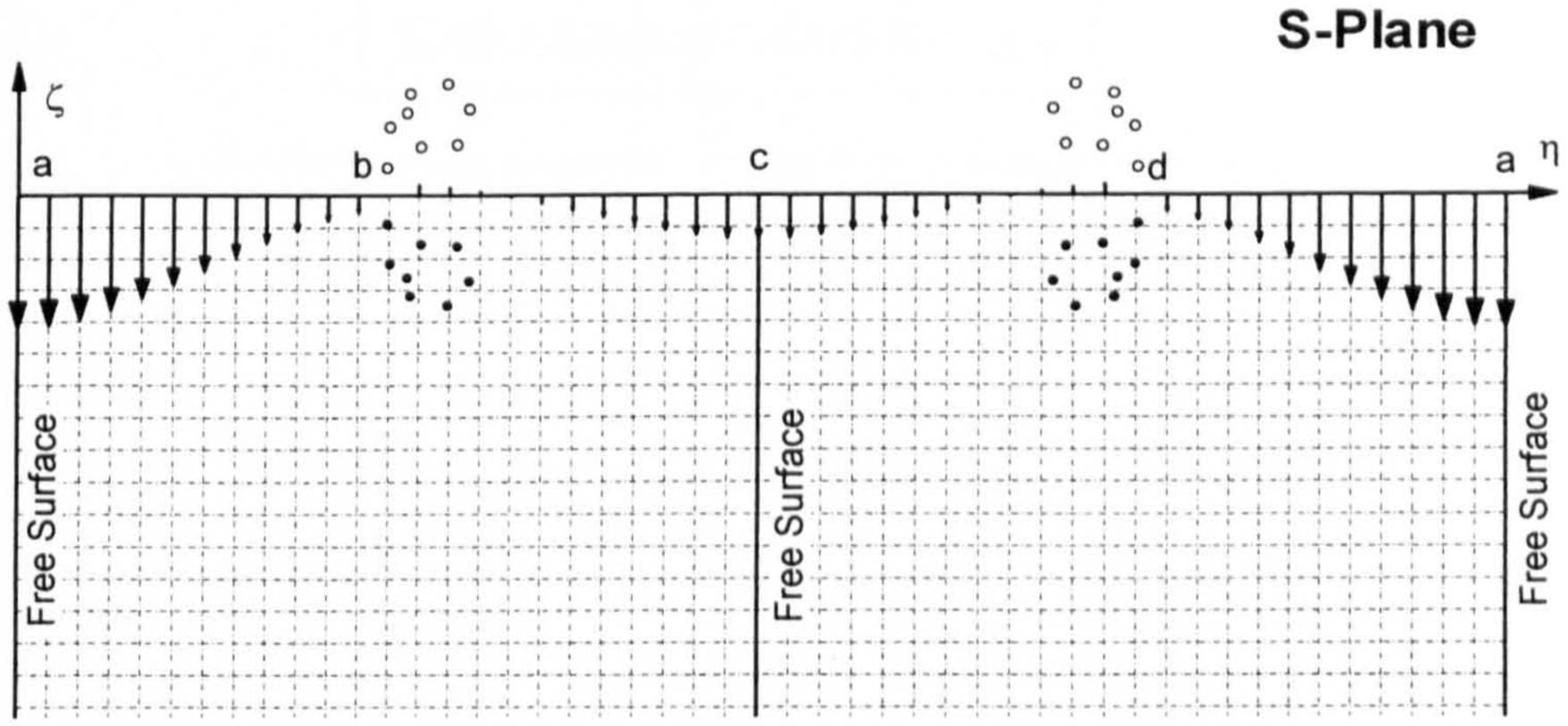

Figure 4.8: The flow field of computational domain for the growing hull with the drift motion.

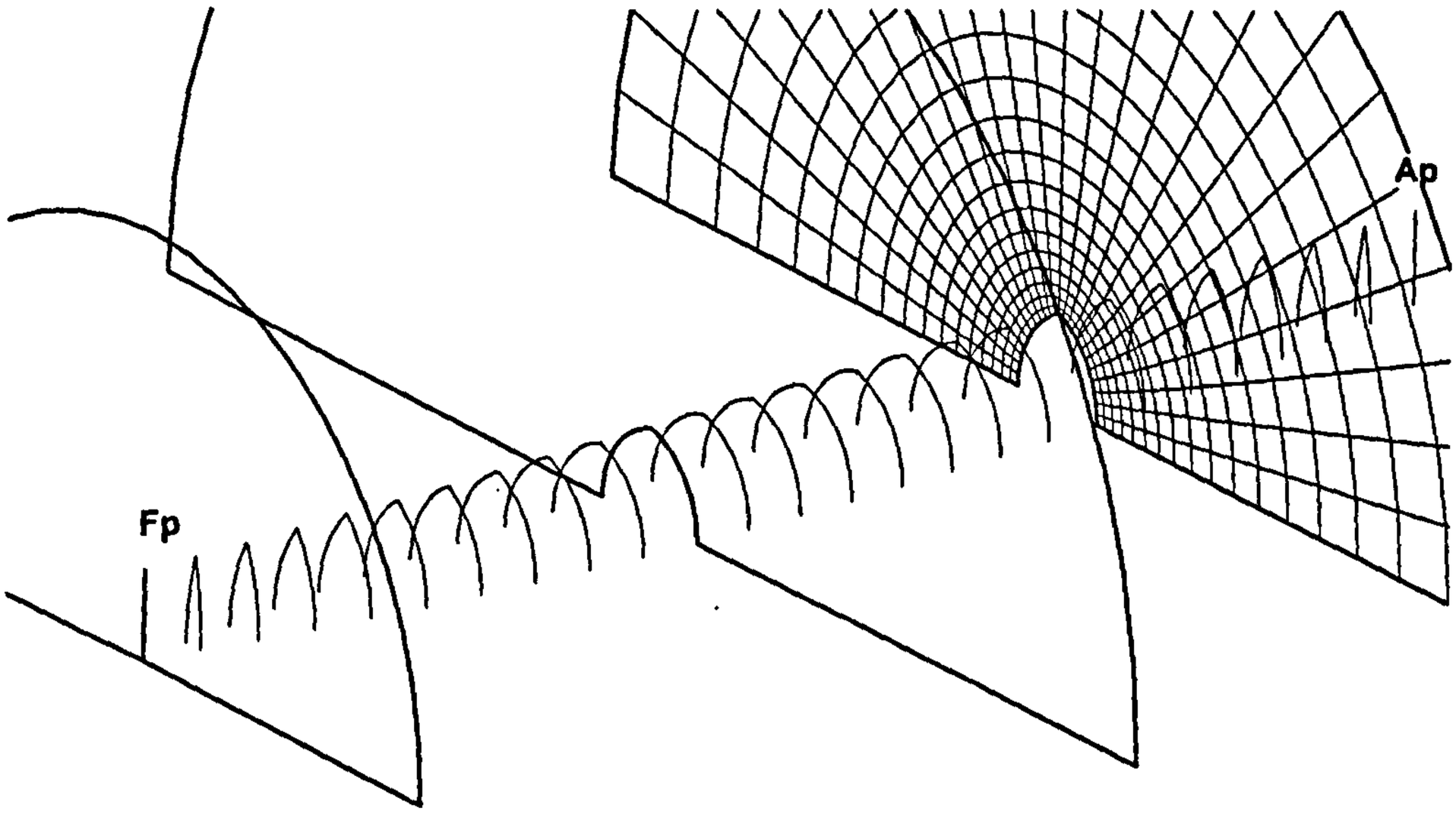

Figure 4.9: The divided two-dimensional hull section including sectional grid domains.

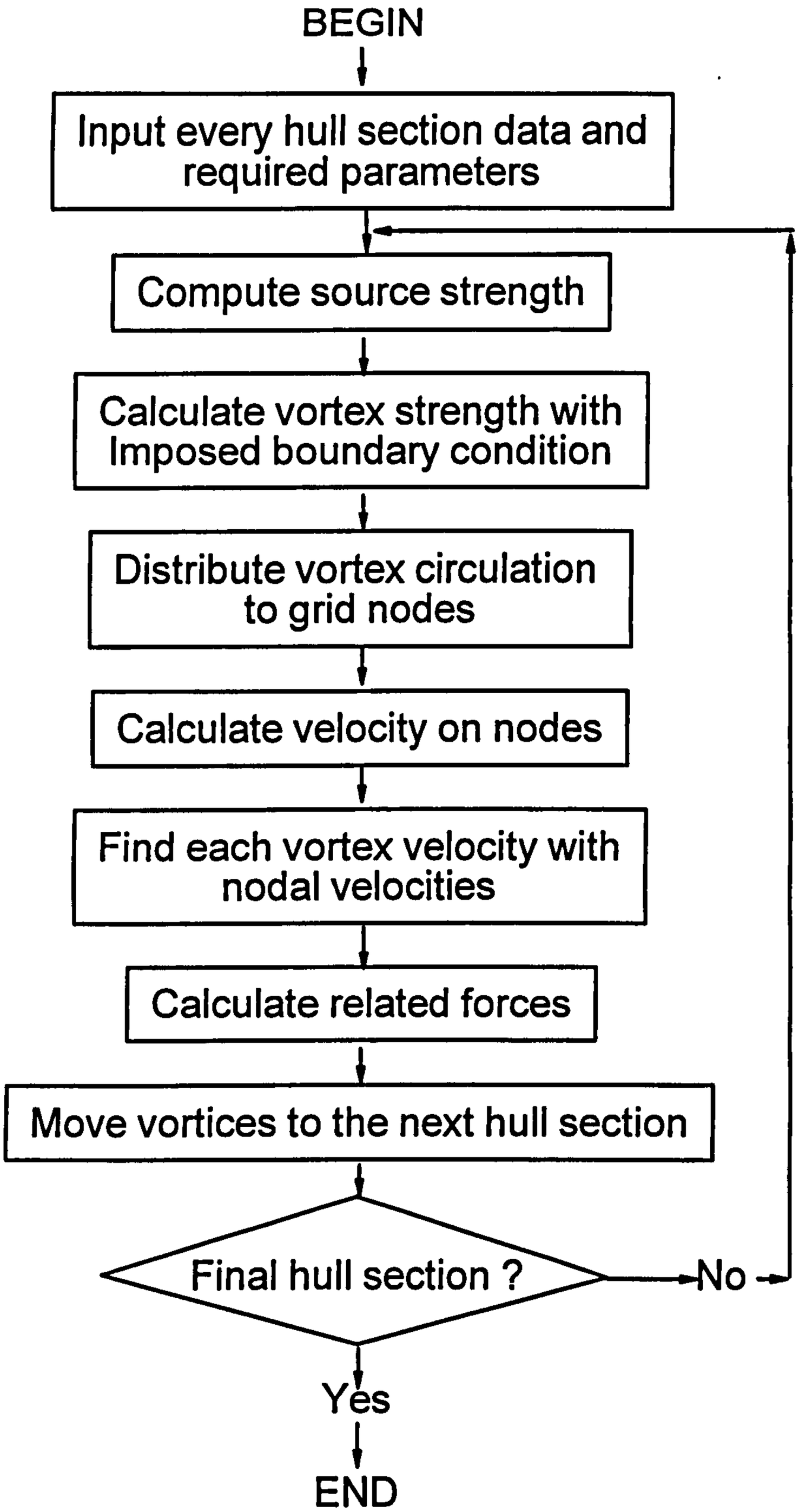

Figure 4.10: Basic flow chart for the proposed discrete vortex method.

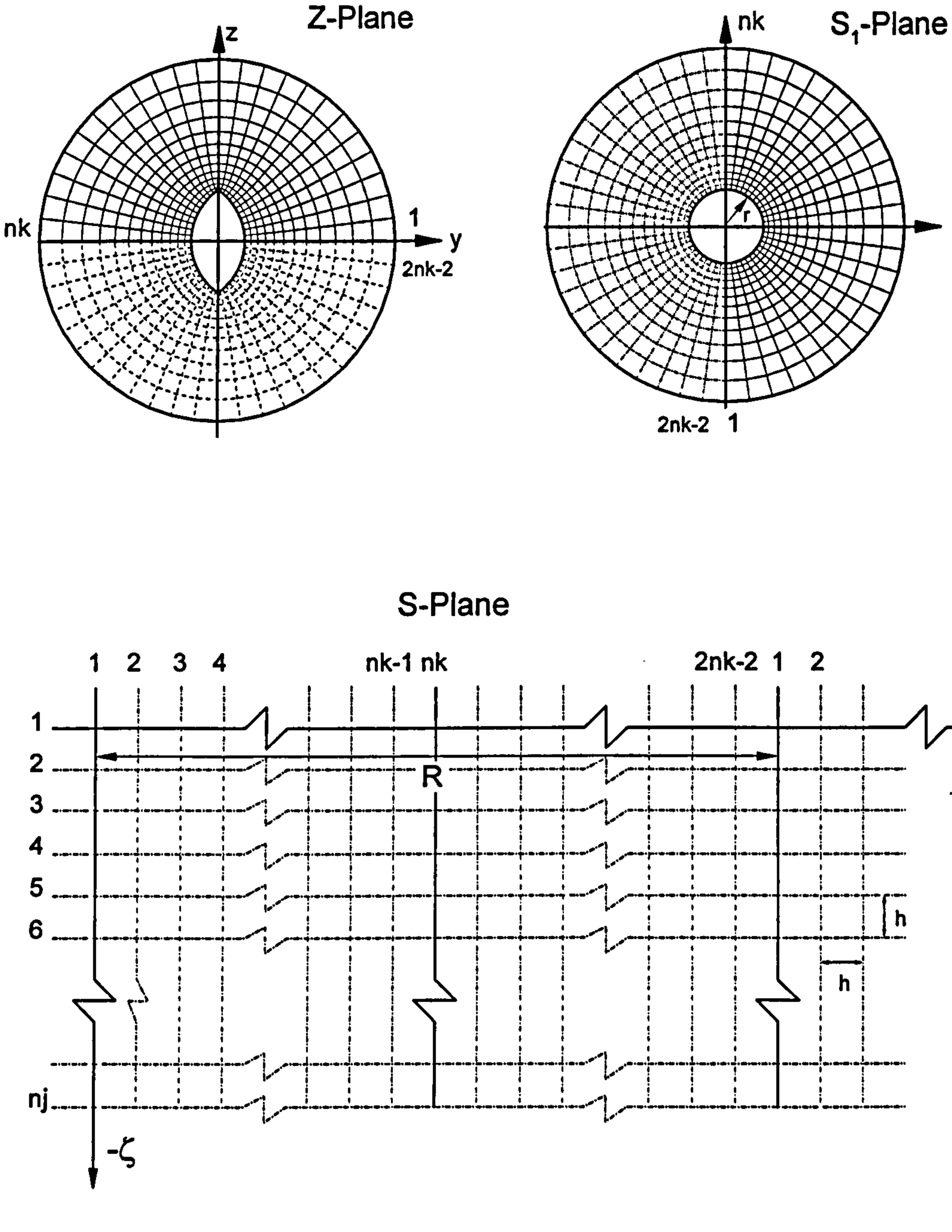

Figure 4.11: Two-stage conformal transformation for the Wigley hull.

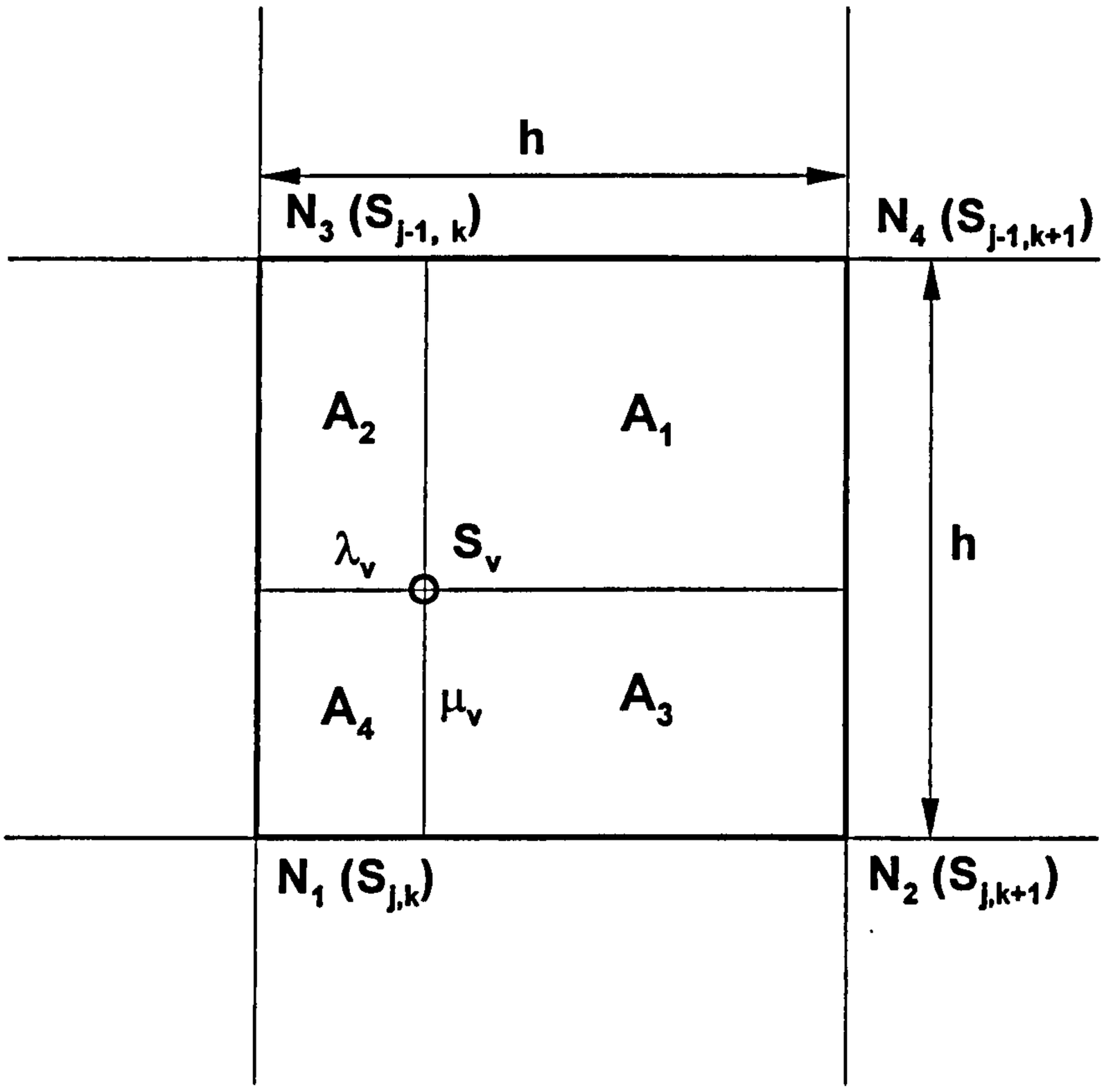

Figure 4.12: The area weightings for discrete vortex at S_v.

Chapter V

A FLAT PLATE AND THE WIGLEY HULL

5.1 General Description

The previous chapter has described the proposed model based on the discrete vortex method and slender body theory. The main purpose of this chapter is to study the flow around a flat plate and the Wigley hull moving at an angle of drift and to validate the model by comparing the results obtained from it with existing numerical and experimental data.

A flat plate and the Wigley hull have similar geometrical characteristics in that they have sharp edges along the keel line. Separation along the keel line is the main flow phenomenon for both hulls during drift motion. As described in previous chapters, the separated vortices are closely associated with the sway force and the yaw moment.

The Wigley hull is a slender body with transverse curvature so that the bilge separation along the hull (as opposed to the keel edge) may be neglected. Even though there is no bilge vortex separation, the longitudinal curvature of the Wigley hull will still change the formation of keel vortices and, consequently affect the related forces. These effects on the flow phenomena and forces are also studied in this chapter by comparing the separated flow patterns of both the flat plate and Wigley hull.

5.2 The Flow around a Flat Plate Hull

A flat plate in an oblique flow is an interesting problem to study because of its simple geometry. In spite of its simplicity, it represents the general features of the flow phenomena of a manoeuvring ship.

For a flat plate with a finite aspect ratio, A_r = Draft/Length, three-dimensional flow effects may be important. The aspect ratio of a typical hull is very small. For example A_r for the Wigley hull and the British Bombardier is 0.0625 and 0.0566 respectively, so the flow of interest at present is a flat plate with a small aspect ratio. In this case, it is well known that the non-linear effects due to the vortex system separating from the keel line are predominant in the flow. The proper modelling of the longitudinal vortex, such as is seen in keel separation from a flat plate, is very important for the prediction of manoeuvring forces

Chapman (1976a, 1976b) has calculated the flow around a surface piercing flat plate with a drift motion using a slender body based method. He was mainly interested in moderate aspect ratios from 0.2 to 0.5 or possibly higher and neglected the flow separation along the keel line of a flat plate. Even though his method can be applied to very low aspect ratio, it is more usually applied to plates of moderate and larger aspect ratio with small drift angles. The lateral forces, calculated by Chapman (1976b), were in better agreement with the experimental data for flat plates of larger aspect ratio.

In an effort to model the separation flow along a keel line, Landrini (1992, 1993) used a simple vortex lattice scheme in his double body panel method. Recent investigation into the influence of the keel vortex by Landrini and Campana (1996) has shown that keel vortex shedding is crucial for the prediction of the hydrodynamic forces associated with the manoeuvring of a low aspect ratio flat plate.

As shown in Figure 5.1, the sectional form of a flat plate hull remains constant from bow to stern. It is assumed to be a double body since wave effects are neglected. Using slender body theory, the flat plate hull problem in a steady drift motion can be reduced to a series of two-dimensional flat plate problems in a transverse plane as shown in Figure 5-2.

The discrete vortex method to be used in this study has been described in the previous chapter. Some of the procedures, discussed, such as the hull transformation, the calculation of source strength and the introduction of discrete vortices into the flow, require more detailed explanations since their implementation differs slightly, depending on the hull type involved.

5.2.1 Flat Plate Transformation

The most well known, frequently used, approach to the calculation of the two-dimensional uni-directional flow about a flat plate is the mapping of a flat plate to a circular cylinder using the Joukowski transformation and calculation in the transformed plane. This conformal mapping technique has been adopted by Kiya and Arie (1977), Kamamoto and Bearman (1978), Naylor (1982) and others.

In this study, a flat plate in the *Z*-plane is mapped into a rectangular grid by a two stage conformal transformation as shown in Figure 5-3. The advantages of a rectangular grid were described in the previous section 4.5. A flat plate is transformed into a circular cylinder using the Joukowski transformation. The cylinder in the *S*1-plane is then mapped into a rectangular grid in the *S*-plane.

$$Z = S1 - \frac{r^2}{S1}$$
$$S1 = r \cdot \exp\left(i\frac{\delta\theta}{2}\right) \cdot \exp(i\alpha S) \qquad (5\text{-}1)$$

where r is the radius of a circular cylinder and is the half length of the draft, $r = T/2$, and $\alpha = 2\pi / R$ in the *S*-plane.

5.2.2 Calculation of Source Strengths

The normal velocity along the hull sections can be found by the appropriate body boundary condition. The normal velocities, V_n, on each sectional hull surface are defined from equation (4-11)

$$V_n = \frac{-U_\infty}{\sqrt{1+(dy/dz)^2}}\left(\frac{dy}{dx}\cos\beta \pm \sin\beta\right) \tag{5-2}$$

For a flat plate hull, there is no change of hull geometry both along the length and *z*-direction. Both *dy/dz* and *dy/dx* terms in the equation (5-2) will be zero and the equation may be simplified as

$$\begin{aligned} V_n &= U_\infty \sin\beta \qquad For \;\; -iT < Z < a, \;\; a < Z < iT \\ &= -U_\infty \sin\beta \qquad For \;\; -iT < Z < b, \;\; b < Z < iT \end{aligned} \tag{5-3}$$

Since there are no changes of hull sections along the x-direction, equation (5-3) only represents the sectional translation subject to a drift motion. Figure 5.4 shows a normal velocity distribution of drift motion on a flat plate surface. The positive sign of the normal velocity represents flow away from the flat plate.

The source strength is related to the normal component of surface movement as described in equation (4-12),

$$m(\eta) = -i2\overline{(V_n)}\frac{dZ}{dS} \tag{5-4}$$

where *dZ/dS* is the derivative of the transformation which can be found from equation (5-1) as

$$\frac{dZ}{dS} = \frac{dZ}{dS1}\frac{dS1}{dS}$$
$$\frac{dZ}{dS1} = 1 + \frac{r^2}{S1^2} \qquad (5\text{-}5)$$
$$\frac{dS1}{dS} = r \cdot \exp\left(i\frac{\delta\theta}{2}\right) \cdot i\alpha \cdot \exp(i\alpha S)$$

Applying equations (5-3) and (5-5) to equation (5-4), the source strength on η-axis in S-plane can be found. Figure 5-5 shows the source distribution representing drift motion of a flat plate in the transformed S-plane.

5.2.3 Introduction of Discrete Vortices into the Flow

After the potential flow analysis at each time step, new nascent vortices are introduced near the separation edges. Since method (1), as described in section 4.8, is used for the introduction of the vortices, the nascent vortex positions are defined in advance.

A comprehensive study into the influence of the introduction position for flow around a flat plate has been carried out by Kamamoto and Bearman (1978). They introduced the non-dimensional parameter

$$P_k = \frac{a_s}{V_\infty \Delta t_m} \qquad (5\text{-}6)$$

where V_∞ is the lateral free stream velocity and Δt_m is the time interval based on V_∞. a_s is the distance between the introduction point and separation point on the circular cylinder in the transformed plane. They studied the influence of P_k with values up to 1.9 and suggested that P_k should be more than 0.3. Their results showed that the rate of growth of circulation and the drag coefficient are good agreement with previous theoretical calculations in the rage $0.3 < P_k < 1.9$. They did not propose an upper bound for P_k. A similar study has also been carried out by Nayler (1982) whose results

showed that with high P_k ($P_k > 1.0$), there emerged a pair of well-defined, tightly rolled-up growing vortex clusters in the downstream vicinity of the separation edges.

In the present study, the new vortex position is located a small distance above the separation point. The distance a_s, between a new vortex position and the separation point, is checked in the transformed $S1$-plane to ensure that P_k is high enough ($P_k > 1.0$). Since in the present study V_∞ and Δt_m in equation (5-6) are equivalent to $U_\infty \sin\beta$, which is the lateral velocity, and $\Delta x/(U_\infty \sin\beta)$, which is the time step based on the lateral velocity, the parameter P_k may be expressed as

$$P_k = \frac{a_s}{\Delta x} \tag{5-7}$$

After the location of the nascent vortex is determined, the vortex strength can be calculated by satisfying the Kutta condition at the separation points. The Kutta condition ensures smooth separation at the shedding edges, and is satisfied when the flow velocities at the separation points in the real hull section are finite. Since the transformation is singular at the separation points, the tangential velocities at the corresponding separation points in the computational domain must be zero, that is,

$$\left.\frac{dW(S)}{dS}\right|_{S=S_p} = 0 \tag{5-8}$$

where, S_p are the separation points in the S-plane corresponding to $\pm iT$ in the Z-plane.

The strengths of the new vortices at both edges are of the same magnitude but with opposite sign, due to the symmetry of the double body model, so that both vortex strengths can be calculated simultaneously. The vortices introduced at the previous time step are transported downstream and no longer enforce the Kutta condition. There is an unbalanced velocity, V_{ub}, that must be countered by the introduction of two more new vortices of the appropriate strength Γ. The complex velocity, V_{ub}, at

the separation point $S = S_p$, which is corresponds to iT in the Z-plane, is given from equation (4-25) by

$$\frac{dW(S_p)}{dS} = V_{ub}$$

$$= \frac{-i}{2\pi}\left[\sum_{S_{j,k}} \Gamma_{j,k}\left(\cot\frac{\pi(S_p - S_{j,k})}{R} - \cot\frac{\pi(S_p - \overline{S}_{j,k})}{R}\right)\right] \qquad (5\text{-}9)$$

$$+ \int_{S_{1,1}}^{S_{1,2nk-1}} \frac{m(\eta)}{2\pi}\cot\frac{\pi(S_p - \eta)}{R}d\eta$$

The velocity V_{ub} at the separation point S_p is negated by introducing new vortices at the defined new vortex points to satisfy the Kutta condition. The strength of the new vortices is calculated to give zero complex velocity at the separation point in the S-plane. This implies that

$$V_{ub} + \Gamma_n(X_1 + X_2 + X_3 + X_4) = 0 \qquad (5\text{-}10)$$

and that

$$\Gamma_n = -\frac{V_{ub}}{(X_1 + X_2 + X_3 + X_4)} \qquad (5\text{-}11)$$

The two equations can be solved to yield the new vortex strengths Γ_n, using

$$X_1 = \frac{-i}{2\pi}\left(\cot\frac{\pi(S_p - S_{vu})}{R}\right) \qquad X_2 = \frac{-i}{2\pi}\left(-\cot\frac{\pi(S_p - \overline{S}_{vu})}{R}\right)$$

$$X_3 = \frac{-i}{2\pi}\left(-\cot\frac{\pi(S_p - S_{wl})}{R}\right) \qquad X_4 = \frac{-i}{2\pi}\left(\cot\frac{\pi(S_p - \overline{S}_{wl})}{R}\right) \qquad (5\text{-}12)$$

where R is the periodic length. As shown in Figure 5.4 and 5.5, S_{vu} and S_{vl} are the positions of the new vortices in the S-plane corresponding to the upper and lower positions respectively of the new vortices in the Z-plane.

5.2.4 Calculation and Results

As a preliminary calculation for validating the numerical method, the model was applied to a flat plate and a Wigley hull, both with a small aspect ratio $A_r = 0.016$, moving with a drift motion.

The time step and vortex introduction length a_s were chosen to make the parameter P_k, defined in equations (5-6) and (5-7), equal to 1.46. Accordingly the transverse flow was computed at one hundred and twenty six sections along the hull, where every fifth station is shown in Figure 5.2. The grid numbers along the girthwise and radial direction of each transverse section, corresponding to nk and nj in Figure 5.3, are twenty five and eighteen respectively.

In order to gain confidence in the proposed method, the development of circulation shed into the flow at the keel line was computed and compared with the results obtained for the two-dimensional unsteady flow about a flat plate, as shown in Figure 5.6. To compare like for like with the two methods, the velocity and time scales, V_∞ and t_m in the time dependant method must be equivalent to $U_\infty \sin\beta$ and $X/(U_\infty \sin\beta)$ respectively in the present method. The parameter X, which can be expressed as $X = L(x+0.5)$, is the distance from the point Fp to specified points in the x-direction. The distribution of the total accumulated circulation presented as a function of time is in good agreement with the results of Fink and Soh (1974), Graham (1977) and Nayler (1982). For the initial flow, the present method follows the results of Graham (1977) and then it fits well with the curve of Fink and Soh (1974) as the flow develops further.

Figure 5.7 shows the distribution of the total circulation along the flat plate hull for the cases of 5, 10 and 15 degrees of drift motion. These curves show that the total vortex strengths grow rapidly at the bow and then more slowly with a nearly linear trend as the stern is approached.

The development of the vortex along the flat plate hull is shown in Figure 5.8 for the case of 10 degrees of drift motion. Because of its simple geometry and constant sectional shape, there is only one well-defined cycle of vortex roll-up along the hull and the flow is identical to the unsteady two-dimensional flat plate results presented by Fink and Soh (1974) and Nayler (1982). The evolution of the flow about a flat plate is illustrated in Figure 5.9.

In the present model, the plate is given a drift motion with a *y*-directional velocity $U_\infty \sin\beta$ in calm water, as shown in Figure 5.10. In order to understand the flow more easily, the sectional velocity distributions shown in Figure 5.10 are based on a reference flow in which the flat plate is fixed and the fluid approaches the plate with a *y*-directional velocity $-U_\infty \sin\beta$. The velocity distribution on each of the sections clearly shows smooth flow separation from the keel line.

Figure 5.11 and 5.12 show the side force and yaw moment coefficients generated by the flat plate plotted against the angle of drift motion for values up to 15 degrees. The numerical results presented by Landrini and Campana (1996) and the theoretical attached flow result are plotted in the same figures. As shown in Figure 5.11 and Figure 5.12, the present method agrees well with the results of Landrini and Campana who used an invicid rotational flow model based on an integral representation of the velocity field in terms of source and surface vorticity distributions. The theoretical results represent the force contribution computed for an attached flow and obtained using the low aspect ratio lifting surface theory, as explained in equation (4-44). The differences between the theoretical method and present calculation as shown in the figures represent the non-linear contribution of the separated flow, as explained in the previous section 4.11.

5.3 The Flow around the Wigley Hull

The present model has also been applied to a Wigley hull moving at an angle of drift and with an aspect ratio A_r and a breadth to length ratio of the hull equal to 0.0625 and 0.1 respectively. The surface geometry of the hull is described by the equation

$$y = \pm\frac{B}{2}\left[1-\left(\frac{2x}{L}\right)^2\right]\left[1-\left(\frac{z}{T}\right)^2\right] \tag{5-13}$$

where L is the length, B is the breadth, and T is the draft of the hull. This shape is generated by simple Karman-Trefftz profiles (Milne-Thomson 1960) and the transformations are described in section 4.5. Both the body plans of the actual Wigley hull and also the hull generated by the Karman-Trefftz transformation are compared in Figure 5.13. The shapes are the same in the bow and stern regions, but there are some differences amidships. The calculations have been carried out using the Karman-Trefftz transformation because it is simple to implement and sufficiently close to the Wigley hull form for preliminary studies. The exact form could be represented by a generalised transformation that will be described in Chapter 7. The present transformation is considered to represent the essential features of flow separation along the keel line for a hull with sectional dilation, such as the Wigley hull.

5.3.1 Results and Comparisons

The calculations were carried out on a Wigley hull with drift motion up to 15 degrees. A single vortex was introduced at each section as the solution progressed from bow to stern so as to satisfy the Kutta condition. The Kutta condition ensures smooth separation at a shedding edge, and is enforced by inducing zero velocity in the transformed S-plane at the points corresponding to the shedding edges. For the first section, the point at which new vortices are introduced is located a small distance above the separation point, using the same approach as for the flat plate. For the following sections, the nascent vortex is introduced between the last shed vortex and

the separation point, to ensure the flow separates smoothly. For fair comparison with the flat plate, sectional numbers and the grid system for the Wigley hull were chosen to be same as for the flat plate. The grid system for the Wigley hull is shown in Figure 4.9.

The distribution of the total vortex circulation shed from the keel line is plotted against the distance from bow in Figure 5.14. These curves show the vortex strengths increase rapidly at the fore part and continue to grow more or less linearly along the middle part. When the stern is approached the growth rate of the vortices starts to increase again as the hull sections begin to shrink.

The development of the vortex flow and the velocity vectors for the 10 degrees of drift motion are shown in Figure 5.15 and 5.16 respectively. These figures are informative because they demonstrate the importance of the sectional dilation in the generation of the structure of the trailing vortex along the keel line.

The interaction of the crossflow and the body dilation for the Wigley hull is such that the two counter each other on the fore part of the hull and reinforce each other on the aft part on the downstream crossflow side. The reverse is true on the upstream crossflow side. This directs the ambient flow away from the free surface on the fore part, and towards it on the aft part. As the bow vortex grows it induces a back flow that counters the ambient crossflow and the rate at which vorticity generated at the keel reduces. This effect is offset as the vortex is convected away from the hull. After the mid section, the ambient flow on the downstream side picks up, the rate of vorticity generation increases, and the separating shear layer begins to roll up to form a second vortex at the stern. The presence of two vortices is a direct consequence of the variation in the rate at which vorticity is fed into the separating shear layers, which itself is controlled by the growth and shrinkage of the hull sections. The evolution of the flow about the Wigley hull is illustrated in Figure 5.17.

The side force and the yaw moment plotted against the drift angle for the Wigley hull are presented in Figures 5.18 and 5.19 respectively. The calculated results

are shown together with numerical results of Zou and Soding (1994), Wong and Calisal (1996) and the experimental results of Kashiwagi, which are taken from Zou and Soding (1994). The theoretical results in both figures show the attached flow results, computed from the sectional added mass and ignoring the contribution of the vortices (Clarke 1972) and will be described in detail in section 7.7. Because the middle part of the present hull is slightly different from that of the Wigley hull, the calculated forces and moments cannot be compared directly, but the results still show reasonable agreement with one another.

5.4 Conclusions

As a preliminary calculation, the present numerical method has been applied to simple slender bodies, like a flat plat and the Wigley hull. The side force and yaw moment coefficient obtained by the present model are in good agreement with those obtained by experiment and those obtained by other numerical methods.

The graphs of total vortex distribution, together with the flow visualisation have shown a good representation of the natural behaviour of the vortex flow expected from both flat plate and Wigley hull. The results have also confirmed that the curvature of the Wigley hull influences the formation of the keel vortices and changes the related forces.

Finally, the evolution of vortex flows along both the flat plate and the Wigley hull is plotted together in Figure 5.20 to illustrate the different flow patterns.

The following section describes the application of the present method to the block hull moving firstly with straight ahead motion and secondly at an angle of drift. The block hull has two separation points and is characterised by bilge vortex separation. The hull will also be modelled by a commercial RANS code, called CFX, and the flowfields so obtained will be presented together.

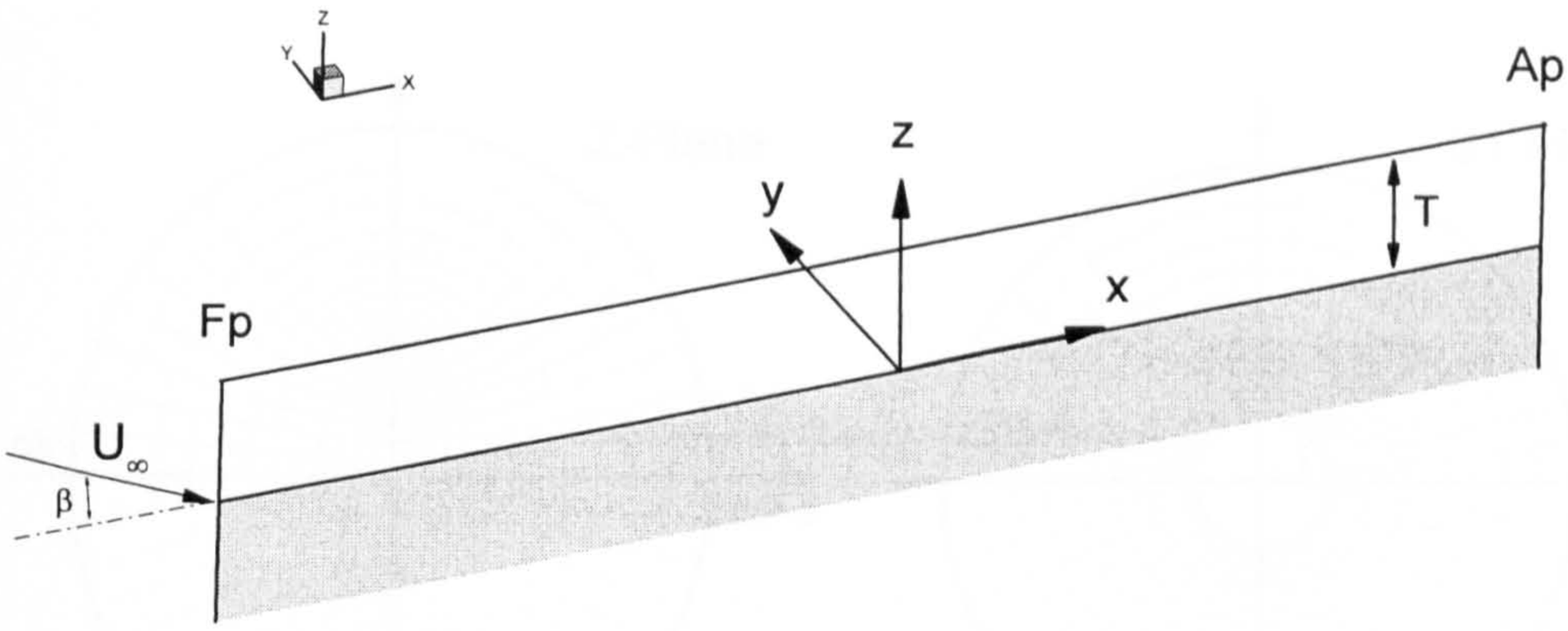

Figure 5.1: Co-ordinate system of a double body hull.

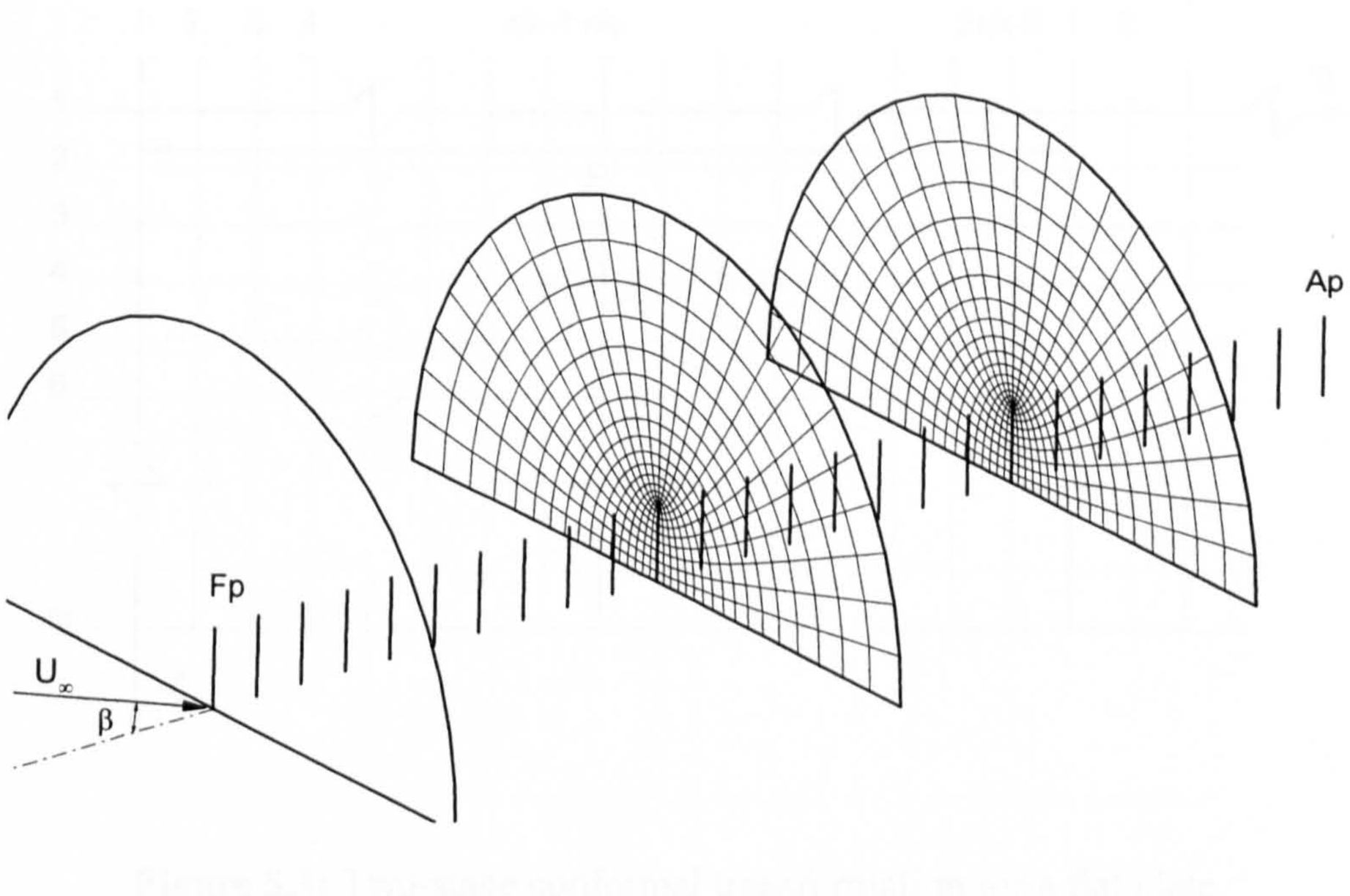

Figure 5.2: The divided two-dimensional hull section including sectional grid domains.

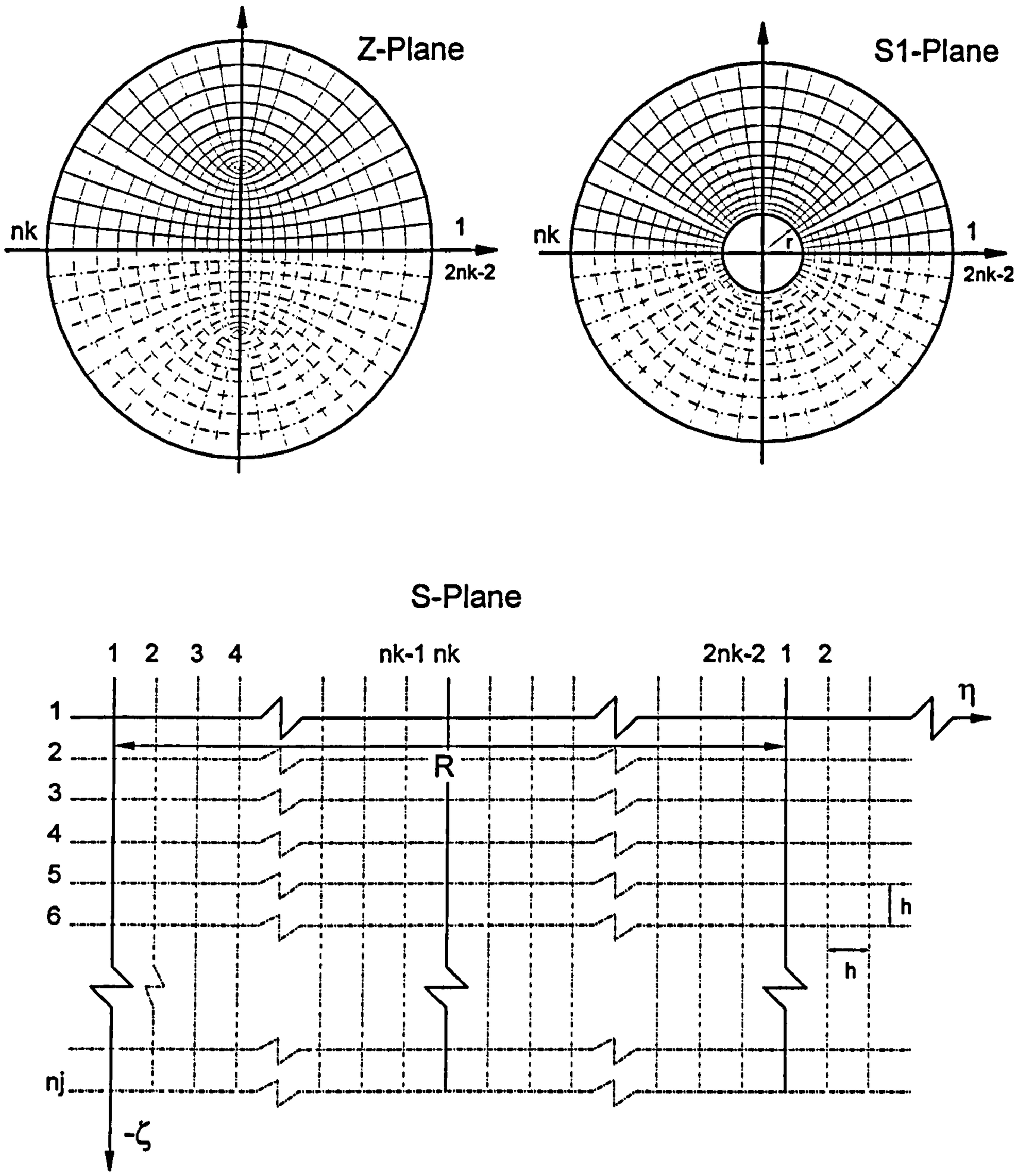

Figure 5.3: Two-stage conformal transformation for a flat plate.

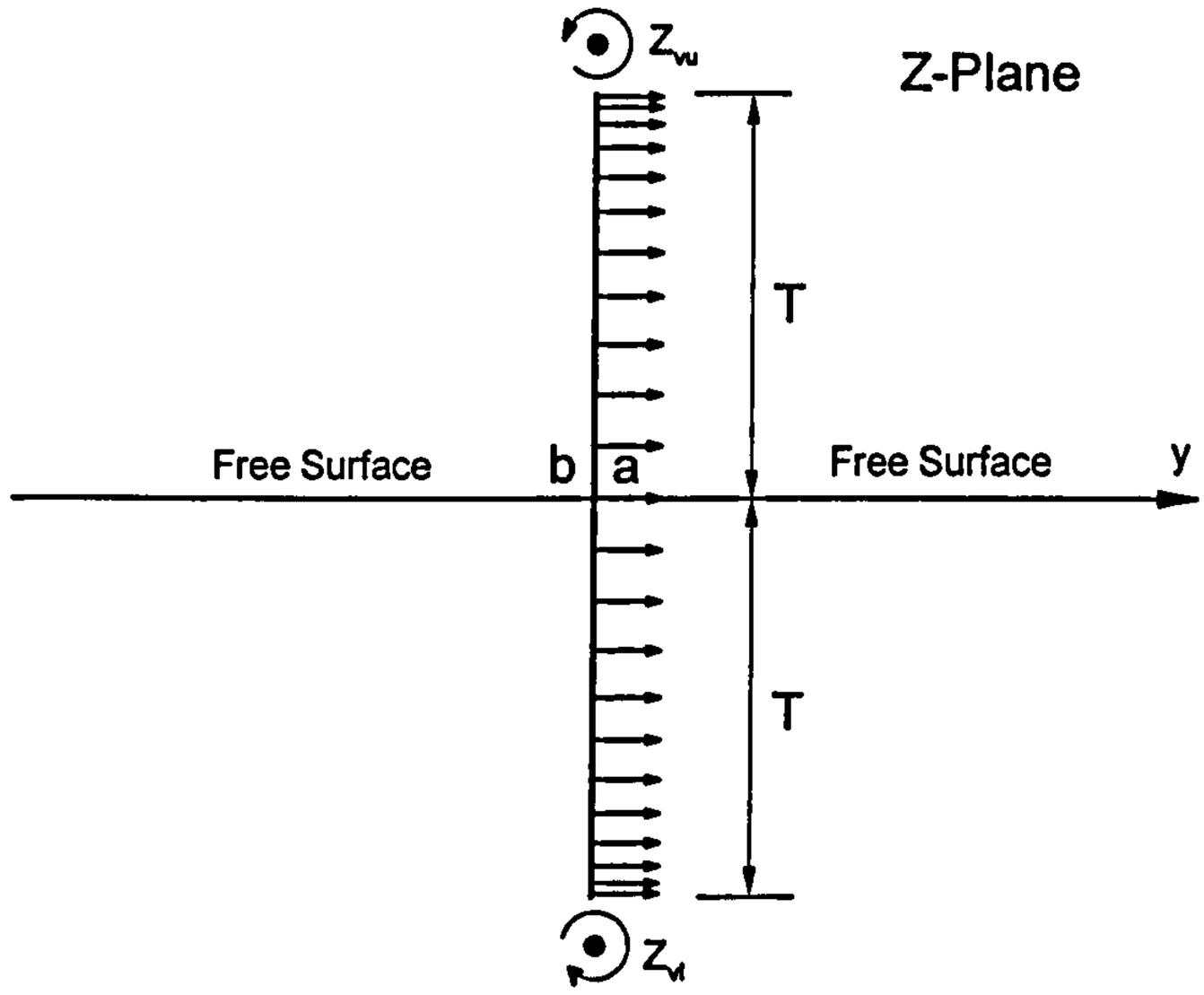

Figure 5.4: The representation of flow field with the drift motion.

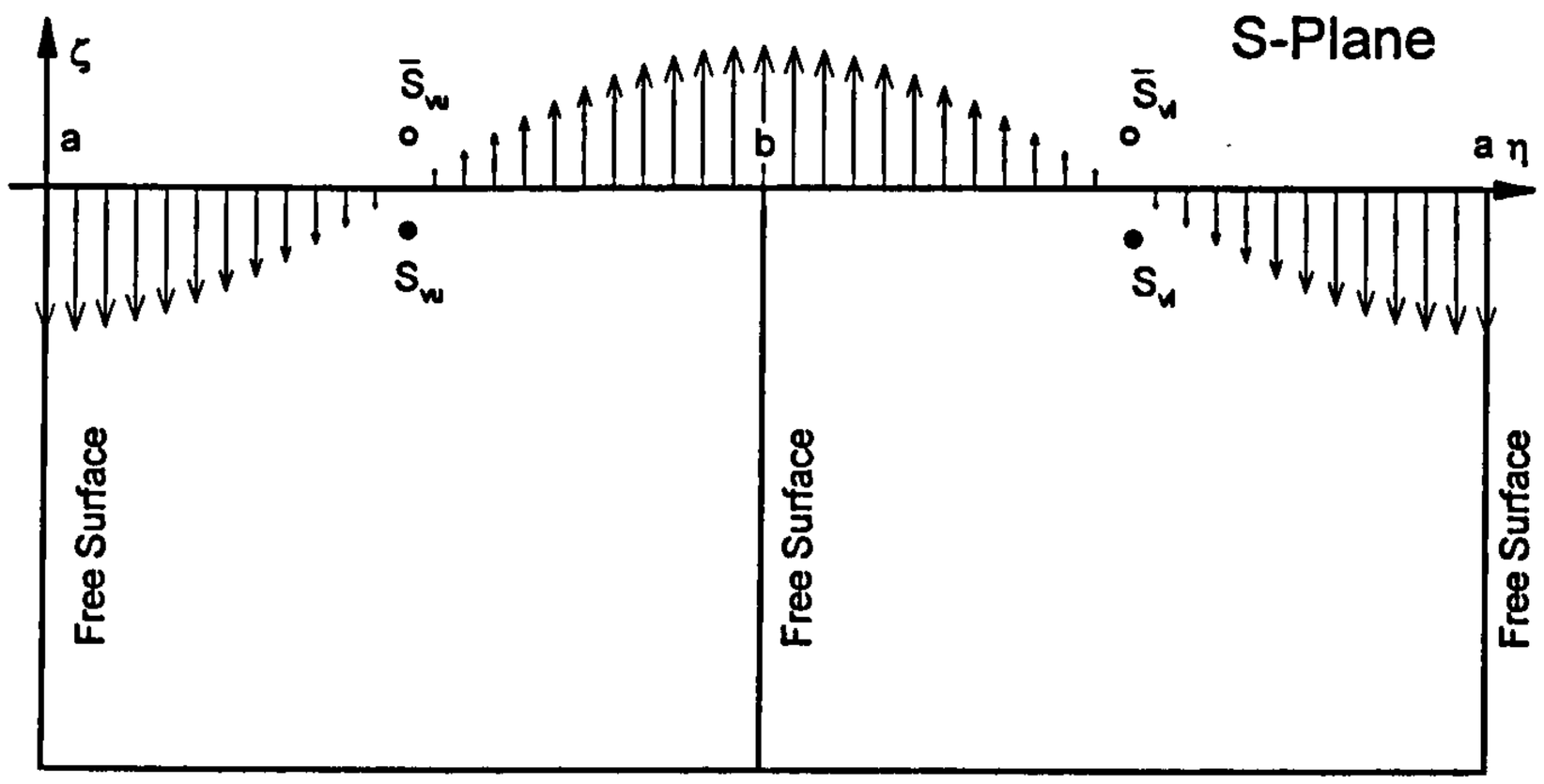

Figure 5.5: The flow field of computational domain.

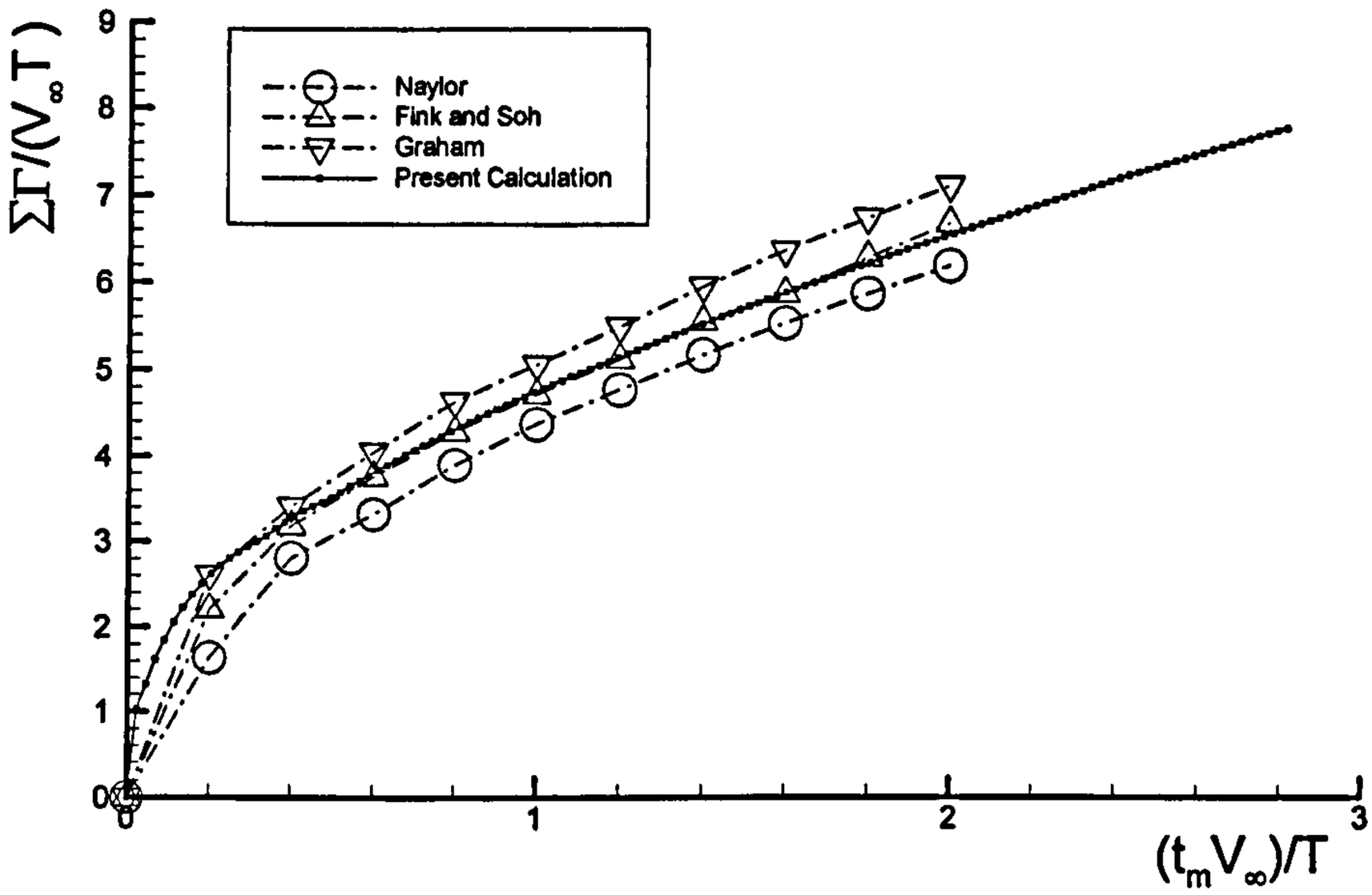

Figure 5.6: Time development of total circulation for a flat plate.

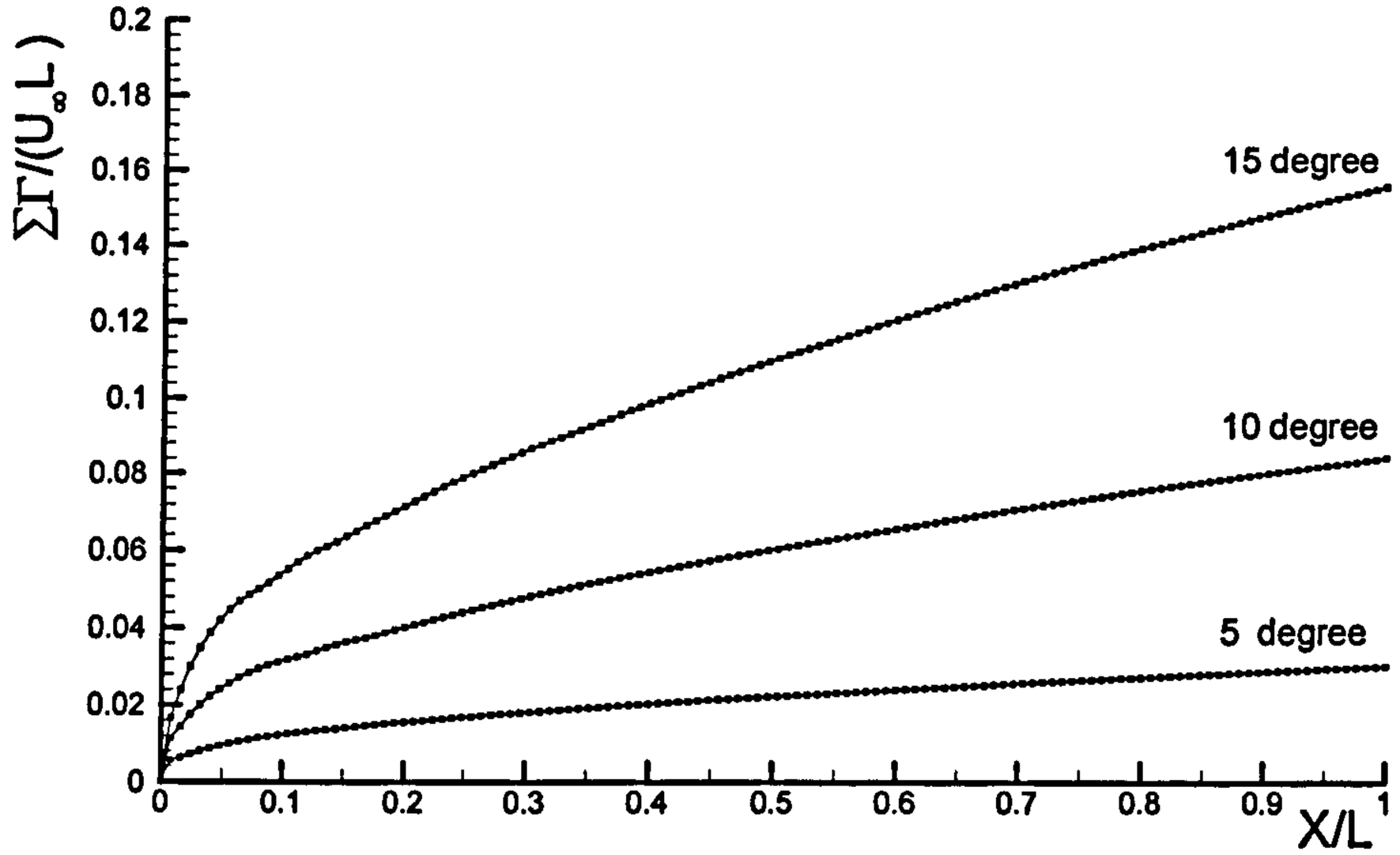

Figure 5.7: The development of total circulation over a flat plate of $A_r = 0.0625$.

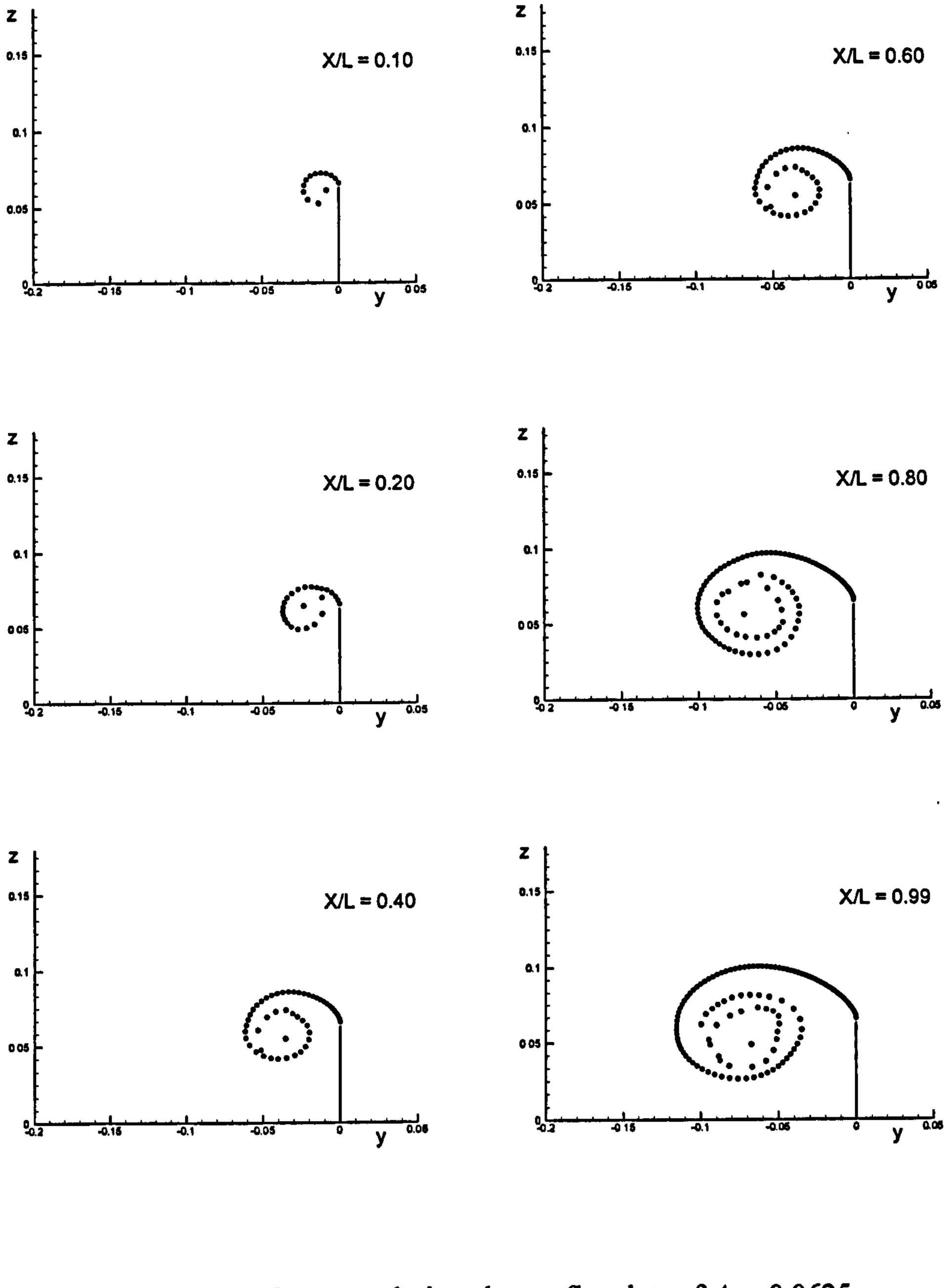

Figure 5.8: Vortex evolution along a flat plate of $A_r = 0.0625$ due to ten degrees of drift motion.

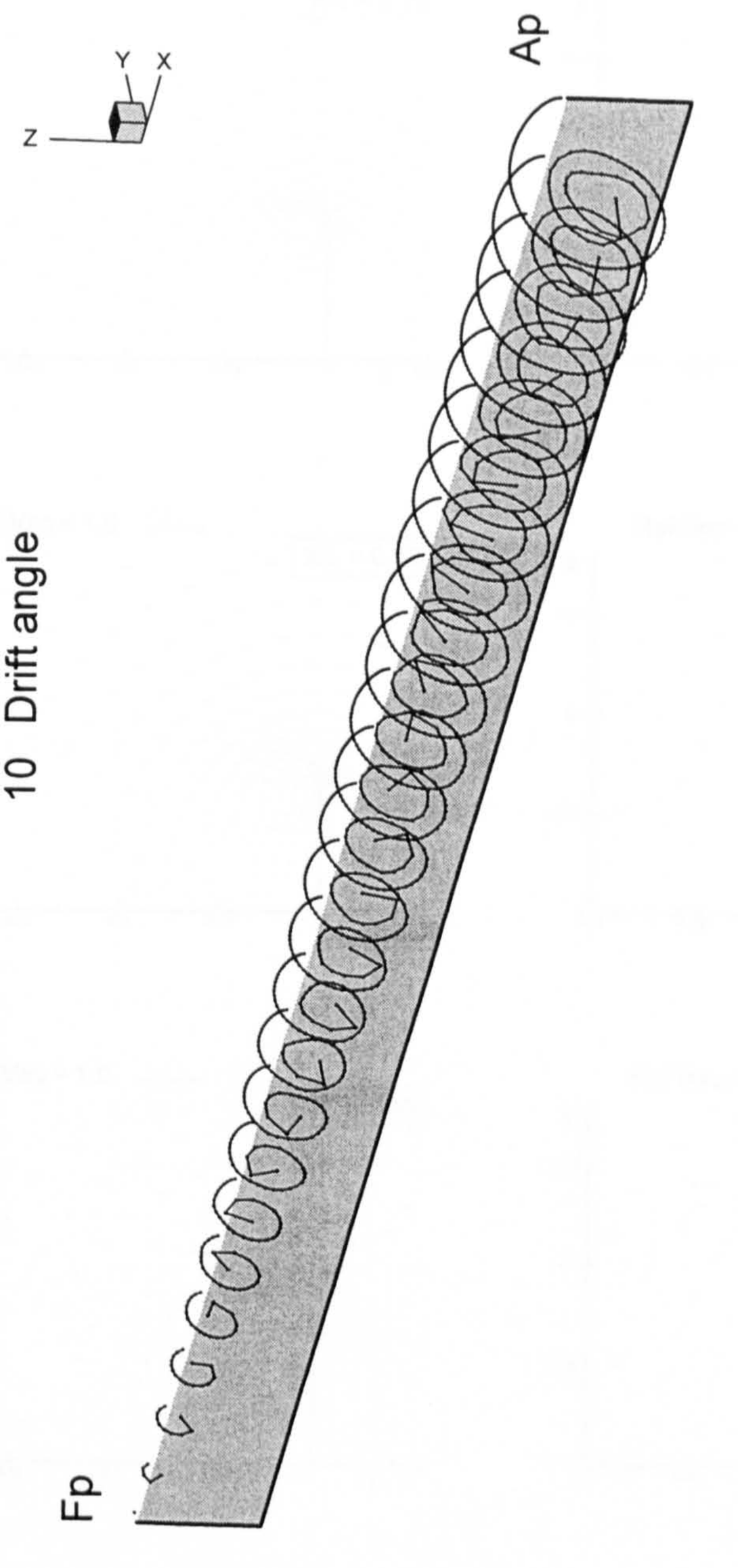

Figure 5.9: Vortex flow around a flat plate of $A_r = 0.0625$ due to ten degrees of drift motion.

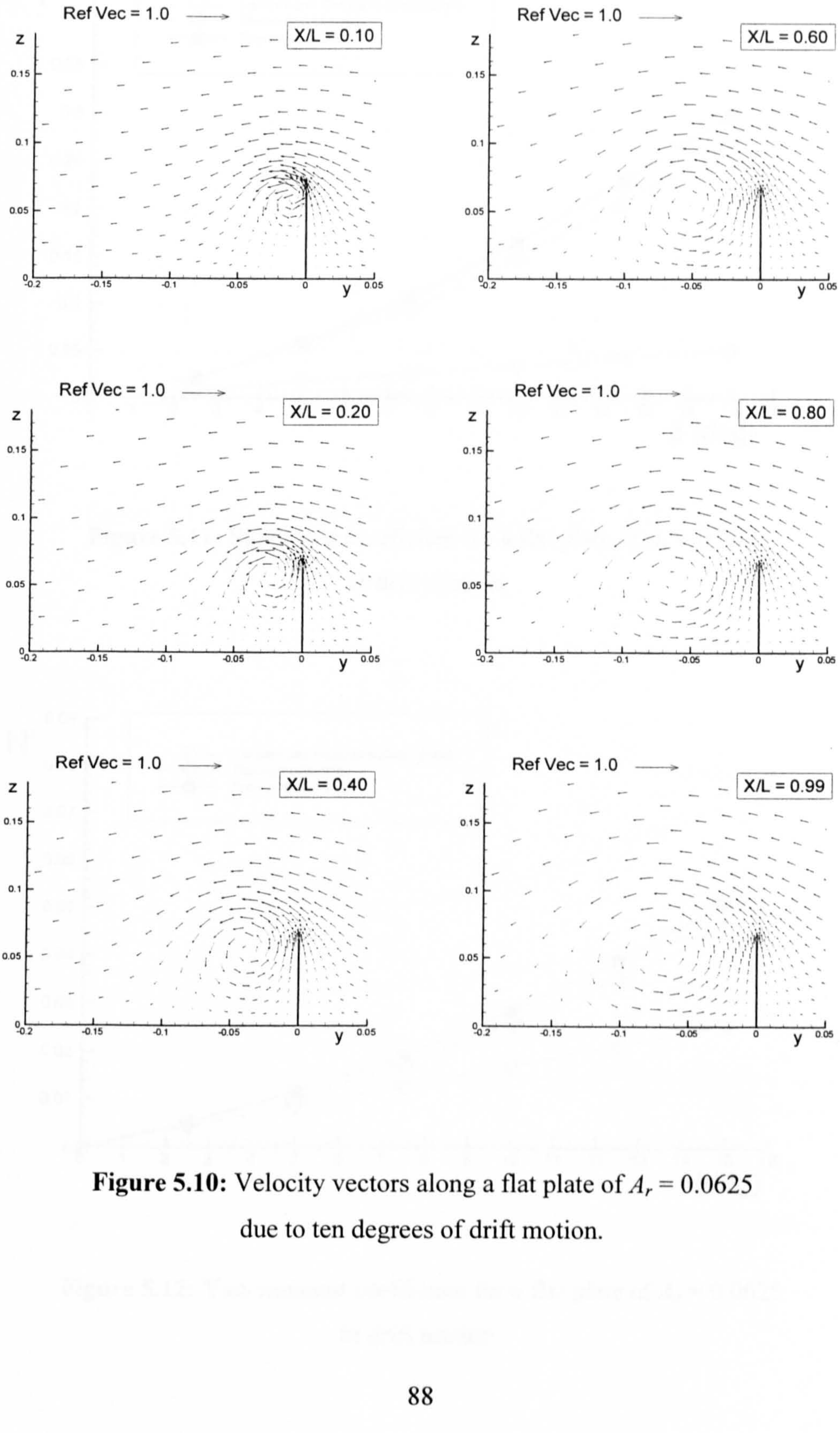

Figure 5.10: Velocity vectors along a flat plate of $A_r = 0.0625$ due to ten degrees of drift motion.

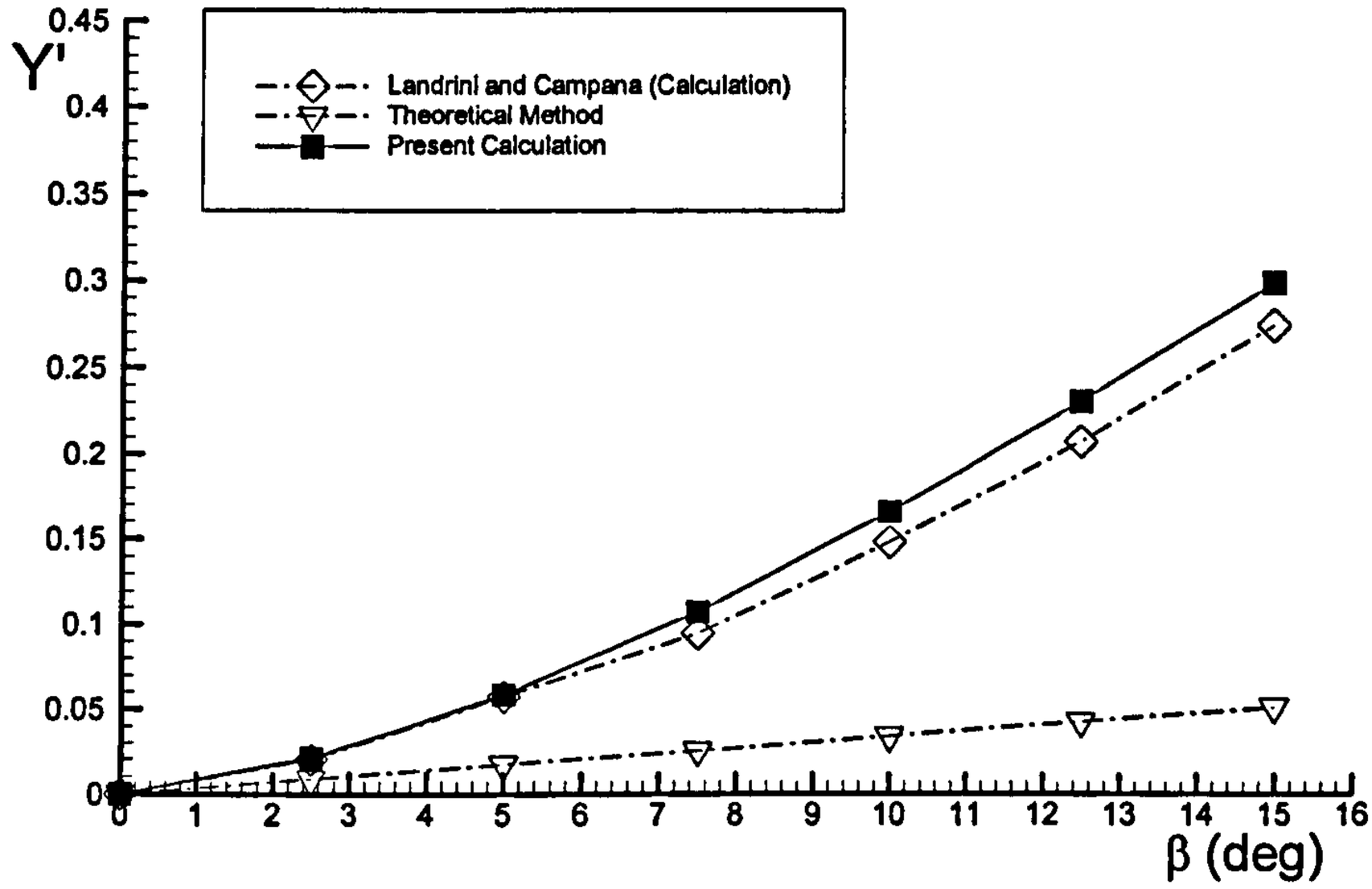

Figure 5.11: Side force coefficient for a flat plate of $A_r = 0.0625$ in drift motion.

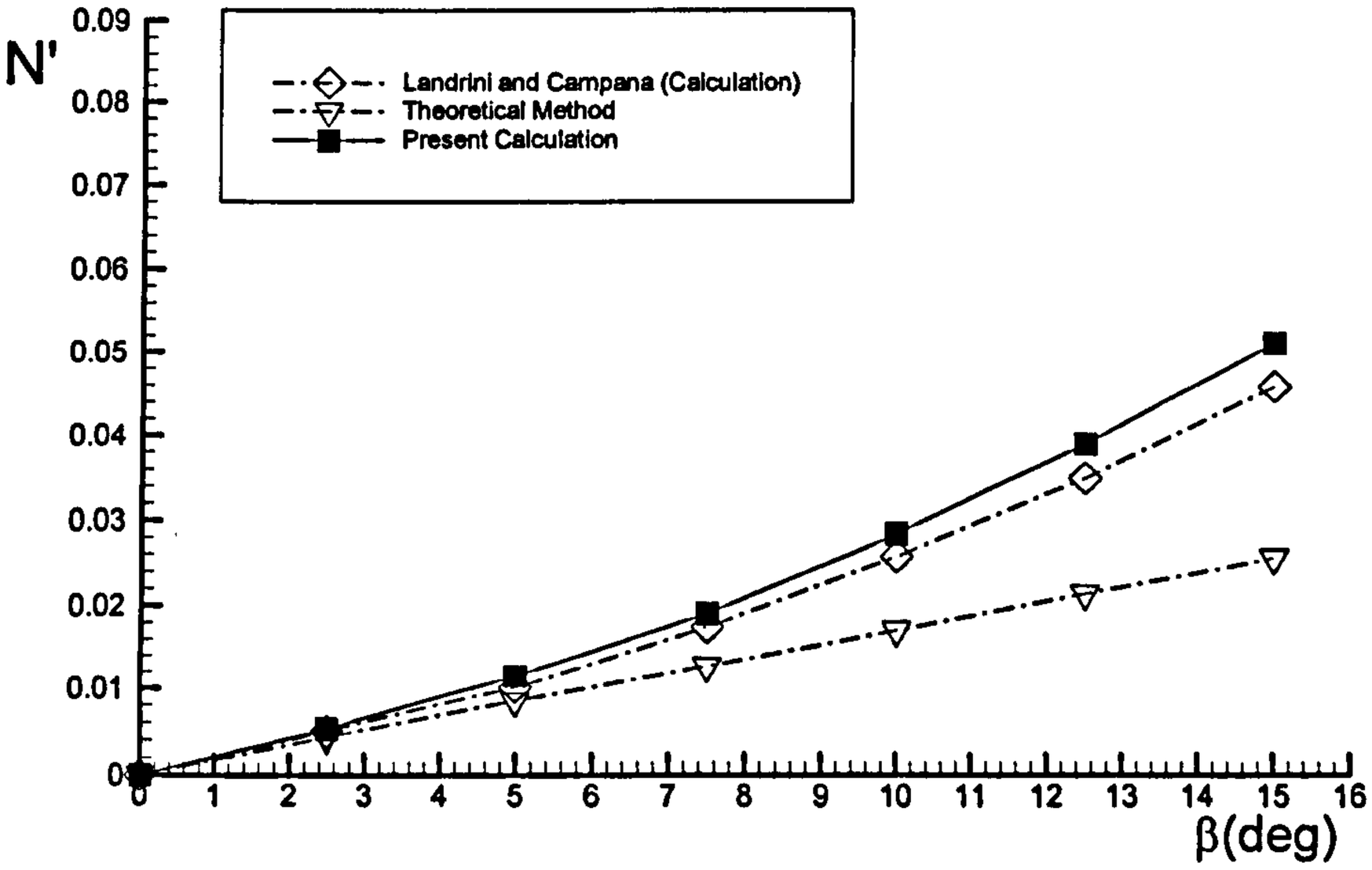

Figure 5.12: Yaw moment coefficient for a flat plate of $A_r = 0.0625$ in drift motion.

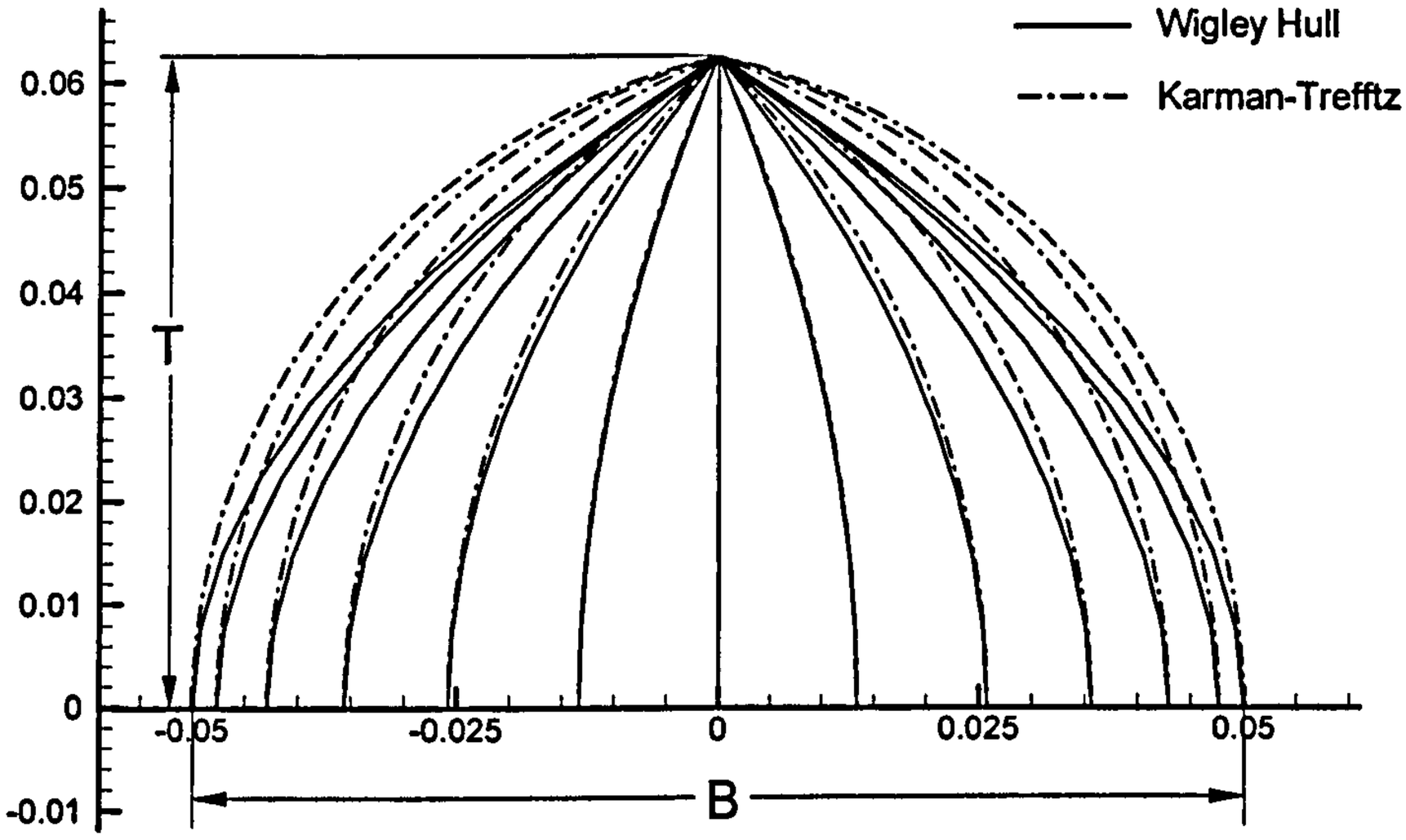

Figure 5.13: Comparison of the Wigley hull and the present hull.

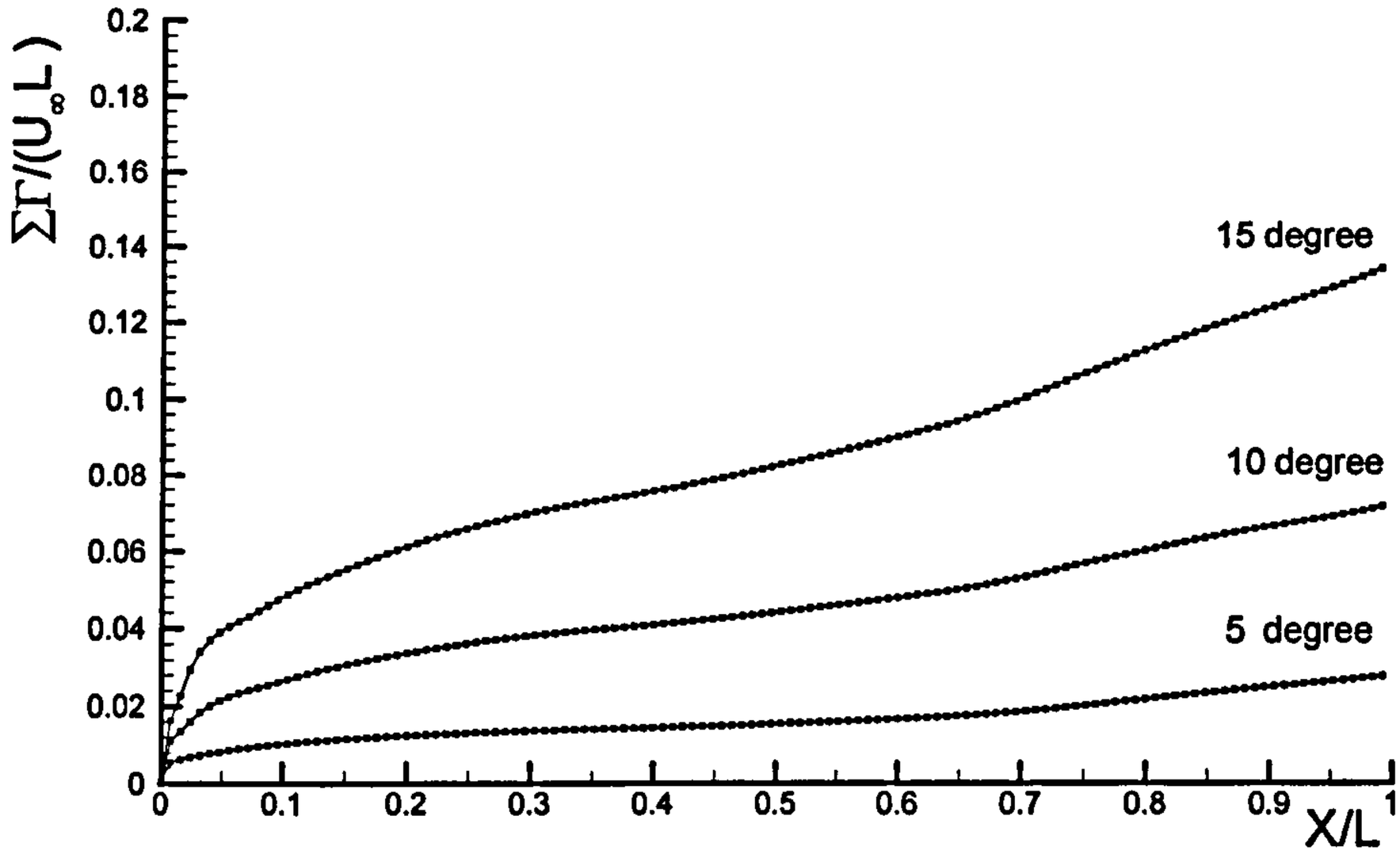

Figure 5.14: The development of total circulation over the Wigley hull.

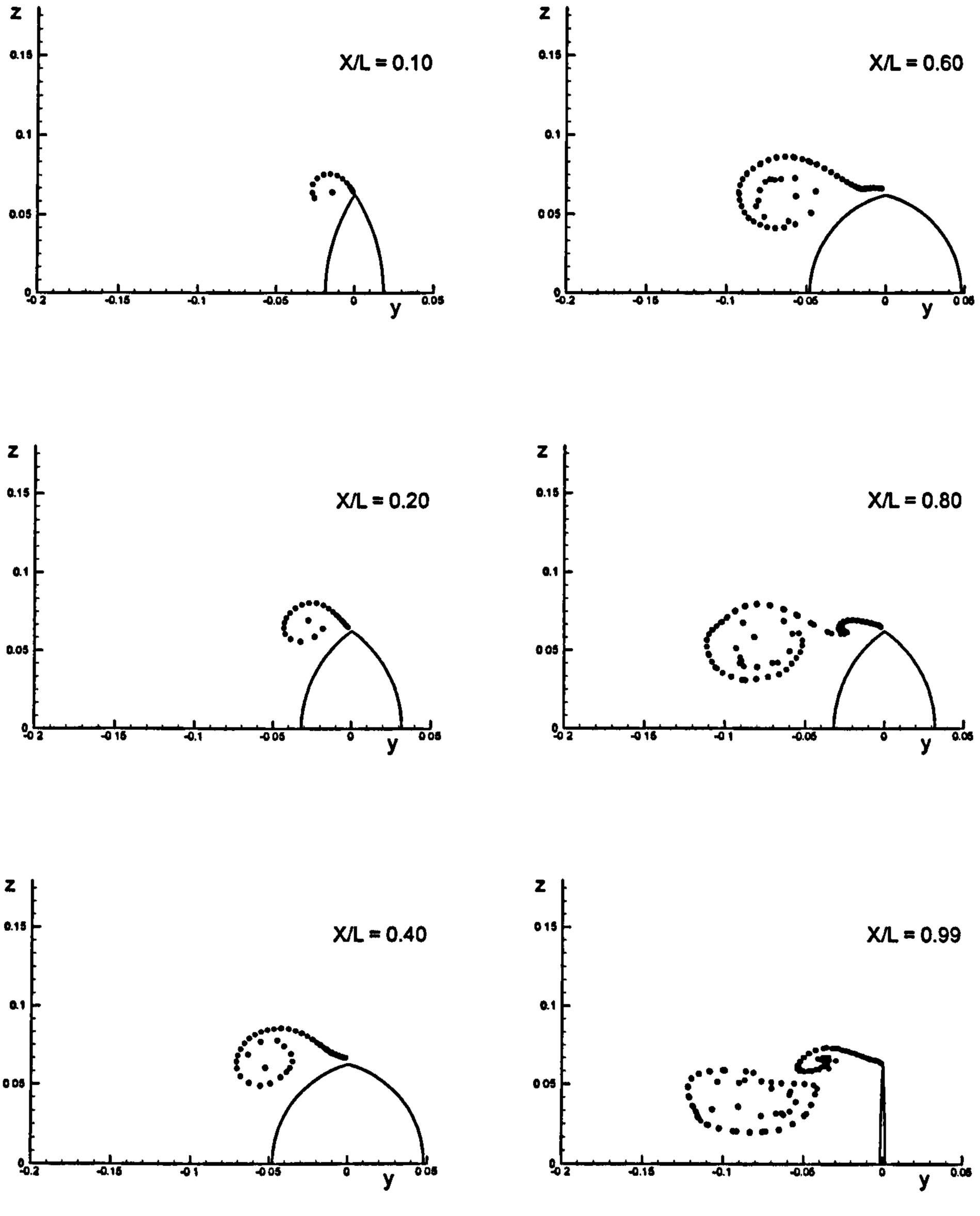

Figure 5.15: Vortex evolution around the Wigley hull due to ten degrees of drift motion.

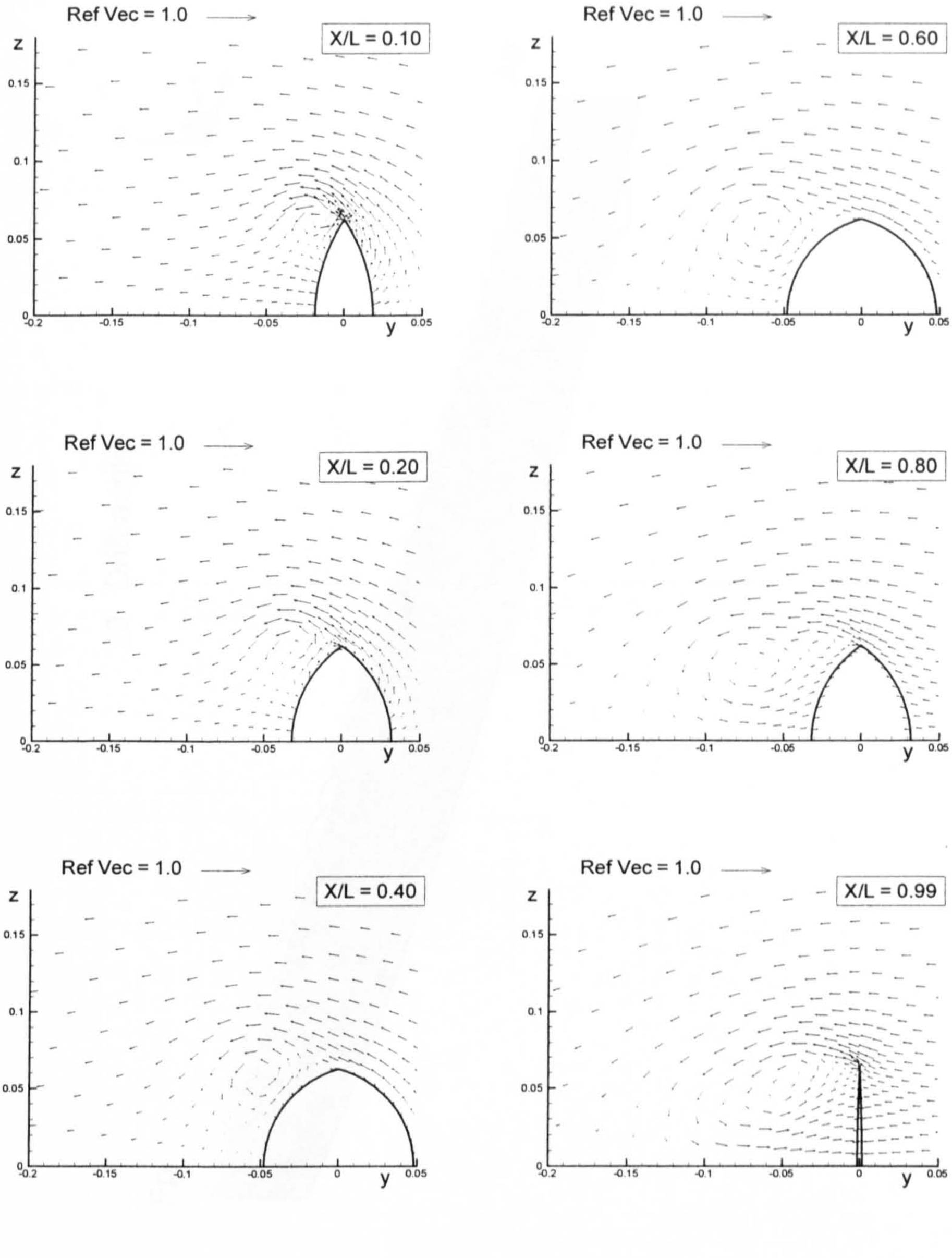

Figure 5.16: Velocity vectors along a Wigley hull due to ten degrees of drift motion.

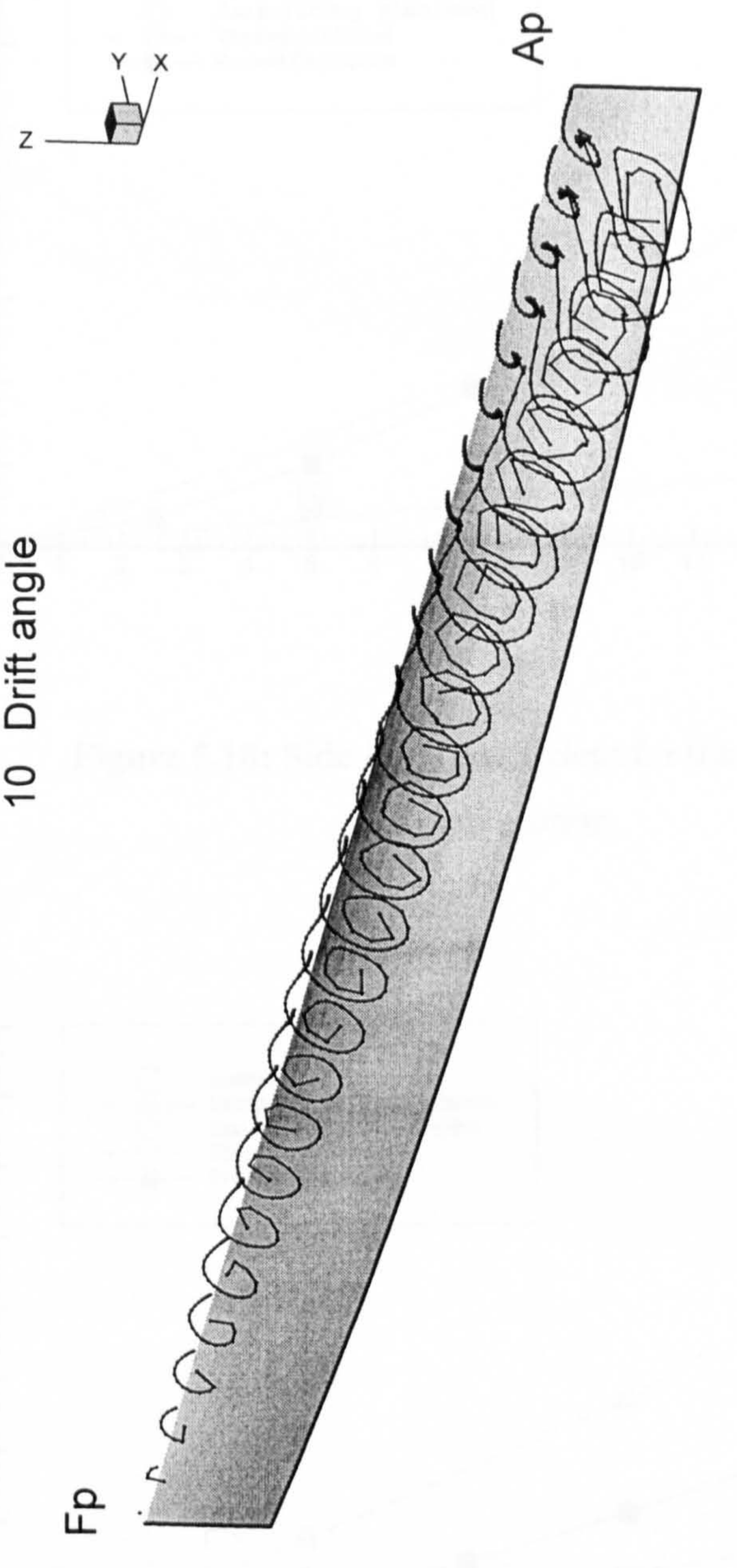

Figure 5.17: Vortex flow around the Wigley hull due to ten degrees of drift motion.

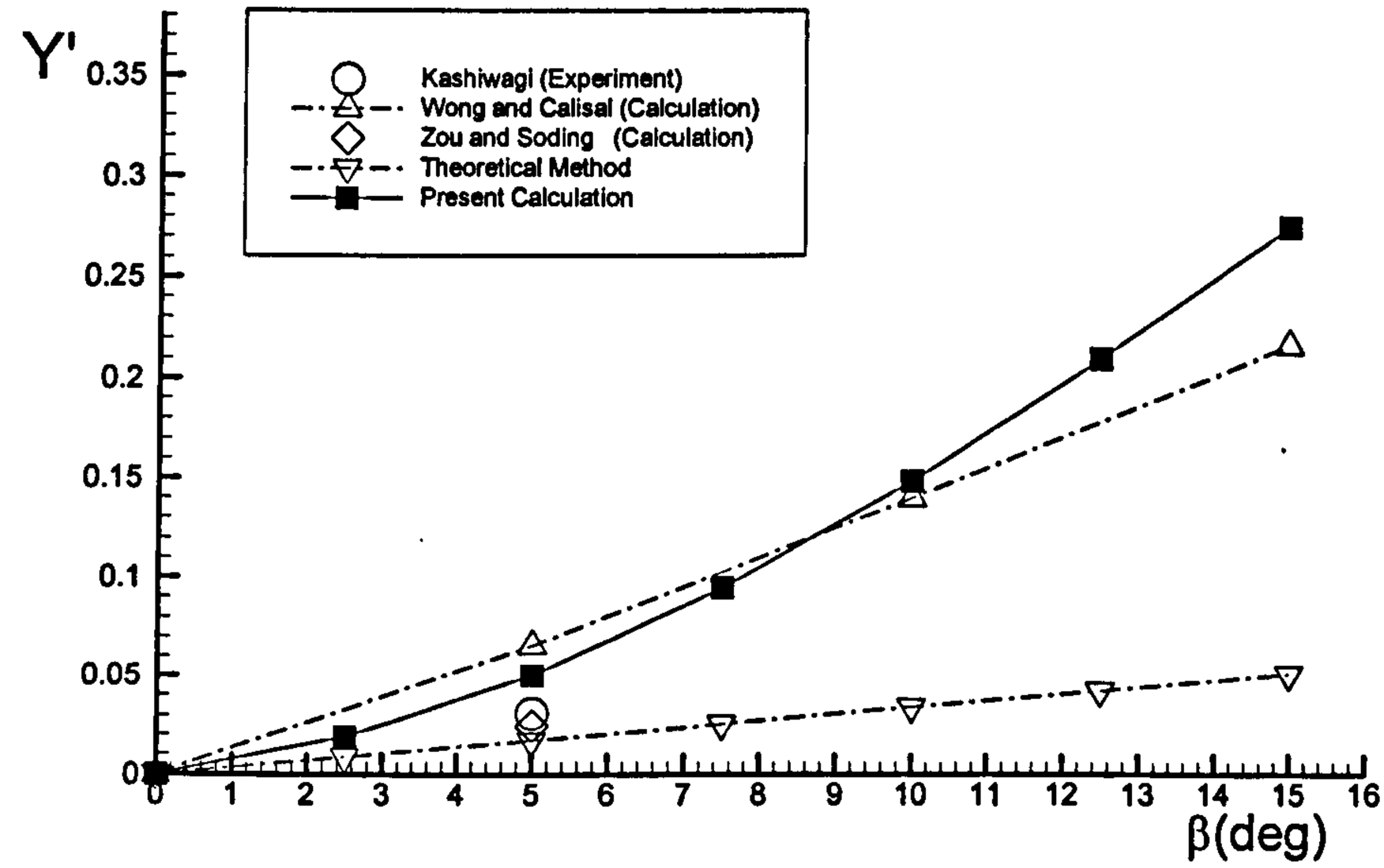

Figure 5.18: Side force coefficient for the Wigley hull in drift motion.

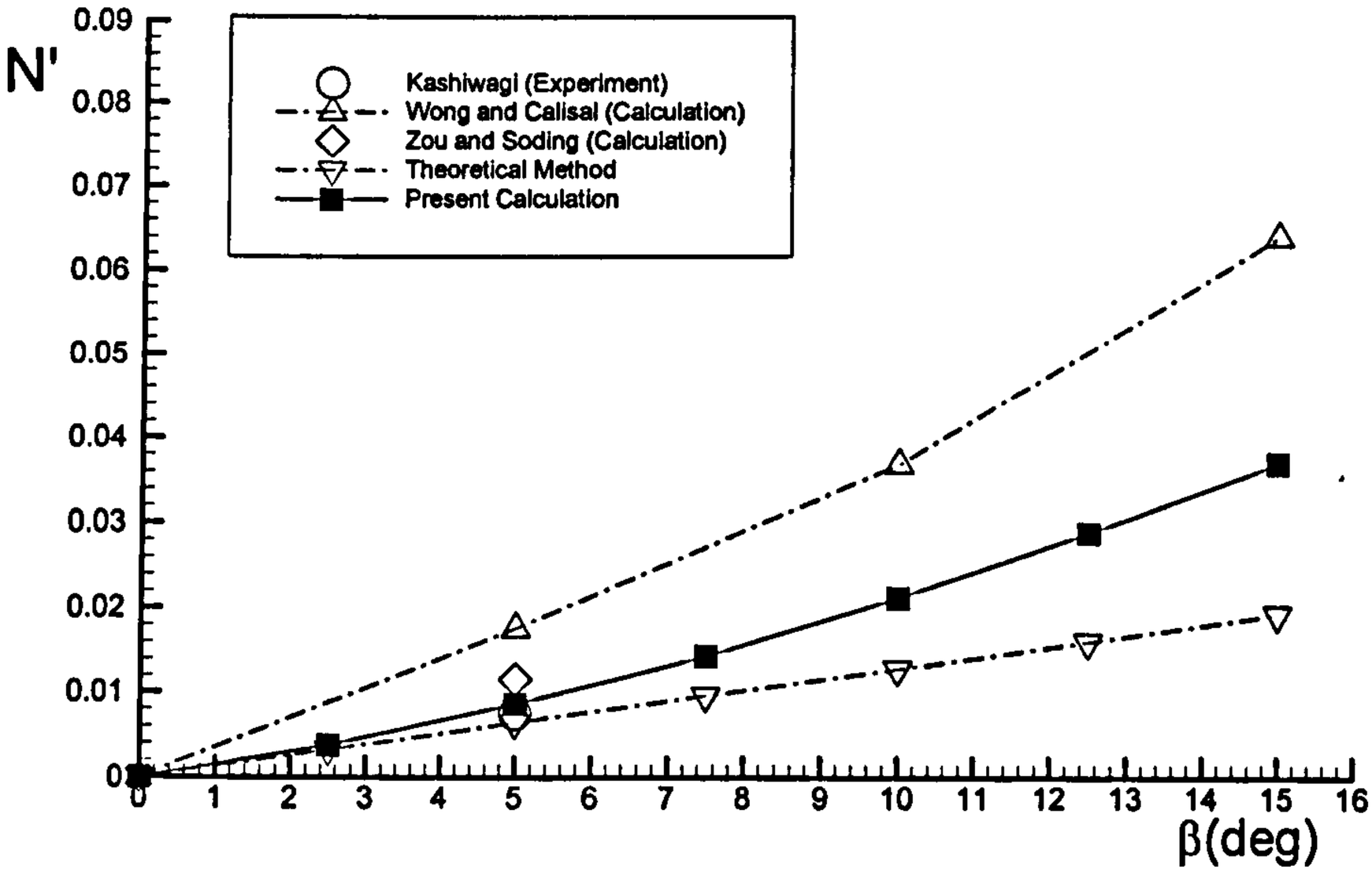

Figure 5.19: Yaw moment coefficient for the Wigley hull in drift motion.

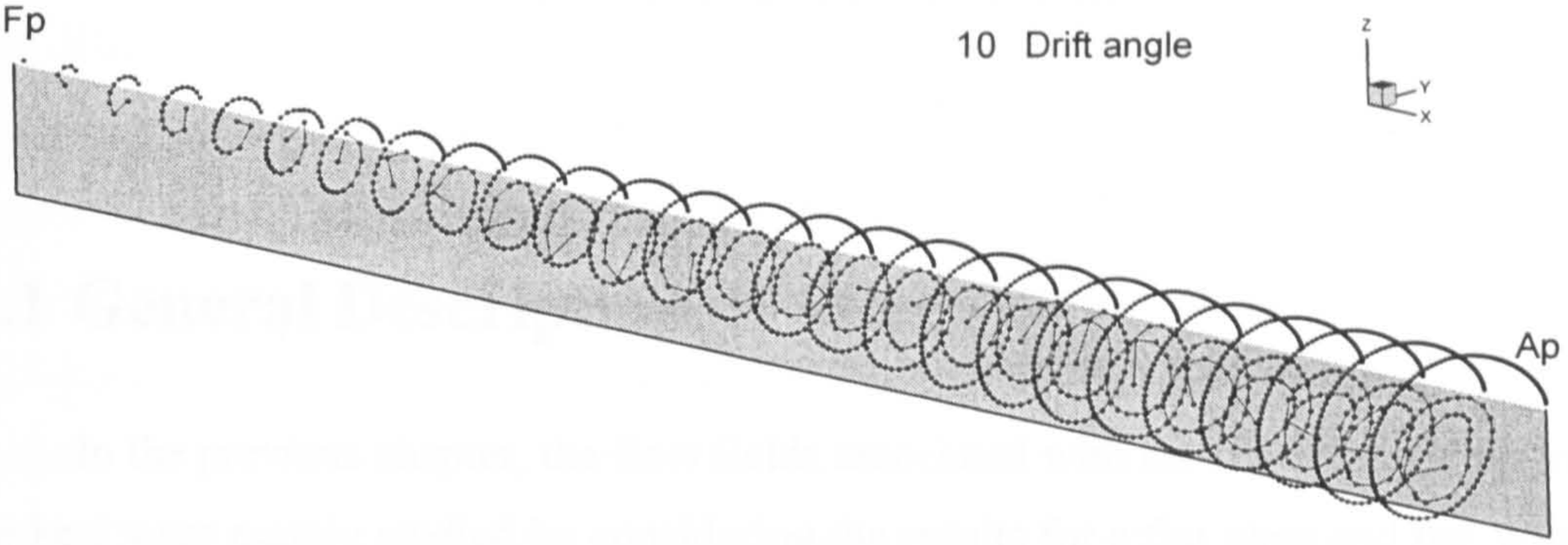

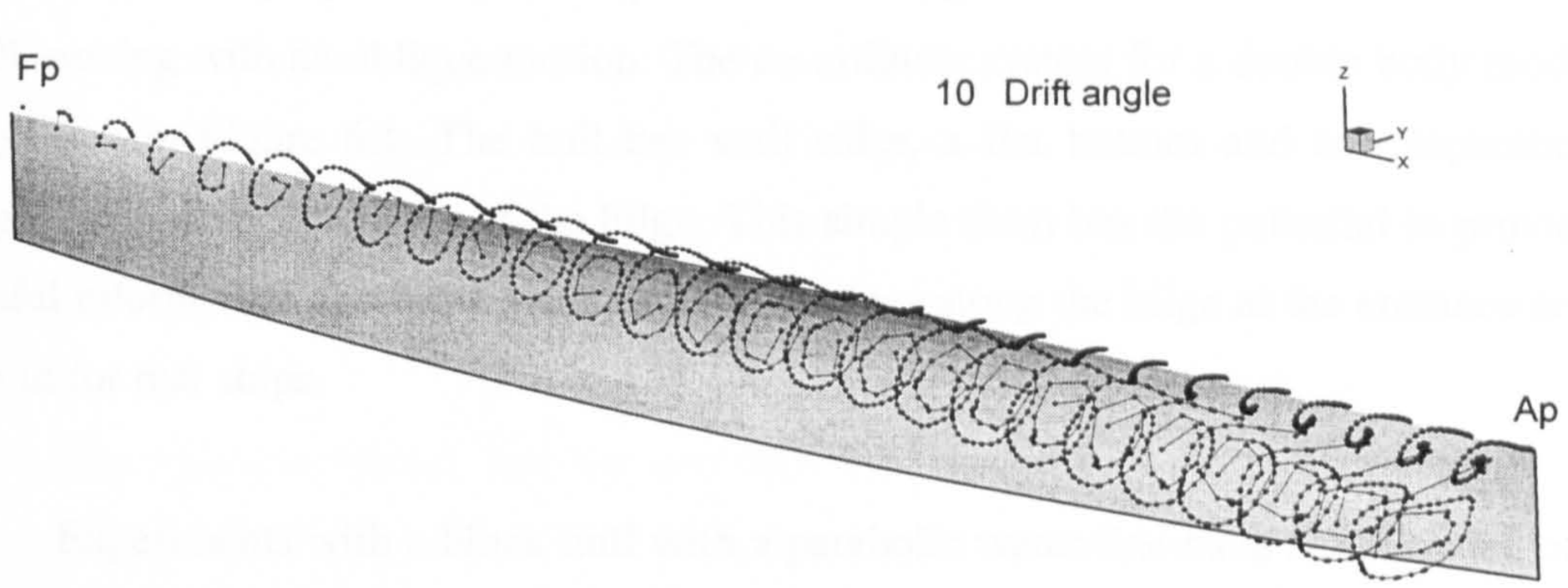

Figure 5.20: Comparison of the vortex flow for a flat plat and the Wigley hull due to ten degrees of drift motion.

Chapter VI

THE BLOCK HULL

6.1 General Description

In the previous chapter, the flow fields associated with the vortex shedding from the keel were mainly studied by considering the results for a flat plate and the Wigley hull. The thickness effect of the Wigley hull was well predicted by the present method, but for both hulls, it was seen that the separation from a single edge along the keel line is the dominant flow phenomena in drift motion.

The main purpose of this chapter is to investigate the flow field around a block hull moving with an oblique motion. The co-ordinate system for a double body model is shown in Figure 6.1. The hull has wall sides, a flat bottom and two separation edges, one along each side of the bilge. This simple form has the potential to provide useful information about the generation of vortices along the bilge at the entrance and run in for real ships.

Experiments with a block hull with a parabolic water line have been carried out by Tagori (1966) in order to study the characteristics of the bilge vortices generated by a ship moving with straight-ahead motion. From flow observations using the tuft grid method, he showed that the down flow along the wall side separates at the bilge, and a set of conical vortices is generated at the fore bottom. This set of vortices is similar to the leading edge vortex of a delta wing. At the afterbody, the flow runs out from the bottom and separates at the bilge, and a new set of large vortices is produced at the side of model.

Later Bradbury (1983) investigated flow separation around different types of block hull with varying drift angles. The tests were conducted in a wind tunnel using a double body block hull and ignored the free surface effect. In his experiment about zero drift motion for a block hull with a Mariner waterplane, he clearly showed the shedding of bow and stern vortices. He also demonstrated the existence of a secondary vortex, shed from the bilge middle body, by means of surface oil flow patterns, but no secondary vortices could be detected by the wool tufts. The secondary vortex shed from the block hull was later confirmed from experimental and numerical results by AL-Hukail (1992). Bradbury's experiment about drift motion showed that asymmetric vortices associated with cross flow become important for this flow configuration. At low drift angles the asymmetric flow is barely apparent, but it becomes increasingly dominant over much of the hull's length as the angle increases.

The vortices generated at the bilge of the entrance and run in, for both straight ahead and drift motions, are investigated in this chapter. The calculations are confined to a block hull with a waterplane based on the Mariner hull (Russo and Sullivan 1953) for the purpose of the comparison of the results with those of Bradbury (1983) and Al-Hukail (1992). Consistent with the slender body theory, the hull is represented as a series of two-dimensional strips. The transverse sections of the block hull have been represented by the Schwartz-Cristoffel transformation.

The straight ahead motion problem has also been compared using the commercial CFD code called CFX and the results are compared with the present discrete vortex method. CFX is a general-purpose finite volume based code using a structured, multi-block body fitted co-ordinate system.

The discrete vortex method to be used in this study has been described in Chapter 4. Some of the procedures discussed, such as the hull transformation, the calculation of source strengths and the introduction of discrete vortices into the flow, require more detailed explanations since their implementation differs slightly on the block hull. These procedures are described in the following sections.

6.2 Block Hull Transformation

For the block hull, each of the transverse sections and associated computational meshes in the *Z*-plane are mapped into a rectangular grid by a three stage conformal transformation. Each block section is transformed into a horizontal flat plate in the *S*2-plane using the Schwarts-Christoffel transformation. The flat plate is then transformed into a circular cylinder in the *S*1-plane using the Joukowski transformation. The circular cylinder in the *S*1-plane is then mapped into a rectangular grid in the *S*-plane. Figure 6.2 only shows the *Z*-plane and the intermediate *S*2-plane, which are different to the transformations described previously, and the other transformed domains, the *S*1-plane and *S*-plane, are shown in Figures 4.11 and 5.3 in the previous chapters. The relevant transformations are given by

$$Z = \int_0^{S2} \left(\frac{S2^2 - a^2}{S2^2 - b^2} \right)^{1/2} dS2 \pm iT$$

$$S2 = S1 + \frac{r^2}{S1} \tag{6-1}$$

$$S1 = r \cdot \exp\left(i \frac{\delta\theta}{2} \right) \cdot \exp(i\alpha S)$$

where r is the radius of a circular cylinder and is the half length of b as seen in Figure 6.2 and a in the *S*2-plane is the point corresponding to the separation points in the *Z*-plane.

6.3 Calculation of Source Strengths

The normal velocity along the hull sections can be expressed in terms of the related body boundary condition. The normal velocities, V_n, on each sectional hull surface are defined from equation (4-11)

$$V_n = \frac{-U_\infty}{\sqrt{1+(dy/dz)^2}}\left(\frac{dy}{dx}\cos\beta \pm \sin\beta\right) \tag{6-2}$$

For the block hull, there is no change of hull geometry along *z*-direction and the *dy/dz* terms of equation (6-2) will be zero so that the equation may be simplified to

$$\begin{aligned} V_n &= U_\infty\left(\frac{dy}{dx}\cos\beta + \sin\beta\right) \qquad For \quad B1 < Z < A1 \\ &= -U_\infty\left(\frac{dy}{dx}\cos\beta + \sin\beta\right) \qquad For \quad B2 < Z < A2 \end{aligned} \tag{6-3}$$

The first term of the right hand side represents the sectional hull dilation, and the second term represents the sectional translation due to drift motion. The total velocity component will be found by the combination of the two normal velocity terms. Figure 6.3 shows the normal velocity distribution representing the growing hull surface with a drift motion. The positive sign of the normal velocity signifies outward motion from the hull surface.

The source strengths over the section are dictated by the normal component of the surface movement, as described in equation (4-6),

$$m(\eta) = -i2\overline{(V_n)}\frac{dZ}{dS} \tag{6-4}$$

where *dZ/dS* is the derivative of the transformation which can be found from equation (6-1) as

$$\frac{dZ}{dS} = \frac{dZ}{dS2}\frac{dS2}{dS1}\frac{dS1}{dS}$$
$$\frac{dZ}{dS2} = \left(\frac{S2^2 - a^2}{S2^2 - b^2}\right)^{1/2}$$
$$\frac{dS2}{dS1} = 1 - \frac{r^2}{S1^2} \qquad (6\text{-}5)$$
$$\frac{dS1}{dS} = r \cdot \exp\left(i\frac{\delta\theta}{2}\right) \cdot i\alpha \cdot \exp(i\alpha S)$$

Figure 6.4 shows the source distributions representing the growing hull with a drift motion in the transformed *S*-plane.

6.4 Introduction of Discrete Vortices into the Flow

In the previous calculation for the flat plate and the Wigley hull, a single vortex was introduced near both upper and lower separation points at each time step. There was only one vortex strength to be determined at each time step due to the symmetry of the double body model as described in the previous section.

As seen in Figure 6.3, introducing vortices into the block hull flow is more complicated than for the Wigley hull in that it has two well-defined shedding edges. In this case a vortex is introduced into the flow at each shedding edge at each succeeding section so as to satisfy the Kutta condition at both edges. Each nascent vortex position is located a small distance above each bilge at the first section. For the following time steps, the new vortices are introduced between the last shed vortex and the separation point to make the flow separate smoothly.

As described in section 5.2.3, the vortices introduced at the previous time step are transported down stream and, by themselves, no longer enforce the Kutta condition. There are unbalanced velocities V_{ub1} and V_{ub2} at the separation points that must be countered by the introduction of four more new vortices of the appropriate strength Γ. Only two vortex strengths need to be determined at each time step due to

the symmetry of the double body model in which the remaining two vortex strengths take the same magnitude but are of opposite sign. The complex velocities, V_{ub1} and V_{ub2} at the separation point S_{p1} and S_{p2} in the S-plane, which correspond to $A1$ and $A2$ respectively in the Z-plane (Figure 6.3), are given from equation (4-25) by

$$\frac{dW(S_{p1})}{dS} = V_{ub1}$$

$$= \frac{-i}{2\pi}\left[\sum_{S_{j,k}} \Gamma_{j,k}\left(\cot\frac{\pi(S_{p1}-S_{j,k})}{R} - \cot\frac{\pi(S_{p1}-\overline{S}_{j,k})}{R}\right)\right] \qquad (6\text{-}6a)$$

$$+ \int_{S_{1,1}}^{S_{1,2nk-1}} \frac{m(\eta)}{2\pi}\cot\frac{\pi(S_{p1}-\eta)}{R}d\eta$$

$$\frac{dW(S_{p2})}{dS} = V_{ub2}$$

$$= \frac{-i}{2\pi}\left[\sum_{S_{j,k}} \Gamma_{j,k}\left(\cot\frac{\pi(S_{p2}-S_{j,k})}{R} - \cot\frac{\pi(S_{p2}-\overline{S}_{j,k})}{R}\right)\right] \qquad (6\text{-}6b)$$

$$+ \int_{S_{1,1}}^{S_{1,2nk-1}} \frac{m(\eta)}{2\pi}\cot\frac{\pi(S_{p2}-\eta)}{R}d\eta$$

The unbalanced velocities at the separation points are negated by introducing new vortices at the defined new vortex points to satisfy the Kutta condition. The strengths of the new vortices Γ_{n1} and Γ_{n2} at the right and left hand side of the bilge are calculated to give zero complex velocities at the separation points in the S-plane. This implies that

$$\begin{aligned} V_{ub1} + \Gamma_{n1}X_1 + \Gamma_{n2}X_2 &= 0 \\ V_{ub2} + \Gamma_{n1}X_3 + \Gamma_{n2}X_4 &= 0 \end{aligned} \qquad (6\text{-}7)$$

and that

$$\Gamma_{n1} = -\frac{V_{ub1}X_4 - V_{ub2}X_2}{X_2X_3 - X_1X_4}$$
$$\Gamma_{n2} = -\frac{V_{ub2}X_1 - V_{ub1}X_3}{X_2X_3 - X_1X_4} \qquad (6\text{-}8)$$

The two equations can be solved to yield the new vortex strengths Γ_{n1} and Γ_{n2}, using

$$X_1 = \frac{-i}{2\pi}\left[\cot\frac{\pi(S_{p1} - S_{1u})}{R} - \cot\frac{\pi(S_{p1} - \overline{S}_{1u})}{R} - \cot\frac{\pi(S_{p1} - S_{1l})}{R} + \cot\frac{\pi(S_{p1} - \overline{S}_{1l})}{R}\right] \qquad (6\text{-}9a)$$

$$X_2 = \frac{-i}{2\pi}\left[\cot\frac{\pi(S_{p1} - S_{2u})}{R} - \cot\frac{\pi(S_{p1} - \overline{S}_{2u})}{R} - \cot\frac{\pi(S_{p1} - S_{2l})}{R} + \cot\frac{\pi(S_{p1} - \overline{S}_{2l})}{R}\right] \qquad (6\text{-}9b)$$

$$X_3 = \frac{-i}{2\pi}\left[\cot\frac{\pi(S_{p2} - S_{1u})}{R} - \cot\frac{\pi(S_{p2} - \overline{S}_{1u})}{R} - \cot\frac{\pi(S_{p2} - S_{1l})}{R} + \cot\frac{\pi(S_{p2} - \overline{S}_{1l})}{R}\right] \qquad (6\text{-}9c)$$

$$X_4 = \frac{-i}{2\pi}\left[\cot\frac{\pi(S_{p2} - S_{2u})}{R} - \cot\frac{\pi(S_{p2} - \overline{S}_{2u})}{R} - \cot\frac{\pi(S_{p2} - S_{2l})}{R} + \cot\frac{\pi(S_{p2} - \overline{S}_{2l})}{R}\right] \qquad (6\text{-}9d)$$

As shown in Figures 6.3 and 6.4, S_{1u}, S_{2u} and S_{1l} and S_{2l} are the positions of the new vortices in the S-plane corresponding to the upper and lower positions respectively of the new vortices in the Z-plane. The overbar in equation (6-9) indicates the complex

conjugate and represents the vortex position inside the body satisfying the body boundary condition as described in the Chapter 4.

6.5 Calculation and Results

The developed model was applied to the block hull moving firstly with straight-ahead motion, and secondly at an angle of drift of up to 15 degrees. The aspect ratio and a breadth to length ratio of the hull are 0.05 and 0.15 respectively. The sectional numbers along the hull length and the grid numbers along the girthwise and radial direction of each transverse sections are kept the same as for the previous calculations, and are 128, 28 and 18 respectively. Figure 6.5 shows some of the two-dimensional hull sections with transverse sectional grid domains.

The distributions of the total vortex circulation shed from each bilge along the block hull is shown in Figure 6.6 for the case of zero drift motion. The positive sign of the vortex is counter clock wise as defined in the previous chapter. The accumulated circulation curves of both right and left hand bilges represents a pair of bow vortices growing in the fore part and then a secondary pair of the opposite sign start to grow due to the influence of the bow vortices. This pairing process continues until vortex strength nearly reaches zero. A pair of new vortices of opposite sign to the bow vortex starts to appear and grow as the stern section is approached.

The development of the vortex flow field and the velocity vectors are shown in Figures 6.7 and 6.8 respectively. These figures show that three sets of vortices separate from the sharp bilge corners along the hull. The flow visualisation experiments by Bradbury (1983) and Al-Hukail (1992) also showed the existence of these three sets of vortices. They are the entrance vortex in the bow part, the secondary vortex in the middle part and the run vortex in the stern part. The stern vortex is the dominant part for the formation of the wake distribution, as seen in Figure 6.8, which is important for propeller design.

For straight-ahead motion, as the solution marches sternwards along the hull, the sections initially appear to growing rapidly, and the fluid flows around the corners away from the free surface. Along the right-hand side shedding edge in Figure 6.7, positive vorticity is shed into the flow and a strong anti-clockwise vortex develops.

Over the parallel middle body the edge flow reverses direction due to the influence of the bow vortex, and relatively small amounts of negative vorticity begin to be shed into the flow until the accumulated vorticity approaches zero. The resulting separated shear layer and the weak positive vortex tend to rotate about each other in an anti-clockwise direction, and the shear layer becomes progressively wound around the vortex core. When the stern is approached, the sections shrink rapidly and the edge flow is accelerated.

The sudden increase in strength of the positive vorticity shed into the flow leads to the formation and roll up of a strong negative vortex close to the hull at the stern. The final vortex structure at the aftermost section is composed of a weak negatively signed shear layer, wound in at one end by a strong negative stern vortex, connected at the other end to a strong outer positive bow vortex.

When the hull is travelling with five degrees of drift motion as seen in Figures 6.9, 6.10 and 6.11, the same process occurs but the additional cross flow also plays a part. In the fore part, the right hand bilge vortex strength is reinforced by the cross flow and the reverse is true at the left hand bilge. As the flow passes over the middle body, there is a second set of vortices shed under the influence of the bow vortex. The second vortex developed at the right hand bilge is not attributable to the bow vortex but starts to be shed due to the influence of the cross flow. As shown in Figures 6.10 and 6.11, this flow carries the bow vortex back and towards the shear layer, which rolls up into a negative vortex as it moves. The uppermost vortex at X/L = 0.99 in Figure 6.10 is formed from the rolled up shear layer, called the second vortex, shed from the middle body, and the bow vortex lies between it and the hull.

The side force and yaw moment coefficients plotted against the drift angle are shown in Figures 6.12 and 6.13 respectively. The experimental data by Bradbury (1983) and numerical results by AL-Hukail (1992) are also shown in Figure 6.12 for the side force coefficient, but there is no published data for comparison with the yaw moment coefficient. The agreement between the present results and the other results produced by experimental and numerical methods is reasonably good for the side force. The big differences between the theoretical method and present method in the Figures 6.12 represent the non-linear effect due to the vortex shedding as explained in section 4.11.

The evolution of vortex flows along the block hull for both zero and five degrees of drift motions are plotted in Figure 6.14 and 6.15 respectively to illustrate the influence of cross flow on the structure of bilge vortices.

6.6 Comparison with RANS Method

Even though there have been attempts to apply the RANS method to ship manoeuvring problems (Patel et al 1990 and Miyazaki et al 2000), the computing resources required are still so large that the approach is generally considered to be impractical at present, as described in section 2.4. In ship design, RANS methods are mainly applied to qualitative calculations of resistance and wake distributions for the hull in straight-ahead motion. In that case, only a quarter of a double body hull needs to be computed, which reduces the required computing resources and times significantly.

Among the existing commercial RANS codes (Freitas 1995 and ITTC 1996), the CFX code (formerly CFDS-FLOW3D) has been chosen to compare the flow field about the block hull with the present discrete vortex model. Because of the demands on computing resource and time made by the RANS method, the calculation has been confined to the straight-ahead motion only.

The CFX 4.1 suite of software consists of three parts, which comprise a pre-processor for grid generation, a flow solver and a post processor for flow visualisation. The CFX solver is a general purpose CFD code which can simulate compressible and incompressible flows, non-Newtonian flows, heat transfer, gaseous combustion, chemical reaction, porous media flow, multi-phase flow, particle transport and transient flows.

In the CFX flow solver, the RANS equations are treated by a finite volume method. Pressure and velocity fields, defined using a staggered grid, are iterated simultaneously by the SIMPLE (Semi-Implicit Method for Pressure Linked Equation) algorithm (Patankar 1980). Spatial discretization can be achieved through a number of approaches. These include a central difference scheme, a second order upwind scheme (Fletcher 1991), the HYBRID scheme, which is a modification of the upwind scheme using central differences, the QUICK (Quadratic Upstream Interpolation for Convective Kinetics) scheme (Leonard, 1979) and the CCCT scheme, which is a modification of the QUICK scheme. The CFX code models turbulent flows using a model chosen from a number of different available turbulence models, including, the standard $k-\varepsilon$ model, the low Reynolds number $k-\varepsilon$ model, the RNG-$k-\varepsilon$ model, the algebraic and differential forms of Reynolds stress model, and the Reynolds flux model. A detailed description of the methods can be found from CFX 4.1 Flow Solver User Guide (1995).

6.6 1 CFX Application to the Block Hull

In the present calculation, only the flow solver from the CFX 4.1 suite is used. The equations are solved by a fully implicit backward difference time stepping procedure, where the convection and diffusion terms are approximated by the HYBRID difference scheme. The standard $k-\varepsilon$ turbulence model (Rodi 1980) is used for the high Reynolds number flow ($Rn=1.0\times10^{6}$).

The flow visualisation of the results is performed using the graphics package, TECPLOT. The CFX solution is computed on the grid derived from the Cloud-in-Cell grid, which is made by conformal mapping (6-1) with some modifications on the hull surface. Grids are concentrated near the hull surface to capture the details of turbulence flow in this region. Figure 6.16 shows the generated grids for the cross sections of X/L = 0.5 and 0.95. The grid system generated by conformal mapping has the advantage that the grids on the hull surface and flow domains are orthogonal to each other. The number of grid points used in the CFX calculation for a quarter of the double body are $71\times24\times26$ in the ξ, η and ζ directions respectively in the body fitted co-ordinate system (Figure 6.17). The grid number is usually decided according to the hull shapes and computational conditions (CFD workshop Tokyo 1994 and Liu and Kodama 1993). The present grid number has been decided on the basis of information contained in the previous studies by Liu and Kodama (1993) and also on the basis of previous work carried out by the present author (Park 1996).

As seen in Figure 6.17, an H-O grid topology (Park 1996) is applied with a three-block grid system, which consists of an upstream block, a ship domain block and a down stream block. In this case, the boundaries can be divided as a body boundary (C1), a symmetric boundary (C2), a free surface boundary (C3), an upstream boundary (C4), a down stream boundary (C5) and an outer boundary (C6).

The no slip condition for the velocity and the zero normal gradient condition for the pressure are enforced on the surfaces of the block hull (C1). Neumann conditions for the pressure and velocity are used on the symmetric plane (C2) and free surface (C3). Uniform flow is assumed on the upstream boundary (C4) and the gradient of the velocity and pressure set to be zero on the down stream boundary (C5). A free stream condition is applied at outer boundary (C6).

6.6 2 Results and Comparisons

Figure 6.18 shows velocity vectors for transverse sections along the hull. The velocity vectors clearly show the existence of a bow vortex, a second vortex and a stern vortex. The development of the bow vortex is shown in the figures for X/L = 0.11 and 0.21. The development of the second vortex, shed in the middle part of the hull, can be found in the figures for X/L = 0.39 and 0.61. The growing and shedding of the stern vortex is shown in the figures for X/L = 0.79 and 0.99.

The flow patterns produced by the discrete vortex method and the CFX method are compared in Figure 6.19. The overall flow patterns from CFX are similar to the discrete vortex method but generally with weaker vortex strengths. The comparison of velocity vectors at X/L = 0.61 in Figure 6.19 shows some differences in the flow vectors given by the vortex method and the CFX calculation. The CFX result shows the shedding of a very weak second vortex compared to the discrete vortex method. At section X/L = 0.98, in the CFX method, there is no evidence of the bow and second vortex, but only the stern vortex. The stern vortex positions in the CFX results are in the same position compared to the discrete vortex method but have weaker strengths. The main reasons for the differences between the two methods are the exclusion of diffusion terms in the discrete vortex methods and the excessive diffusion occurring in the CFX method, which might be influenced by the convection schemes and turbulence models.

As discussed in the CFD Workshop 1994, the RANS methods usually tend to underpredict the strength of the vortices. The main reasons given for their failure to predict the vortex strength correctly relate to the numerical scheme (Kim and Choudhury 1994) and turbulence models (Sotiropoulos and Patel 1995 and Deng and Visonneau 1996) adopted.

Kim and Choudhury (1994) improved their wake distribution results by upgrading a discretization scheme of convection terms from the second-order upwind scheme to the third order QUICK scheme. Sotiropoulos and Patel (1995) introduced a Reynolds stress turbulence model in their wake calculation and showed better wake distributions than those obtained using the standard $k-\varepsilon$ model. Because of

constraints in computing resources imposed by the application of higher order convection schemes and sophisticated turbulence models, both calculations were restricted to the afterbodies of the ships and ignored the influences of ships' forebodies.

Since the discrete vortex method, in its present application, ignores the diffusion terms in the Navier-Stokes equations, in theory the RANS method is a more accurate and advanced method. However, the computing time for the discrete vortex method is only several minutes for the calculation of a half body of the double body hull, whereas the CFX calculation takes several hours even to calculate a quarter of the double body hull. In addition, for a number of reasons, the very high Reynolds number flows of the order of 1.0×10^6, which might be expected at the real scale ship, have not been easy to calculate by the RANS method until recently. For practical purposes, especially, for ship manoeuvring problems, the vortex discrete methods have some advantages over the RANS methods in relation to computing resources, times and a reasonable accuracy. In addition, the discrete vortex method can be relatively easily extended to include other degrees of freedom, such as roll (Patel and Brown 1986), that are even more difficult to treat using the RANS approach.

6.7 Conclusions

The present calculations applied to the block hull have proved to be very useful in gaining an insight into the primary mechanisms associated with the generation and development of bilge vortices along ship hulls. Comparison with the RANS method has demonstrated that the vortex method, which uses considerably less computing resources and times than the RANS method, is a useful approach for practical applications to ship manoeuvring problems and is reasonably accurate.

The previous chapters have mainly described the preliminary applications of the discrete vortex method to hulls with well-defined separation points, such as a flat plate hull, a Wigley hull and the Block hull. The calculations have confirmed that the vortex

method can capture the relative vortex strengths, and the locations, of the different components of the stern flow generated over the topology of the entire hull. Calculations starting part way down the hull will inevitably miss out essential ingredients of the structure and the interaction of the trailing vortices at the stern.

In the case of real hull shapes, there are usually no defined separation points around the hull sections and it is not easy to find separation points before numerical calculations are performed. The mechanism for the development of the vortex structure for real type hulls, such as the combinations of the bilge vortex and the keel vortex depending on hull types, will be more complicated than for the previous idealised hull forms.

The following chapter will mainly describe an improved discrete vortex method procedure for realistic ship hulls. A multi-vortex capability (Downie 1981) will be introduced to satisfy pointwise no-slip boundary conditions on the hull sections and the transformation procedure will be refined to match real hull shapes.

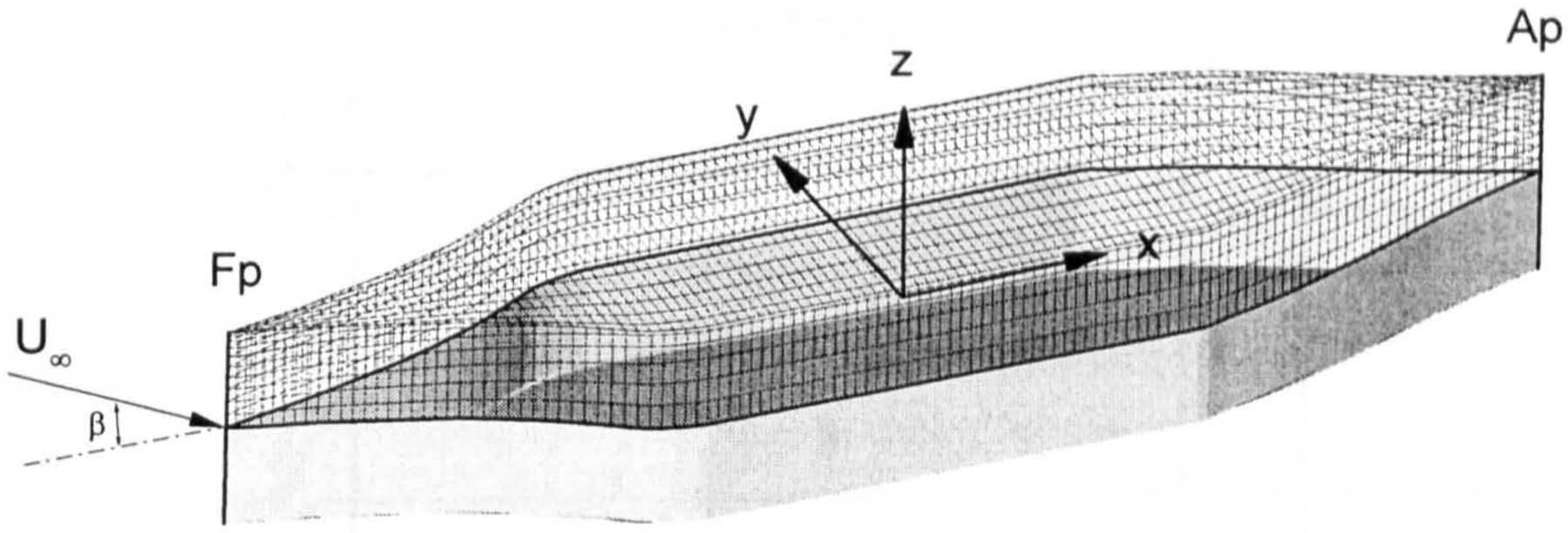

Figure 6.1: Co-ordinate system of a double body block hull.

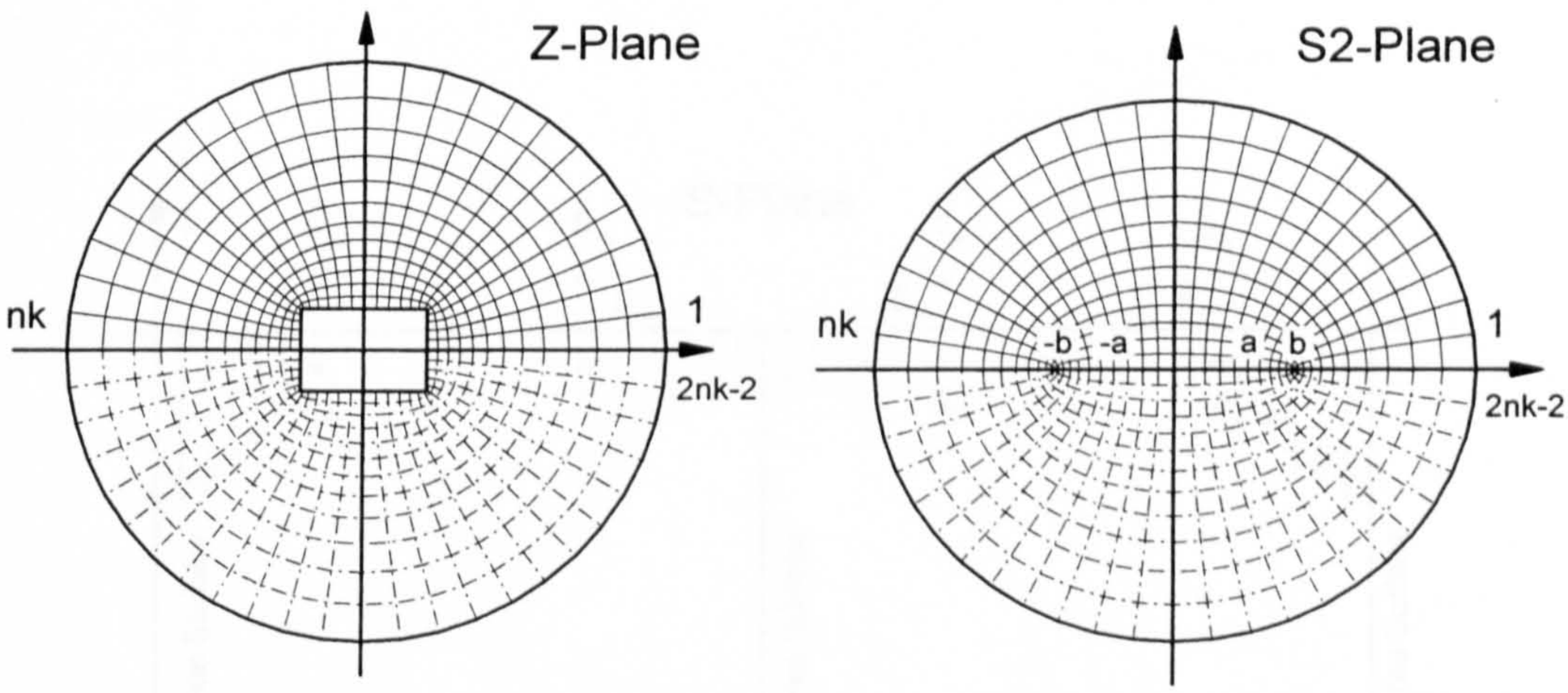

Figure 6.2: Conformal transformation for the block hull.

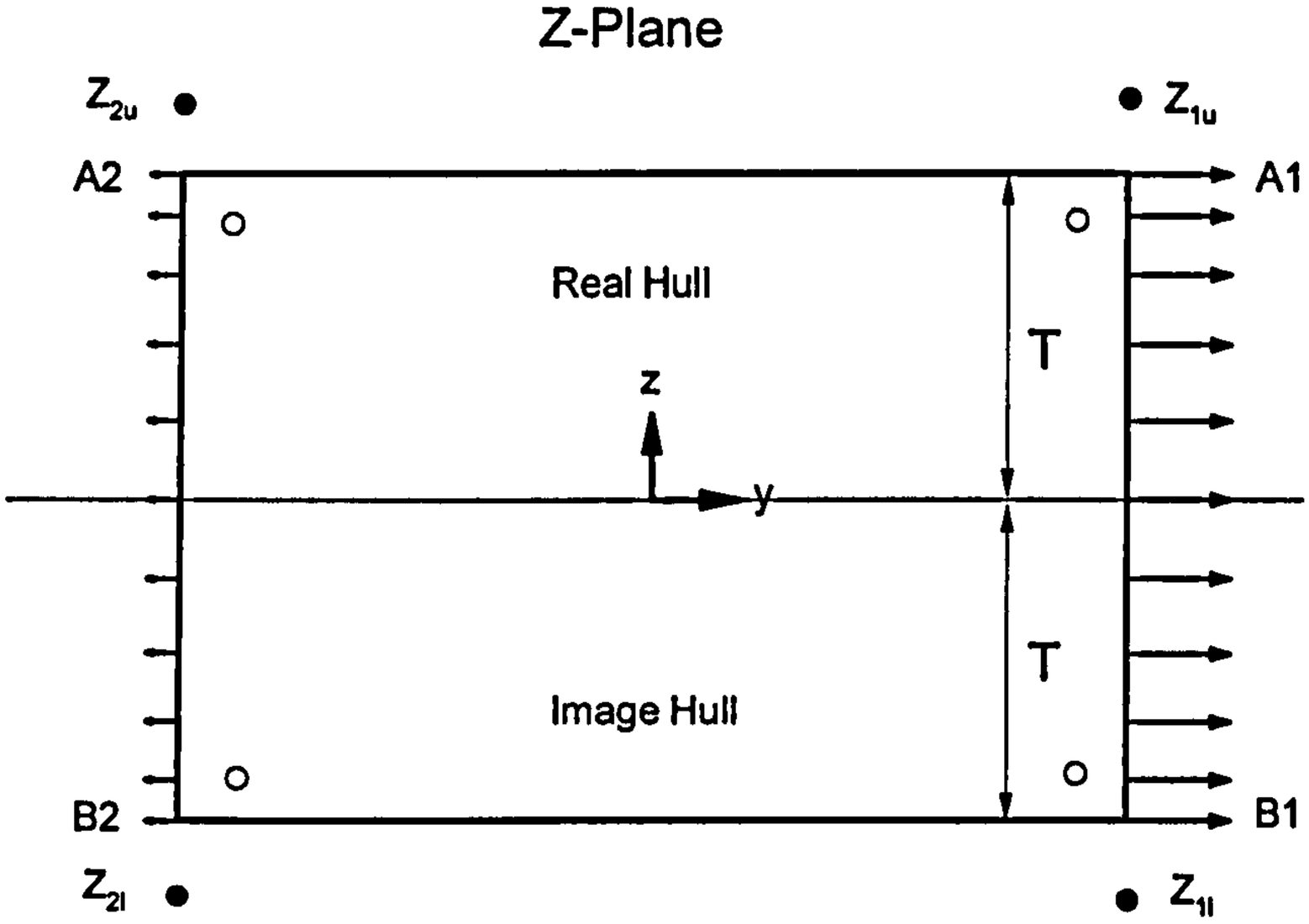

Figure 6.3: The representation of flow field of growing hull section with the drift motion.

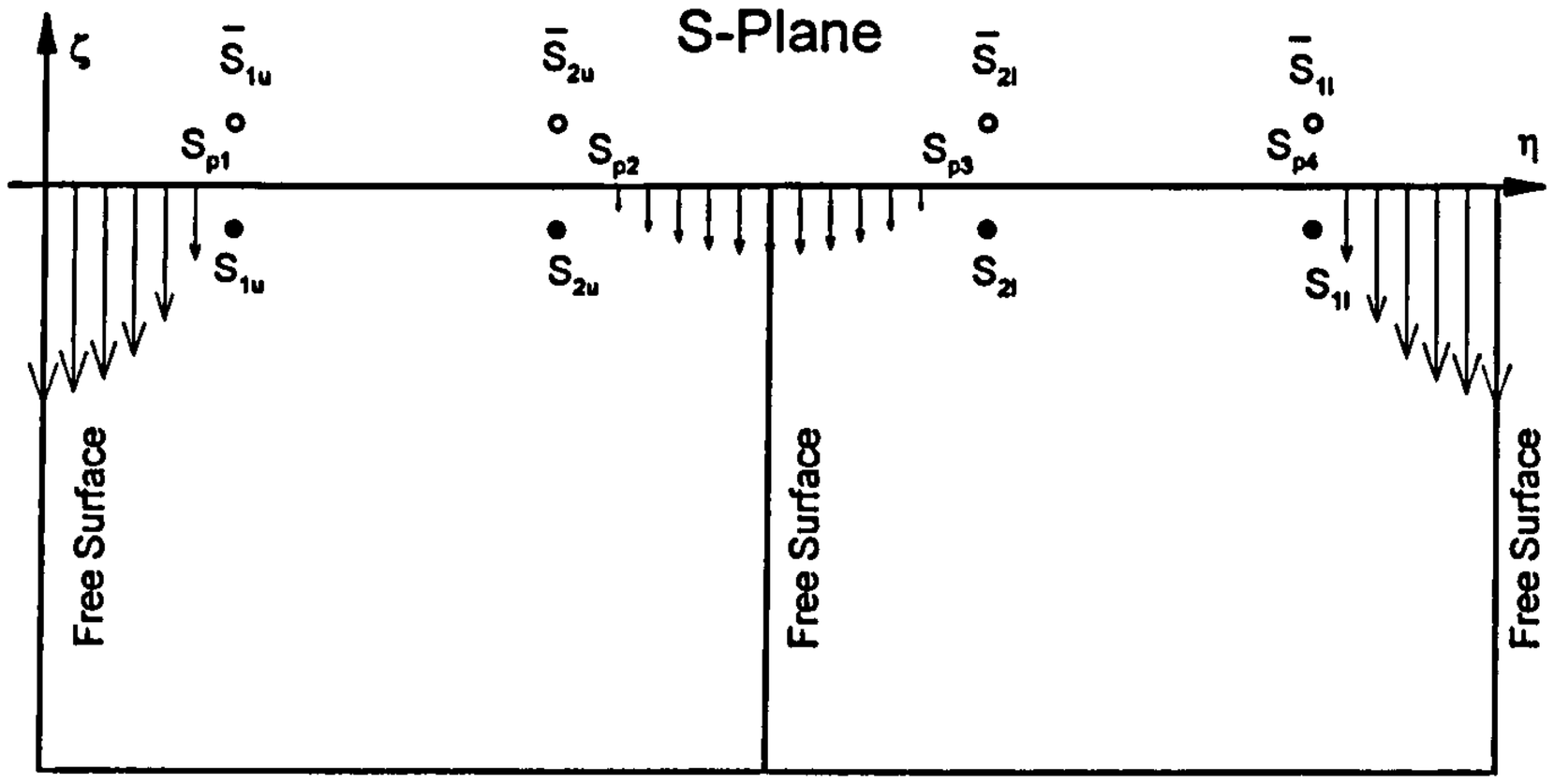

Figure 6.4: The flow field of computational domain for the growing hull with the drift motion.

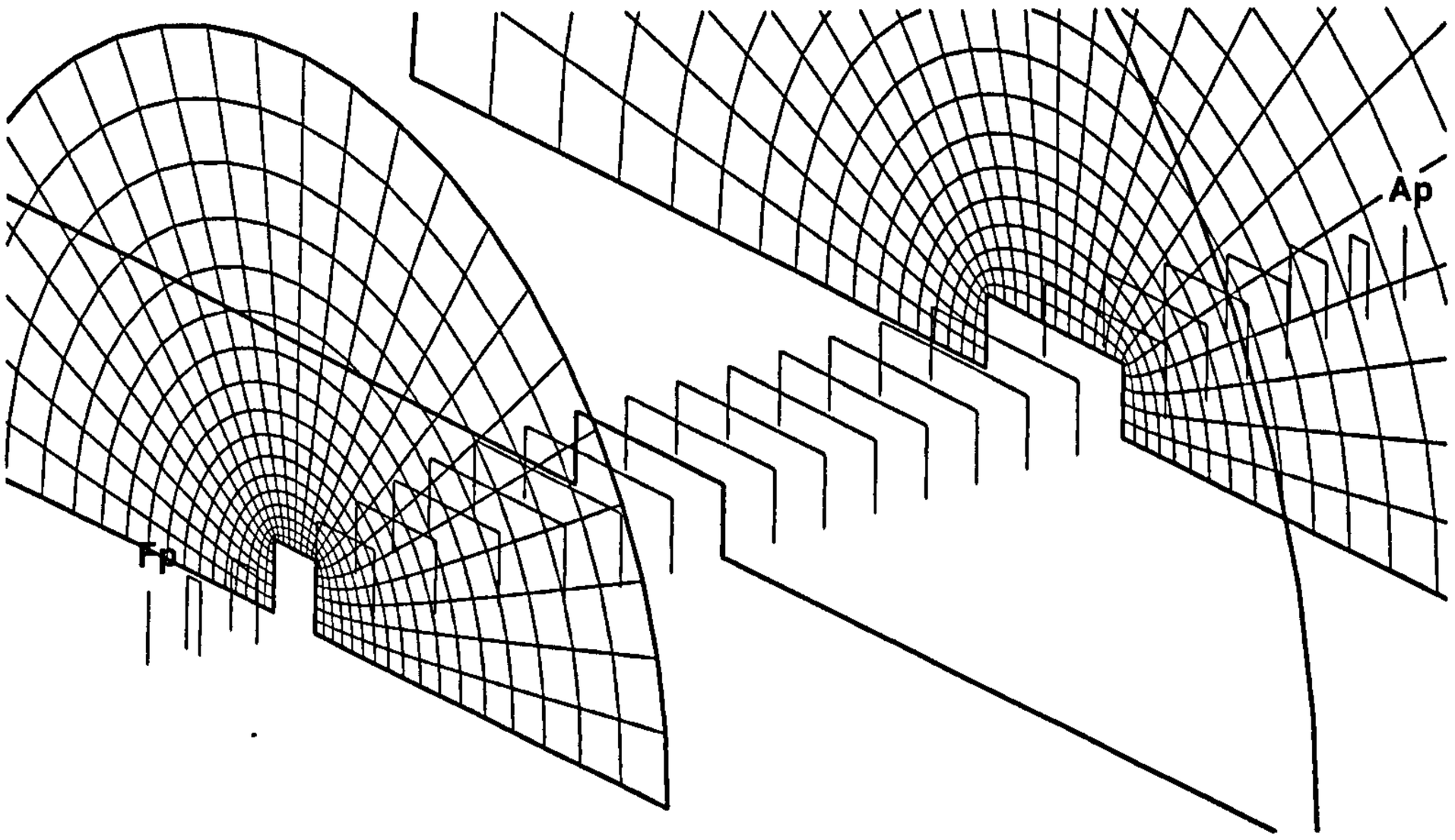

Figure 6.5: The divided two-dimensional hull section including sectional grid domains.

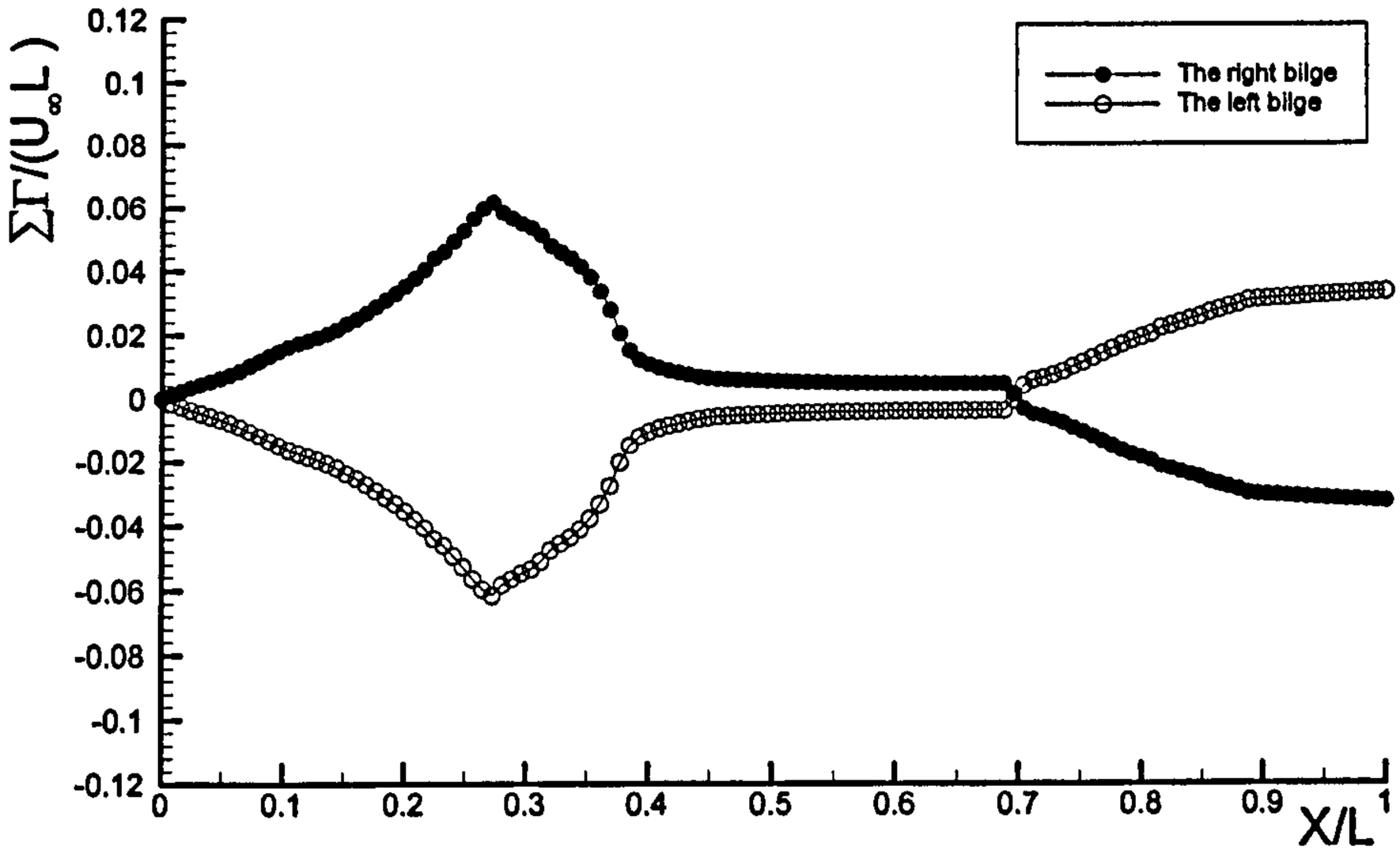

Figure 6.6: The development of total circulation over the block hull with zero degree drift motion.

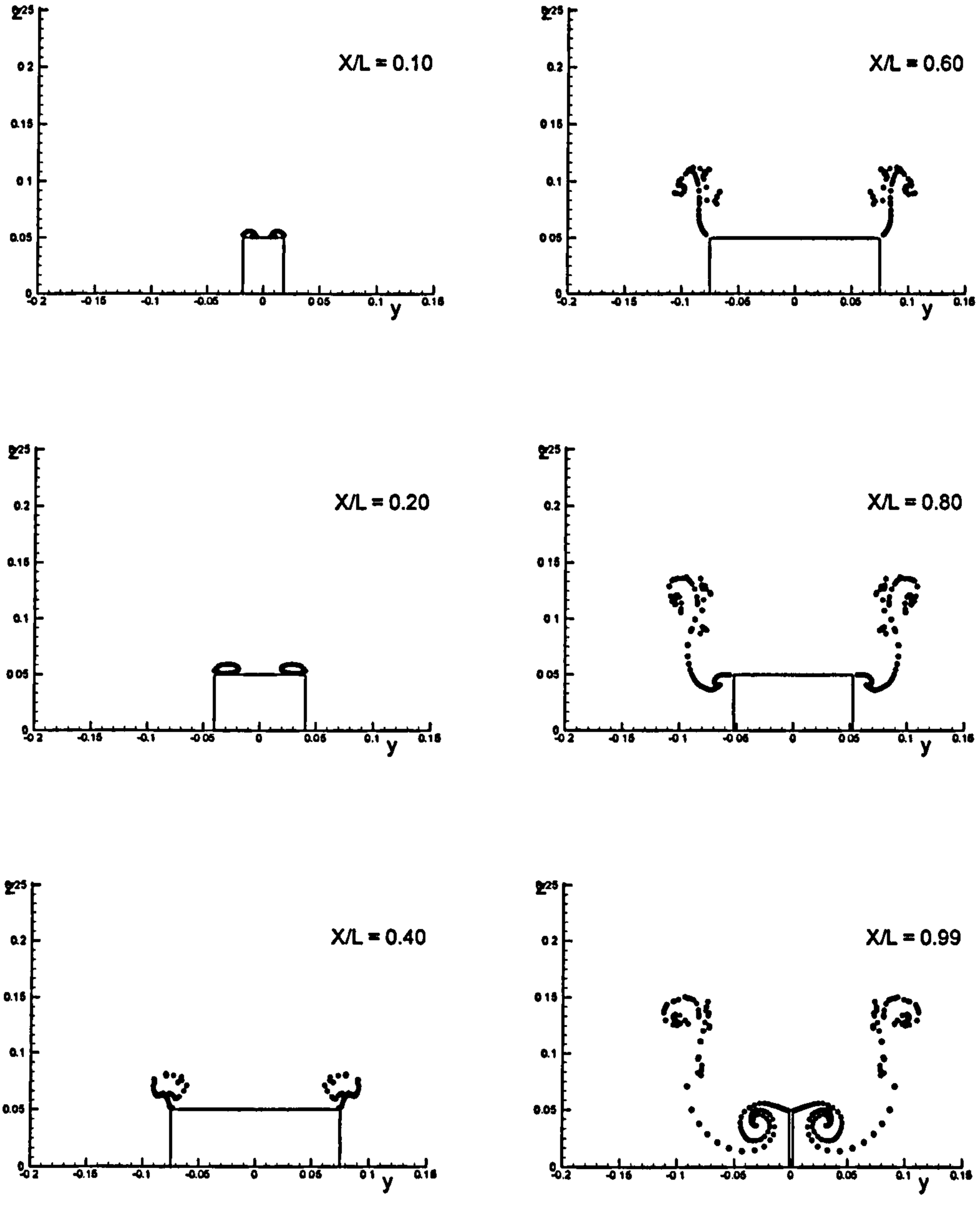

Figure 6.7: Vortex evolution along the block hull due to zero degree of drift motion.

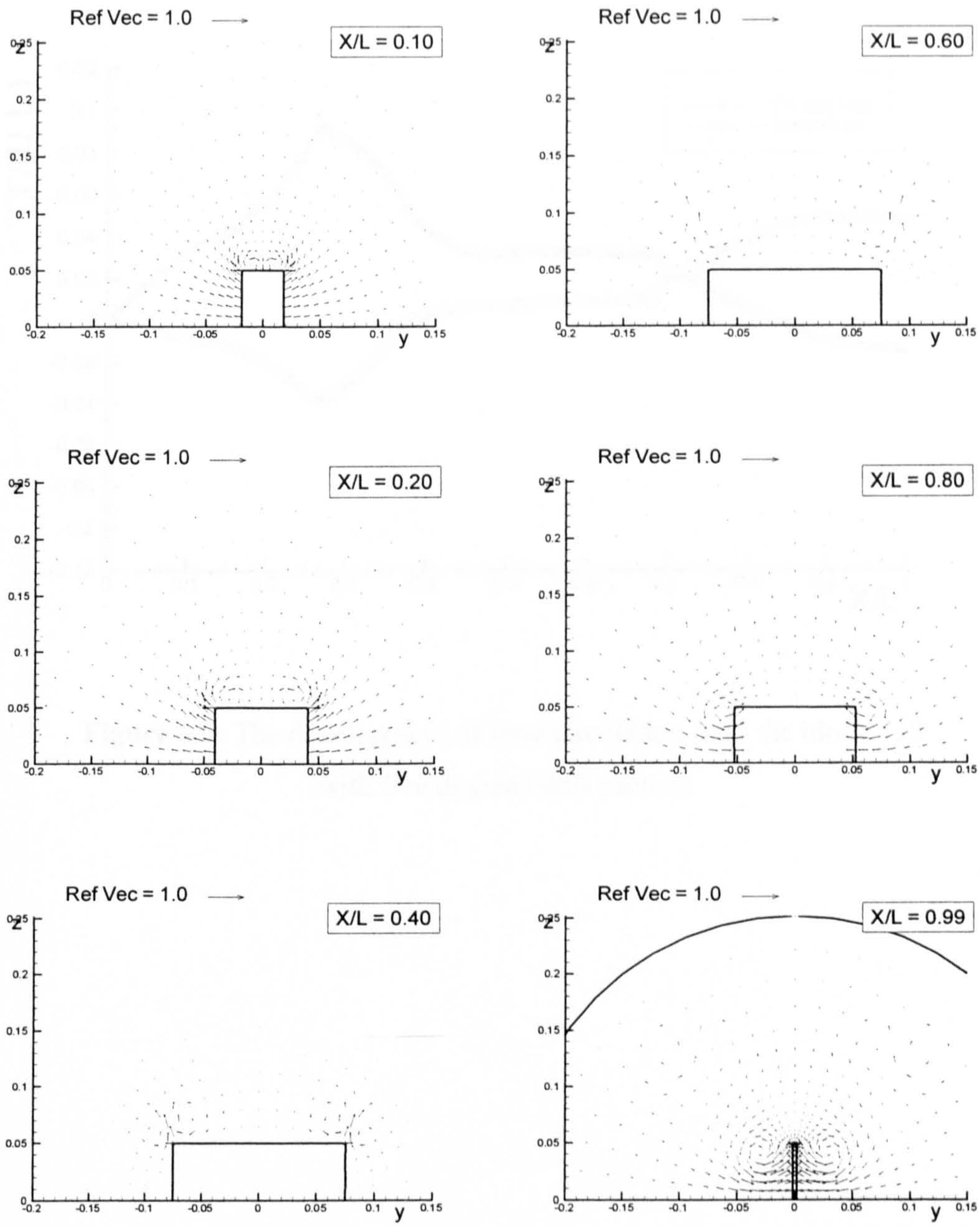

Figure 6.8: Velocity vectors along the block hull due to zero degree of drift motion.

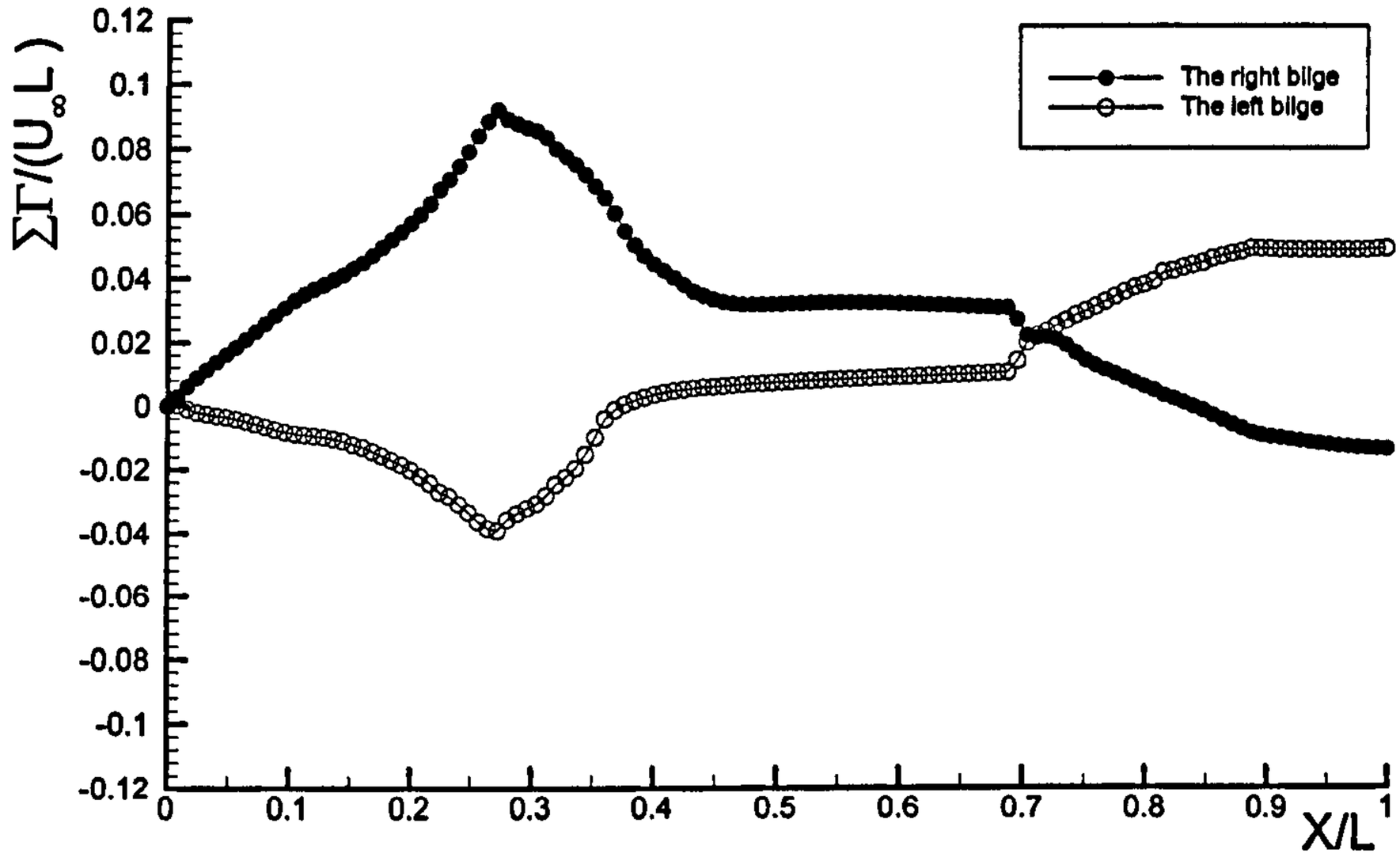

Figure 6.9: The development of total circulation over the block hull with five degrees drift motion.

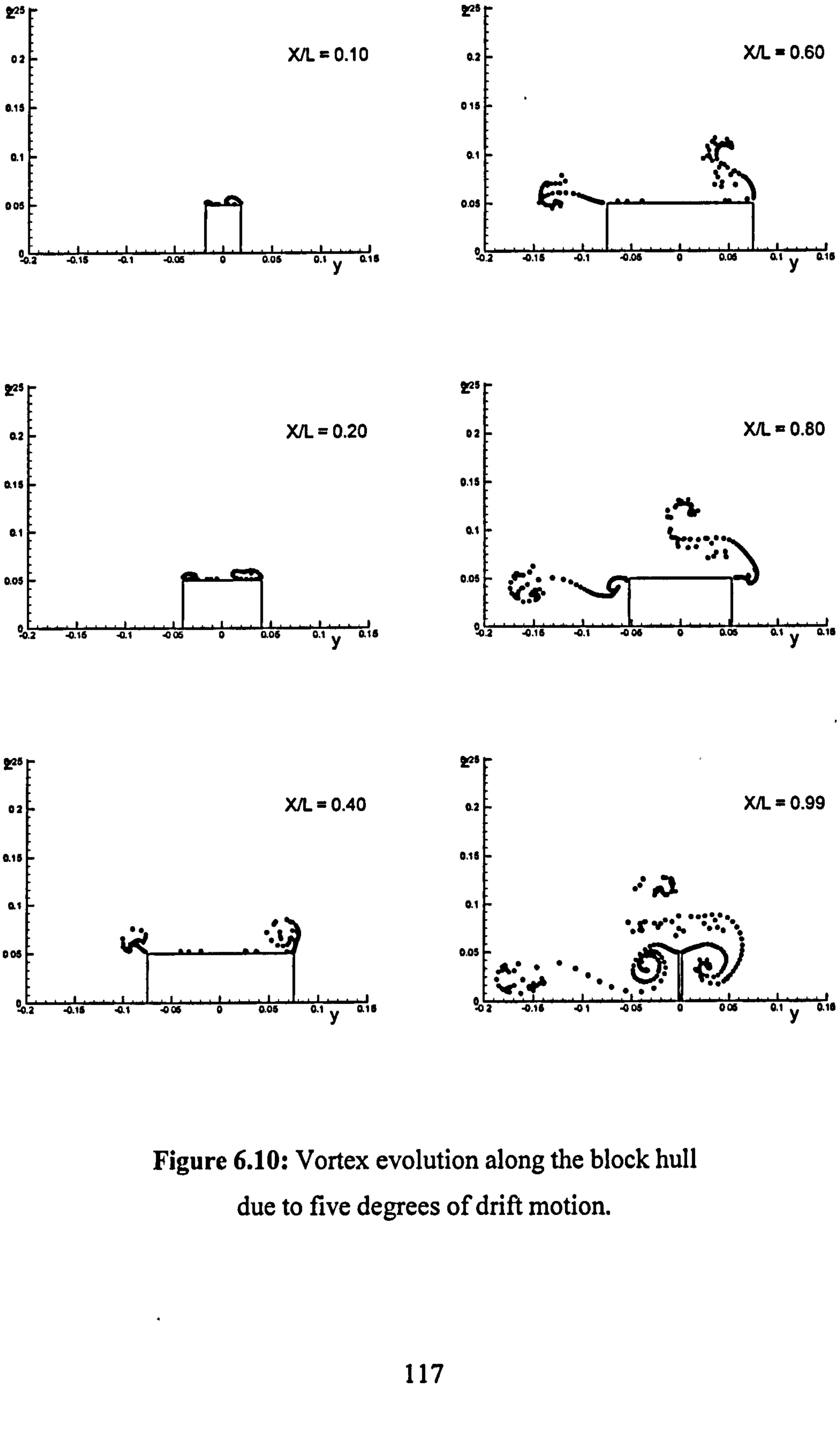

Figure 6.10: Vortex evolution along the block hull due to five degrees of drift motion.

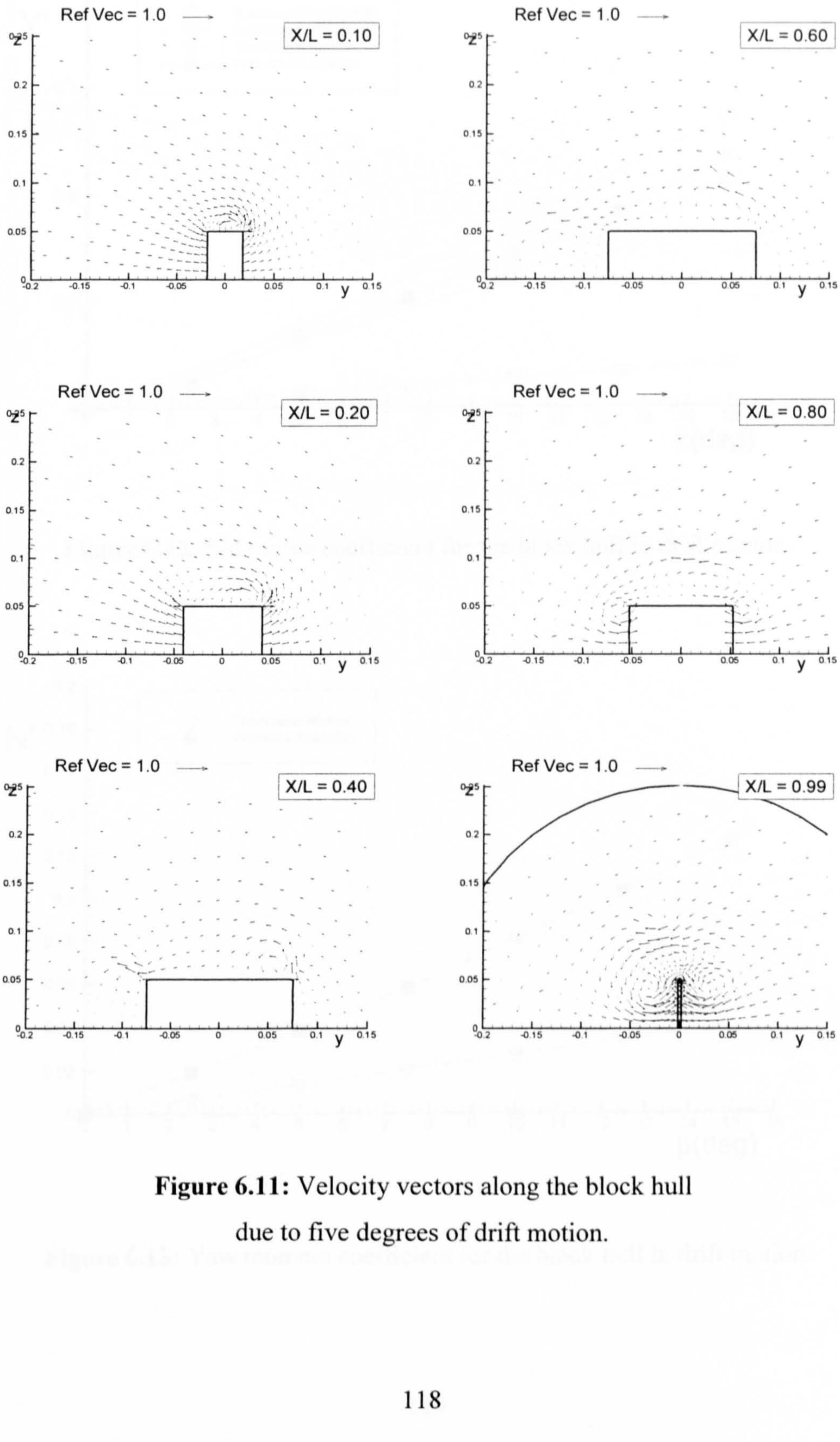

Figure 6.11: Velocity vectors along the block hull due to five degrees of drift motion.

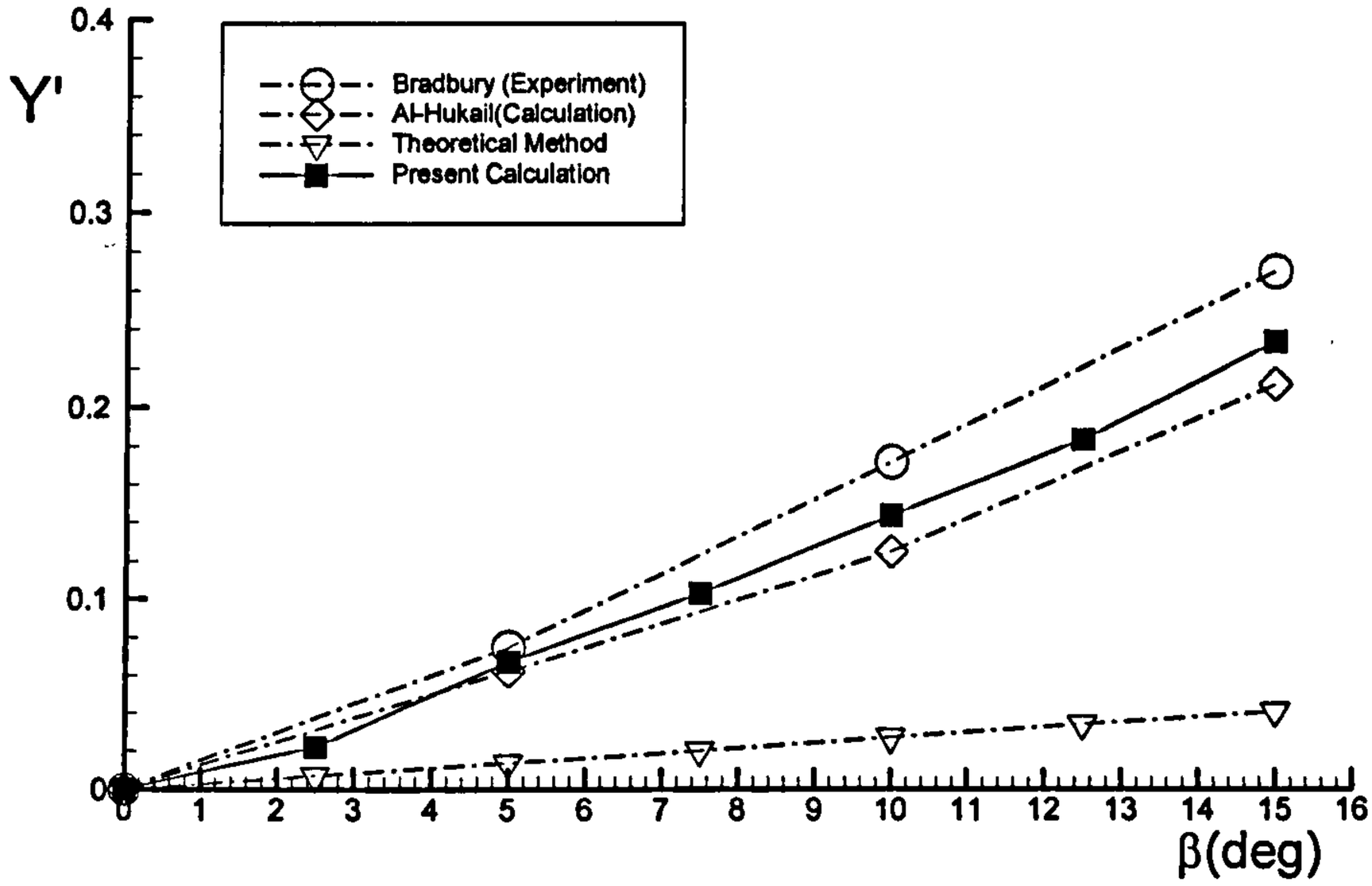

Figure 6.12: Side force coefficient for the block hull in drift motion.

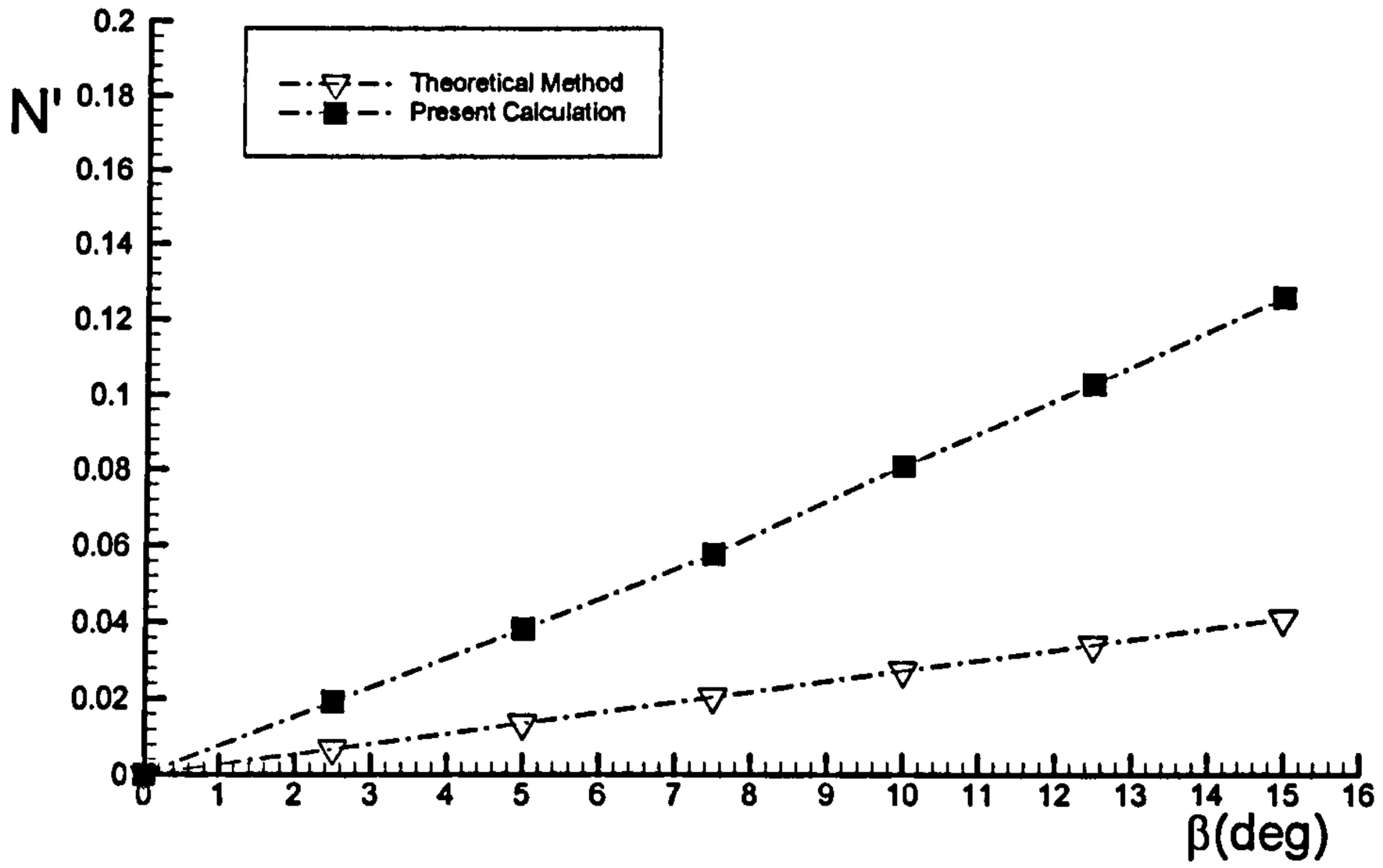

Figure 6.13: Yaw moment coefficient for the block hull in drift motion.

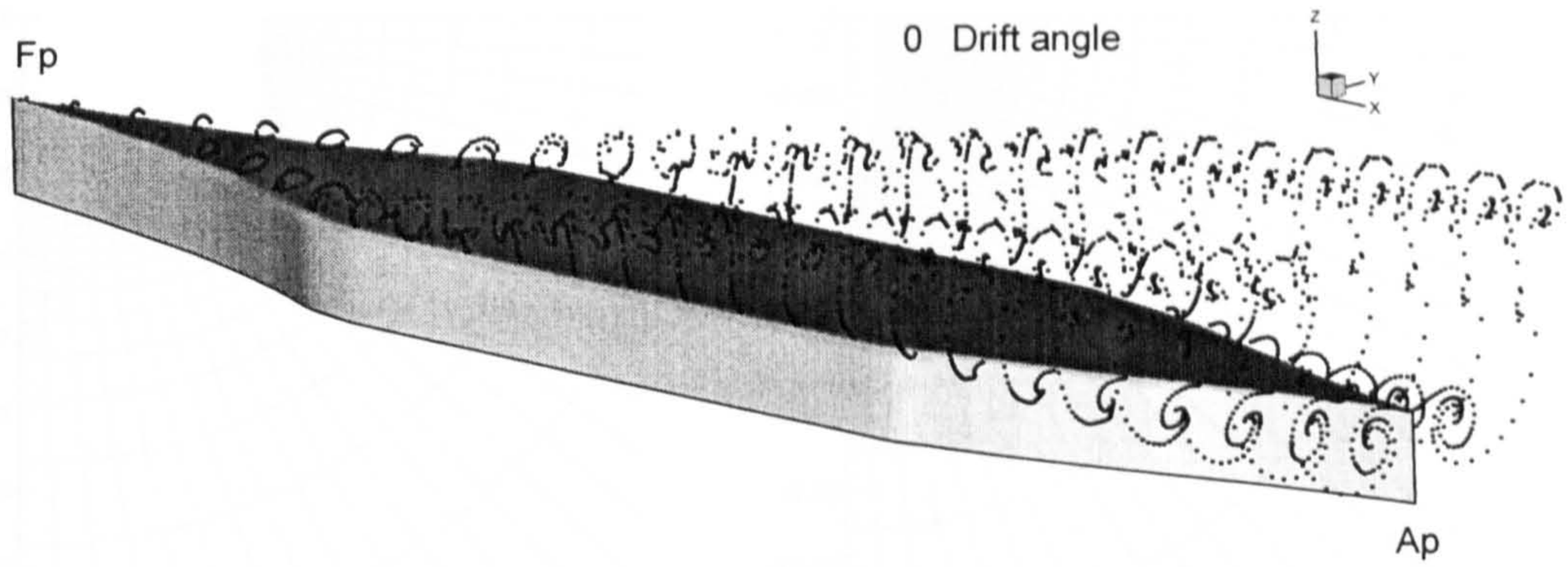

Figure 6.14: Vortex flow around the block hull due to zero degree of drift motion.

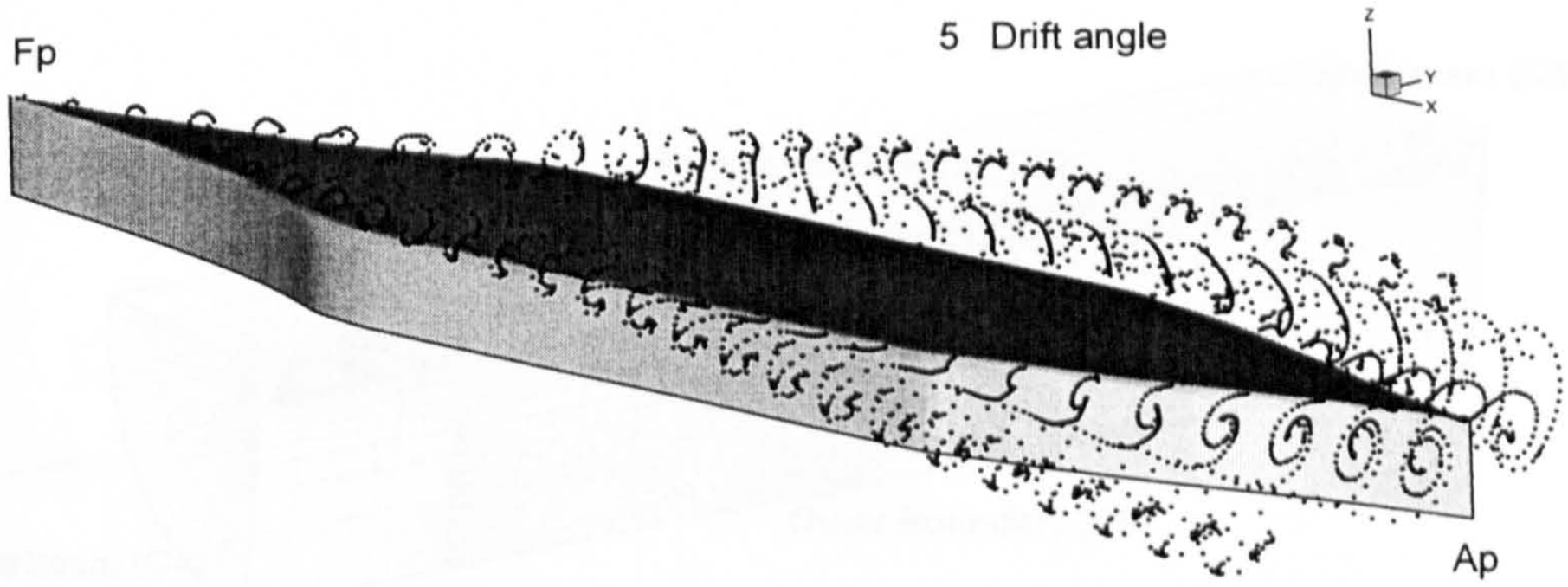

Figure 6.15: Vortex flow around the block hull due to five degrees of drift motion.

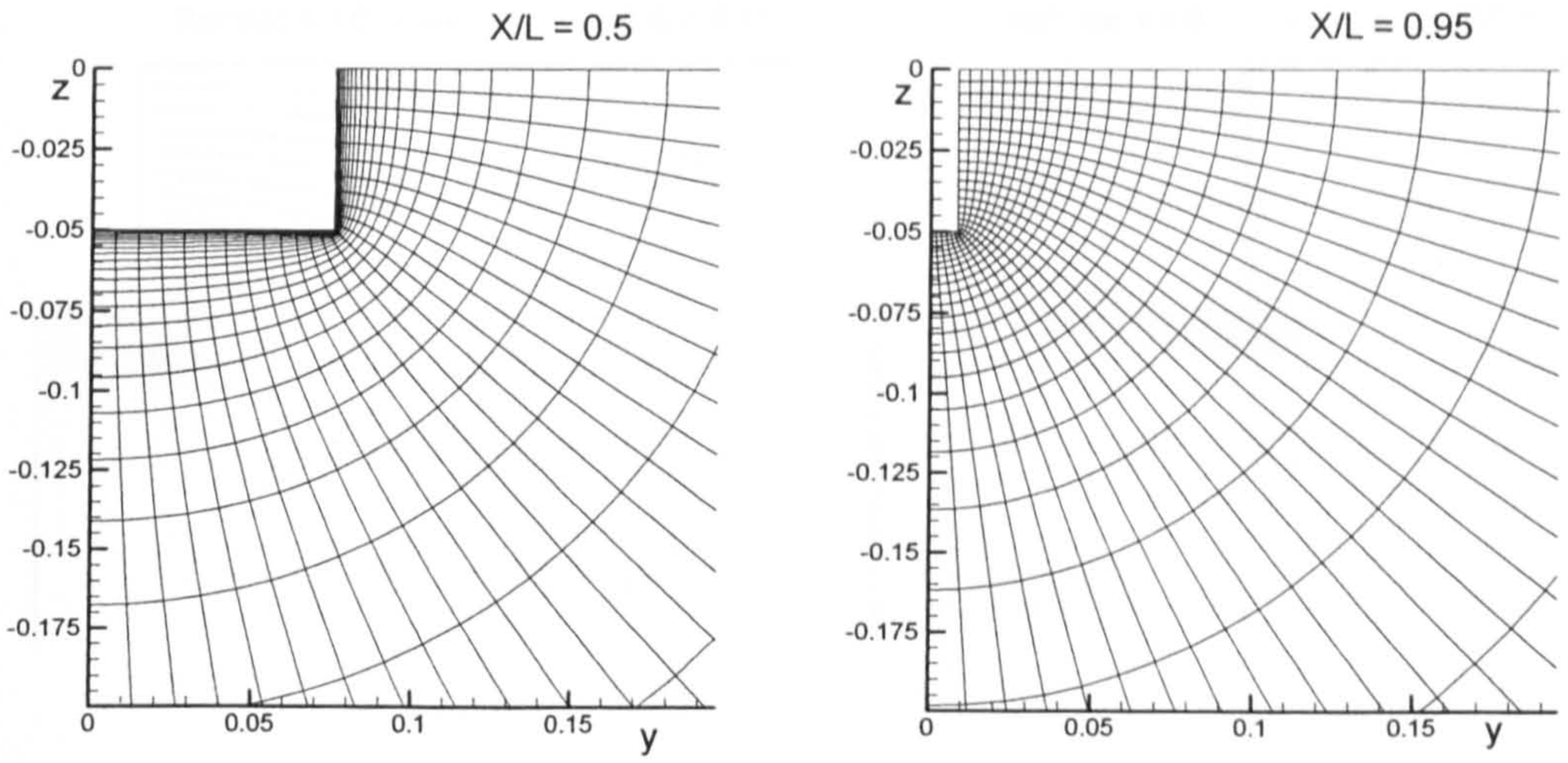

Figure 6.16: Generated grid system for cross section

(Right: $X/L = 0.5$, Left: $X/L = 0.95$).

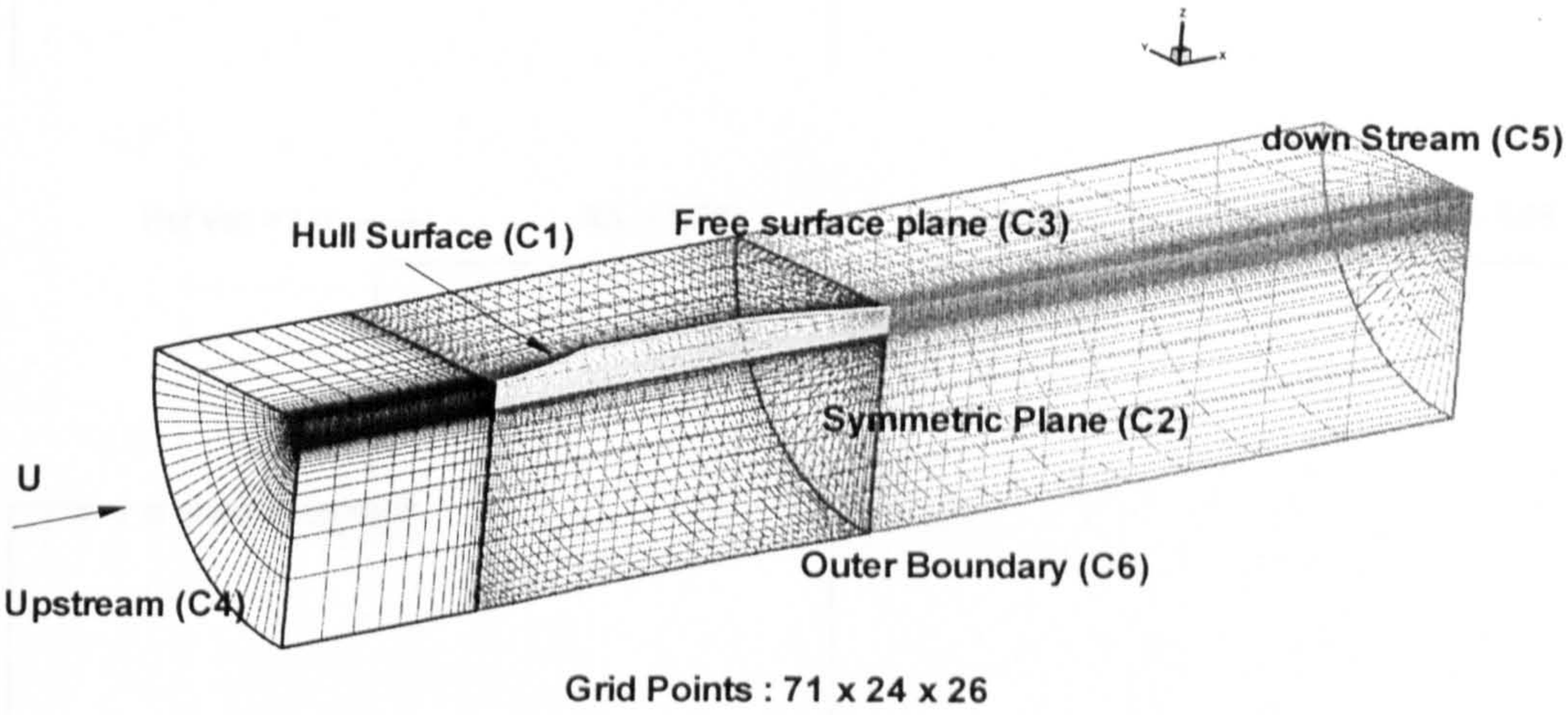

Figure 6.17: Computational grid system for CFX.

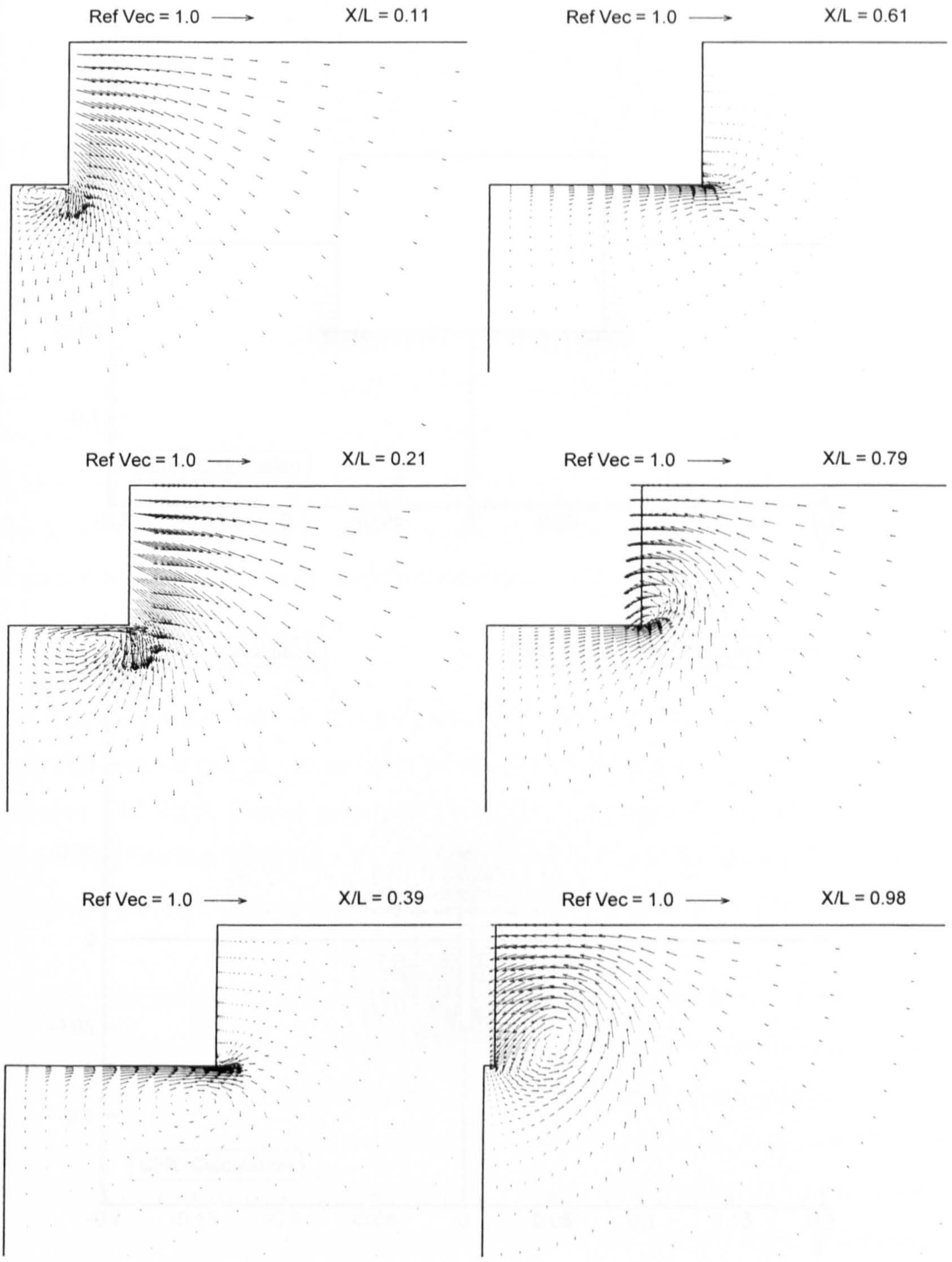

Figure 6.18: Velocity vectors along the block hull due to zero degree of drift motion (CFX).

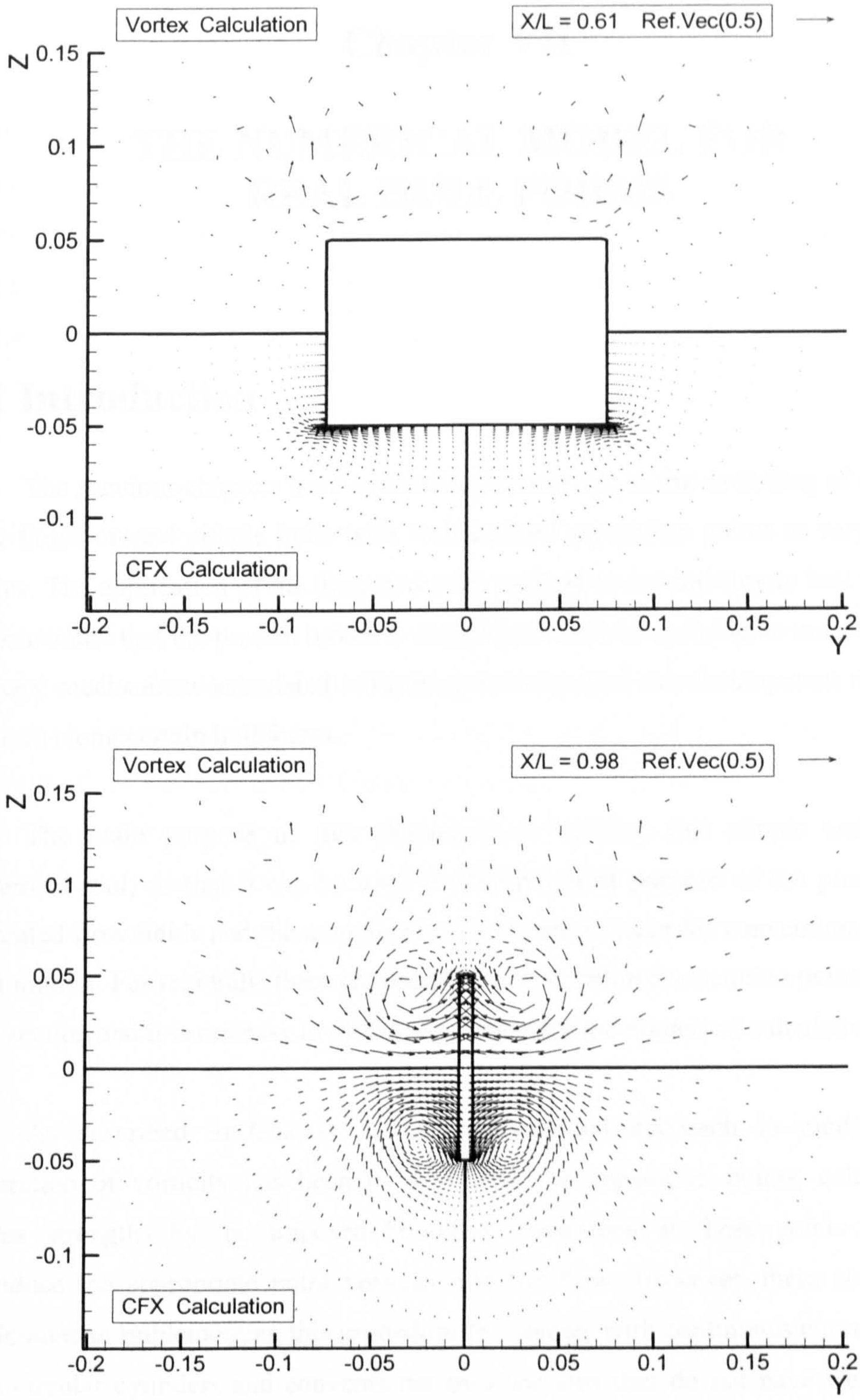

Figure 6.19: Comparison of velocity vectors between vortex method and CFX.

Chapter VII

THE NUMERICAL MODEL FOR REAL HULL FORMS

7.1 Introduction

The previous chapters have covered topics relating to the modelling of separated flow fields around simple hulls with well-defined separation points at varying drift angles. The application of the discrete vortex method to several simple hull types has demonstrated that the present model is simple and useful in gaining an insight into the primary mechanisms associated with the generation and the development of trailing vortices along certain hull forms.

The main purpose of this chapter is to develop this simple and reliable numerical tool, so that it can be used for the practical purpose of the prediction of separated flow fields and the associated manoeuvring forces for conventional hulls in drift motion. For real hulls there are usually no well defined separation points for each hull section and it is not easy to model separation for the numerical calculations.

As described in Chapter 4, the conventional approach to modelling the generation of vorticity has been to determine the separation points, calculate the vortex strengths by the imposed boundary conditions at those points and then introduce the appropriate point vortices into the flow. However, there are obvious difficulties in implementing this procedure for objects with continuous curvature such as a circular cylinders and conventional hull sections that do not have well defined separation points.

There have been various suggestions for modelling such flows. Some of the simple discrete vortex models have assumed a fixed separation position (Stansby 1977), based on the experimental values of the mean position of zero shear stress. However, in reality, it is well known that the separation point oscillates about the mean position and the motion of the separation point is dependent on the interaction between the boundary layer and the unsteady external flow. Numerical models with fixed separation points, therefore, may be criticised on the basis that they not only ignore this interaction, but also artificially constrain the evolution of the separated flow.

In an attempt to overcome this problem, some researchers have proposed models in which they try to locate the position of mobile separation points through the use of a boundary layer calculation. This approach does not require any experimental information but it also has its drawbacks, as explained by Downie (1981) and Sarpkaya (1989), particularly for unsteady flow calculations. Even in steady flow, separation points can only be predicted approximately and with some difficulty. In unsteady flow, not only are the separation points more complicated to locate but even their actual definition is not straight forward. What is meaningful for all kinds of unsteady flows, has not yet been fully established. In such flows, for instance, the surface shear stress can change sign with flow reversal, but without separation. Conversely, separation can occur before any flow reversal is encountered (Telionis 1979).

The above two methods have been used in modelling separated flows for circular cylinders in steady and unsteady motions with some success (Stansby 1977 and Sarpkaya and Schoaff 1979). In the case of flow separation calculations for smooth hull surface sections, even simpler assumptions have been used for defining the separation positions.

Kijima and Furukawa (1996) used fixed separation points and assumed that the separation occured at both bilge corners without any experimental information. They fixed the separation points on a line at the angle of 60 degrees from the waterline in

the transformed circle plane and introduced two vortices at each transverse section along the hull.

Wellicome et al (1995, 1997) modelled moving separation positions by assuming that flow separation usually occurs at the point where the velocity has attained its maximum speed. They only introduced one vortex into the flow at each hull section irrespective of hull type. Xiong and Kose (1996) and Kose et al (1997) compared several fixed separation points around both bilge corners and found that the calculated forces are very sensitive to the position of the separation points. They suggested that they should be located at the lowest pressure points on each side of the hull section and introduced two vortices at a time at each time step.

In the present study, it has been decided to introduce vortices into the flow by a method that does not involve a boundary layer calculation or fixed separation points to avoid the difficulties arising from finding separation points. A continuous layer of discrete vortices is distributed all the way around each hull section without specifying separation points. Since the vorticity in the flow is related to the interaction between the fluid and the solid boundary, the vortex strengths are chosen to satisfy the no-slip condition at collocation points on the body surface at each section. The method is primarily intended to provide a means of generating vorticity through the approximate representation of the physical phenomena involved. The present model differs in this respect from the other vortex models used in the manoeuvring problem, which only satisfy the no-slip condition at fixed separation points. The present multi-vortex method is not intend to be a detailed model of boundary layer separation or the boundary layer itself in any detail, but has been found to reproduce the gross feature of the separated flow reasonably well in two-dimensional bluff body flow (Downie 1981, Downie at al 1989, Murray 1992 and Wardhana 1995).

The other difficulty involved in the present calculation of the flow around real hulls is the conformal mapping of the arbitrary hull section into a circular cylinder in the two-stage transformation. For the simple hull types of the previous chapters, the transformation was simple and straightforward. A common approach to representing

hull sections has been to use the Lewis transformation (Lewis 1929), but this method can not produce a detailed description of complicated realistic hull sections. In the present method, the basic Lewis transformation will be generalised to represent a more accurate description of such real hull sections.

In this chapter, the improved numerical model adapted for studying separated flow around real hulls without well-defined separation points will be described. The vortex calculations are carried out using a multi-vortex based grid method (Downie et al 1989) and the transformation has been generalised so that conventional hull shapes can be represented accurately.

As before, consistent with slender body theory, the chosen hull is represented as a series of two-dimensional strips. Each hull section and its associated computational mesh in the real plane, the Z-plane, is mapped into the working plane, the S-plane, by a generalised conformal transformation. For each strip, the sectional dilation is modelled by a distribution of sources together with a second array of sources representing the drifting motion. A continuous layer of discrete vortices is distributed around the section in the working plane so as to satisfy a pointwise no-slip condition on the sectional hull surfaces. These vortices are convected away from the hull by the ambient flow in the same way as for the single point vortex calculations described in Chapter 4.

The basic structure of the discrete vortex method algorithm for conventional hulls, which is shown in Figure 7.1, is slightly different from that described in Chapter 4, especially with regard to the transformation, surface boundary conditions and the introduction of the vortices into the flow. The remaining sections of this chapter will describe the different numerical procedures developed in the present method to calculate the flow about real hull forms, such as the British bombardier and the Series 60 hull.

7.2 Boundary Conditions in the Real Plane

The boundary conditions on each hull section in the real domain are similar to those described in section 4.4. The main difference to the previously described boundary conditions relates to the body boundary condition on hull surface. The body surface is assumed to be both continuously impermeable and to satisfy a pointwise no-slip condition. All normal velocities on the body boundary must be equal to the normal velocity of hull surface so as to satisfy the impermeable boundary condition. The normal components of the velocities are represented by a source distribution around each sectional surface. The tangential velocities at collocation points on the hull surface are set zero so as to satisfy the no-slip condition. This condition can be satisfied by the introduction of a layer of discrete vortices around the hull surface. The number of points equals the number of vortices in the layer. Since the vortices are supposed to be generated by satisfying the no-slip condition on the hull surface, the separation condition adopted in section 4.4 is not necessary in this approach.

7.3 Hull Transformation

The advantages of conformal mapping and the transformations of simple hull shapes have been described in the previous chapters. For the calculation of real hull forms, it is not quite so straightforward to transform the complex hull shapes by simple mapping methods.

In the present calculation, each transverse hull section in the Z-plane, ($Z = y + iz$) is mapped into a rectangular grid in the S-plane, ($S = \eta + i\zeta$) by a two stage conformal mapping as shown in Figure 7.2. At first, the ship transformation maps the ship transverse section in the complex Z-plane to the exterior of a circle in the $S1$-plane by means of a Laurent series. Since all double body hull sections are symmetrical in both y and z-axis as seen in Figure 7.2, the transformation function may be written as equation (7-1). The circle in the $S1$-plane is then transformed into a rectangular grid in S-plane by equation (7-2).

$$Z = S1 + \sum_{n=1}^{N} a_n S1^{(1-2n)} \tag{7-1}$$

$$S1 = r \cdot \exp\left(i\frac{\delta\theta}{2}\right) \cdot \exp(i\alpha S) \tag{7-2}$$

The coefficients a_n in equation (7-1) are determined by the hull geometry, the number of terms required depending on the complexity of its shape. The first three terms only, for example, lead to the Lewis forms.

The determination of the mapping constants a_n in equation (7-1) is not straightforward and various ways of accomplishing it have been suggested by von Kerczek and Tuck (1969), Reed and Nowacki (1974) and Westlake and Wilson (2000), depending on their purposes. A detailed expression for finding the mapping terms in the present method is described in Appendix A.

For the British Bombardier, the British Bombardier with a pram stern and the Series 60 hull, eleven terms ($N = 10$) have been used in the series. Figures 7.3, 7.4 and 7.5 show the comparison between the generated hull surfaces and real hull surfaces. The solid lines and the dash-dotted lines in the figures represent the actual hull form and the hull generated by the present transformation respectively. The figures show that the present mappings using eleven terms describe all three hulls very well.

As described by von Kerczek and Tuck (1969) and Westlake and Wilson (2000), the conformal transformation (7-1), which maps the arbitrary hull sections to a circle, can be used for several purposes as well as the present one. The mathematical representation of a ship hull can be applied to calculate the hydrodynamic properties of the ship (Tuck and von Kerczek 1968, Clarke 1972, Grigoropolos and Athanassoulis 1997), and it may also be used in the design and construction process of ships (Reed and Nowacki 1974).

One of the useful items of information that can be obtained from the coefficients of the Laurent series equation (7-1), is the value of the added mass coefficient C_H for given hulls (Clarke 1972).

$$C_H = \frac{1}{T^2}\left[r^2 - 2a_1 + \sum_{n=1}^{N} \frac{n a_n^2}{r^{2n}}\right] \tag{7-3}$$

where r is the radius of the transformed circular cylinder in the intermediate $S1$-plane. The manoeuvring forces and moment associated with an attached flow for a given hull can be found straightforwardly using this added mass coefficient. The detailed application of this term in the present method will be described in section 7.7.

7.4 Boundary Conditions in the Transformed Plane

The boundary conditions in the Z-plane must be transformed to give corresponding boundary conditions in the transformed S-plane. Apart from the body boundary and separation conditions, the boundary conditions in the transformed S-plane are the same as those given in the previous description of section 4.6. Since the body surface in the Z-plane is transformed into the η-axis in the S-plane, both no-slip and impermeable conditions should be satisfied at the $\zeta = 0$ in the S-plane as shown in Figure 7.2. The impermeability condition is satisfied by the introduction of a source distribution, which represents the movement of the surface. The no-slip condition is satisfied by introducing a layer of discrete vortices above the body surface. This boundary condition differs from the one for the point vortex methods in the previous chapters. The present no-slip condition enforces zero tangential velocities at the collocation points on the transformed body surface whereas the point vortex method only enforces zero tangential velocities at the separation points by satisfying Kutta condition.

7.5 Calculation of Source Strengths

The source strengths at the point $\zeta = 0$ in the transformed *S*-plane can be specified by satisfying the impermeable boundary condition on the body surface. As described in Section 4.7, the relationship between the normal velocities, V_n, on the hull surface in the Z-plane and source strength $m(\eta)$ in the S-plane can be written as

$$m(\eta) = -i2\overline{(V_n)}\frac{dZ}{dS} \tag{7-4}$$

where

$$V_n = \frac{-U_\infty}{\sqrt{1+(dy/dz)^2}}\left(\frac{dy}{dx}\cos\beta \pm \sin\beta\right) \tag{7-5}$$

and from the mapping equations (7-1) and (7-2),

$$\frac{dZ}{dS} = \frac{dZ}{dS1}\frac{dS1}{dS}$$

$$\frac{dZ}{dS1} = 1 + \sum_{n=1}^{N}\frac{a_n(1-2n)}{S1^{2n}} \tag{7-6}$$

$$\frac{dS1}{dS} = r\cdot\exp\left(i\frac{\delta\theta}{2}\right)\cdot i\alpha\cdot\exp(i\alpha S)$$

Figures 7.6 and 7.7 show the normal velocities in the Z-plane and the source distributions in the S-plane representing the growing hull section with a drift motion respectively.

As well as this method, the source strength representing the growing and shrinking of the hull sections in the *S*-plane can also be found analytically from the coefficients of the mapping equation. As described by Tuck and von Kerczek (1968), the appropriate solution for the potential function on the given hull can be found directly from knowledge of the transformation coefficients. Since they mapped the hull section to the unit circle equation (7-1) may be written in a different form (see appendix A) as

$$Z = A_1 S1 + \sum_{m=2}^{M} A_m S1^{(1-2m)} \tag{7-7}$$

where A_m are the mapping coefficients. M is the number of mapping coefficients used and is related to N in equation (7-1) by $M = N+1$. The complex potential $f(S1)$ in the $S1$-plane, which satisfies the appropriate boundary condition, may be written down with the mapping coefficients A_m, in the form

$$f(S1) = c_0 \ln(A_1 S1) + b_0 - \sum_{m=1}^{M-1} \frac{c_m}{2m} S1^{-2m} \tag{7-8}$$

and

$$\begin{aligned} c_0(x) &= \sum_{v=1}^{M} (3-2v) A_v(x) \frac{dA_v(x)}{dx} \\ c_m(x) &= \sum_{v=1}^{M} (3-2v) A_v(x) [dA_{v+m}(x)/dx + dA_{v-m}(x)/dx] \\ dA_m(x)/dx &\equiv 0, \quad for \ \ m<1 \ or \ m>M \\ b_0(x) &= -\frac{1}{2} c_0(x) \ln(L^2 - 4s^2) + \frac{1}{2} \int_{-L/2}^{l/2} dS1 \frac{c_0(x) - c_0(S1)}{|x - S1|} \end{aligned} \tag{7-9}$$

where b_0(x) is the three-dimensional correction or interaction term (Tuck 1964) and may be neglected for the present purpose. With the given complex potential $f(S1)$, the complex velocity representing sectional hull dilation in the transformed S-plane is given by

$$\overline{\frac{df(S1)}{dS}} = \overline{\frac{df(S1)}{dS1}} \overline{\frac{dS1}{dS}} \tag{7-10}$$

and the source strength representing the sectional hull dilation in the S-plane is given by

$$m(\eta) = -i2\left[\Im m\left(\overline{\frac{df(S1)}{dS}}\right)\right] \tag{7-11}$$

7.6 Introduction of Discrete Vortices into the Flow

For the point vortex method described in the previous chapters, one or two sets of vortices were introduced at each time step so as to satisfy the Kutta condition at defined separation points. In the present method, a number of vortices are introduced around each sectional hull surface. Both the impermeability and a pointwise no-slip condition should be satisfied on the hull surface after the introduction of multi-vortices into the flow.

The impermeable condition is already satisfied by the source distribution on the hull surface so there must be no normal velocity components induced by introduction of vortices into the flow. As described in section 3.6, this condition can be satisfied by the simultaneous introduction of image vortices, which are located on the inside of the hull section with opposite strengths, for every vortex introduced. In the transformed S-plane, the image vortices will be introduced at the conjugate points of the real vortex position.

The other boundary condition to be satisfied on the body surface is the pointwise no-slip condition, which means that all the tangential velocities at the collocation points on the transformed body surface in S-plane must be zero. This can be expressed as

$$\Re e\left(\left.\frac{dW(S)}{dS}\right|_{S=S_s}\right) = 0 \tag{7-12}$$

where S_s, which corresponds to $\zeta = 0$, is a transformed body surface point in the S-plane.

To satisfy the no-slip condition (7-12), a layer of vortices should be introduced at certain positions and with appropriate strengths. The vortex introduction positions around the body surface are set before the calculation of the new vortex strengths. The new vortex positions are normally located at the centre of the grid nodes above the body surface grid. The distance between the body surface and the separation point is set in the same manner as described for applications in section 5.2.3 and by other researchers (Murray 1992 and Wardhana 1995) to make sure that the value of P_k in equation (5.7) is sufficiently high (P_k>1.0). Since new vortices are introduced above the mid points between the surface grid nodes in the S-plane, the surface velocity $V_{1,k+1/2}$ at corresponding point on the surface $S_{1,k+1/2}$, can be found from equation (4-25) by

$$\frac{dW(S_{1,k+1/2})}{dS} = V_{1,k+1/2}$$

$$= \frac{-i}{2\pi}\left[\sum_{S_{j,k}} \Gamma_{j,k}\left(\cot\frac{\pi(S_{1,k+1/2}-S_{j,k})}{R} - \cot\frac{\pi(S_{1,k+1/2}-\overline{S}_{j,k})}{R}\right)\right] \qquad (7\text{-}13)$$

$$+ \int_{S_{1,1}}^{S_{1,2nk-1}} \frac{m(\eta)}{2\pi}\cot\frac{\pi(S_{1,k+1/2}-\eta)}{R}d\eta$$

The tangential velocities, which are the real parts of the complex surface velocities $V_{1,k+1/2}$, are not initially zero but are cancelled by the introduction of m vortices on the both the upper and lower parts of the double body hull section at each time step. The introduction of m new vortices on both the upper and lower part of the double body hull section in the present method will lead to the introduction of nk-1 vortices on each time step. The strengths of the new vortices are obtained through the solution of the m by m matrix, which is the extended form of equation (6-7), and can be written as

$$\Re e\begin{bmatrix} X_{11} & X_{12} & \cdot & \cdot & X_{1m} \\ X_{21} & X_{22} & \cdot & \cdot & X_{2m} \\ \cdot & \cdot & \cdot & \cdot & \cdot \\ \cdot & \cdot & \cdot & \cdot & \cdot \\ X_{m1} & X_{m2} & \cdot & \cdot & X_{mm} \end{bmatrix}\begin{bmatrix} \Gamma_{n1} \\ \Gamma_{n2} \\ \cdot \\ \cdot \\ \Gamma_{nm} \end{bmatrix} = -\Re e\begin{bmatrix} V_{1,1+1/2} \\ V_{1,2+1/2} \\ \cdot \\ \cdot \\ V_{1,m+1/2} \end{bmatrix} \tag{7-14}$$

and

$$X_{j,k} = \frac{-i}{2\pi}\sum_{j,k=1}^{m}\left[\cot\frac{\pi(S_{1,j+1/2}-S_{uk})}{R} - \cot\frac{\pi(S_{1,j+1/2}-\overline{S}_{uk})}{R}\right.$$
$$\left. - \cot\frac{\pi(S_{1,j+1/2}-S_{lk})}{R} + \cot\frac{\pi(S_{1,j+1/2}-\overline{S}_{lk})}{R}\right] \tag{7-15}$$

where S_{uk} and S_{lk} are the introduction points of the new vortices in the S-plane and subscripts u and l represent the upper and lower part of the double body hull respectively. $\overline{S}_{uk}$ and $\overline{S}_{lk}$ represent the positions of the image vortices.

Since the matrix in equation (7-14) has to be solved at each time step, the procedure to find new vortex strengths is computationally intensive. In the present application, a simpler method, which has been used by Downie (1981) and Murray (1992) in their multi-vortex application to separated flows around a circular cylinder, has been adopted. Since the sectional hull shape has been transformed to a circular cylinder in the $S1$-plane as an intermediate stage (7-1), their technique for finding the new vortex strengths can be applied in the present method without any difficulty and can be written as

$$\Gamma_{nm} = \frac{\pi r_m}{m} V_{\theta m} \tag{7-16}$$

and

$$V_{\theta m} = \left[\Re e(V_{1,m+1/2})\right]\frac{dS}{dS1} \tag{7-17}$$

where $V_{\theta m}$ is the tangential velocity on the circular cylinder surface, which can be found easily using the tangential component of the complex surface velocity $V_{1,k+1/2}$ in equation (7-13) and the transformation derivative in equation (7-6). r_m is the radius of the new vortex introduction points in the transformed $S1$-plane and is kept constant for all new vortices. The calculated strengths of the new vortices using both equations (7-14) and (7-16) are identical. A detailed description of the method and a full investigation into its accuracy is available in Downie (1981).

After introducing new vortices, the vortex circulation of all the vortices is distributed to the neighbouring grid nodes using bi-linear interpolation. The complex velocity at each grid node is then calculated using equation (4-25) and the vortices are convected to the next section by the appropriate complex velocities in the same manner as for the single vortex methods described in section 4.10.

7.7 Calculation of Forces

The forces acting on the hull can be considered to be made up of a contribution from the attached flow and a contribution associated with the trailing vortices as described in section 4.11. The side force per unit length acting on a hull, of length L and draught T, associated with the attached flow can be calculated at each section. It can be shown from slender body theory to be a function of the two-dimensional added mass coefficient at zero frequency, C_H. This quantity can itself be simply computed from equation (7-3) from knowledge of the coefficients of the Laurent Series as described in section 7.3.

$$C_H = \frac{1}{T^2}\left[r^2 - 2a_1 + \sum_{n=1}^{N}\frac{na_n^2}{r^{2n}}\right] \tag{7-18}$$

As explained by Clarke (1972), the non-dimensional attached flow side force Y_a' and yaw moment N_a' for a given hull form can be written, from equation (2-4), as

$$Y_s' = \pi \sin\beta \left(\frac{T}{L}\right)\left[C_H\right]_{Stern}^{Bow}$$
$$N_s' = \pi \sin\beta \left(\frac{T}{L}\right)\left\langle\left[(C_H)x'\right]_{Stern}^{Bow} - \int_{Stern}^{Bow}(C_H)dx'\right\rangle \qquad (7\text{-}19)$$

where $\sin\beta$ represents non-dimensional lateral velocity. The presence of the (T/L) term in equation (7-19) replacing the $(T/L)^2$ term in equation (2-4) is due to different non-dimensional forms of the side force and yaw moment in the two equations. For the present calculation, the lateral force and yaw moment are non-dimensionalised by $1/2\rho U_\infty^2 LT$ and $1/2\rho U_\infty^2 L^2 T$, whereas they are non-dimensionalised by $1/2\rho U_\infty^2 L^2$ and $1/2\rho U_\infty^2 L^3$ respectively in Chapter 2.

In using equation (7-19) for ship hull calculations, the assumption is implicit that C_H at the bow section must be zero. As mentioned by Clarke (1972) and Horn (2000), the assumption reflects physical reality at the bow section where the flow around the body must be three-dimensional and therefore violate the basic requirements of slender body theory.

For the case of the flat plate hull, C_H has a constant value of 1.0 along the hull and equation (7-19) reduces to the expression obtained by low aspect ratio lifting body theory (4-44). The attached flow lateral force and yaw moment for the other simple hulls in the previous chapters, such as the Wigley hull and the block hull, were also obtained using equation (7-19). C_H for simple rectangle sections in the block hull can be found from Clarke (1972).

Clarke (1972) has calculated the sway and yaw coefficients for the British Bombardier using theoretical attached flow calculations and compared the results with the data from segmented model tests. His calculations have shown that the estimation

of the manoeuvring coefficients based only on the attached flow leads to results that do not agree well with experiment in the region of the stern.

As pointed out by Hearn et al (1994) and Clarke and Horn (1997), much closer agreement can be obtained by including the influence of the trailing vortices. The expression for vortex influenced side force and yaw moments can be written as

$$Y_s' = \pi \sin\beta \left(\frac{T}{L}\right)\left[I_H\right]_{Stern}^{Bow}$$
$$N_s' = \pi \sin\beta \left(\frac{T}{L}\right)\left\langle\left[(I_H)x'\right]_{Stern}^{Bow} - \int_{Stern}^{Bow}(I_H)dx'\right\rangle \tag{7-20}$$

where I_H is the vortex influence coefficient. The total side force and yaw moment may be found from equations (7-19) and (7-20).

$$Y' = \pi \sin\beta \left(\frac{T}{L}\right)\left[C_H + I_H\right]_{Stern}^{Bow}$$
$$N' = \pi \sin\beta \left(\frac{T}{L}\right)\left\langle\left[(C_H + I_H)x'\right]_{Stern}^{Bow} - \int_{Stern}^{Bow}(C_H + I_H)dx'\right\rangle \tag{7-21}$$

To find the value of I_H, it is necessary to know the vortex strengths and positions and the initial generation points for a given hull. In the past, this information has been obtained, if at all, from experiments carried out for specific hull forms. For this reason the approach has not been easy to follow for practical purposes.

However, since the separation flow for realistic hull forms can be modelled by the present multi-vortex method, the non-dimensional form of the lateral force and yaw moment induced by the trailing vortices in the equation (7-21) can be determined by computing the terms,

$$Y_s' = \frac{1}{1/2\rho U_\infty^2 LT}\int_{L/2}^{L/2} Y(x)dx$$
$$N_s' = \frac{1}{1/2\rho U_\infty^2 L^2 T}\int_{L/2}^{L/2} Y(x)\cdot x dx \tag{7-22}$$

where *Y(x)* is the real part of the vortex induced force in equation (4-41) at the given hull section and can be written as

$$Y(x) = \Re e\left[-i\rho\sum_{\nu=1}^{N_\nu}\left(U1_\nu - U1_\nu^*\right)\Gamma_\nu + i\rho\sum_{\nu=1}^{N_\nu}\left(S1_\nu^* + r\right)\frac{\partial\Gamma_\nu}{\partial t}\right] \tag{7-23}$$

In the present multi-vortex method, vorticity is introduced into the flow in a manner that observes the physical phenomena on the hull surface and is dictated by the ship form. The location and strength of the vortices evolve naturally out of this process to allow the determination of the vortex influence coefficient. The second term on the right hand side in equation (7-23) has been ignored in the present calculations since they do not model viscous diffusion and the vortex strengths remain constant (Downie 1981 and Murrary 1992). For this reason, equation (7-23) simplifies to

$$Y(x) = \Re e\left[-i\rho\sum_{\nu=1}^{N_\nu}\left(U1_\nu - U1_\nu^*\right)\Gamma_\nu\right] \tag{7-24}$$

The total side force and yaw moment coefficients in the present method will be found from equations (7-19) and (7-22) as

$$\begin{aligned} Y' &= Y_a' + Y_s' \\ N' &= N_a' + N_s' \end{aligned} \tag{7-25}$$

In the following chapter, the multi-vortex method will be applied to the following realistic hull forms; a Series 60 hull, the British Bombardier and the British Bombardier with a pram stern. The different flow patterns obtained for the three hulls for various drift motions will be discussed in the context of a comparison between the present numerical results and existing experimental data. The influence of pram sterns on the wake pattern and manoeuvring derivatives will be discussed in relation to the results for the British Bombardier with a pram stern.

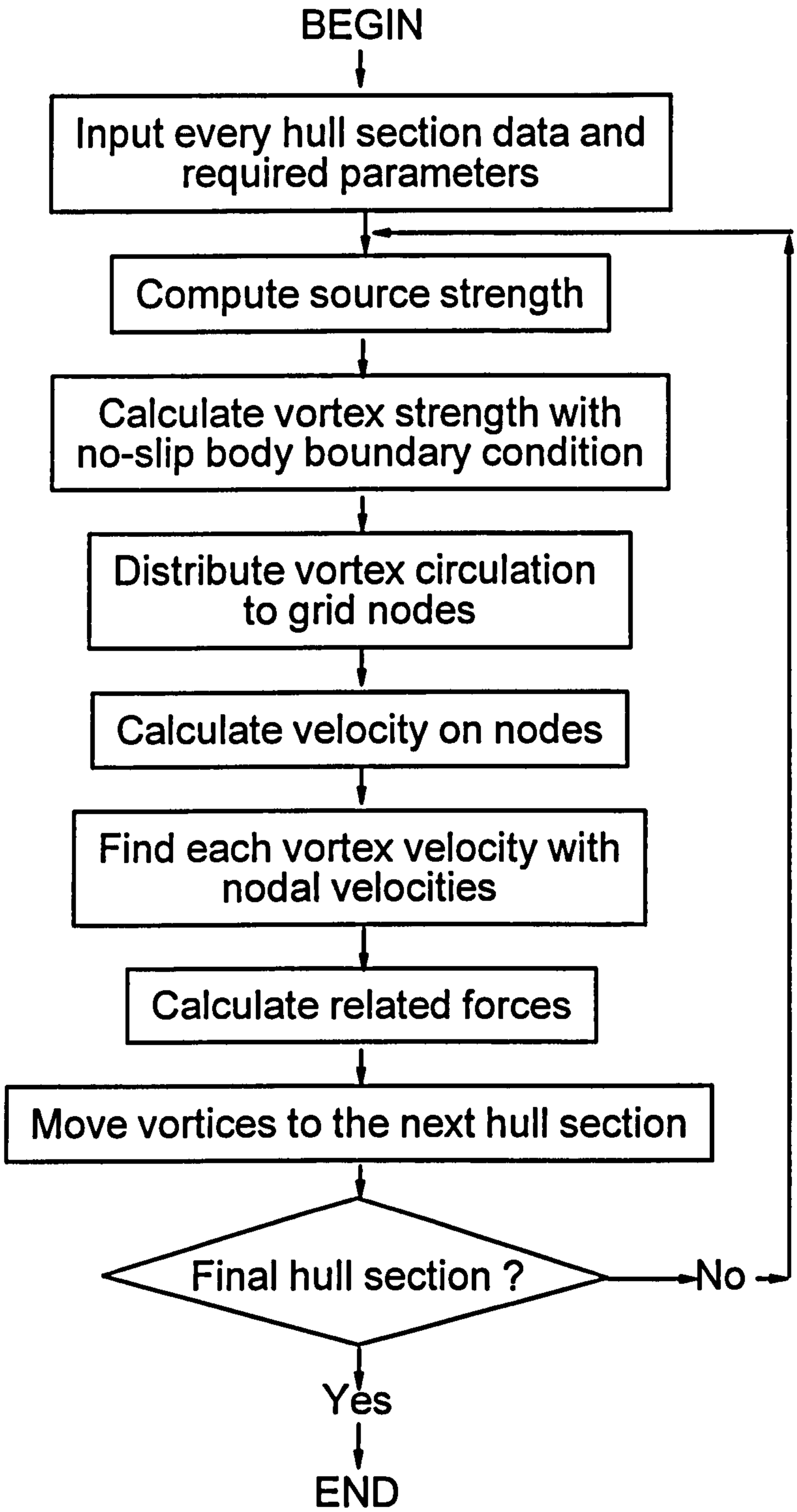

Figure 7.1: Basic flow chart for the improved discrete vortex method.

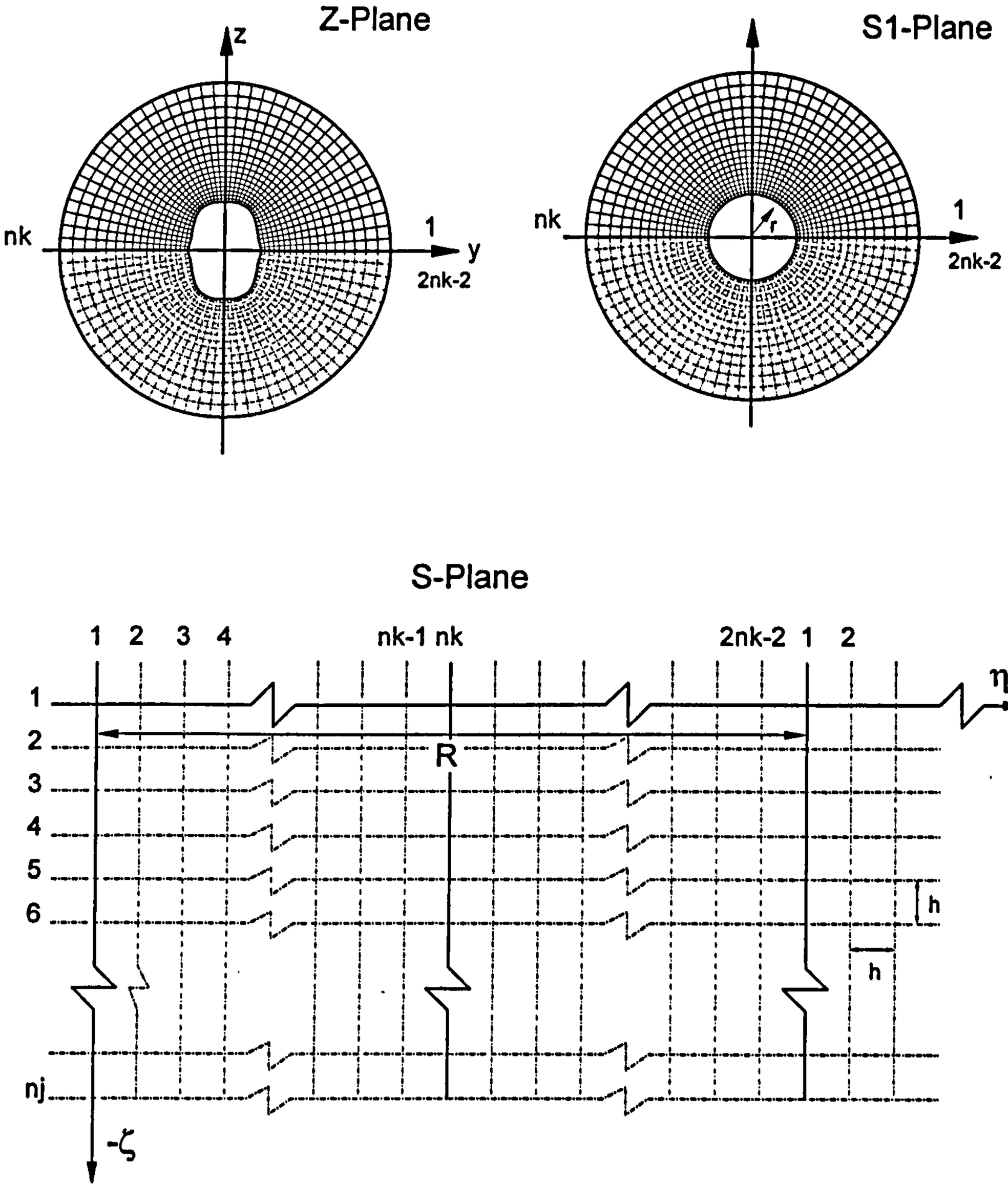

Figure 7.2: Two-stage conformal transformation for a real type hull.

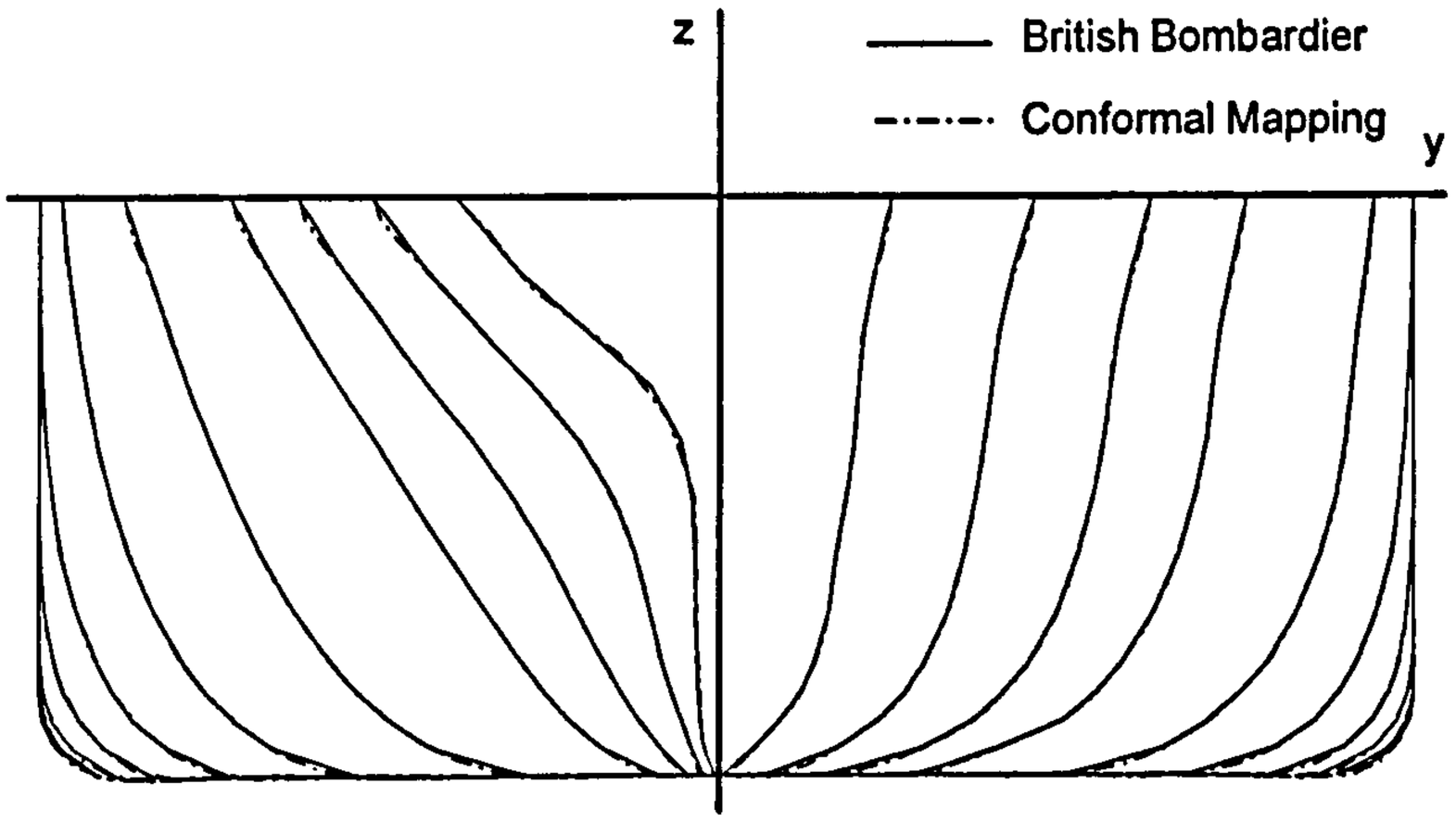

Figure 7.3: Comparison of the British Bombardier and the conformal mapping.

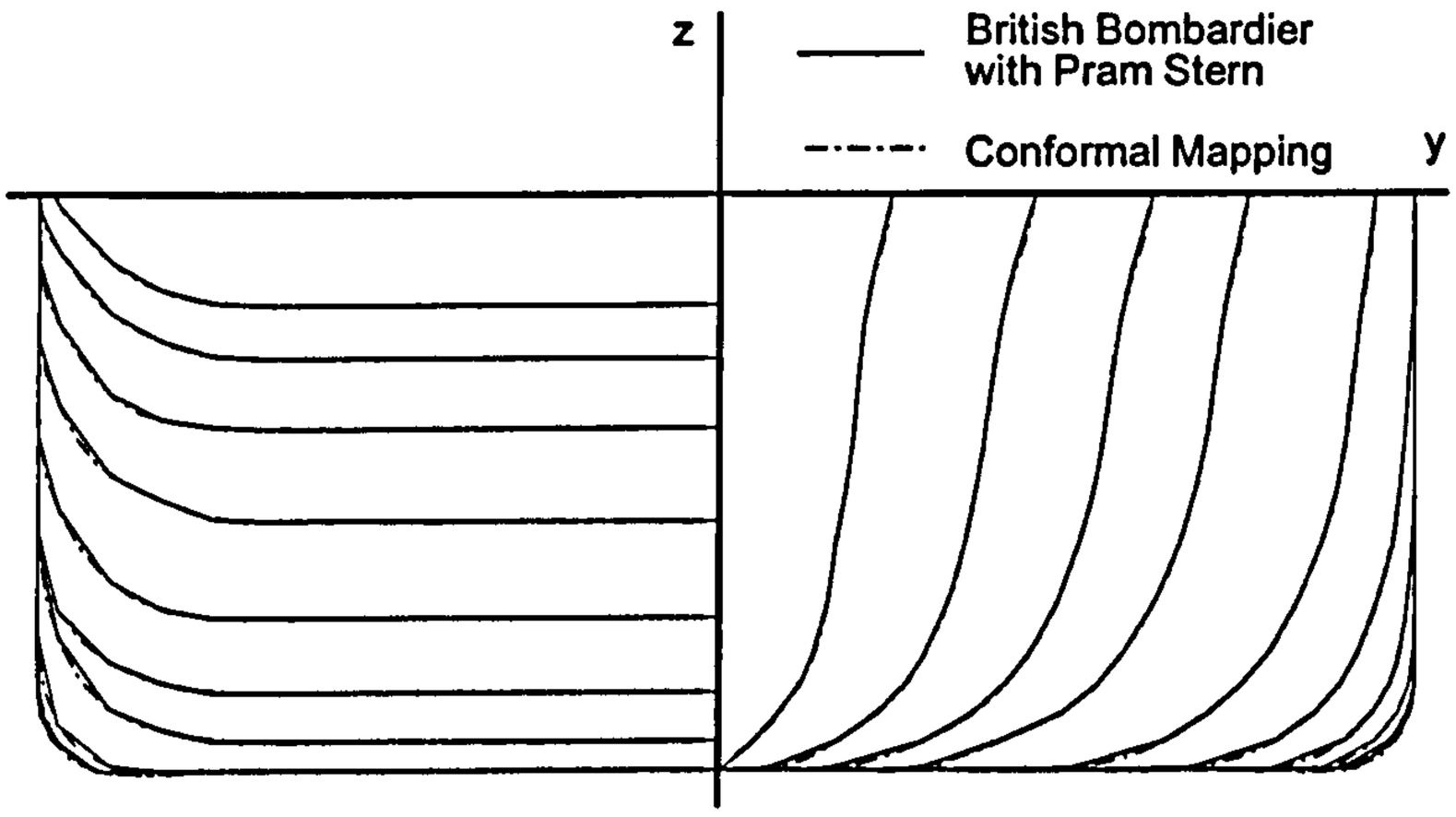

Figure 7.4: Comparison of the British Bombardier with a pram stern and the conformal mapping.

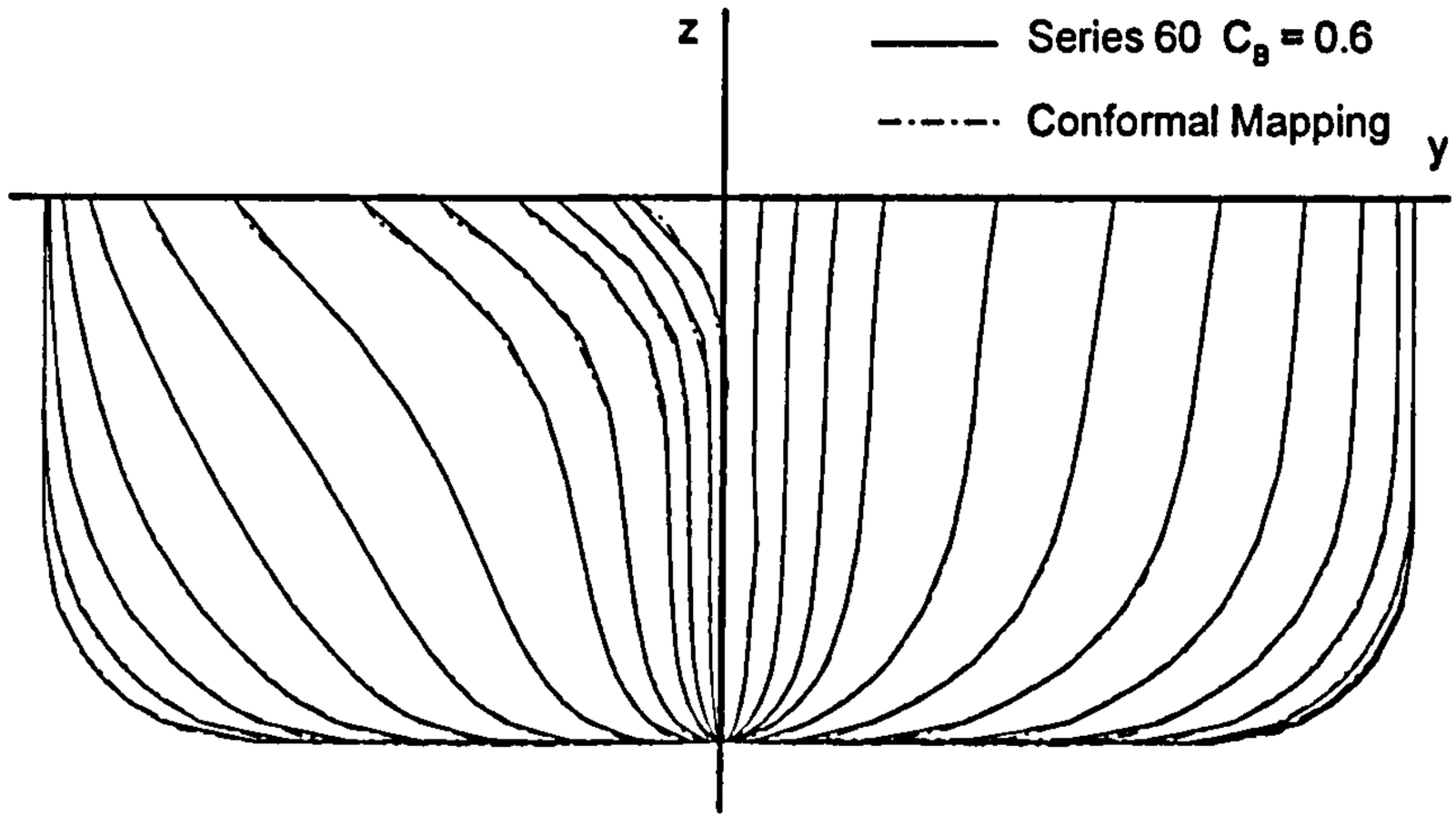

Figure 7.5: Comparison of the Series 60 $C_B = 0.6$ and the conformal mapping.

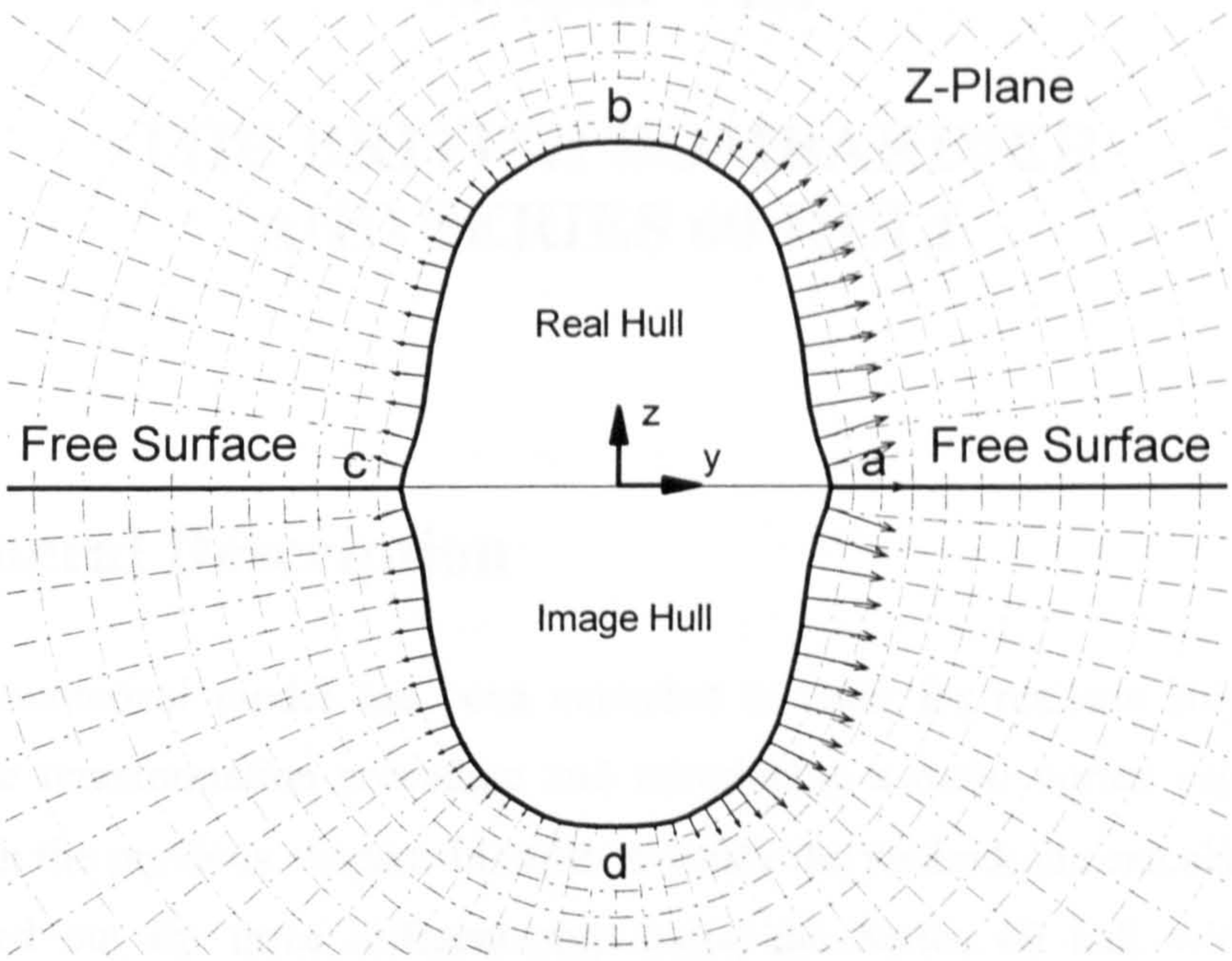

Figure 7.6: The representation o flow field for a growing hull section with the drift motion.

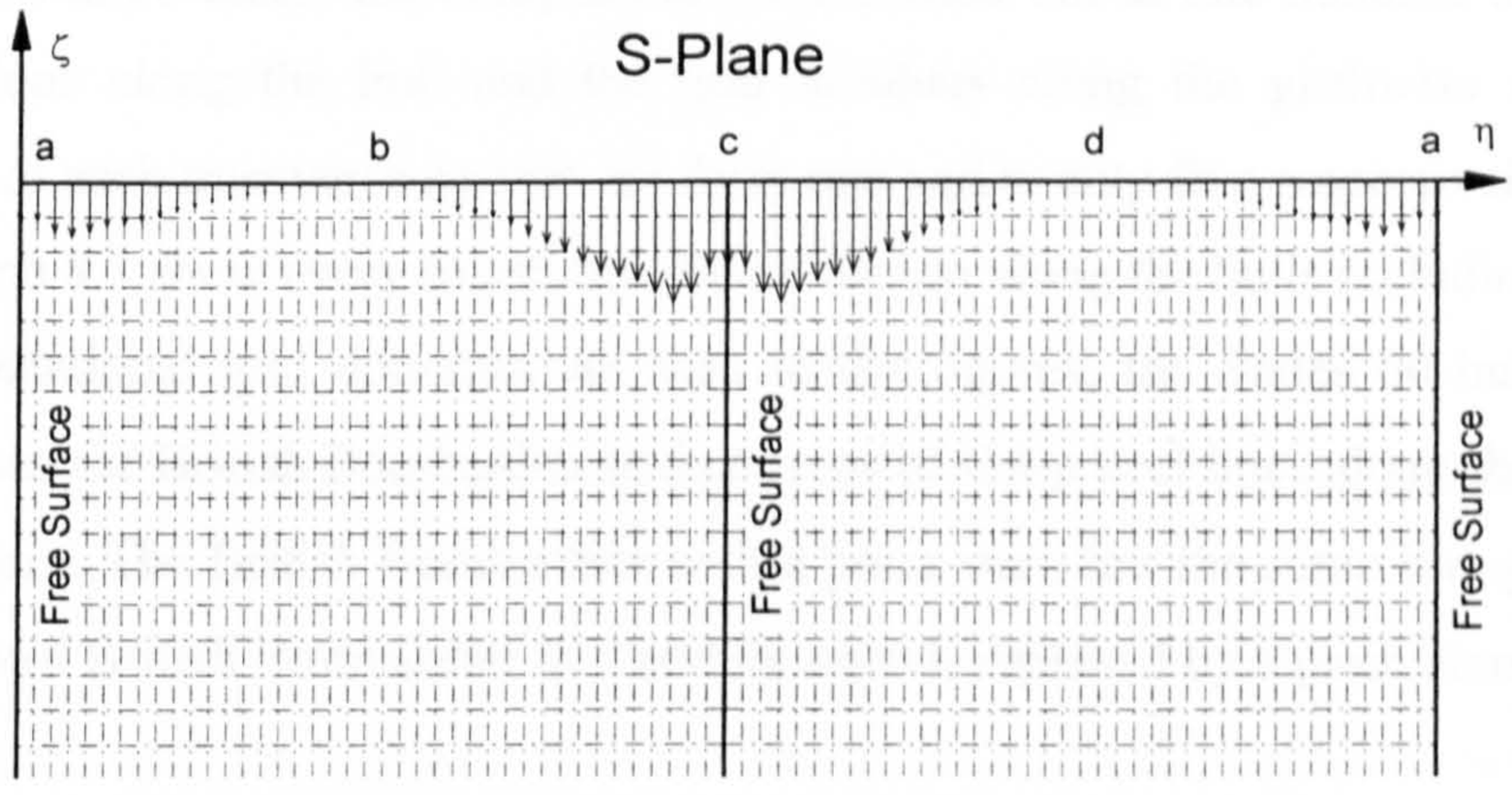

Figure 7.7: The flow field of computational domain for a growing hull section with the drift motion.

Chapter VIII

THE BRITISH BOMBARDIER AND SERIES 60 HULL

8.1 General Description

The numerical model has been extended to cater for realistic ship hulls by refining the transformation procedure and introducing a multi vortex capability, as described in the previous chapter. In order to verify the method, the calculations have been carried out for three different ship hulls; the Series 60 hull with a block coefficient of 0.6, the British Bombardier and the British Bombardier with a pram stern, at various drift angles. The body plans of the three ship hulls have been shown in the previous chapter (Figures 7.3, 7.4 and 7.5). The principal particulars of the three ships are listed in Table 8.1.

In all three cases, the computations are carried out at one hundred and twenty four stations along the hull and the grid numbers along the girthwise and radial direction of each transverse section are forty one and twenty five respectively. Figures 8.1, 8.2 and 8.3 show every fourth transverse section along the hulls including some of the computational grid domains. As seen in the figures, the Series 60 hull is more slender than the British Bombardier and consists of sharp keel lines along the bow and stern regions. The British Bombardier with a pram stern has the same fore part as the conventional British Bombardier hull and its stern is replaced by a pram stern.

Ships with pram sterns have proved to be more efficient in terms of resistance and propulsion performances but are known to have a tendency towards directional instability. An explanation for this behaviour was proposed by Clarke (1992), who showed that the side force generated by a skeg attached to a rectangular section,

characteristic of pram sterns, was less than that generated by a skeg attached to a triangular section, which is more characteristic of conventional stern designs.

Subsequently, Clarke and Horn (1997) postulated that a pram stern generates a vortex pair that has a much lower circulation, and which possibly rotates in the opposite sense (Kupier 1994) to those shed from a conventional stern. In this case the side force generated by the pram stern is less than that for the conventional stern, and if the direction of rotation of the trailing vortices is reversed, the side force generated by the pram stern is actually diminished. For the pram stern, this effect further reduces the effectiveness of the skeg and may explain some of the problems reported on ships with this type of stern.

In the following sections, the numerical calculations carried out for the three different hulls at various drift angles will be described. The flow fields and forces obtained by the present numerical method will be compared with available experimental data. Since there is no complete experimental data including both flow field and comprehensive distribution of side forces and yaw moments, the detailed discussion of the results will depend on the available experimental data. The flow field including the sectional velocity and vorticity field will be mainly discussed for the case of the Series 60 hull. In the case of British Bombardier, the detailed distributions of the sway forces and yaw moments along the hull will be compared with segmented model test data.

As mentioned previously, there have been some experimental and semi-empirical attempts to explain the flow fields about, and the manoeuvrability of, a ship with a pram stern in oblique motion. However, no numerical calculation for that particular ship has been carried out until now. In section 8.3, the extended numerical model will be used to calculate the flow about the British Bombardier with a pram stern advancing obliquely, and the result will be assessed by comparison with experimental data.

8.2 The flow around the Series 60 hull

The Series 60 is a merchant ship hull form that has been frequently used for ship hydrodynamic research. The body plan and divided two-dimensional hull sections for the hull are shown in Figures 7.5 and 8.1 respectively. The numerical calculations have been carried out for the hull with drift motions of up to 10 degrees.

The development of the calculated vortex flow patterns along the hull at 10 degrees of drift motion is shown in Figure 8.4. Each point in the figures shows the location of a discrete vortex and the size of the vortices represents the absolute magnitude of their strengths. As seen at $X/L = 0.09$, a keel vortex is the dominant flow phenomenon at the beginning of the forebody. As flow advances to the middle body, the keel vortex is moving away and weak bilge vortices are visible at $X/L = 0.44$. The bilge and the keel vortices interact together on the afterbody. At $X/L = 0.98$, the separation flow forms a strong anti-clockwise vortex. The high velocity of the side flow, induced by a ten degrees of drift angle, cancels out the formation of the clockwise stern vortex in the right hand side of the stern, which is expected at zero degrees of drift angle (Matheson and Joubert 1973). In contrast, the side velocity enforces the formation of anti-clockwise stern vortex in the left side. Then the anti-clockwise stern vortex is combined with a keel vortex at $X/L = 0.98$.

The actual vorticity distribution is not always easy to interpret in these figures as all the discrete vortices have different strengths, some of them relatively small, and vorticity can appear to be concentrated in areas in which it is actually rather small. In Figure 8.5, sectional velocity vectors corresponding to the same stations as Figure 8.4 show clearer information about the flow development.

Longo (1996) carried out a very detailed study of the flow field and free surface around this hull form. As well as plots of forces and moments, he presented velocity and vorticity fields at sections along the hull. The calculated and the measured velocity field at the penultimate section of the hull are presented in the upper and lower parts of Figure.8.6 respectively. The corresponding computed and measured

vorticity fields are presented in Figure 8.7. The measured axial vorticity fields in the figure can be easily found by differentiating the given experimental velocity vectors. The equation for axial vorticity can be written as

$$\omega_x = \left(\frac{\partial w}{\partial y} - \frac{\partial v}{\partial z} \right) \tag{8-1}$$

where v and w are the velocity components in y and z directions.

The experimental results for the velocity and vorticity fields presented by Longo (1996) do not extend all the way to the free surface. In the present study zero frequency boundary condition has been applied at the free surface whereas the experimental results include the actual free surface effects. It is therefore to be expected that some differences will appear between numerical and experimental results in this region. Apart from this, the agreement between the two cases for the velocity and vorticity fields shown in the Figures 8.6 and 8.7 is good.

The flow fields along the Series 60 hull represent similar flow patterns to the Wigley hull, which was presented in section 5.3. Since the Series 60 hull has relatively sharp keel separation points at the forebody and the afterbody, the flow pattern is more likely to be dominated by the keel line separation. The radius of the bilge corners in the middle body is relatively large, so that the bilge separation in that region does not have a significant effect on the formation of the wake.

The side force and yaw moment coefficients plotted against the drift angle for the Series 60 hull are presented in Figures 8.8 and 8.9 respectively. The calculated results, shown as squares connected by a solid curve, are presented together with the experimental results from Longo (1996) and the numerical results from Zou and Soding (1995), who implemented a panel method using Rankine singularities. In the case of the side force coefficient, the agreement with experiment deteriorates as the drift angle increases, although the present method still compares well with other numerical results where they are available (Zou and Soding 1995).

The exact reasons of differences on the side forces are not easy to establish because of the lack of detail in the experimental results. They can be explained to some extent by the difficulties in modelling the rapid and extreme changes in geometry occurring at the stern of the ship. Another contribution may be due to the flow separation along the sharp keel edge of the forebody and the stern of the hull, which the multi-vortex method might have some difficulties in modelling.

8.3 The Flow around the British Bombardier

8.3.1 The British Bombardier

The British Bombardier is a tanker hull form that has been frequently used for investigating ship manoeuvrability. There have been various segmented model experiments (Clarke 1972, Clarke and Hearn 1992 and Horn 2000). The detailed experimental data for force and moment distributions along the hull can be used for evaluating the present calculation. The body plan and divided two-dimensional hull sections for the British bombardier have been shown in Figures 7.3 and 8.2 respectively. The numerical calculations have been carried out for the hull with up to 10 degrees of drift angle.

The evolution of the vortex flow and the velocity fields about the British Bombardier hull at 10 degrees of drift motion are illustrated in Figures 8.10 and 8.11 respectively.

Overall, the flow pattern is different from the one around the Series 60 hull and is more like the combined flow fields of the Wigley hull and the Block hull. The flow separation on the British Bombardier is combined with the keel vortex and bilge vortex. As seen in Figures 7.3 and 8.2, the hull has the blunt forbody and the long middle body region. Unlike the Series 60 hull, the midship sections of the hull have a small bilge radius. As seen at $X/L = 0.44$ and 0.67 in Figure 8.10, the flow separation

at the bilge corners on the middle body is strong and more like the block hull in Chapter 6. Bilge separation is an important part of the formation of the wake flow.

The distribution of the cumulative side force coefficients, $Y'(X/L)$, is shown in Figure 8.12 plotted at stations along the hull. The curves represent the calculated results and the symbols show the experimental results from DRA Haslar (Clarke and Hearn 1992) for different drift angles. The dashed curve shows the attached flow results for a drift angle of eight degrees, computed from the sectional added mass, equation (7-19), and ignoring the contribution of the vortices. The difference between the dashed curve and the uppermost solid curve is a measure of the growing contribution of the trailing vortices as the flow develops along the hull. The side force coefficient plotted against the drift angle is shown in Figure 8.13.

The corresponding figures showing the cumulative distribution of yaw moment, $N'(X/L)$, and the yaw moment plotted against drift angle, are shown in Figures 8.14 and 8.15 respectively.

In both Figures 8.13 and 8.15, the predicted results are compared with experimental results form Clarke and Hearn (1992) and Horn (2000) and numerical results from Wellicome et al (1997), which are based on the slender body theory and which introduce a single vortex at each time step. The present method gives good results for the both side force and yaw moment coefficients for the hull. The result by Wellicome et al (1997) showed a similar result for the side forces but a significant overestimation of the yaw moment, which is the result of an unrealistic distribution of the side forces.

8.3.2 The British Bombardier with a Pram Stern

A segmented model of a hull form made up of the British Bombardier forebody but equipped with a pram stern was recently tested by Horn (2000) to investigate its manoeuvrability. The body plan and the divided two-dimensional hull sections for the

British bombardier with a pram stern have been shown in Figures 7.4 and 8.3 respectively. Numerical calculations have been carried out for the hull with up to 10 degrees of drift angle.

In the case of the straight-ahead motion, an experiment by Kuiper (1994) showed that the direction of the vortex shed from a pram stern is in the opposite sense of rotation compared to that of a conventional stern (Figure 2.4). The present model was applied to the British Bombardier with a pram stern moving with straight-ahead motion to see whether the present model can capture the wake distribution. As seen in Figures 8.16 and 8.17, the direction of the calculated wake flow of the British bombardier with a pram stern is very similar to the experimental result presented by Kuiper (1994). For the purposes of comparison, the figure showing the present results is rotated by 180 degrees.

Figures 8.18 and 8.19 illustrate the development of the vortex and the velocity fields about the hull at 10 degrees of drift motion respectively. The flow fields on the fore part of the hull are identical to those of the British Bombardier in Figures 8.10 and 8.11 as the forebody of the two hulls is identical. As the flow advances along the afterbody, the two hulls develop totally different flow patterns. Since there are no keel edges along the afterbody, only the bilge vortices are important in the formation of the wake flow for the hull moving with 10 degrees of drift angle. The flow separation at the bilge corners is also affected by the downwash induced by the shrinking of the sectional depth as the hull approaches the stern.

In Figure 8.20, the distribution of the cumulative side force coefficients is plotted along the hull. The curves represent the calculated results and the symbols show the experimental results from Horn (2000) up to six degrees of drift angle. The dashed curve shows the attached flow results for a drift angle of six degrees computed from the sectional added mass and ignoring the contribution of the vortices. There are huge differences between the attached flow results and experimental results as the stern is approached. The present method including the contribution of the trailing vortices is an improvement on the theoretical attached flow calculation. Unlike the

results for the British Bombardier in Figure 8.12, the present results still have some differences compared to the experimental data. In Figures 8.21 and 8.22, the side force and the yaw moment coefficients are plotted against the drift angle together with measurements of Horn (2000) respectively.

The possible explanation of the differences between the experimental and the numerical results for the side forces may be an up-swept flow separation, which is shown schematically in Figure 8.23. This separation might increase the draft of each pram stern section and consequently increase the value of the sectional added mass. In the case of a conventional stern, such as for the British Bombardier, the up-swept flow separation does not happen and so the added mass coefficient is not affected in this way.

8.3.3 Discussion of Results

The present method gives impressive results for the side force and yaw moment coefficients for the British bombardier. The agreement is not quite so good in the case the British bombardier with a pram stern but even so the results show the correct trends and are a significant improvement on the attached flow results. A possible reason for the disagreement in the side force coefficient around the stern region is the flow separation due to an up-swept flow on the pram stern, which is not modelled in the present method.

In the case of conventional stern hulls, such as the British Bombardier hull, the numerical model gives good results for both the side force and yaw moments. In the practical case of a hull with a pram stern, the hull usually has a skeg, to which the propeller is attached, and the up-swept flow separation might not have such a large influence on the value of the added mass. The present model could still be applied in that case.

8.4 Conclusions

The numerical calculations applied to the three different hulls have proved to be very useful in gaining an insight into the primary mechanisms associated with the generation and development of trailing vortices along different types of ship hull. Attached flow calculations of side force and yaw moment have been shown to disagree significantly with experimental results. The inclusion of the contribution of the trailing vortices as computed by the present method can be seen to virtually remove such discrepancies over most of the hull.

There remain some differences in the computed and experimental results at the very stern of the ship. The exact differences are not easy to establish because of the lack of detail in the experimental results. It is reasonable to assume that they can be explained to some extent by the difficulties in modelling the rapid and extreme changes in geometry occurring over this part of the ship.

The present method does not include all the fine detail of the flow at the extreme stern, but the flow predicted by it is sufficiently realistic to be used in the investigation of problems related to the manoeuvring characteristics of realistically shaped ships including pram sterns.

Finally, the evolution of vortex flows along the three ship hulls for ten degrees of drift motion are illustrated together in Figure 8.24 to compare the three different flow patterns generated by the different hull forms.

Ship	Series 60	British Bombardier	British Bombardier with a pram stern
Length(L/L)	1.0	1.0	1.0
Breadth(B/L)	0.1334	0.1339	0.1339
Draft(T/L)	0.0533	0.0567	0.0567
C_B	0.600	0.829	0.819

Table 8.1: The principal particulars of three ships.

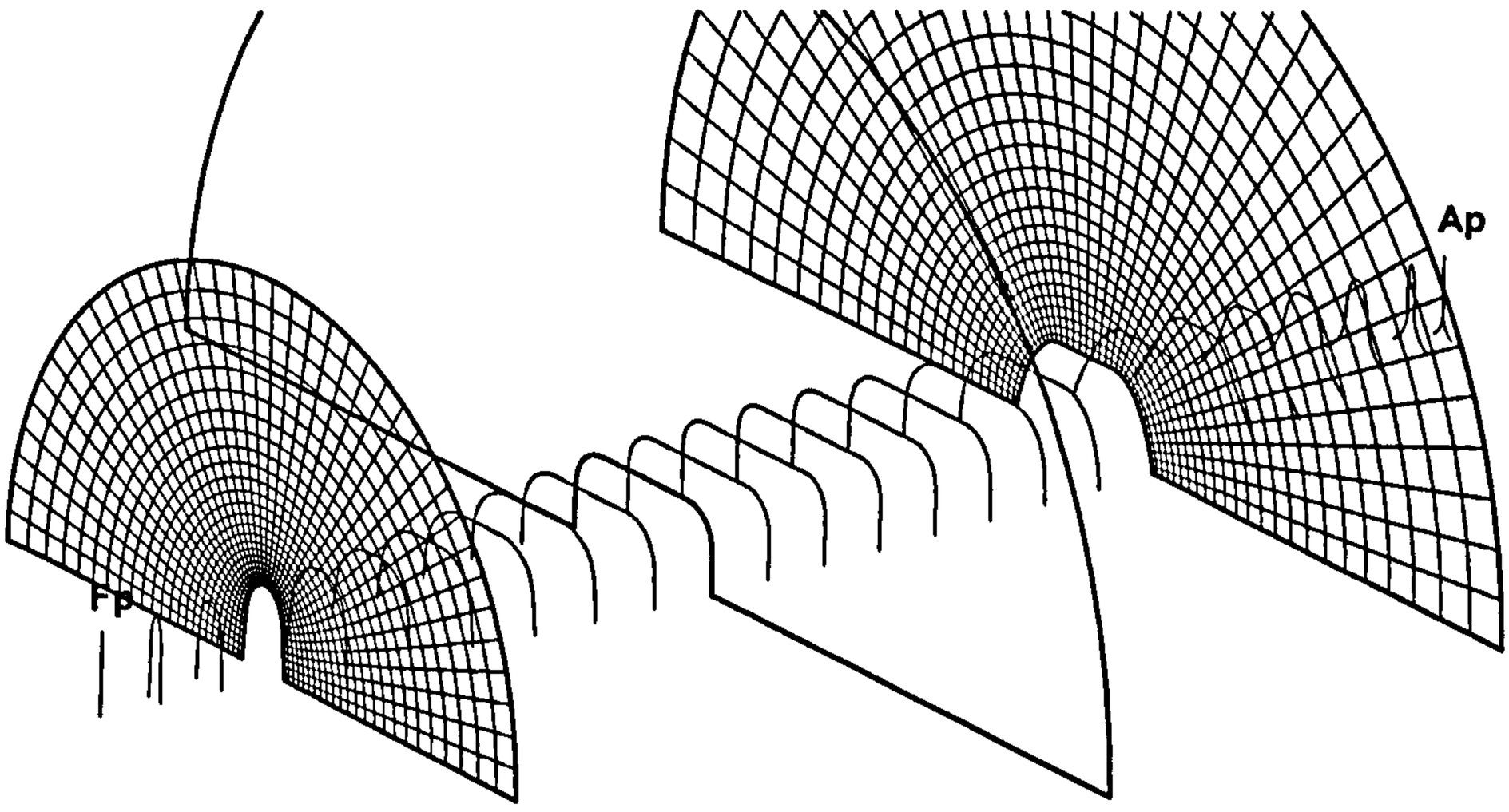

Figure 8.1: The divided two-dimensional hull section for the Series 60 $C_B = 0.6$ including sectional grid domains.

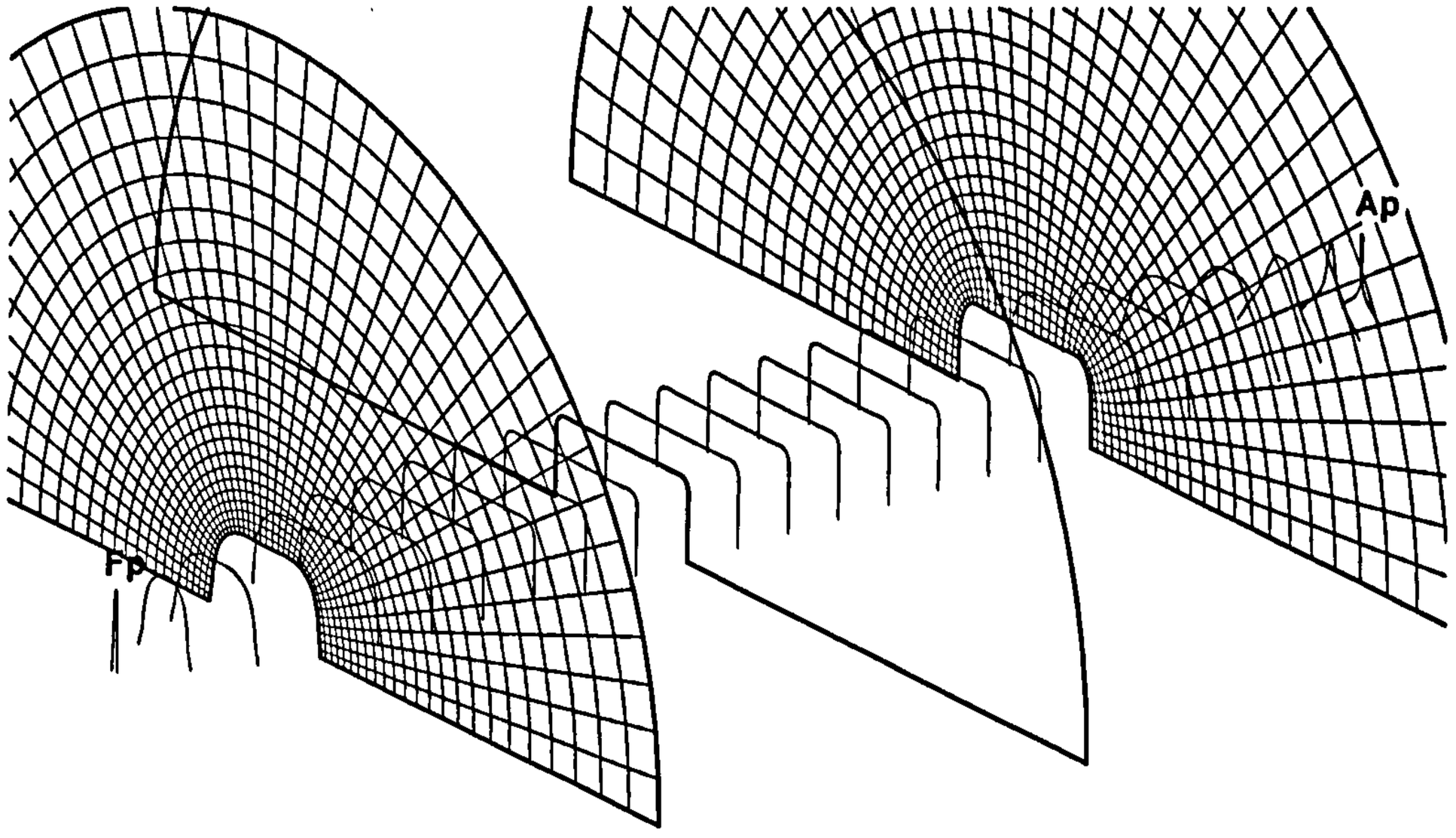

Figure 8.2: The divided two-dimensional hull section for the British Bombardier including sectional grid domains.

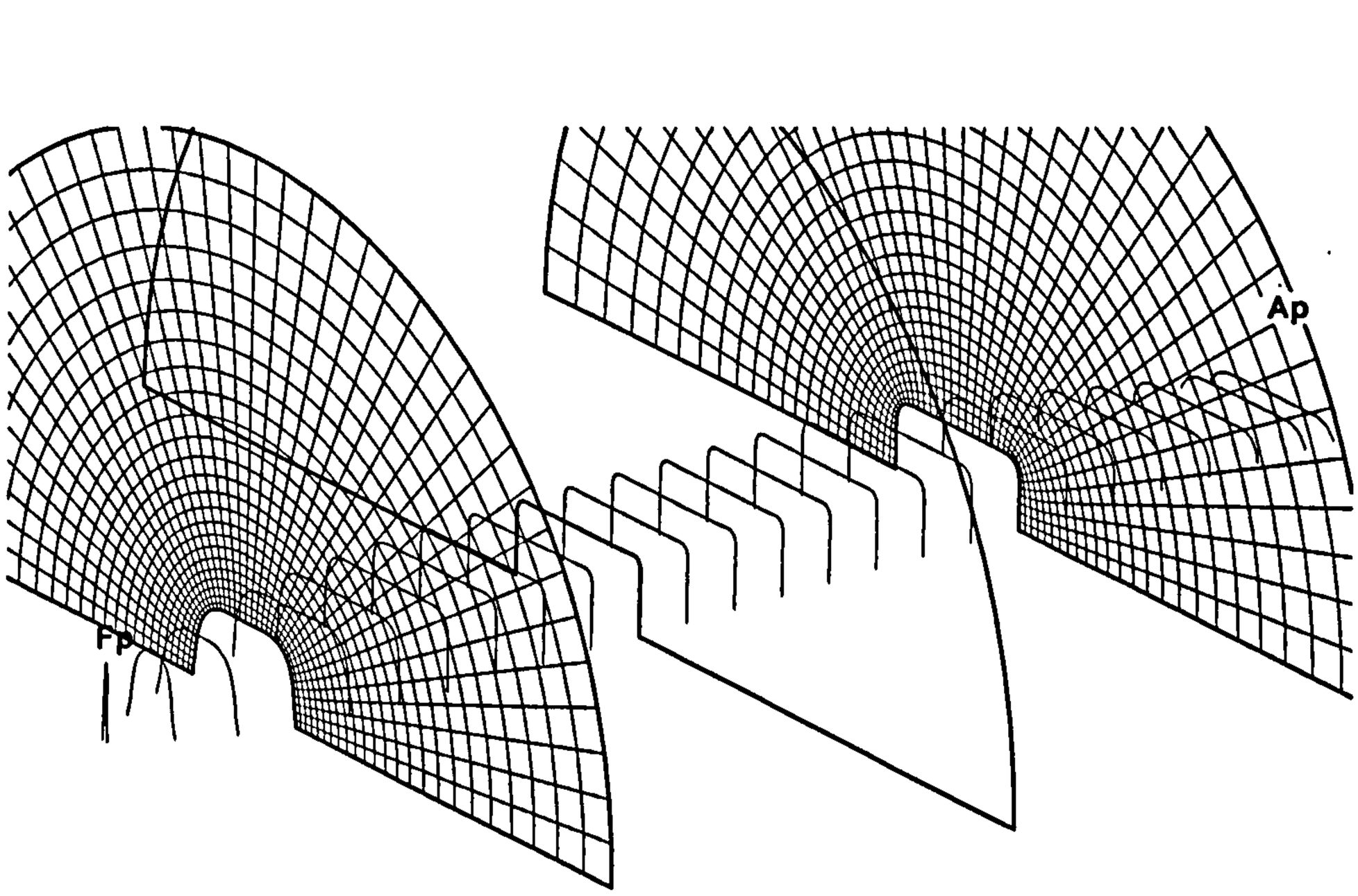

Figure 8.3: The divided two-dimensional hull section for the British Bombardier with a pram stern including sectional grid domains.

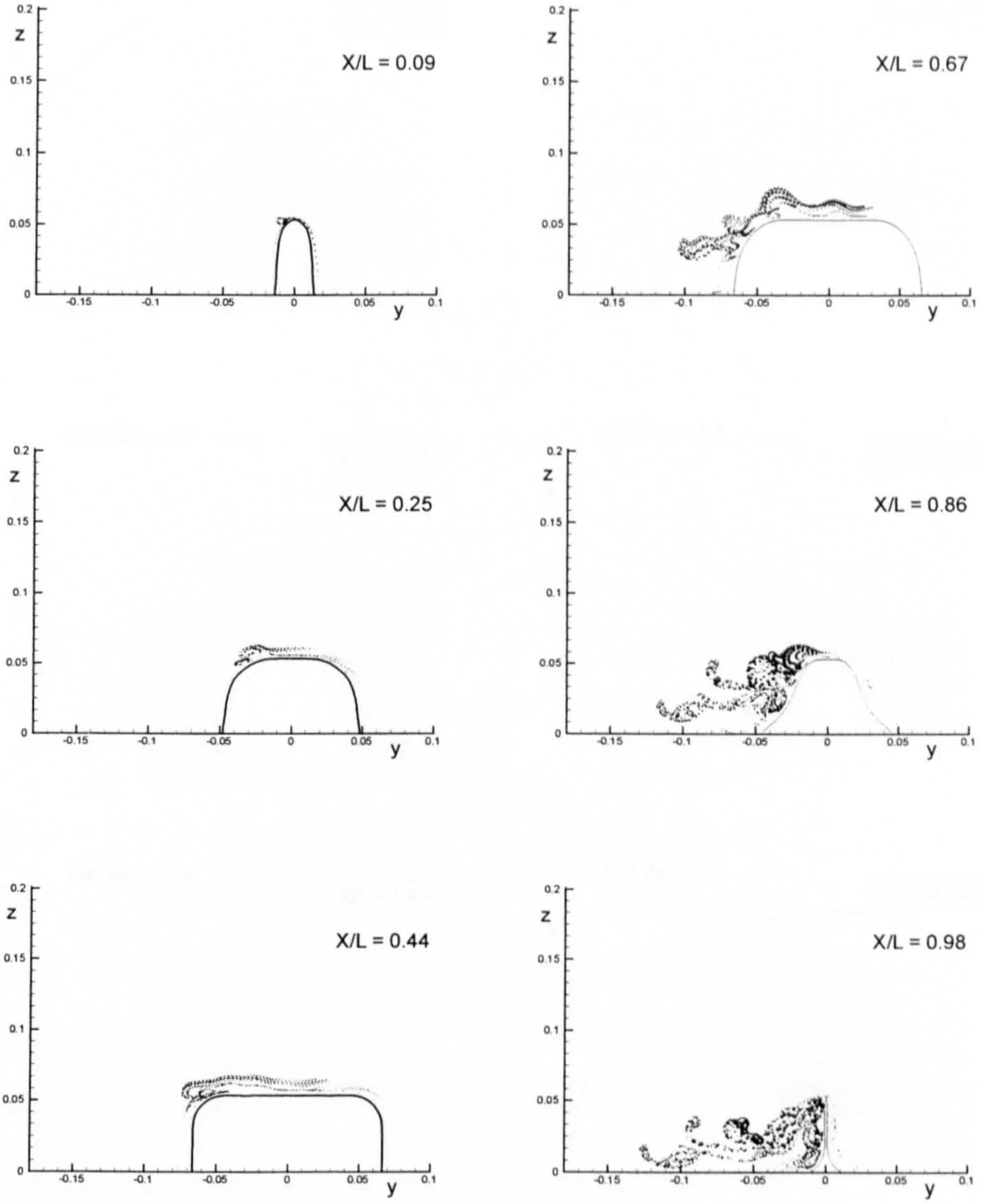

Figure 8.4: Vortex evolution along the Series 60 hull due to ten degrees of drift motion.

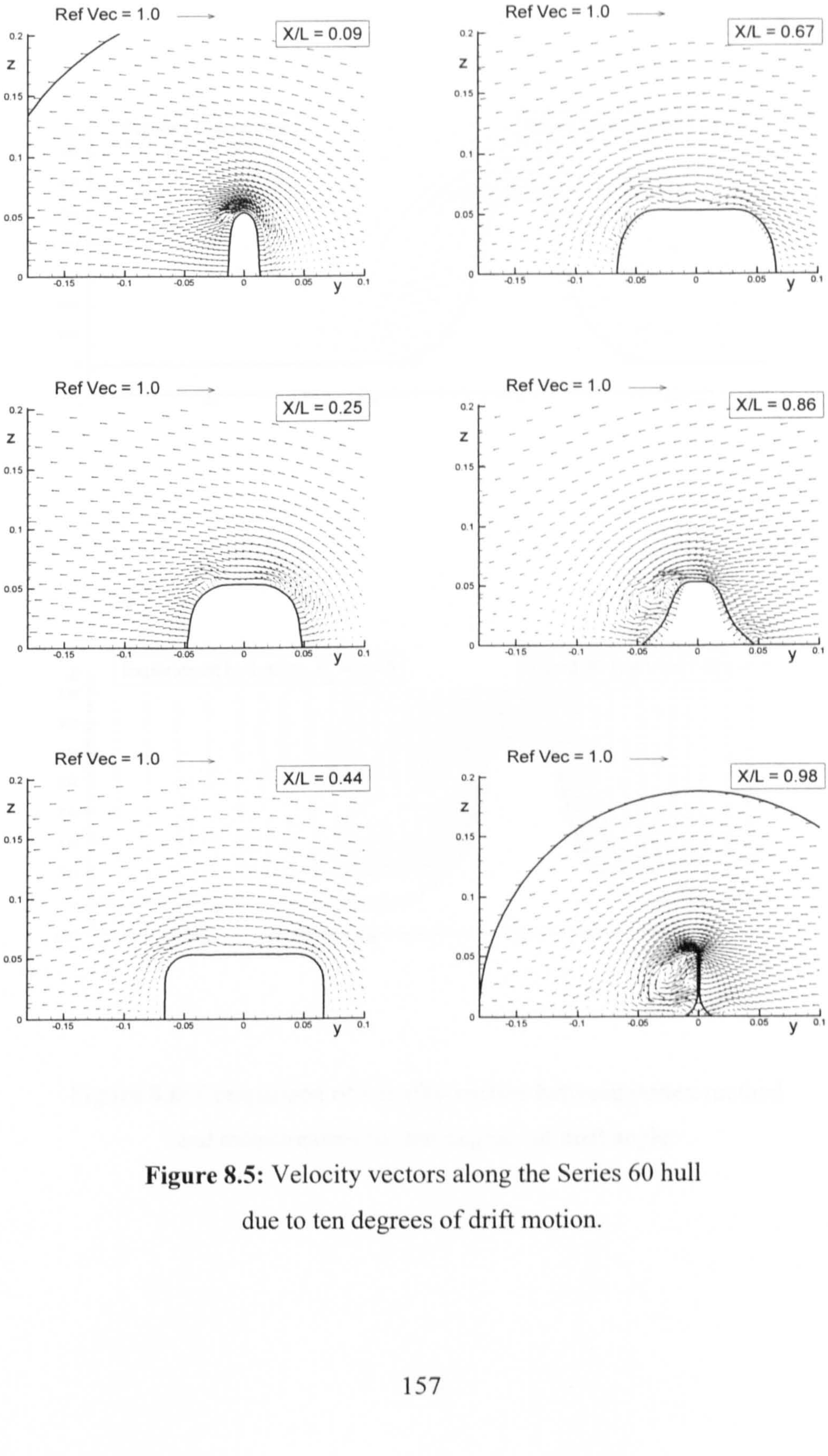

Figure 8.5: Velocity vectors along the Series 60 hull due to ten degrees of drift motion.

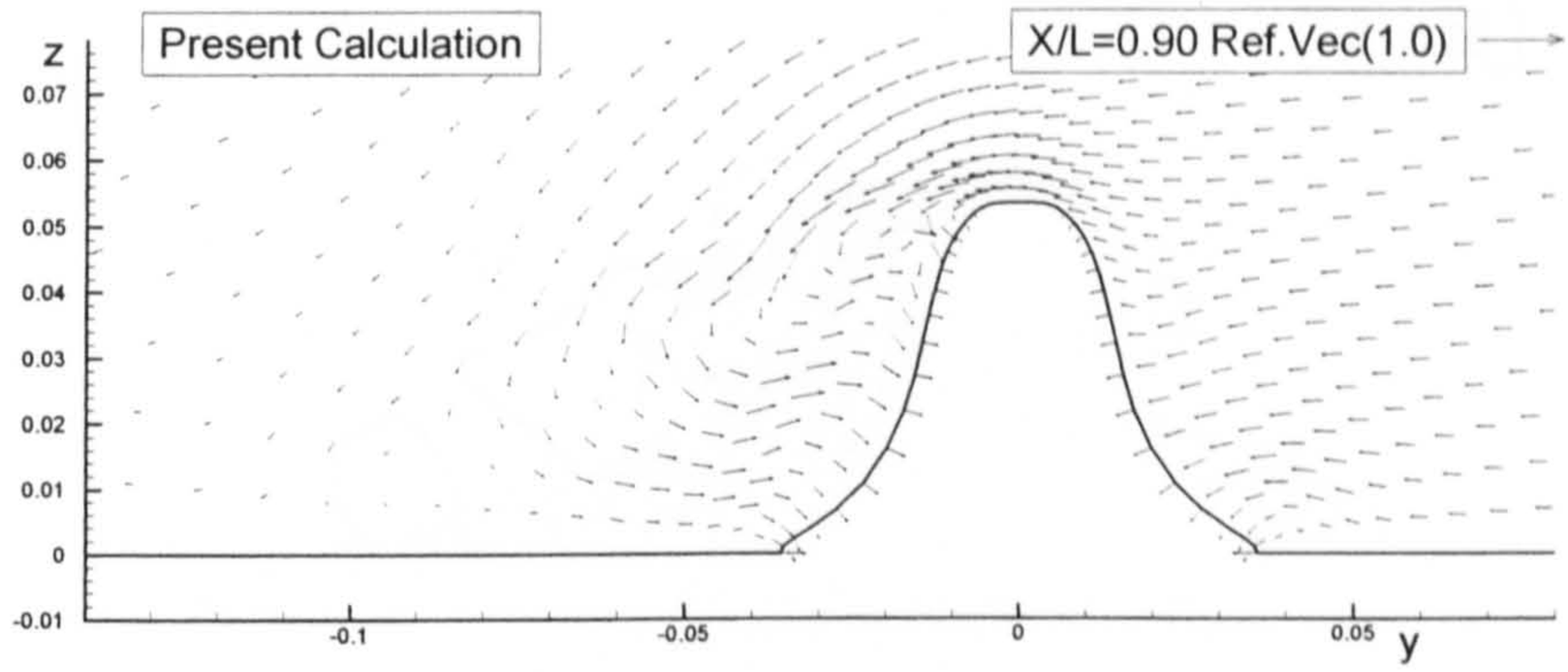

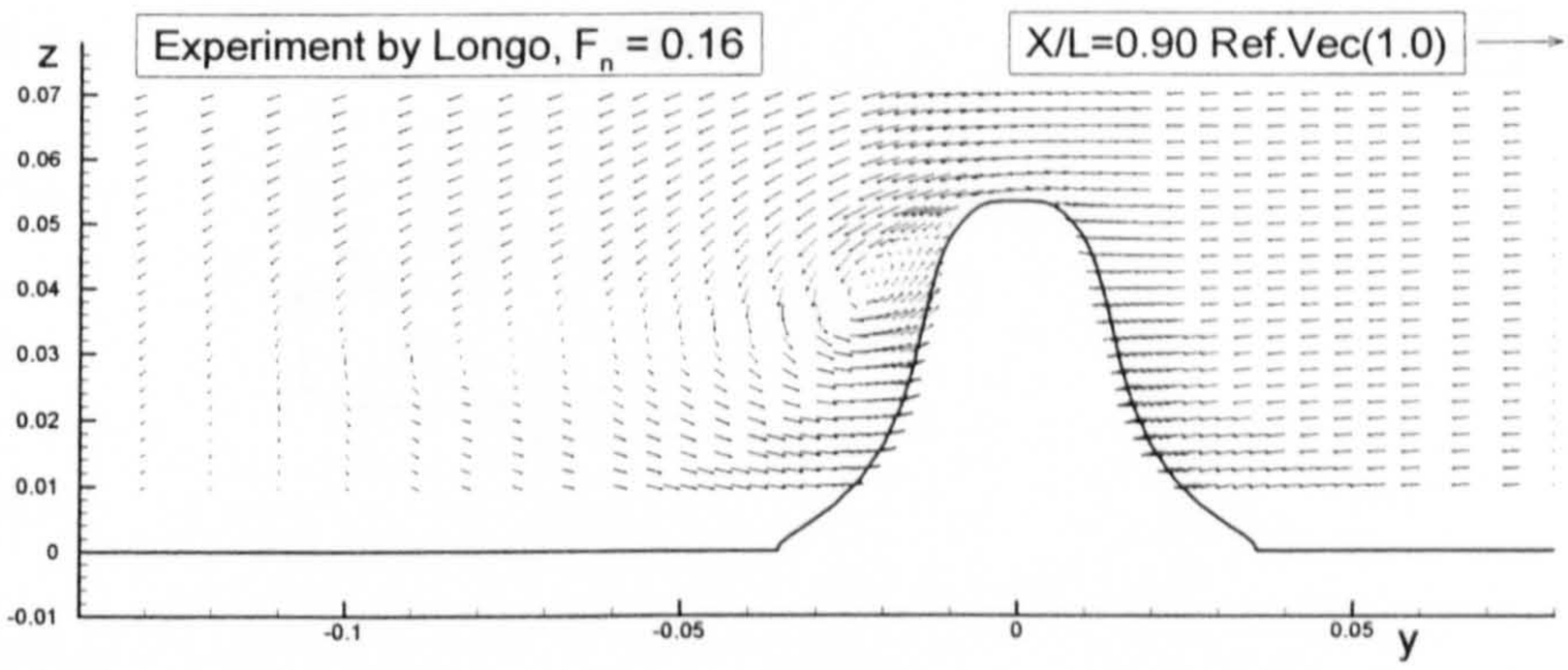

Figure 8.6: Comparison of velocity vectors between vortex method and measurement for ten degrees of drift angle.

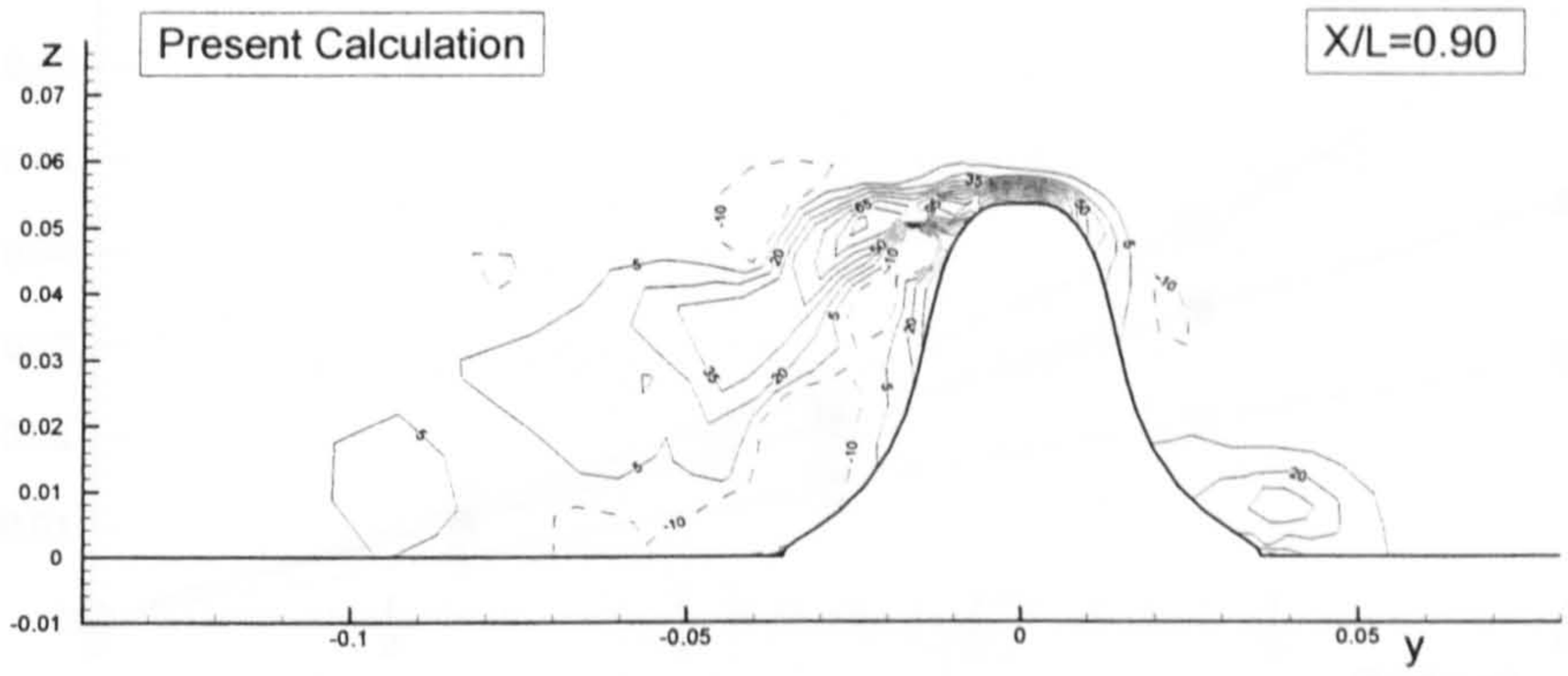

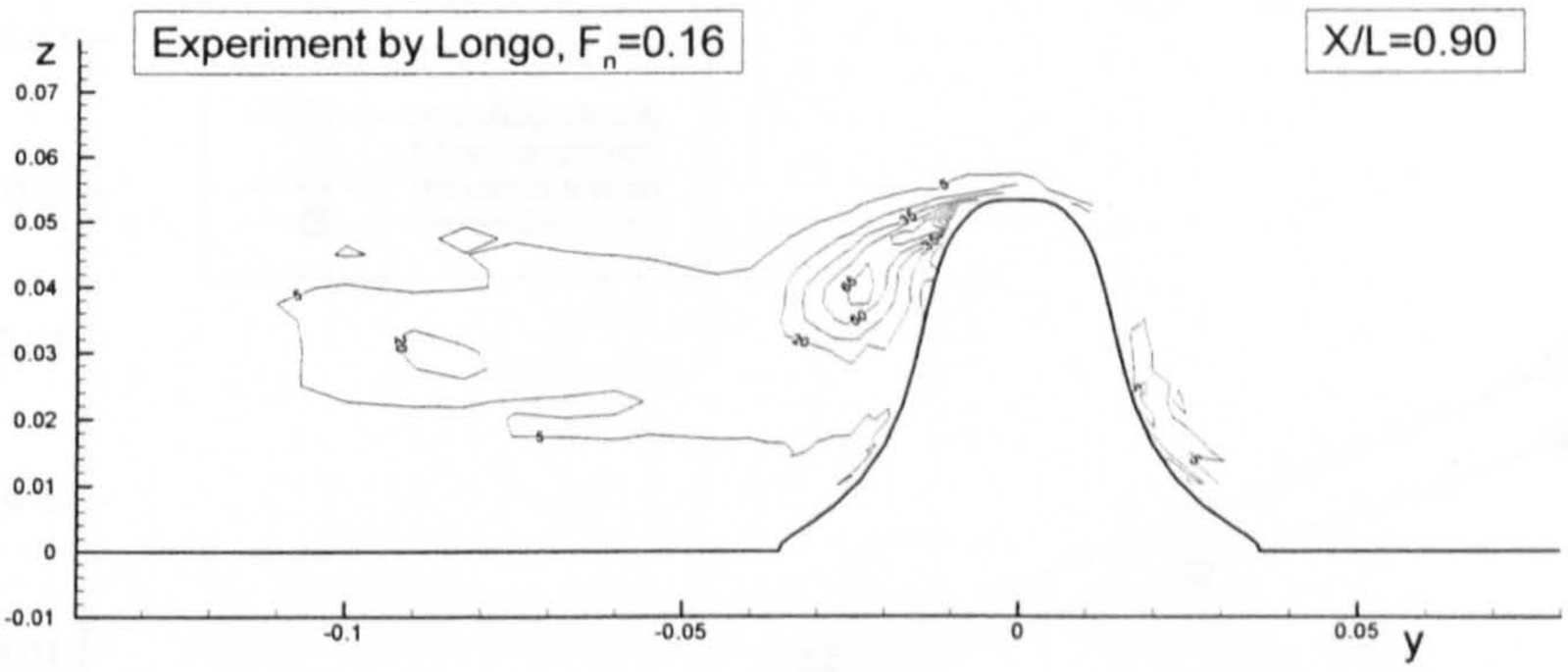

Figure 8.7: Comparison of vorticity fields between vortex method and measurement for ten degrees of drift angle.

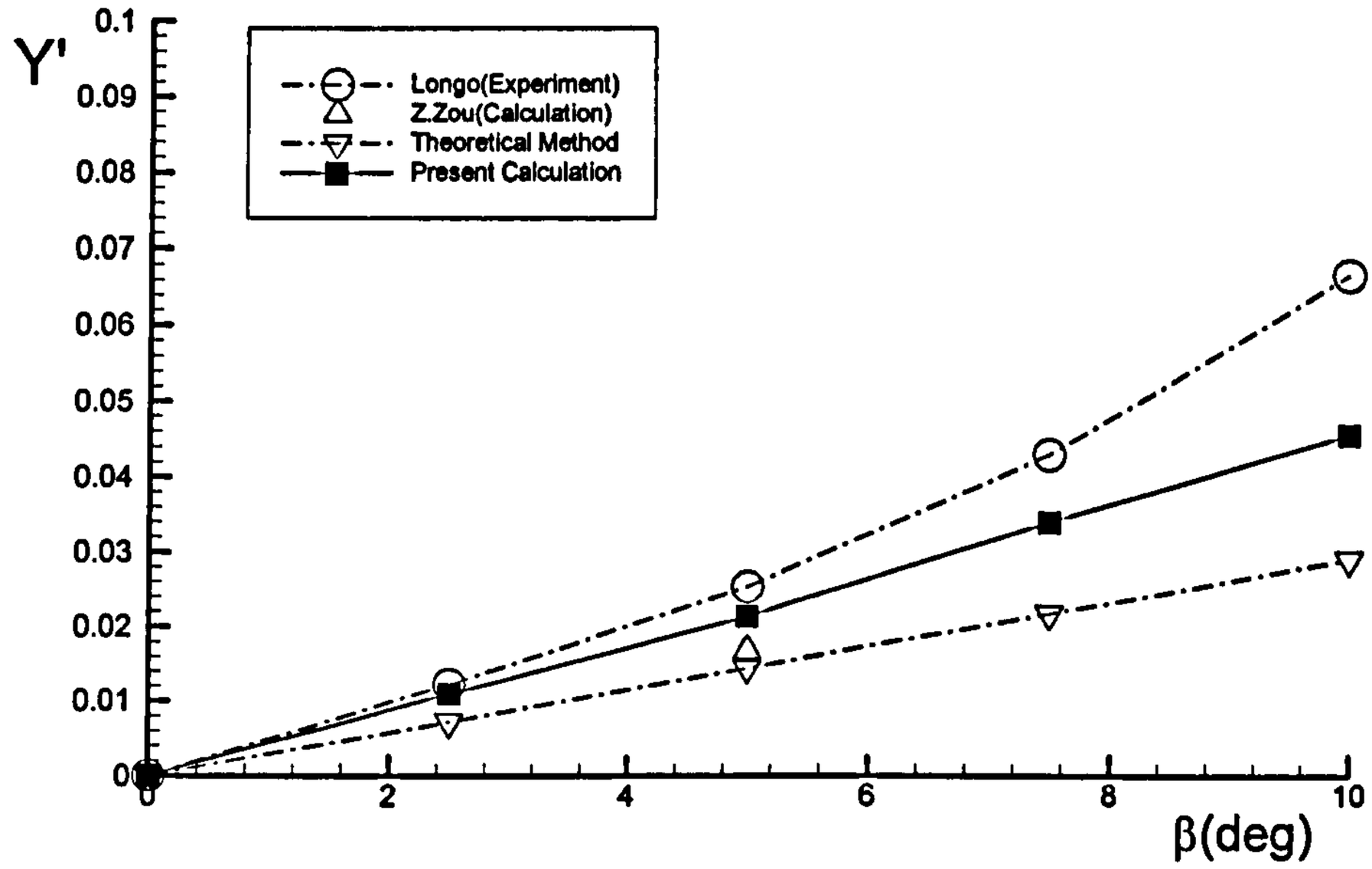

Figure 8.8: Side force coefficient for the Series 60 C_B =0.6 hull in drift motion.

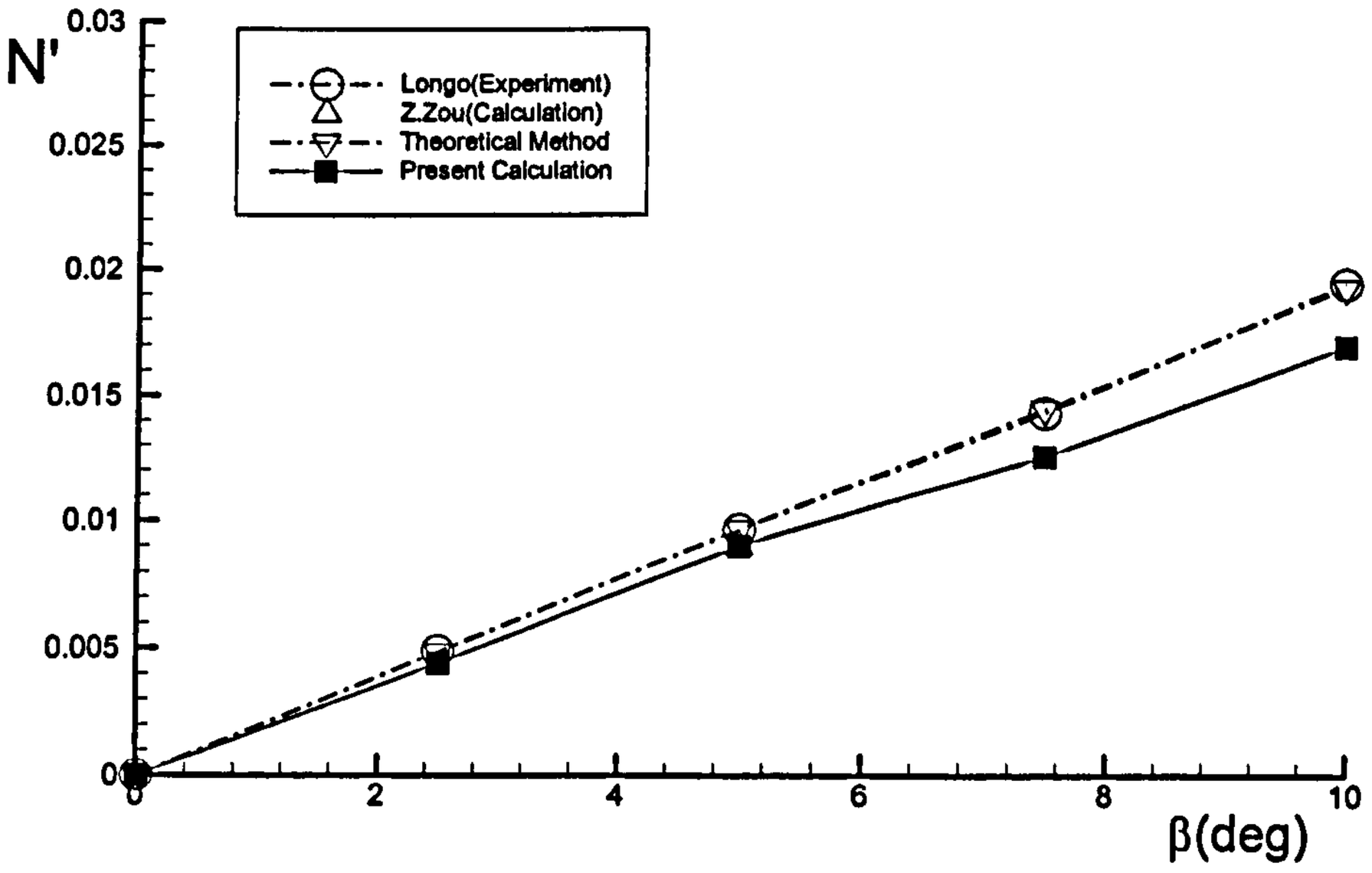

Figure 8.9: Yaw moment coefficient for Series 60 C_B =0.6 hull in drift motion.

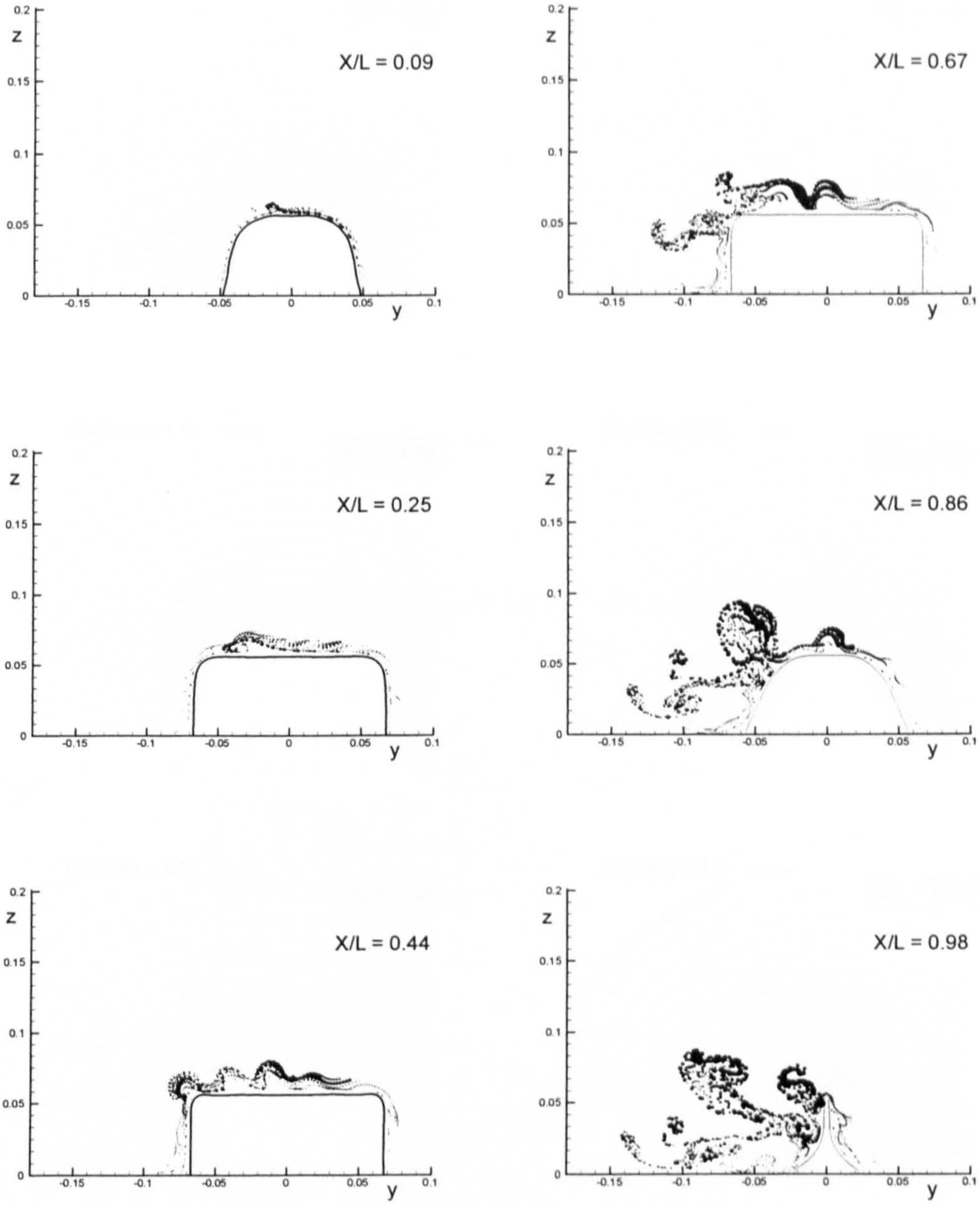

Figure 8.10: Vortex evolution along the British Bombardier due to ten degrees of drift motion.

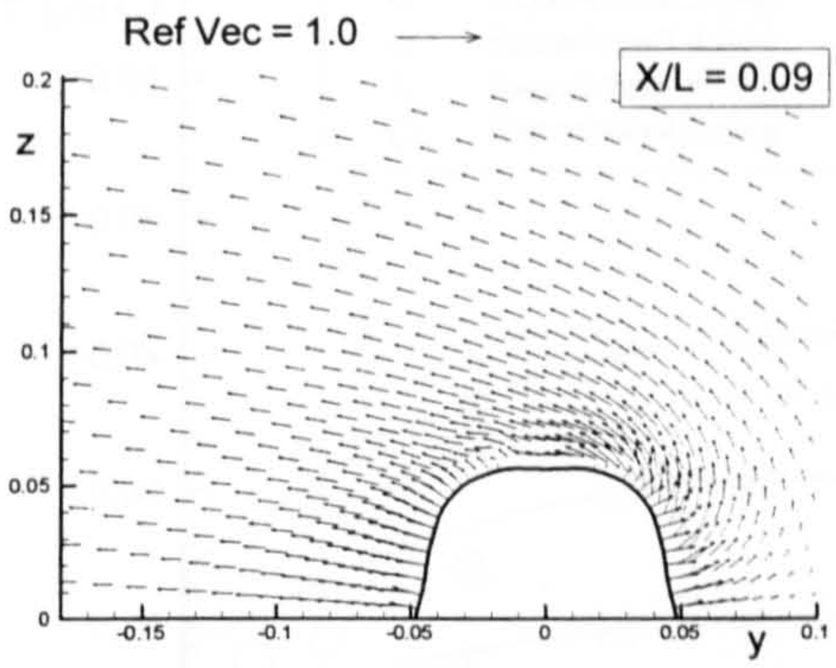

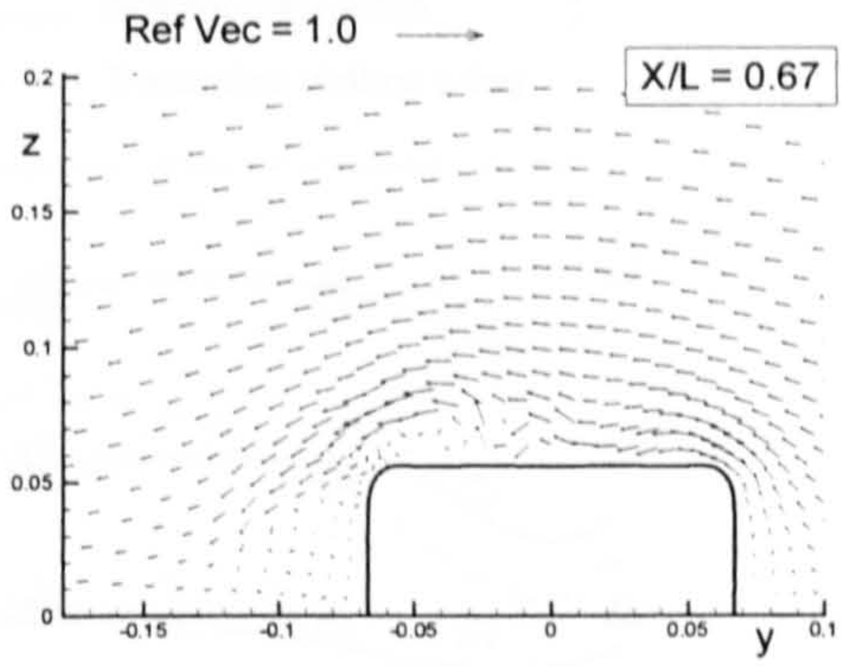

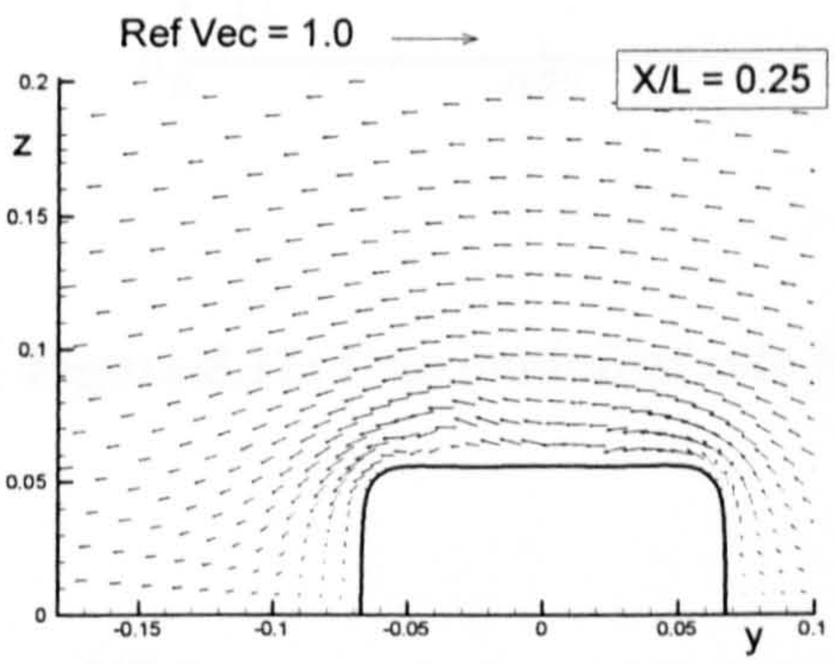

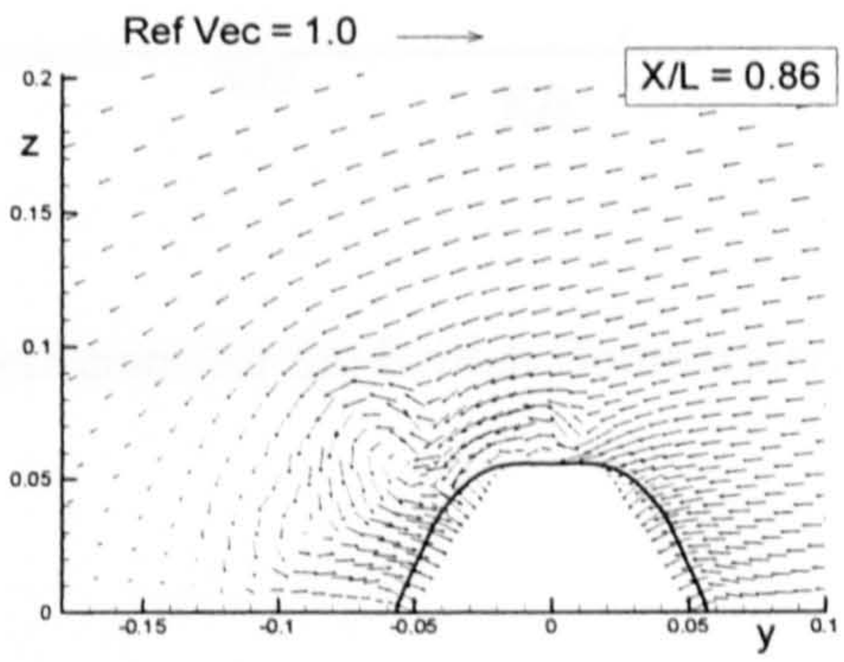

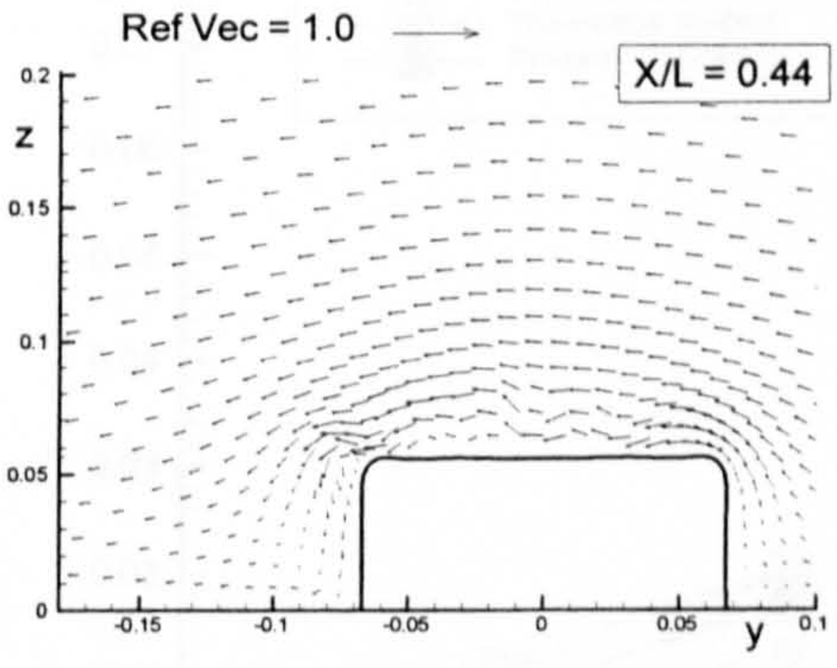

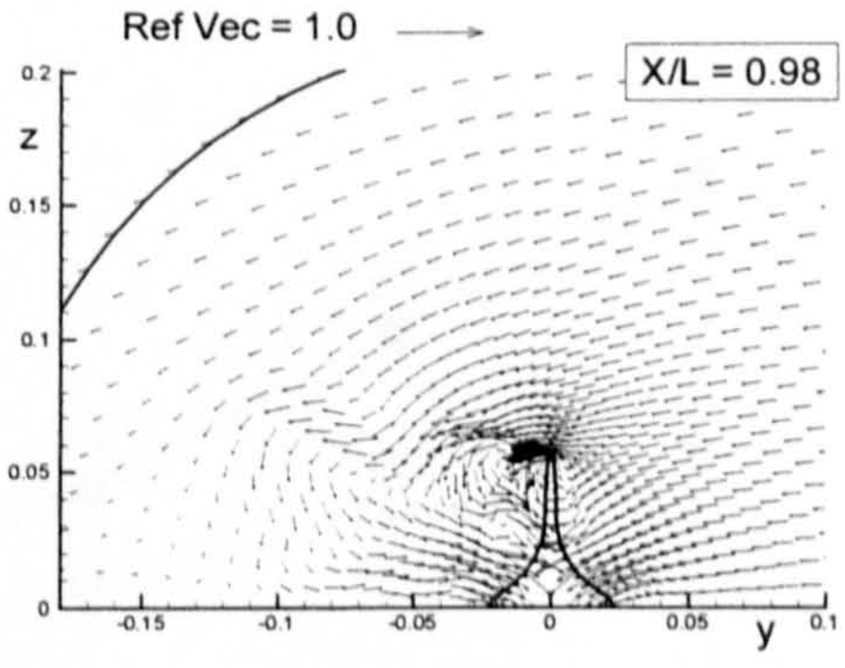

Figure 8.11: Velocity vectors along the British Bombardier due to ten degrees of drift motion.

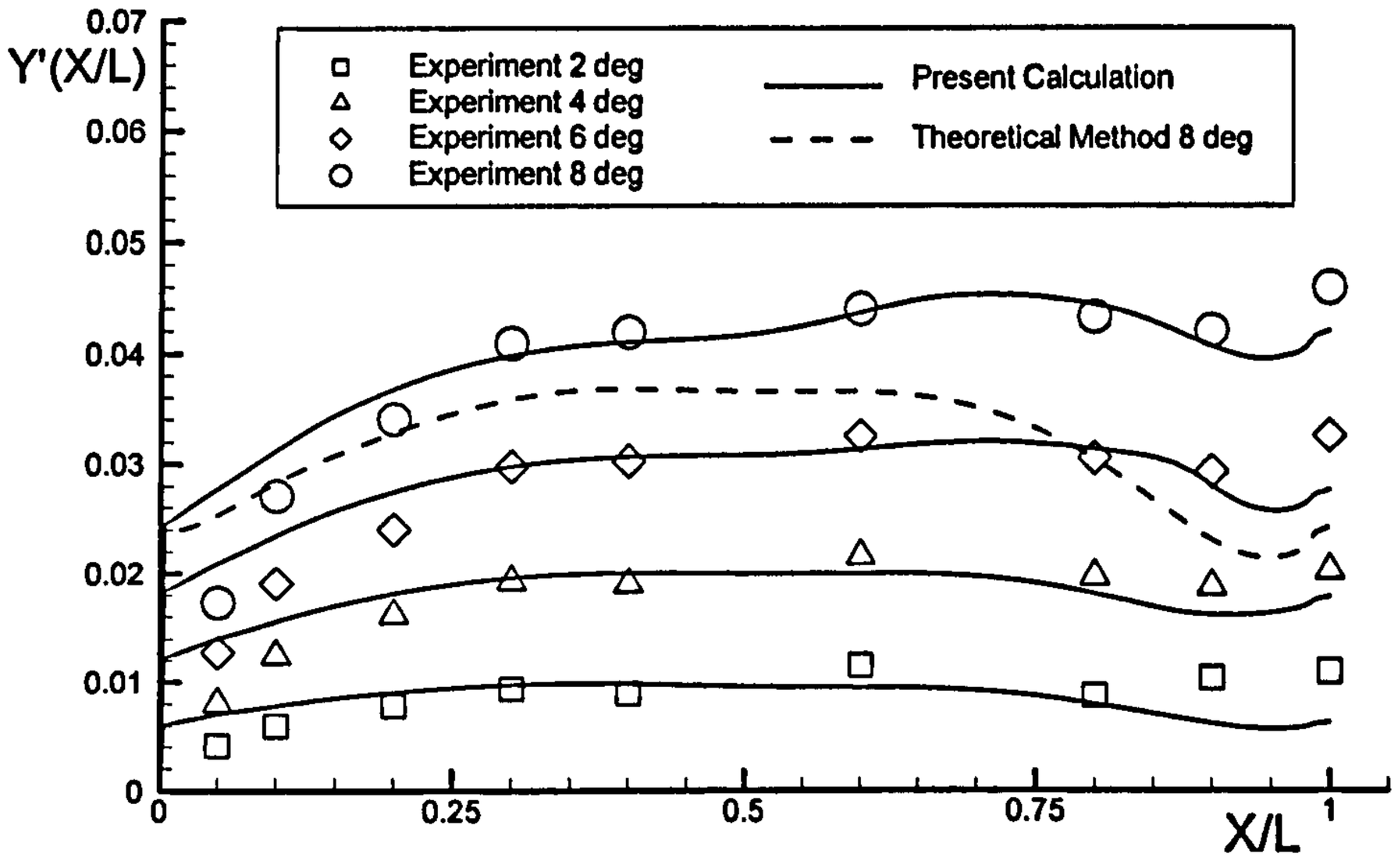

Figure 8.12: Distribution of side force coefficient for the British Bombardier.

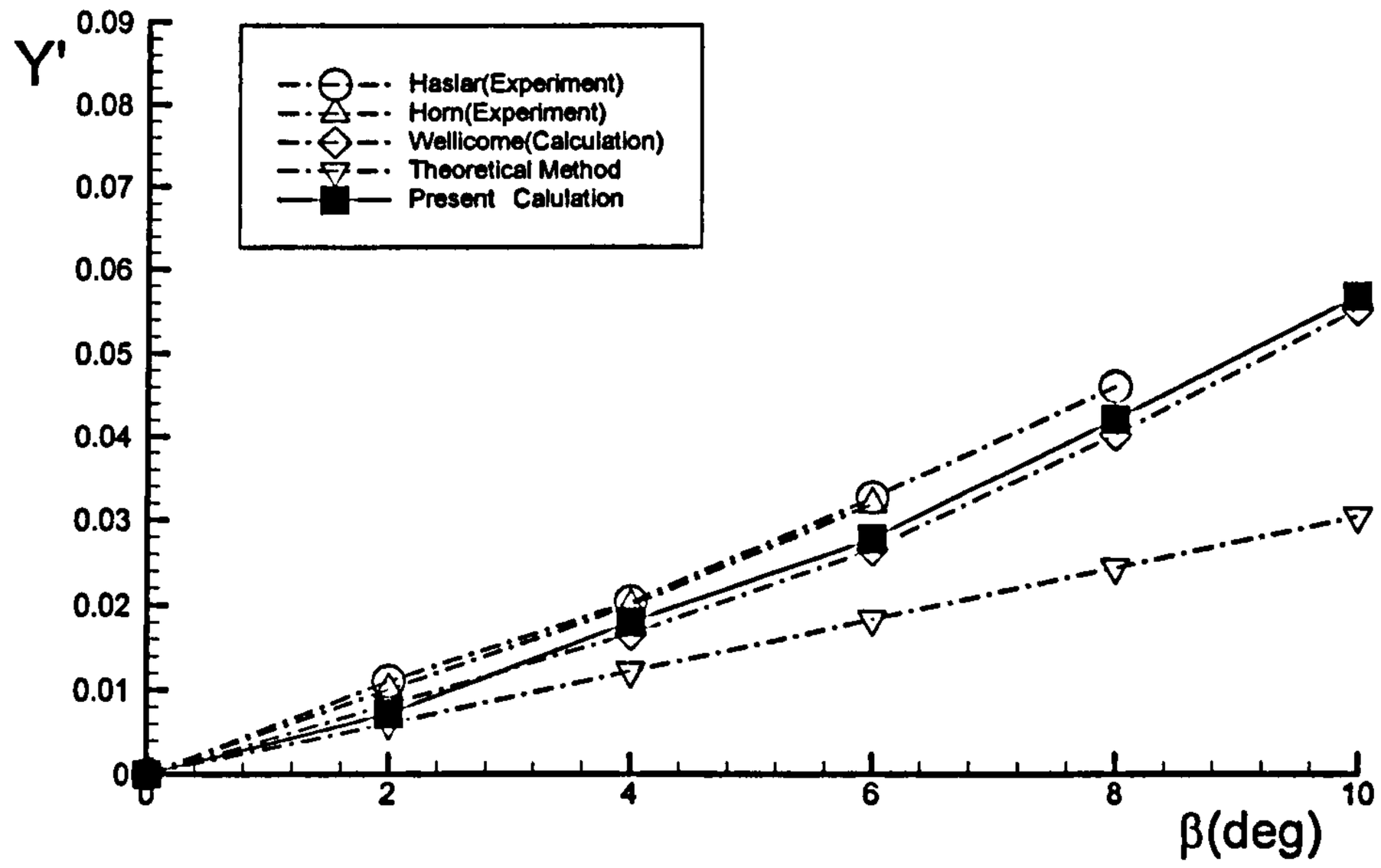

Figure 8.13: Side force coefficient for the British Bombardier in drift motion.

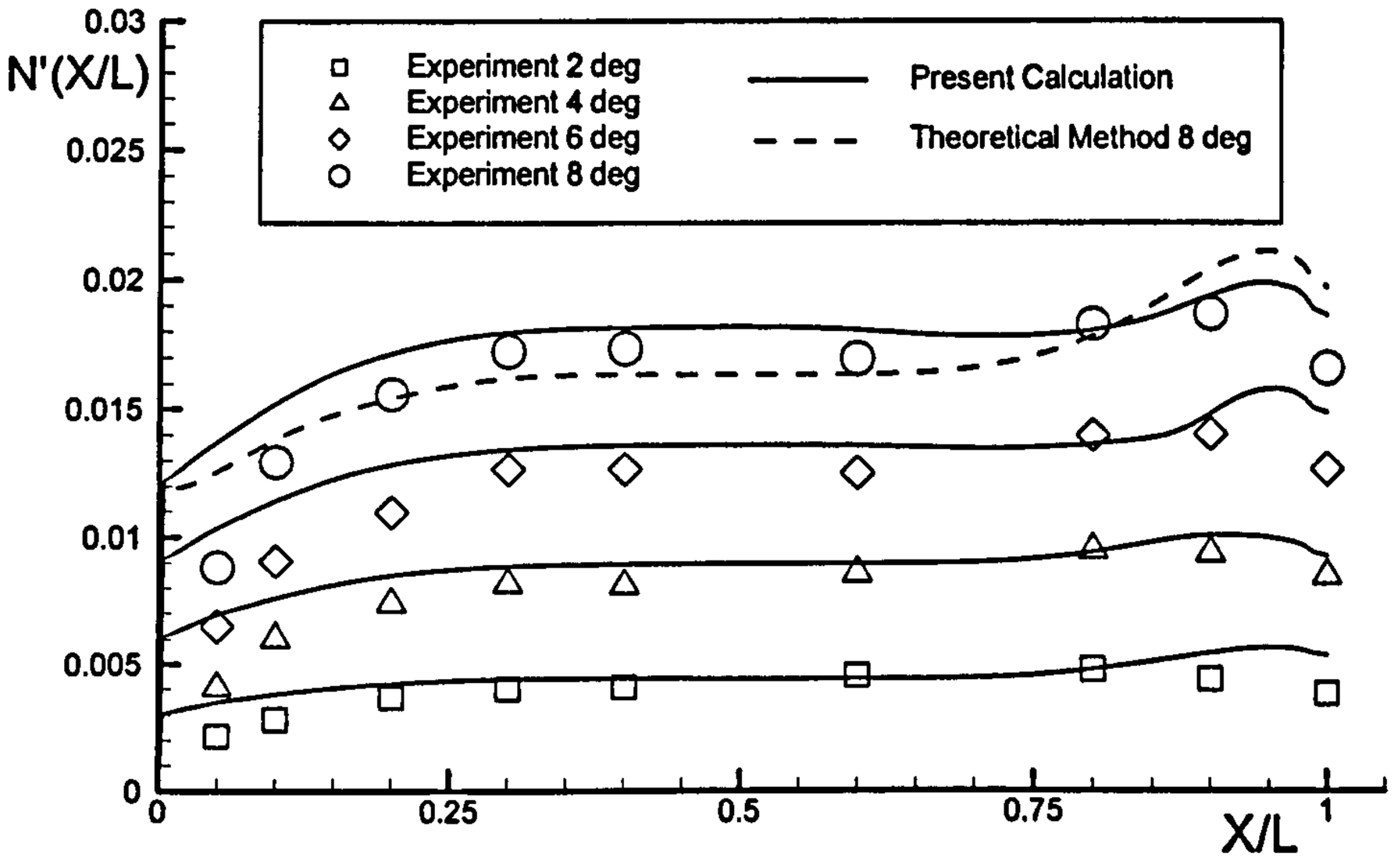

Figure 8.14: Distribution of yaw moment coefficient for the British Bombardier.

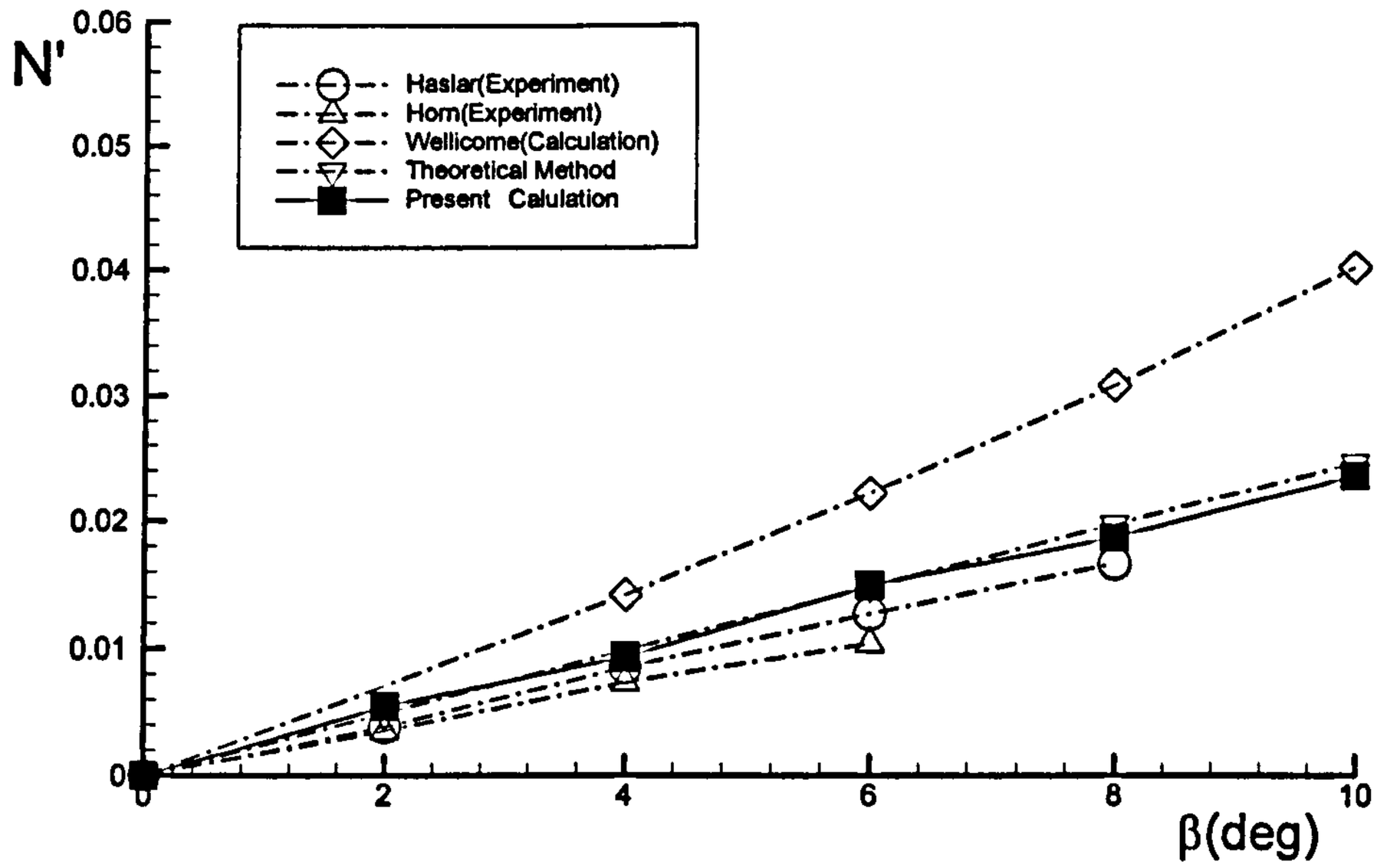

Figure 8.15: Yaw moment coefficient for the British Bombardier in drift motion.

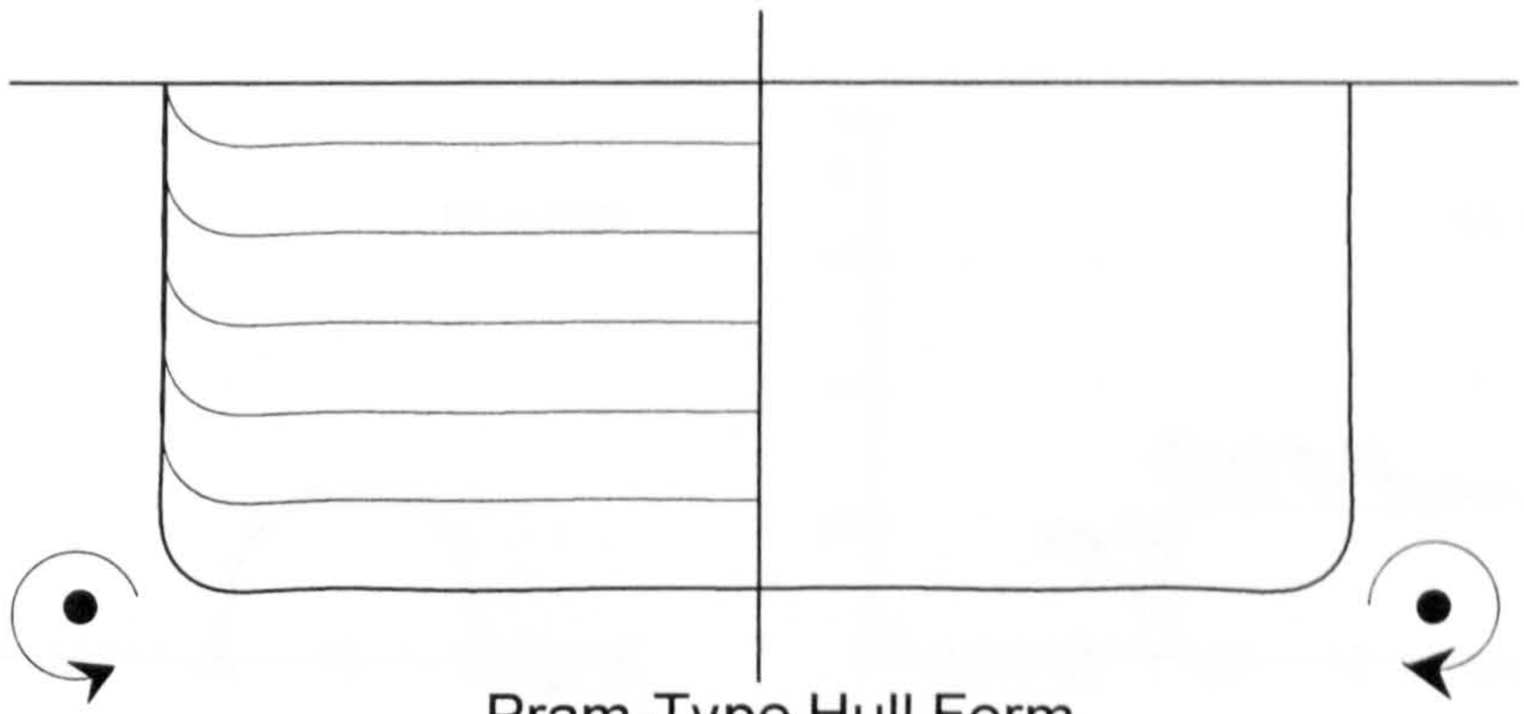

Figure 8.16: The representation of vortex generation from a pram-type hull form as measured by Kuiper (1994).

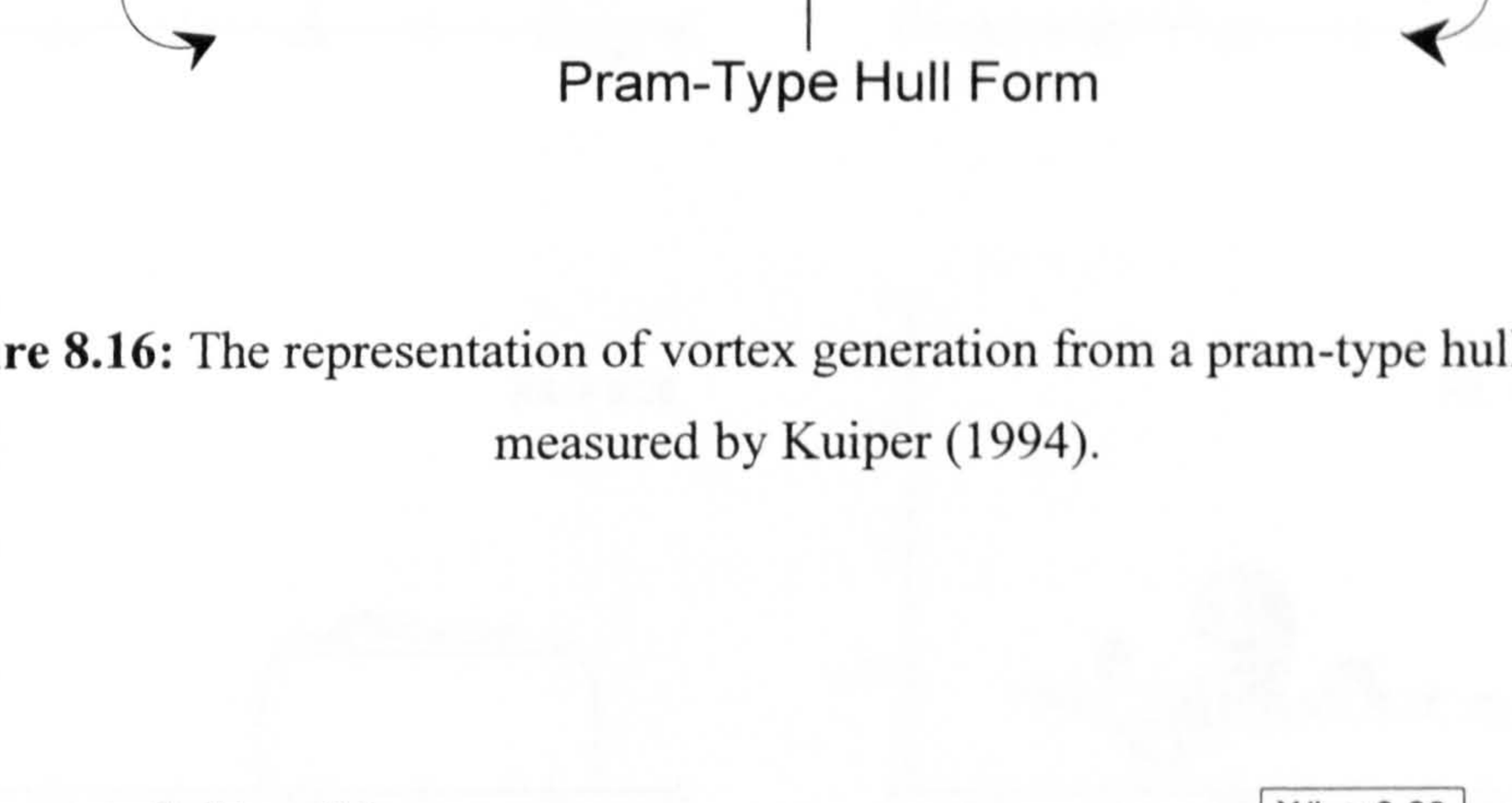

Figure 8.17: Wake distribution of the British Bombardier with a pram stern due to straight-ahead motion.

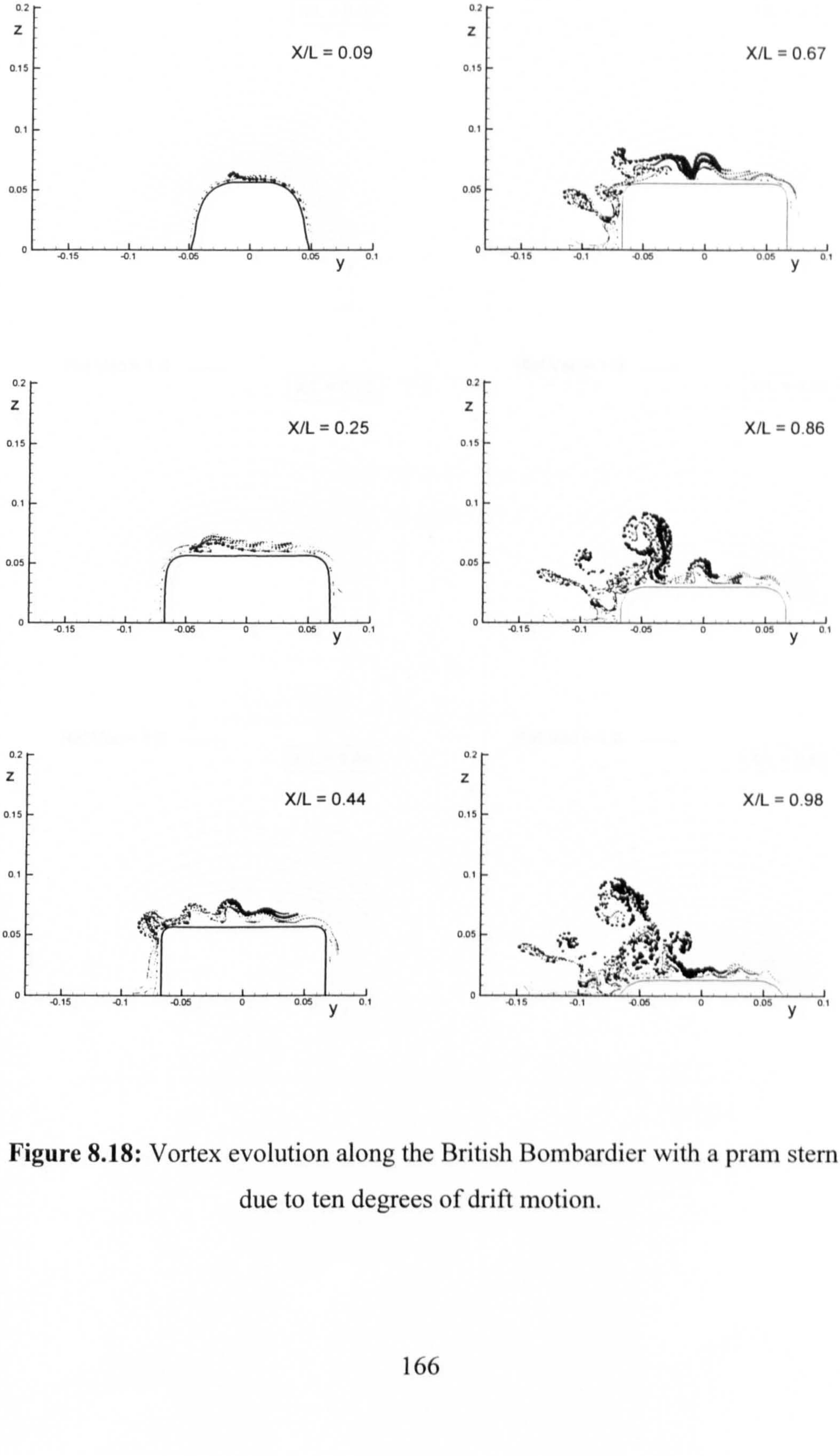

Figure 8.18: Vortex evolution along the British Bombardier with a pram stern due to ten degrees of drift motion.

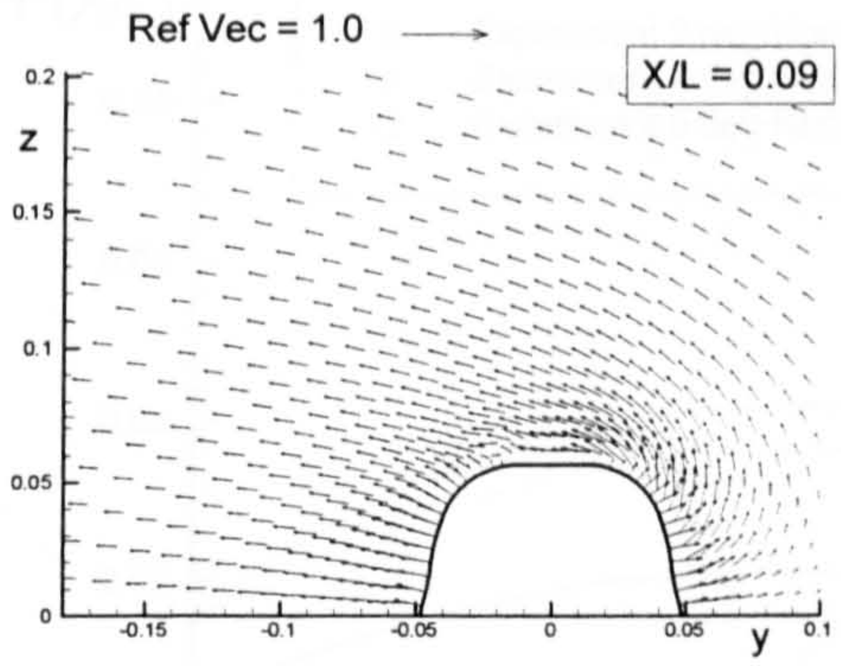

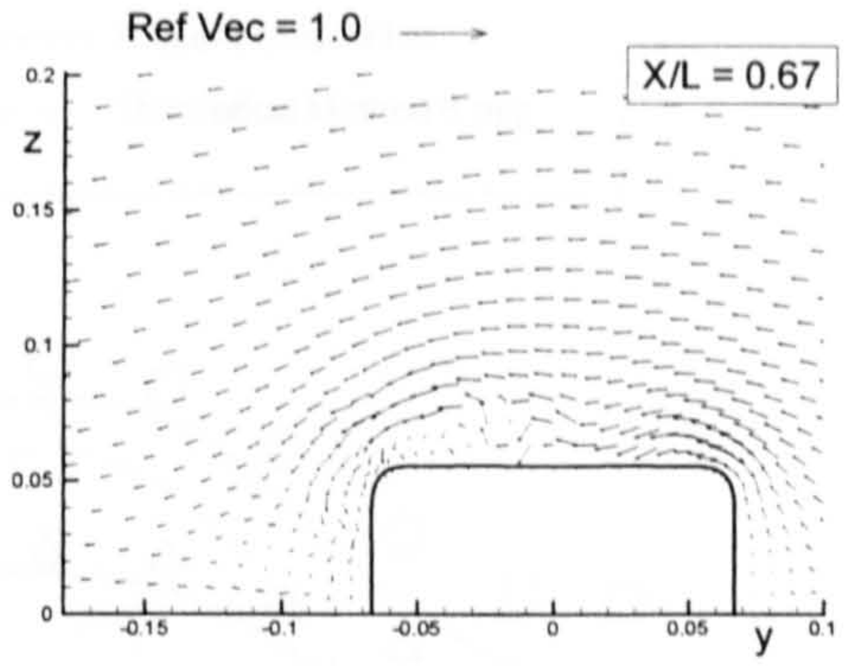

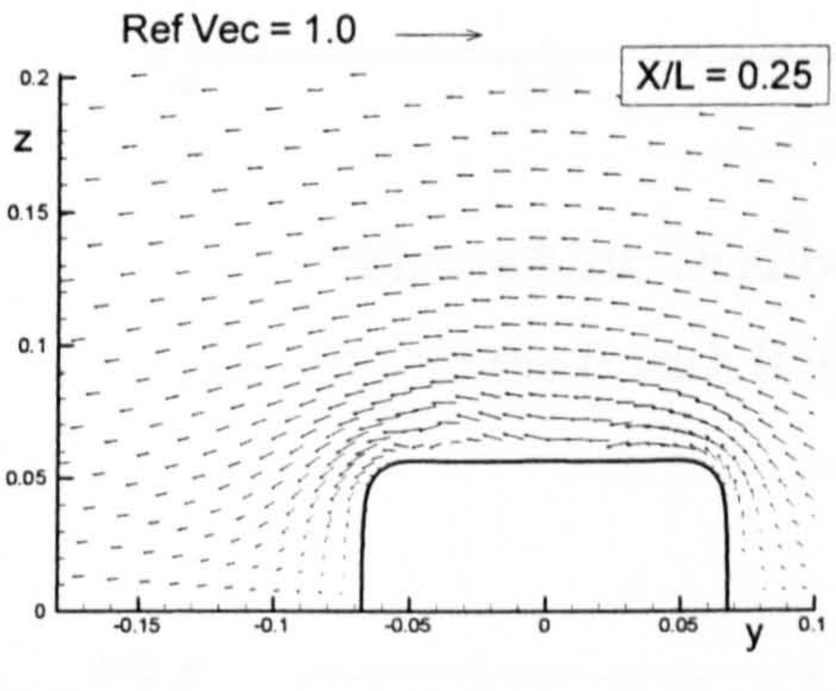

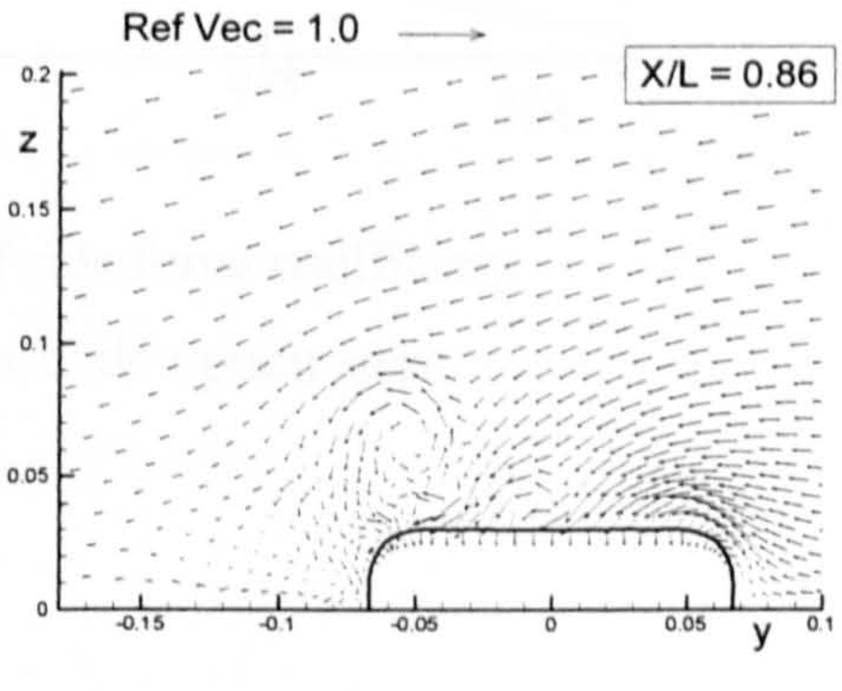

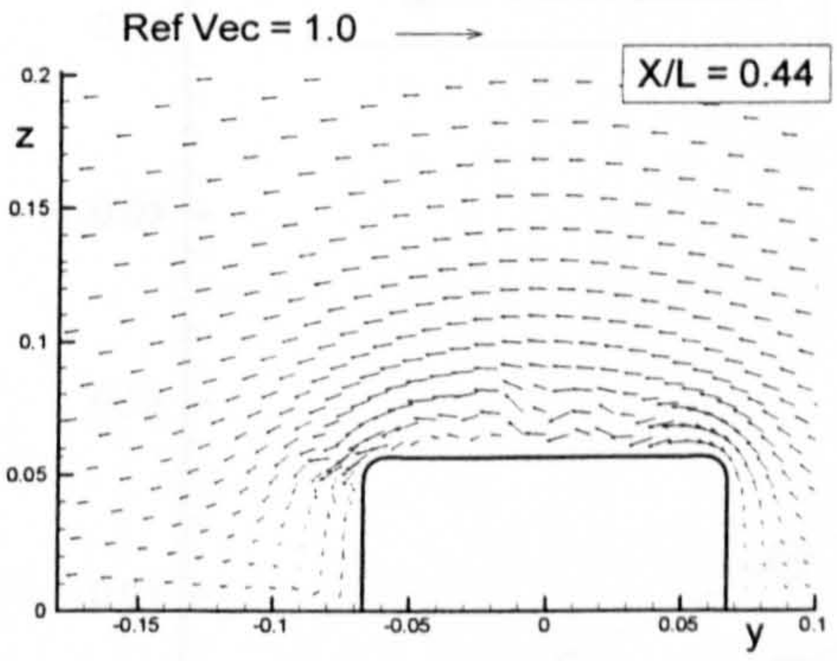

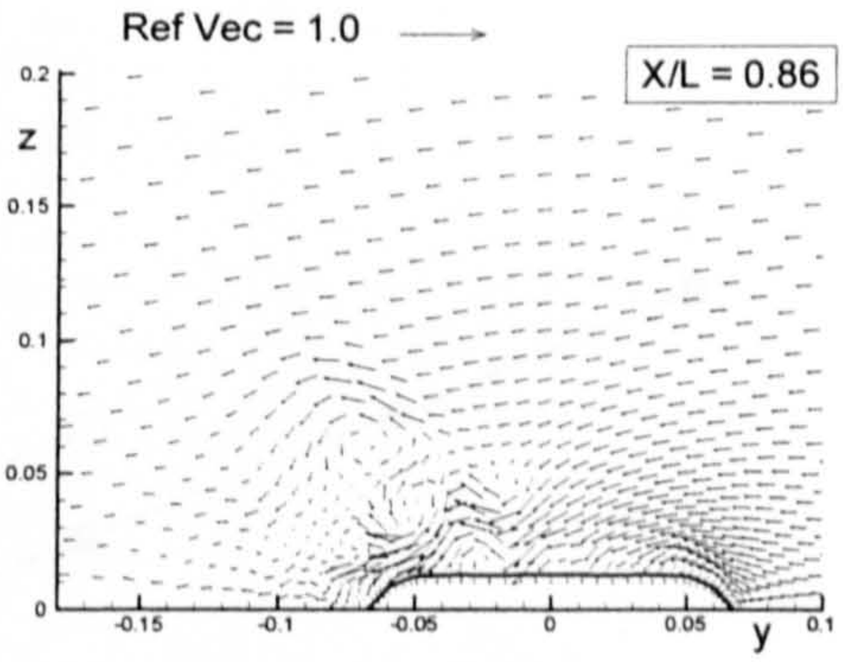

Figure 8.19: Velocity vectors along the British Bombardier with a pram stern due to ten degrees of drift motion.

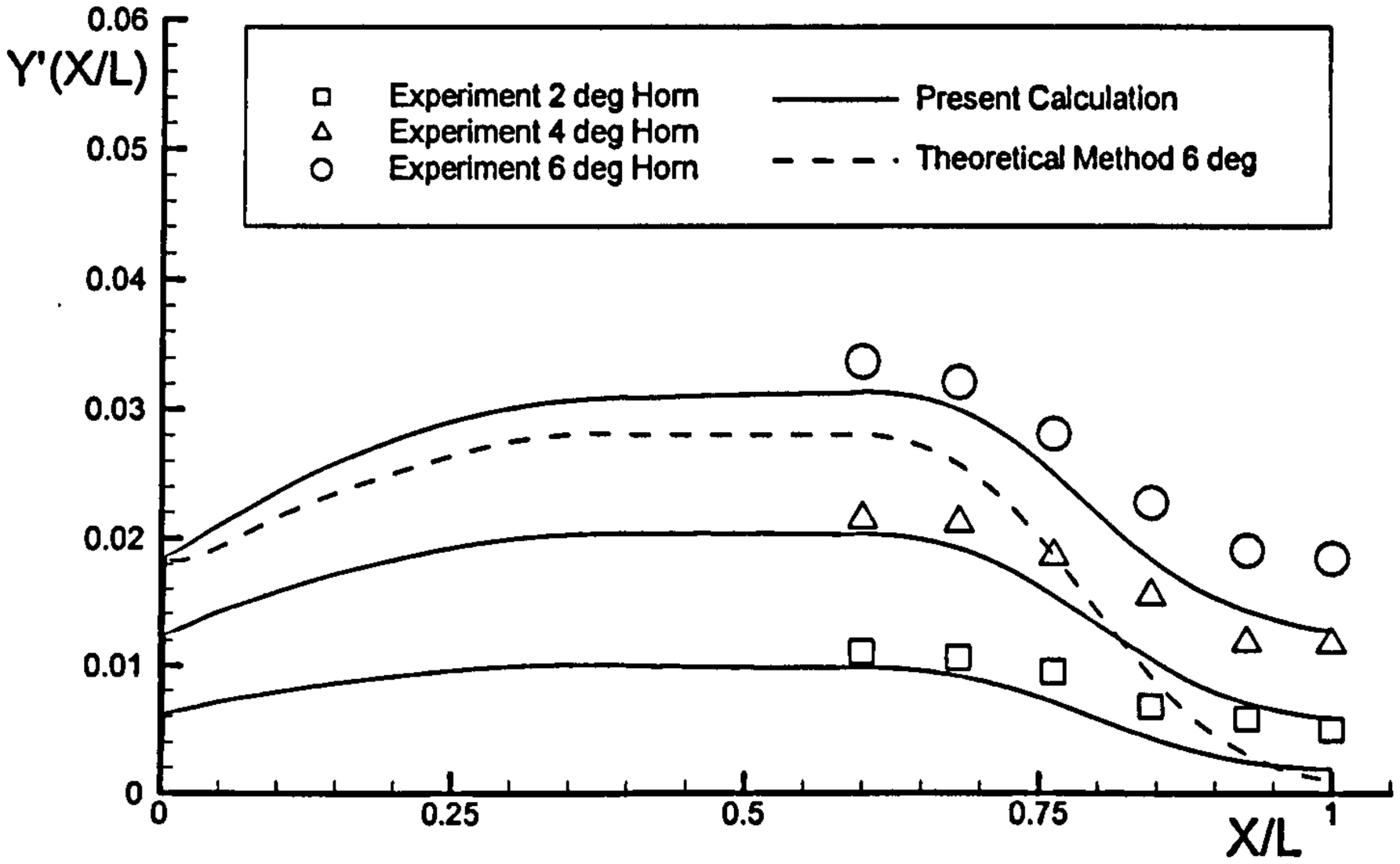

Figure 8.20: Distribution of side force coefficient for the British Bombardier with a pram stern.

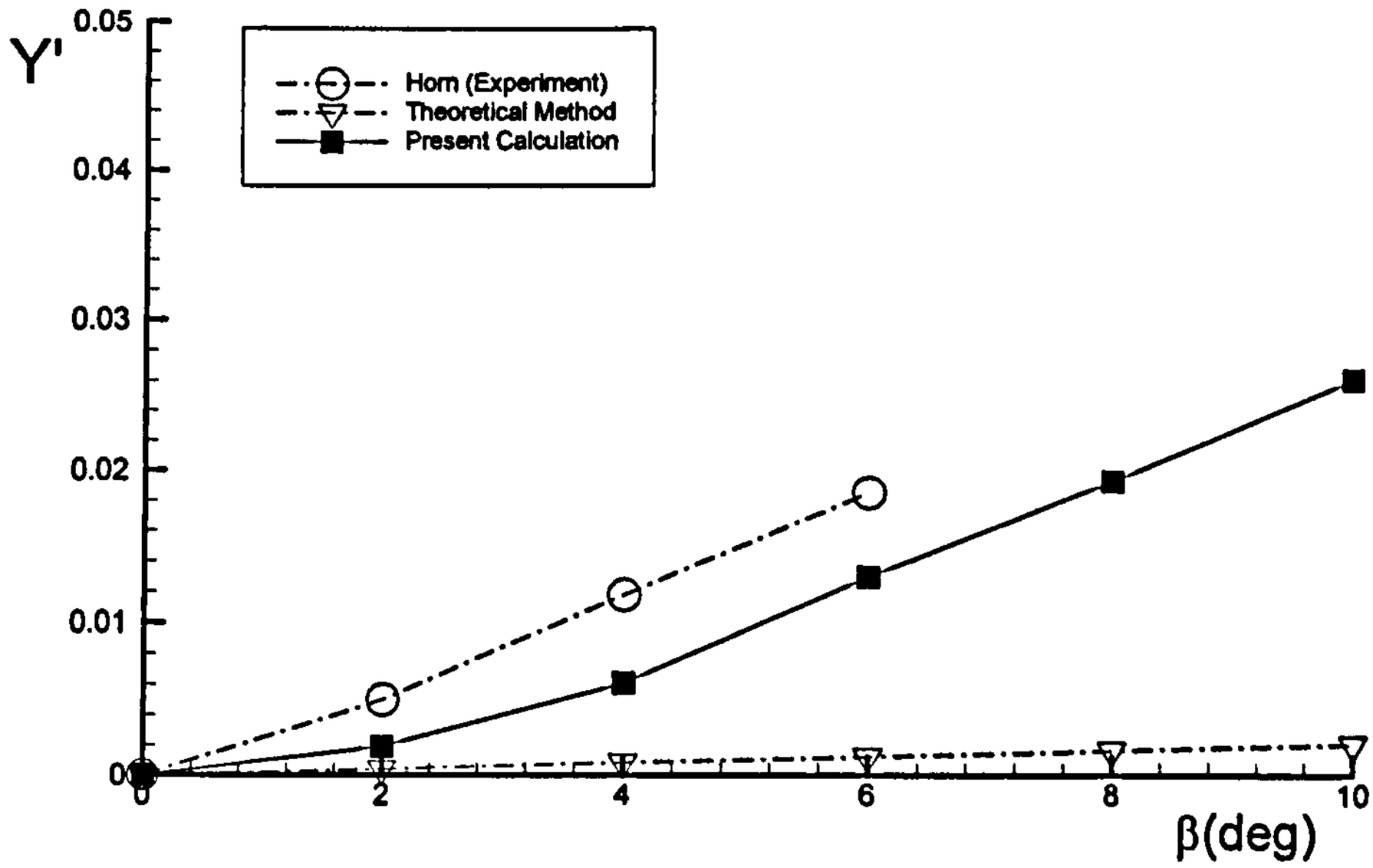

Figure 8.21: Side force coefficient for the British Bombardier with a pram stern in drift motion.

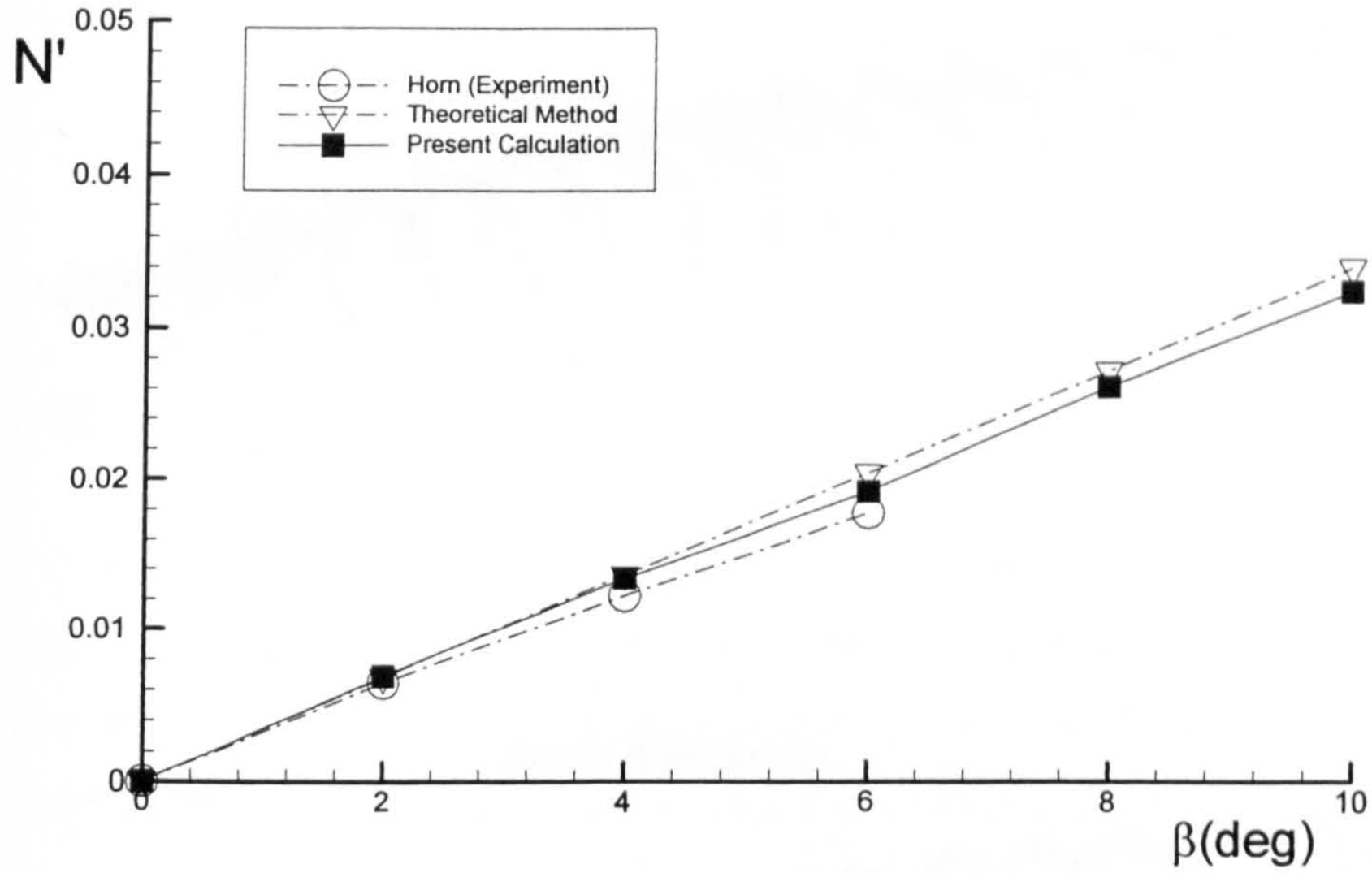

Figure 8.22: Yaw moment coefficient for the British Bombardier with a pram stern in drift motion.

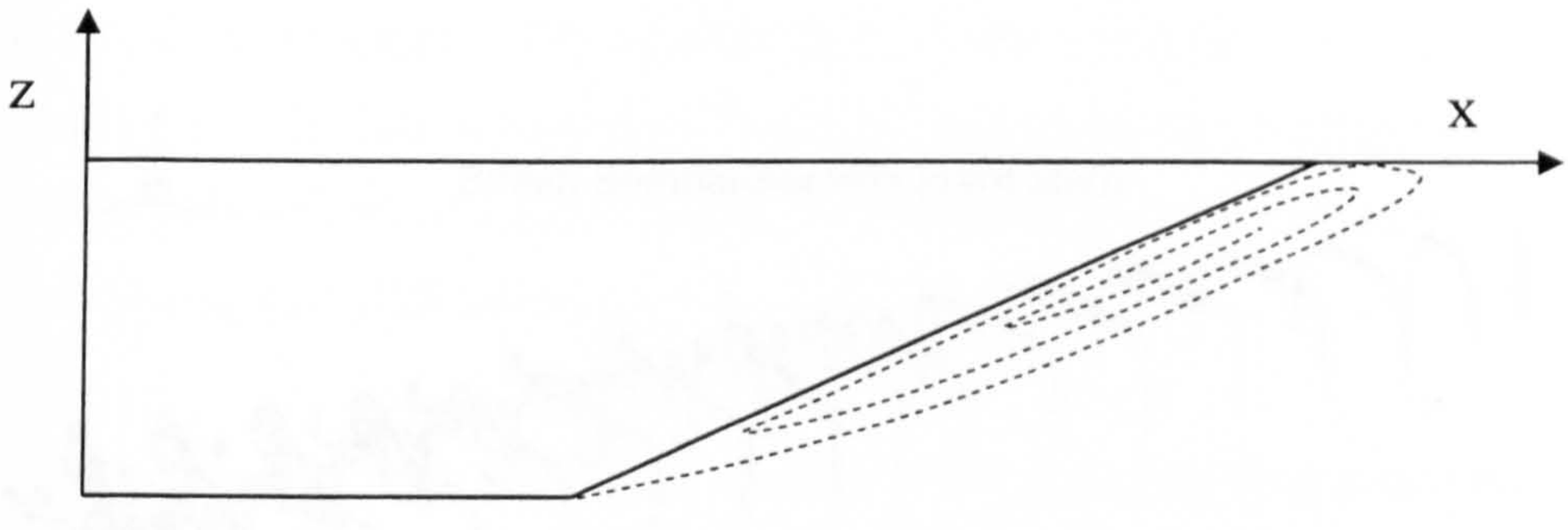

Figure 8.23: The side view of flow separation due to up-swept flow along a hull with a pram stern.

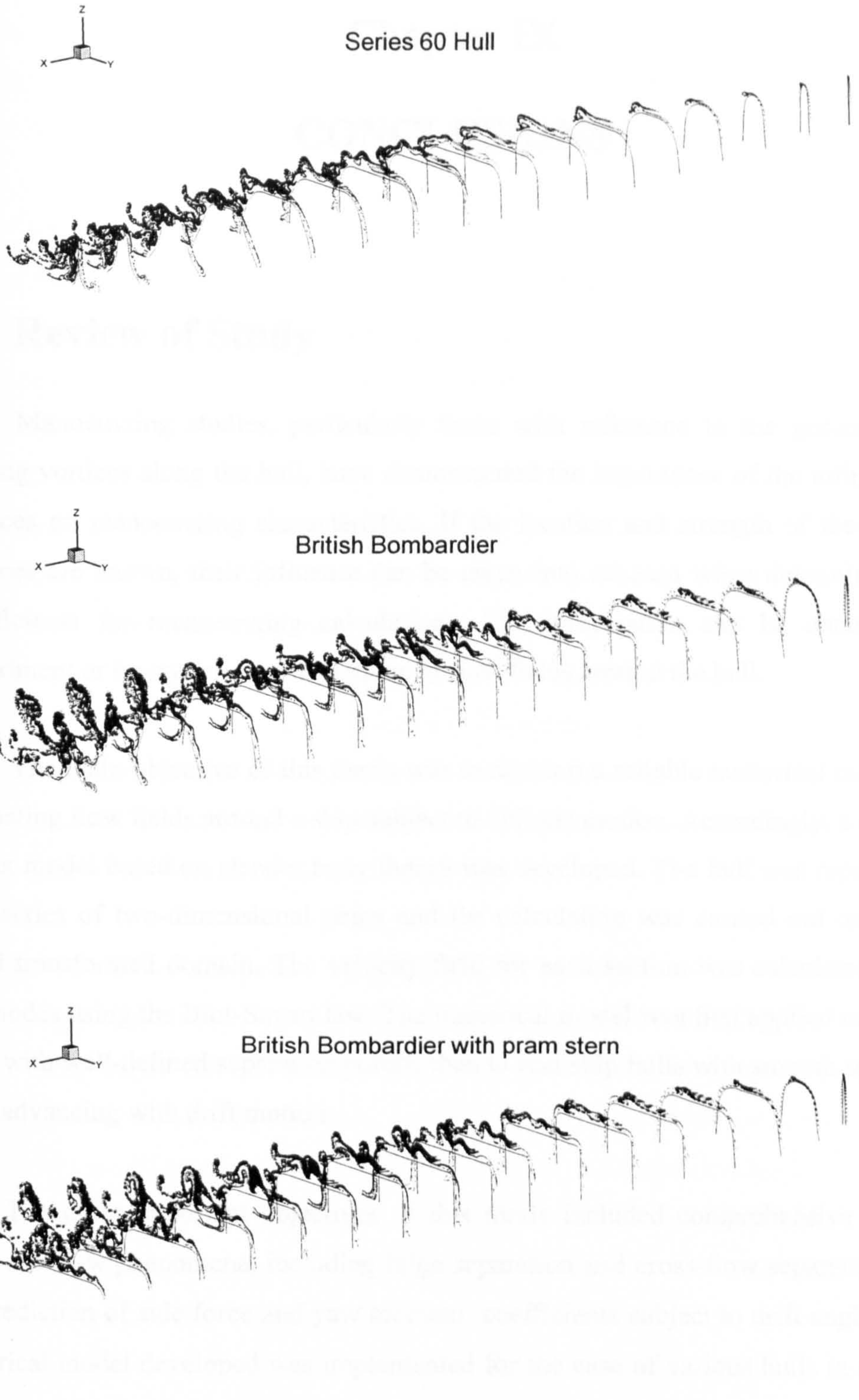

Figure 8.24: Comparison of the vortex flow for three ship hulls due to ten degrees of drift motion.

Chapter IX

CONCLUSIONS

9.1 Review of Study

Manoeuvring studies, particularly those with reference to the generation of trailing vortices along the hull, have demonstrated the importance of the influence of vortices on manoeuvring characteristics. If the location and strength of the trailing vortices are known, their influence can be taken into account when determining the coefficients for manoeuvring calculations. The information can be obtained by experiment or by numerical calculations of flow fields around the hull.

The main objective of this thesis was to develop a reliable numerical model for estimating flow fields around a ship subject to oblique motion. Accordingly, a discrete vortex model based on slender body theory was developed. The hull was represented as a series of two-dimensional strips and the calculation was carried out on a grid based transformed domain. The velocity field for each section was calculated at the grid nodes using the Biot-Savart law. The numerical model was first applied to simple hulls with well-defined separation points, then to real ship hulls with smooth sectional hulls advancing with drift motion.

The other important objectives of this thesis included comprehensive studies about the flow phenomena, including bilge separation and cross-flow separation, and the prediction of side force and yaw moment coefficients subject to drift angles. The numerical model developed was implemented for the case of various hulls in oblique motion.

In the case of the simple hulls, such as the flat plate, the Wigley hull and the Block hull, flow separation was assumed to occur only at well-defined separation points and single vortices were introduced into the flow to satisfy the Kutta conditions at the separation points.

The flow patterns produced by the present model showed a good representation of the natural behaviour of the vortex flow expected from all three simple hulls. The lateral force and yaw moment coefficients obtained by the model were in good agreement with those obtained by experiment and those obtained by other numerical methods.

Comparisons between a flat plate and the Wigley hull confirmed that the curvature of the Wigley hull influences the formation of the keel vortices and changes the related forces. The calculations applied to the block hull proved to be very useful in gaining an insight into the primary mechanisms associated with the generation and development of bilge vortices along the hull. Comparison with the RANS method also demonstrated that the present vortex method, which uses considerably less computing resources and runs more quickly than the RANS method, was a useful approach for practical applications to ship manoeuvring problems.

In the case of the general ship hulls, such as a Series 60 hull and the British Bombardier, with a conventional and also a pram stern, some modification was made to the numerical model. The transformation was generalised to represent the complex general hull forms and multi-vortex method was used to overcome the difficulties related to smooth surfaces of the real ship hulls. A continuous layer of discrete vortices was introduced around the section to satisfy a no-slip condition on the sectional hull surface. To the authors knowledge, this has not been done before.

Attached flow calculations of the side force and yaw moments for such hulls have been shown to disagree significantly with experimental results. The inclusion of the contribution of the trailing vortices as computed by the present method was seen to virtually remove such discrepancies over most of the hull.

The present model gave very good results for the side force and yaw moment for the British Bombardier. There were still some differences between the computed and experimental results in the case of the British Bombardier with a pram stern and the Series 60 hull, although the present model still produced good results that were closer to experiment than those of other numerical methods, where they are available. The approach represents a significant advance on the attached flow method of calculation.

The exact reasons for the differences where they did occur were not easy to establish because of the lack of detail in the experimental results. They may be explained to some extent by the difficulties in modelling the rapid and extreme changes in geometry occurring at the stern part of the ship. In the case of the British Bombardier with the pram stern, it may be hypothesised that the main reason for the differences at the stern region is due to flow separation arising from the up-swept flow over that region.

The calculation demonstrated that vortex and velocity fields on real ships are more complicated than for simple hulls, showing combined flow fields of both keel and bilge vortices. In the case of the Series 60 hull, the flow fields were dominated by keel vortices. Relatively strong bilge vortices were also noticed in the case of the British Bombardier, but when fitted with a pram stern the shrinking depth of the sections at the stern changed the wake flow significantly.

The numerical study about the six ship hulls demonstrated that the discrete vortex model can be used to predict the trailing vortices around various hull shapes, including the hull with a pram stern, with reliable accuracy. It also showed that the side forces and yaw moments computed in this way can provide very useful information on the assessment of ship manoeuvrability for practical purposes at the early design stage.

A comprehensive comparison of the flow fields around all six ship hulls computed for present studies are presented together for various hull sections in Appendix B.

9.2 Suggestions for Future Work

Although the present method has been proved to be a useful method in the calculation of flow fields for a hull with drift motion, there are a number of ways in which the present method can be further refined. The numerical model has been developed with future works in mind.

At present the model neglects the diffusion terms in the Navier-Stokes equations assuming the Reynolds number is high enough. For a more complete description of real flows, the diffusion terms could be included. There are two different ways of introducing the diffusion terms in the present discrete vortex method. The Random walk method is the simpler and it can be easily incorporated in the method. A finite difference scheme is more rigorous and is the favoured method but it is more complicated to implement. Difference formulae for the diffusion terms should be preferably implemented on a rectangular grid for simplicity. The present vortex model is computed over transformed rectangular grids, so that a finite difference scheme can be adopted easily with relatively minor modifications.

Since full scale ships have high Reynolds numbers, it may be informative to investigate the influence of turbulence on the generation of trailing vortices, although initial calculations with CFX did not indicate it to be profound. Turbulent flow is a fully three-dimensional unsteady flow so that three-dimensional calculations may be necessary. Since the direct simulation of turbulent flow for a complete ship hull is not possible in the near future, turbulence models are commonly used to represent the phenomena. There are various turbulence models available. Even though it is not straightforward, most two dimensional turbulence models can be implemented in the

present vortex model, and can be computed over the transformed rectangular gridded domains, although some three dimensional aspects of turbulence will be excluded.

Another area that may be included in the model in the future is the free surface elevation. In the present calculation, the free surface was assumed to be flat and its motion was ignored. Since the hydrodynamic forces have some dependency on the free surface elevations, particularly for the high Froude number flow, the inclusion of the free surface effect could improve the present results, although available experimental evidence did not indicate a significant influence of the free surface on the trailing vortices in the cases considered.

Although the present study has only been concerned with hulls with drift motions, the model could be applied to other ship motions, such as roll, heave, pitch and yaw. These extra motions can be easily included in the present model by additional layers of source distributions on the hull surface. One of the interesting problems that could be tackled in the short term future is roll motion combined with drift motions.

In addition, the classical manoeuvring motion tests, such as full scale turning circle motions and zig-zag motions, can also be simulated by the present model with some modifications. The turning circle, which is a quasi-steady motion, can be easily modelled by combinations of sway and yaw motions together. The zig-zag motion is a fully unsteady motion in which it is necessary to consider time dependant modelling.

Finally, another possible application of the present method in the future may be the manoeuvring of a ship with a multi-body hull, such as a catamaran, moving with various motions. The representation of a ship with multi-body hull can be achieved by a refinement of the present transformations, or using overlapping grid systems.

9.3 Concluding Remarks

The numerical model developed during the study represents a significant advance in explaining and modelling the evolution of trailing vortices along a ship hull moving with a drift angle. The method does not include all the fine details of the flow at the extreme stern, but the flow predicted by it is sufficiently realistic to be used in the investigation of problems related to the manoeuvring characteristics of many hull types of interest. With some modifications, this method can be easily applied to ships with more complicated motions, such as ships with both rolling motions and with a drift angle.

The advantages of the method are that it is both computationally economic, and also flexible in its applications, in comparison to CFD techniques involving the solution of the Navier-Stokes equations, where possible, using approaches such as the Finite Volume method. The method is, by the nature of its output, better suited than most for understanding the physics of flow and its implications for design for manoeuvring.

Appendix A

Conformal Mapping for Given Hull Sections

The transverse hull section at a given location in the complex Z-plane, ($Z = y + iz$) can be mapped into a unit circle in the $S1$-plane, ($S1 = \eta + i\zeta$) by means of a Laurent series.

$$Z = (c_1 + id_1)S1 + \sum_{n=2}^{N}(c_n + id_n)S1^{(1-n)} \tag{A-1}$$

As the hull is modelled as a double body, the hull section is symmetric along the free surface, the y-axis, and the terms $d_n, n = 1,...,N.$, are zero. In addition, if the hull section is symmetric about the centre line, the z-axis, n is made up of even terms. Equation (A-1) can be reduced in the case of a hull section with symmety about both y and z-axis to

$$Z = \sum_{n=1}^{N} A_n S1^{(3-2n)} \tag{A-2}$$

where $A_1 = c_1$ and $A_n = c_{2n-2}$, $n = 2,....,N$. For symmetry in both the y –axis and the z-axis, it is only necessary to match a quarter of the double body hull section in the transformation and the remaining parts are determined by symmetry.

If it is assumed that a quarter of a double body hull section is defined by a number of points (y_p, z_p), $p = 1,2,...,P.$, then the real and imaginary parts of the p'th point can be written as

$$y_p = \sum_{n=1}^{n=N} A_n \cos\left[(3-2n)\theta_p\right]$$
$$z_p = \sum_{n=1}^{n=N} A_n \sin\left[(3-2n)\theta_p\right] \qquad \text{(A-3)}$$

where θ_p is the angle of p'th point on the unit circle in the S1-plane. This equation provides $2P$ equations to solve for the mapping coefficients A_n and the angles θ_p. To obtain an accurate solution, the number of mapping coefficients, N, should be less than the given sectional data points P (of order of $1/2P$ or $2/3P$).

These equations can be solved by an iterative least squares method in which the squared distance E between the given hull data points and the generated form is minimised. Initially, it is assumed that the angles θ_p are known and then the least square equations, which involve the minimisation of E, can be expressed as

$$y_p = \sum_{n=1}^{n=N} A_n \cos\left[(3-2n)\theta_p\right] + E_{1p}$$
$$z_p = \sum_{n=1}^{n=N} A_n \sin\left[(3-2n)\theta_p\right] + E_{2p} \qquad \text{(A-4)}$$

and

$$E = \sum_{p=1}^{P} \left(E_{1p}^2 + E_{2p}^2\right) \qquad \text{(A-5)}$$

The method gives N equations, given by

$$\frac{\partial E}{\partial A_m} = \sum_{p=1}^{P}\sum_{n=1}^{N} A_n \cos\left[2(m-n)\theta_p\right] - \sum_{p=1}^{N}\left\langle x_p \cos\left[(3-2m)\theta_p\right] + y_p \sin\left[(3-2m)\theta_p\right]\right\rangle = 0 \qquad m = 1,2,\ldots\ldots,N \qquad \text{(A-6)}$$

These equations are linear in the A_n coefficients and can be solved directly once the θ_p terms are known. In addition, if it is assumed that the A_n coefficients are known but the θ_p terms are yet to be determined, minimisation with respect to θ_p yields

$$\begin{aligned}\frac{\partial E}{\partial \theta_l} &= \sum_{n=1}^{N}\sum_{m=1}^{N} A_n A_m (3-2m)\sin[2(n-m)\theta_l] \\ &\quad -\sum_{m=1}^{N} A_m (3-2m)\langle x_l \sin[(3-2m)\theta_l] - y_l \cos[(3-2m)\theta_l]\rangle \\ &= 0 \qquad\qquad l = 1,2,\ldots\ldots,P\end{aligned} \tag{A-7}$$

These equations are non-linear so that the θ_p cannot be determined straightforwardly. They can be solved by an appropriate numerical technique such as the Newton-Raphson method or by a simpler approach in which each of the P equations are solved separately for the θ_p using standard techniques such as inverse interpolation.

For the iteration procedure, it is necessary to start with an initial guess. The first approximation for A_n is given by the well known Lewis form with three defined coefficients,

$$Z = A_1 S1 + \frac{A_2}{S1} + \frac{A_3}{S1^3} \tag{A-8}$$

and

$$\begin{aligned}A_1 &= \frac{1}{2}(b+T) - A_3 \\ A_2 &= \frac{1}{2}(b-T) \\ A_3 &= -\frac{1}{4}(b+T) + \frac{1}{4}\left[(b+T)^2 + 8\left(bT - \frac{2}{\pi}S_A\right)\right]^{1/2}\end{aligned} \tag{A-9}$$

where b is half the length of breadth B, T is a draft and S_A is an area of a given hull section. To avoid reentrant forms, the Lewis form should be restricted to the regions

$$\begin{aligned} &\frac{3\pi}{32}(2-\lambda) \le \sigma \le \frac{3\pi}{32}(3+\frac{\lambda}{4}) \quad for \quad \lambda \le 1 \\ &\frac{3\pi}{32}(2-\frac{1}{\lambda}) \le \sigma \le \frac{3\pi}{32}(3+\frac{1}{4\lambda}) \quad for \quad \lambda > 1 \end{aligned} \tag{A-10}$$

where $\lambda = b/T$ and σ is the section-area coefficient, $\sigma = S_A / 2bT$.

From a given set of A_n in equation (A-9), θ_p can be determined using equation (A-7) and then the four-term mapping coefficients can be found by solving equation (A-6) with the previously approximated θ_p. Retaining the four terms, iteration between (A-7) and (A-6) will be carried out until convergence has been obtained to the given error limit. This iteration procedure may be continued with an increasing number of mapping coefficients until the desired N-terms are reached.

After finding the mapping coefficients at selected sections, it is necessary to find the other coefficients for the sections between them. More computational sections in the present application are usually needed than those given by the body plan sections. These coefficients for the extra sections can be determined by a polynomial representation of each coefficient in x, which is the lengthwise position along a given hull, and can be written as

$$A_n(x) = \sum_{m=1}^{M} A_{mn} x^{m-1} \tag{A-11}$$

where M-1 is the degree of the polynomial. The polynomial equations are fitted by the least squares method, a nine degree polynomial being used in the present method. The mapping coefficients $A_n(x)$ at any position x can be easily calculated using equation (A-11).

The first mapping coefficient A_1 coefficient in equation (A-2) operates as a scale factor. For example, if a hull section is a circular cylinder with radius *r*, the mapping terms A_n, $n = 2,....,N$, in equation (A-2) will be zero. The A_1 can only be used to fit the unit circle in the transformed *S*1-plane to a circular hull section with radius *r* in the *Z*-plane. Equation (A-2) can be expressed in a different form, which maps given hull sections to the circle with radius *r* at the same scale, and is given by.

$$Z = S1 + \sum_{n=1}^{N-1} a_n S1^{(1-2n)} \tag{A-12}$$

where a_n are the mapping coefficients for transforming a hull section to the same scale circle with radius *r*. The relationship between A_n in equation (A-2) and a_n in equation (A-12) may be written as

$$a_n = A_{n+1} / A_1^{1-2n} \tag{A-13}$$

Appendix B

Comparison of Flow Fields around the Six Ship Hulls

Comparisons of vortex and velocity fields around the six ship hulls, a flat plate hull, the Wigley hull, the block hull, the Series 60 $C_B = 0.6$, the British Bombardier and the British Bombardier with a pram stern, are presented at various sections due to five and ten degrees of drift motion. The principal particulars of the ships are listed in Table B.1.

Ship	Breadth(B/L)	Draft(T/L)
Flat Plate	0.0000	0.0625
Wigley Hull	0.1000	0.0625
Block Hull	0.1500	0.0500
Series 60 $C_B = 0.6$	0.1334	0.0533
British Bombardier	0.1339	0.0567
British Bombardier with a pram stern	0.1339	0.0567

Table B.1: Principal particulars of the six ships.

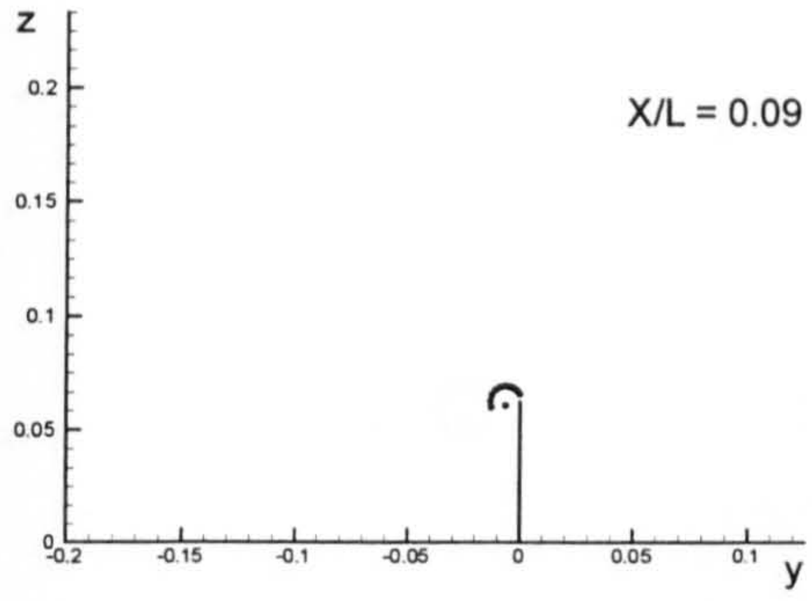

(Flat Plate)

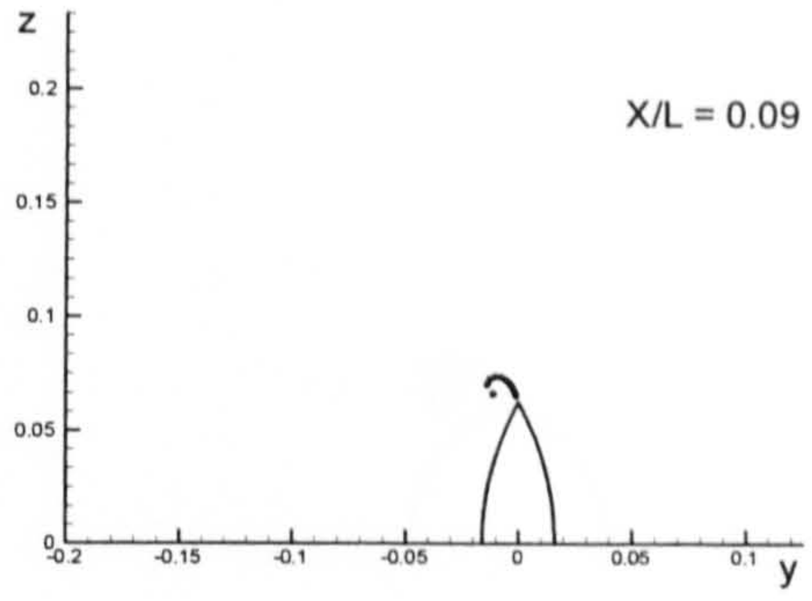

(Wigley Hull)

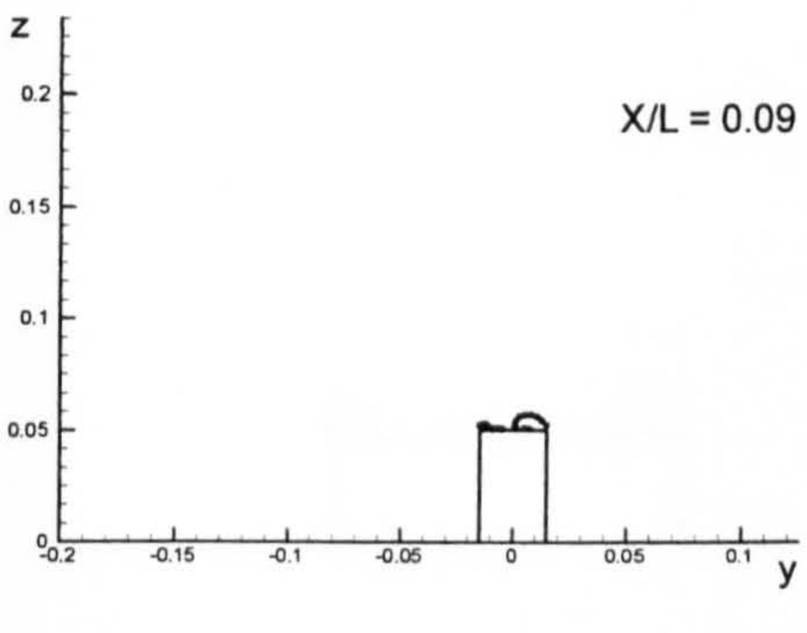

(Block Hull)

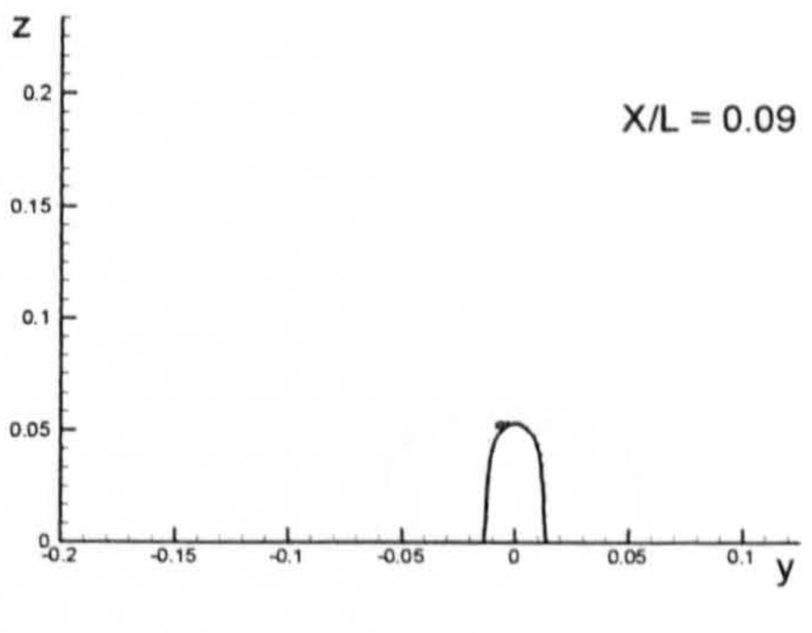

(Series 60 Hull)

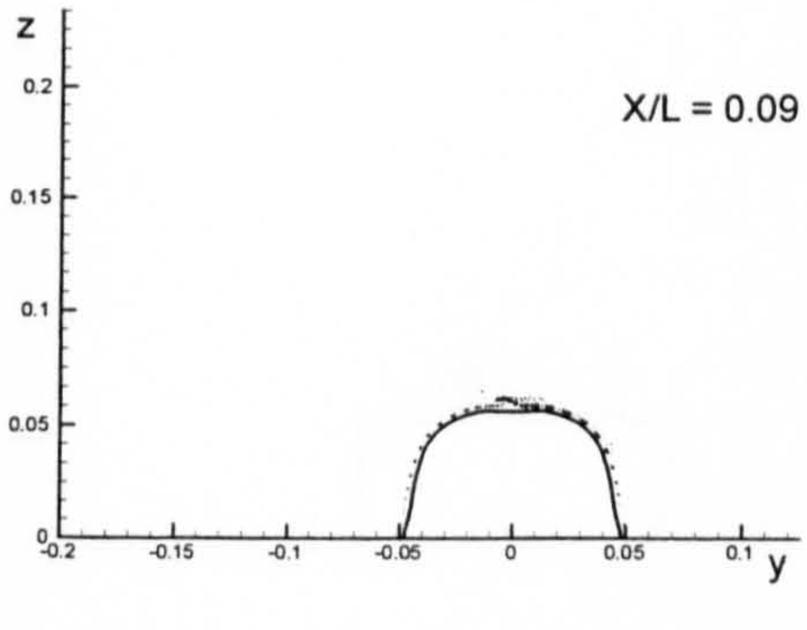

(British Bombardier)

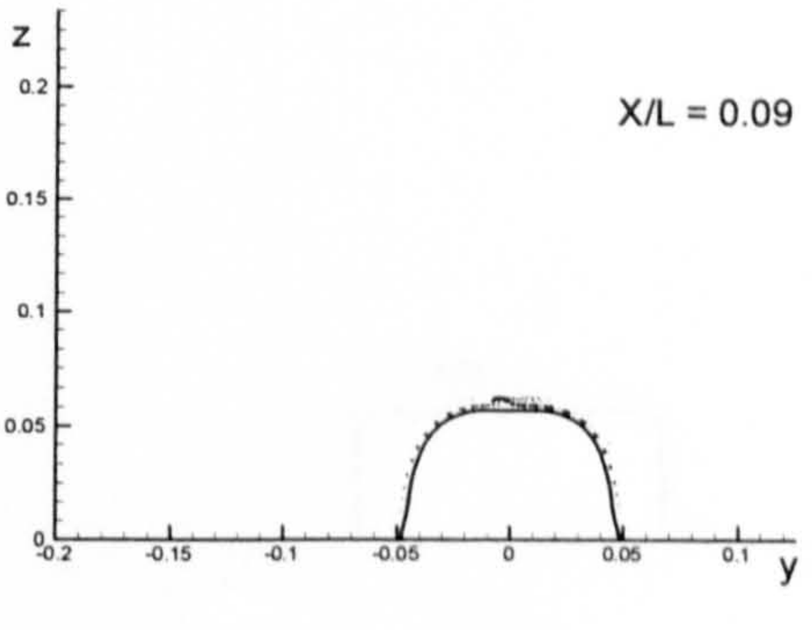

(British Bombardier with a pram stern)

Figure B.7: Comparison of vortex fields for the six ship hulls at $X/L = 0.09$ due to 5 degrees of drift motion.

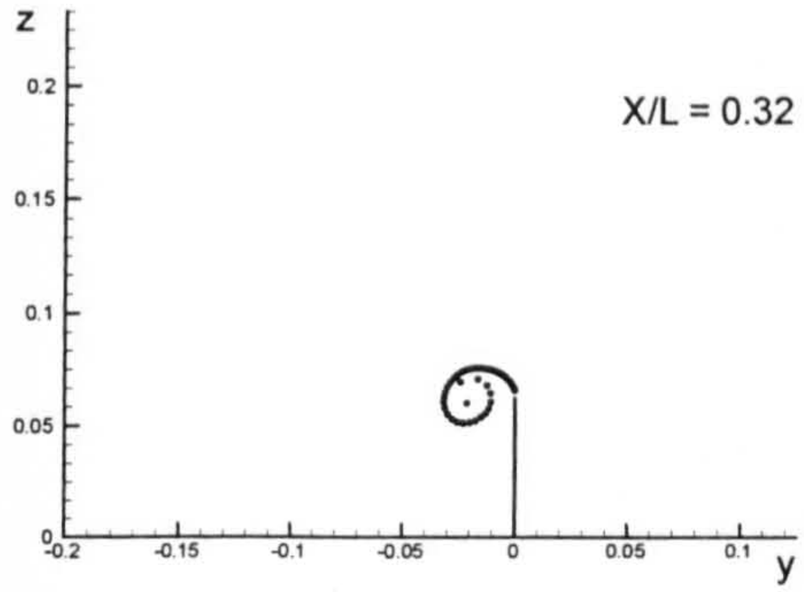

(Flat Plate)

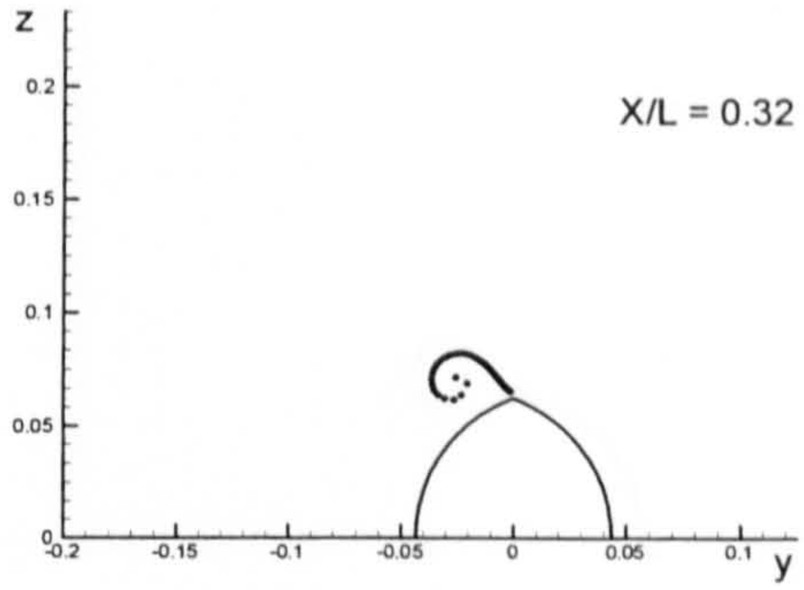

(Wigley Hull)

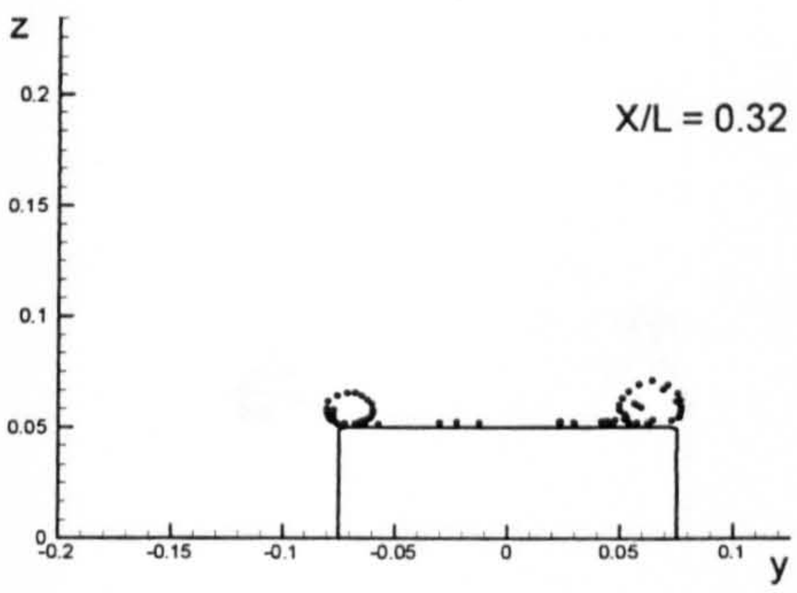

(Block Hull)

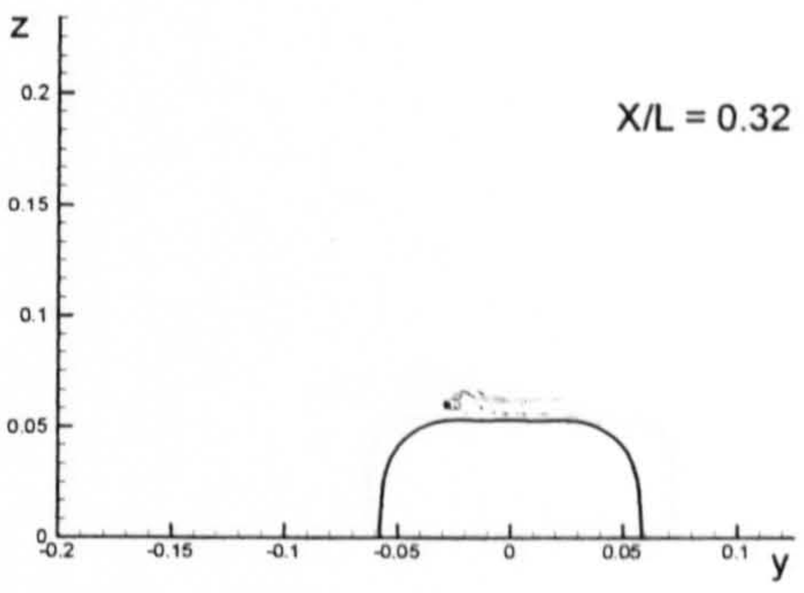

(Series 60 Hull)

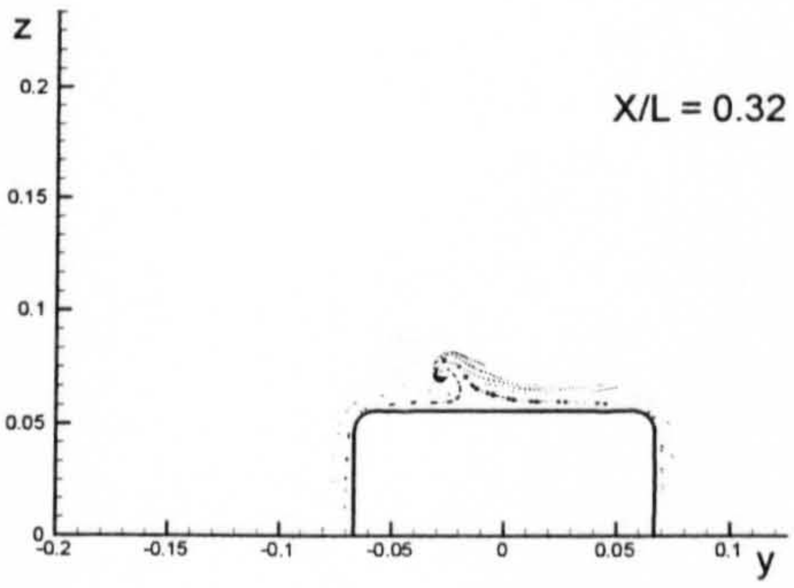

(British Bombardier)

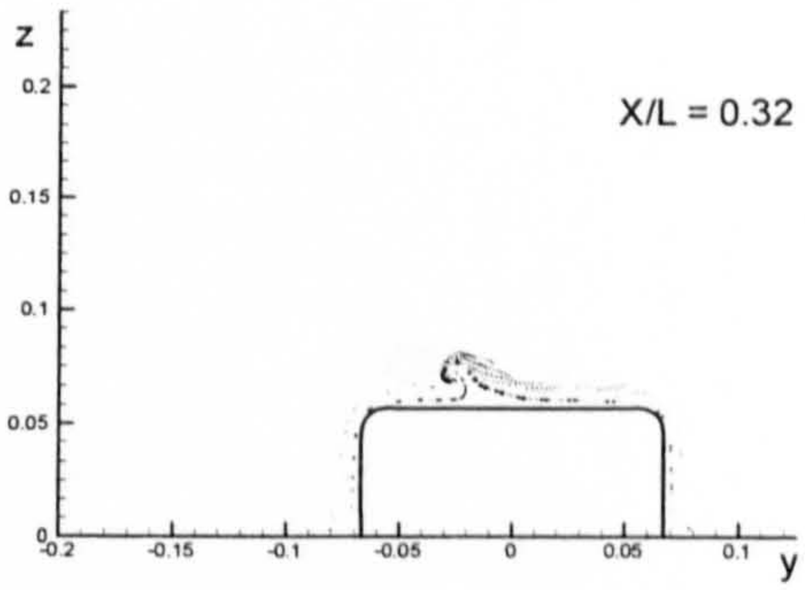

(British Bombardier with a pram stern)

Figure B.7: Comparison of vortex fields for the six ship hulls at $X/L = 0.32$ due to 5 degrees of drift motion.

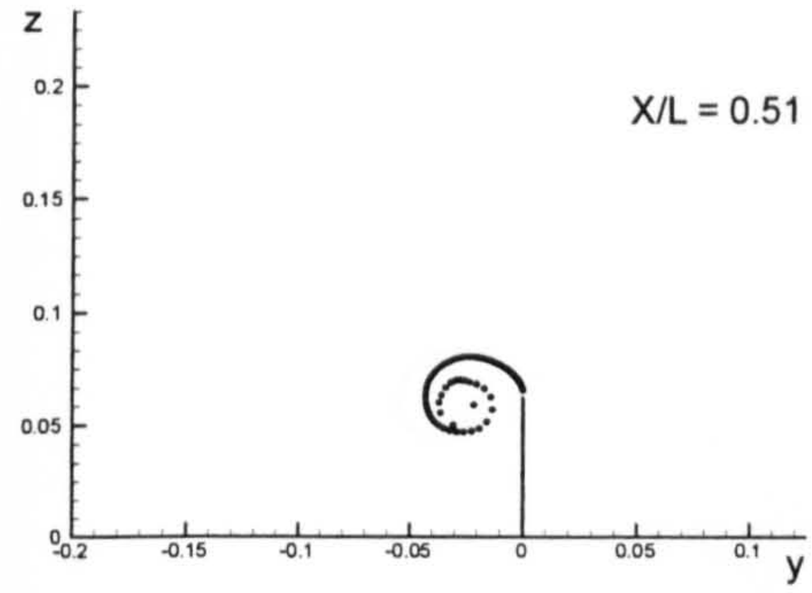

(Flat Plate)

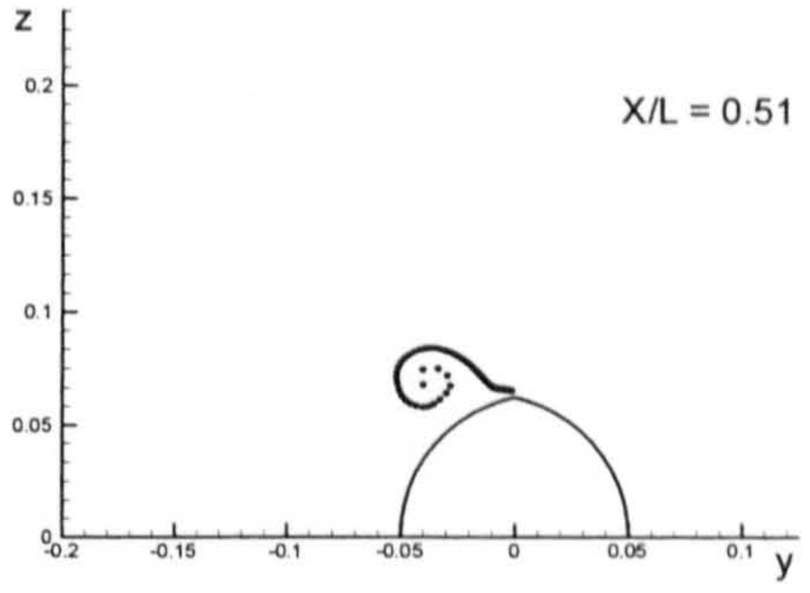

(Wigley Hull)

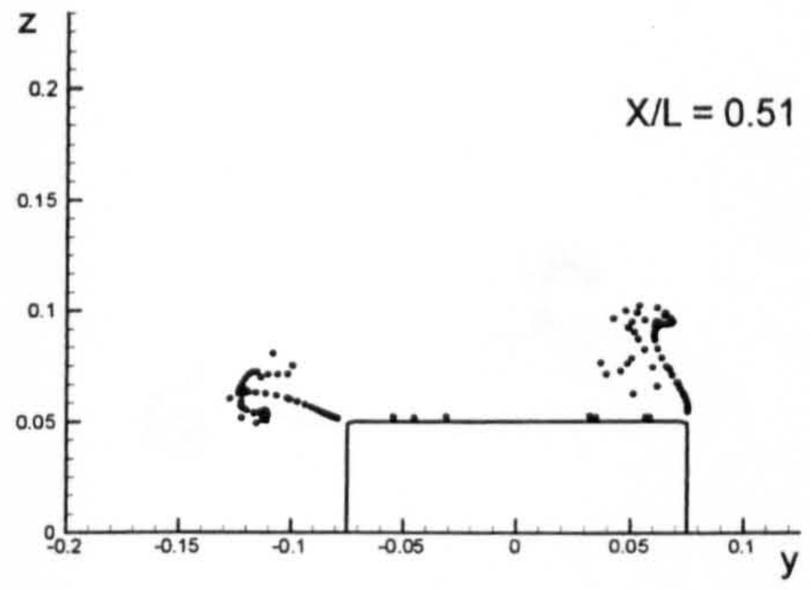

(Block Hull)

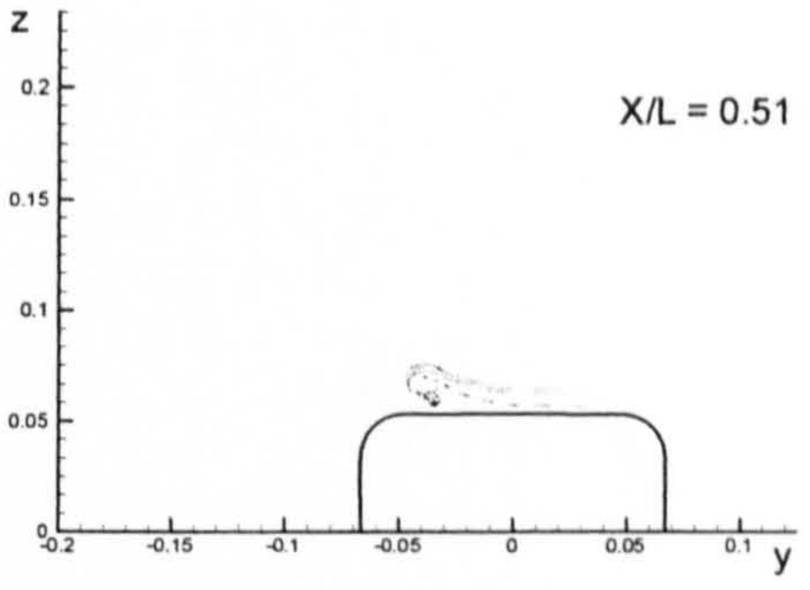

(Series 60 Hull)

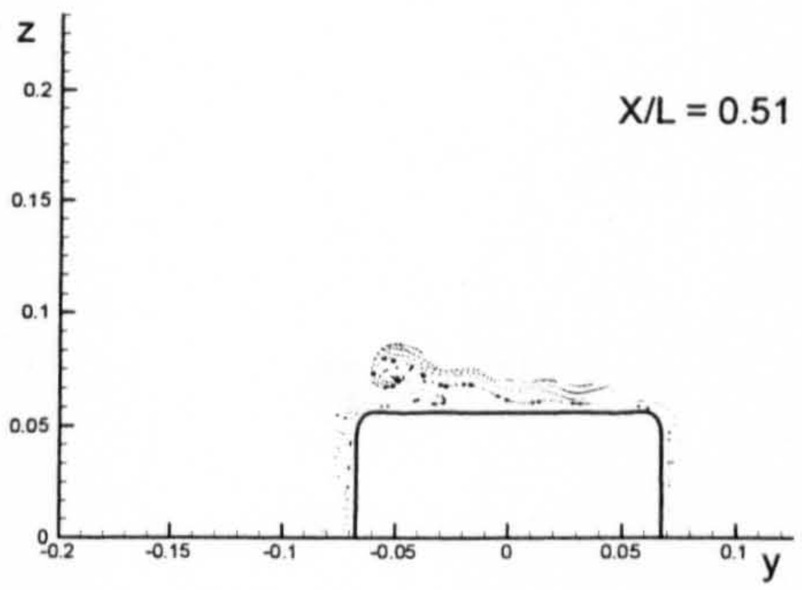

(British Bombardier)

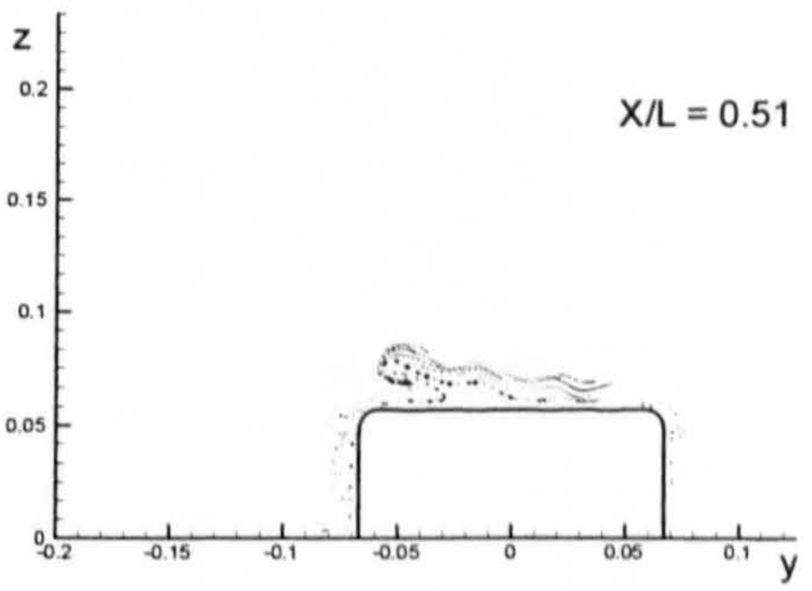

(British Bombardier with a pram stern)

Figure B.7: Comparison of vortex fields for the six ship hulls at $X/L = 0.51$ due to 5 degrees of drift motion.

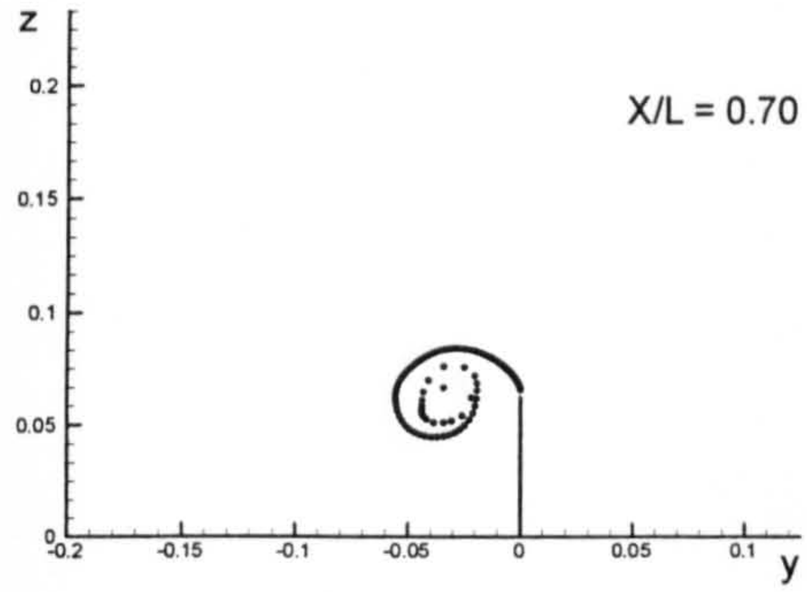

(Flat Plate)

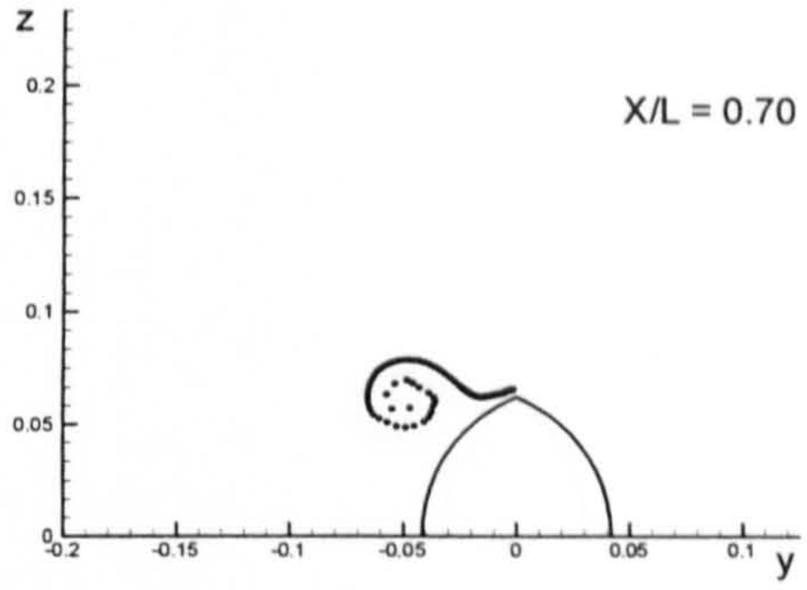

(Wigley Hull)

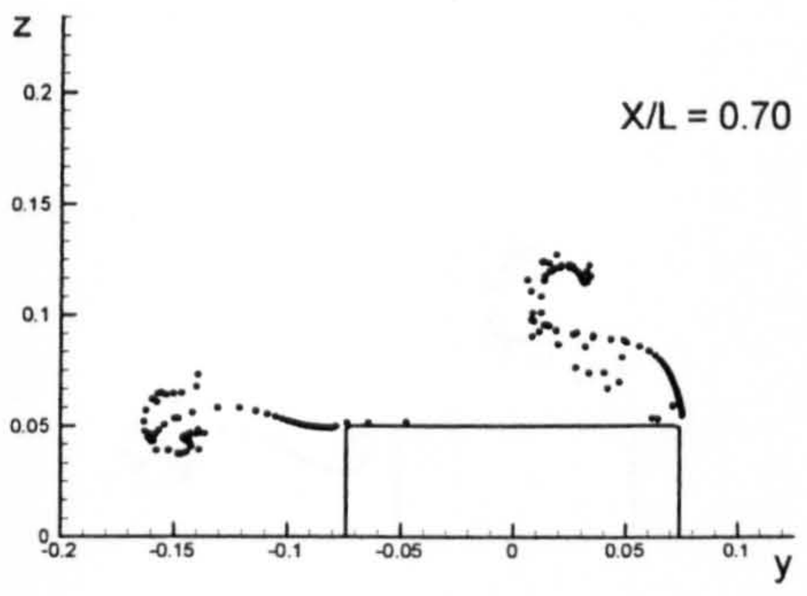

(Block Hull)

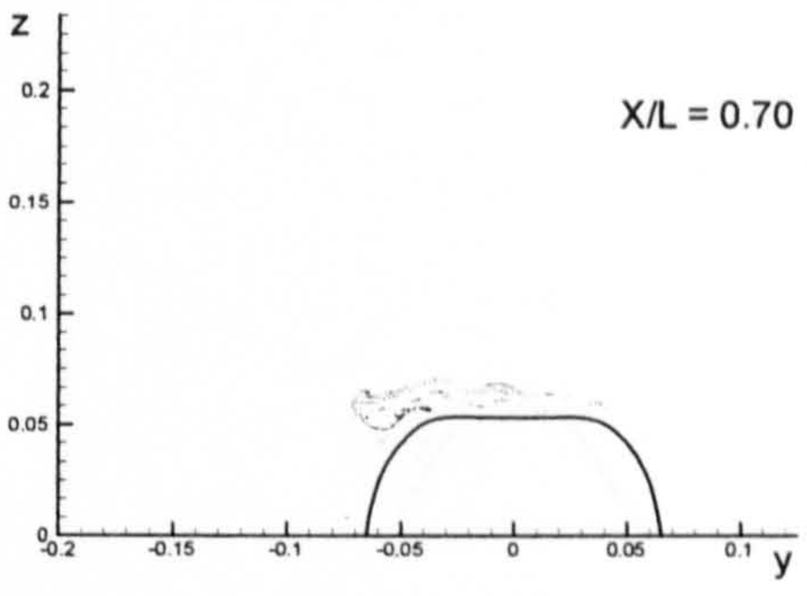

(Series 60 Hull)

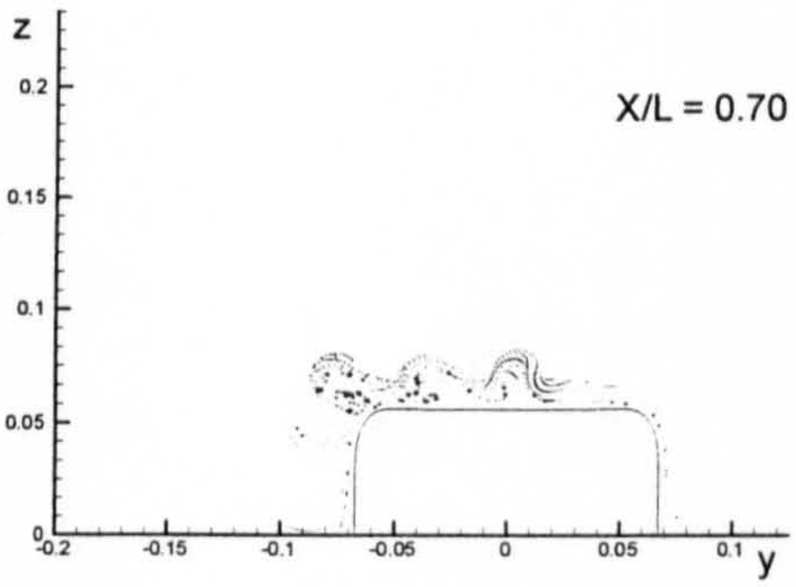

(British Bombardier)

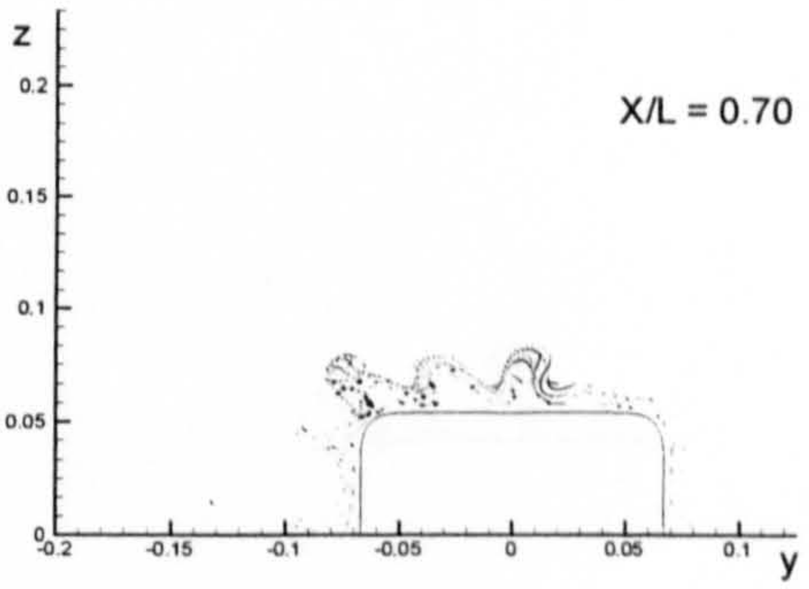

(British Bombardier with a pram stern)

Figure B.7: Comparison of vortex fields for the six ship hulls at $X/L = 0.70$ due to 5 degrees of drift motion.

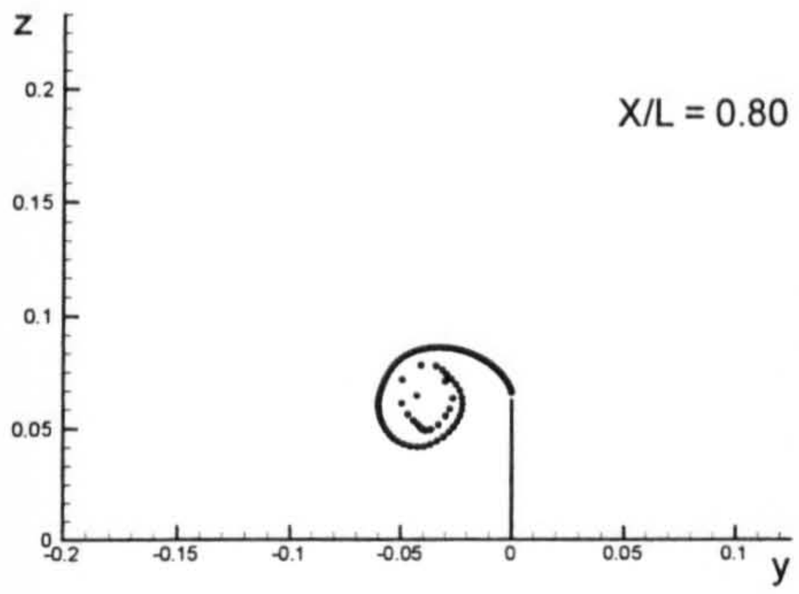

(Flat Plate)

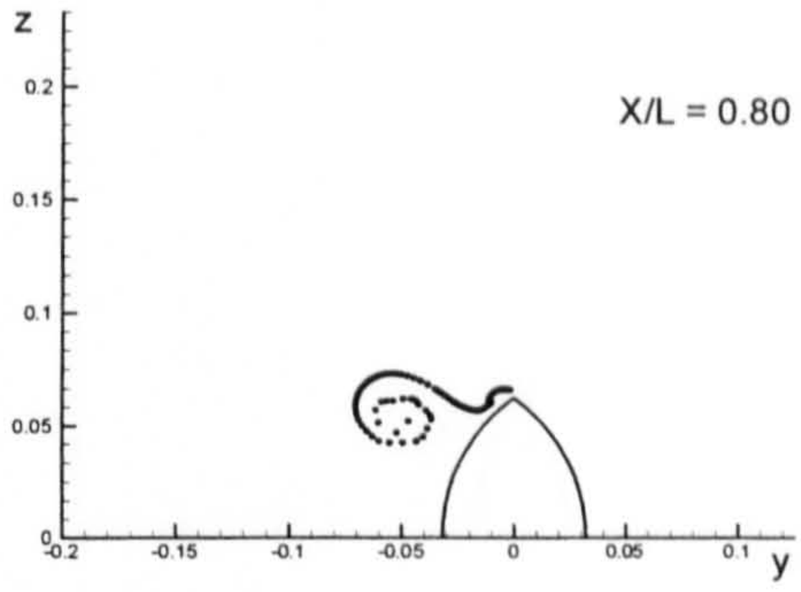

(Wigley Hull)

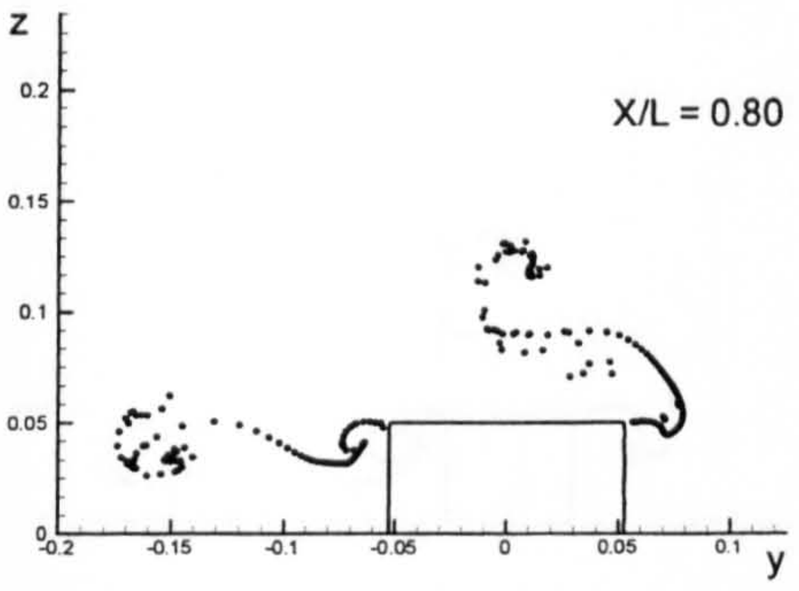

(Block Hull)

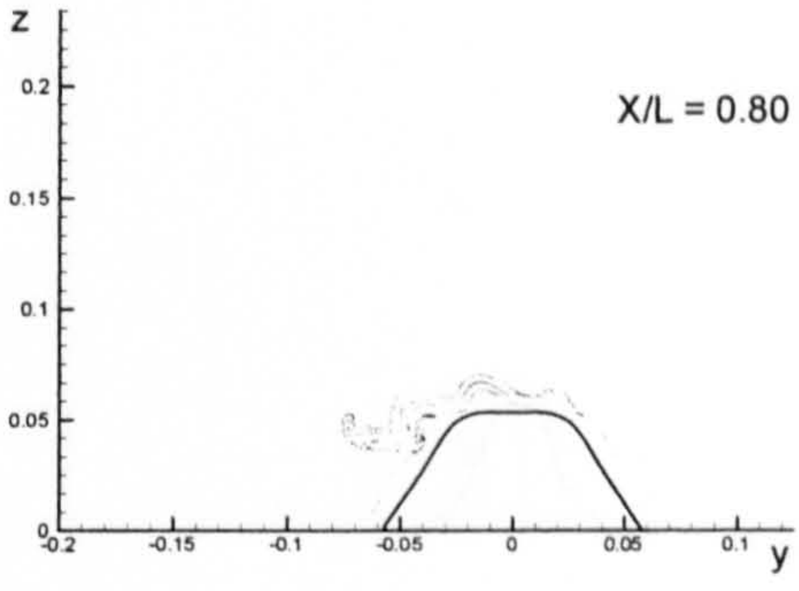

(Series 60 Hull)

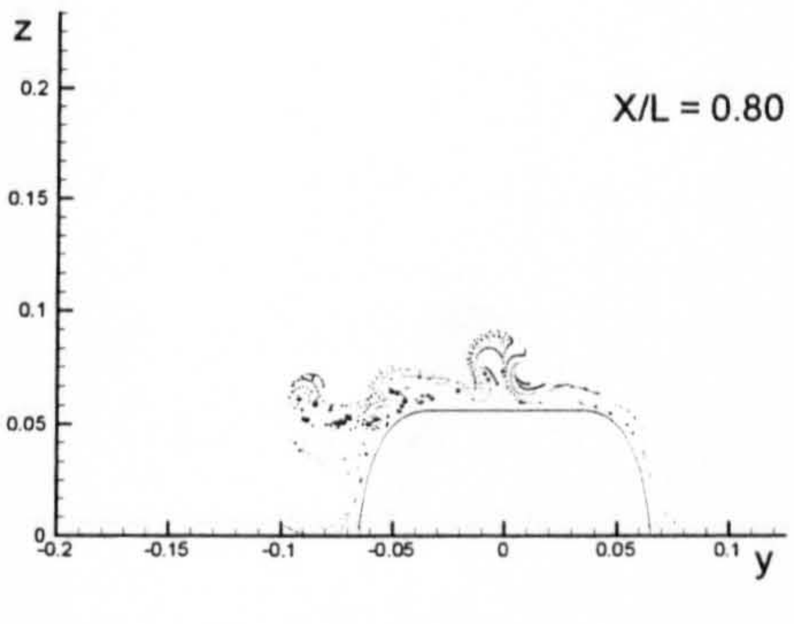

(British Bombardier)

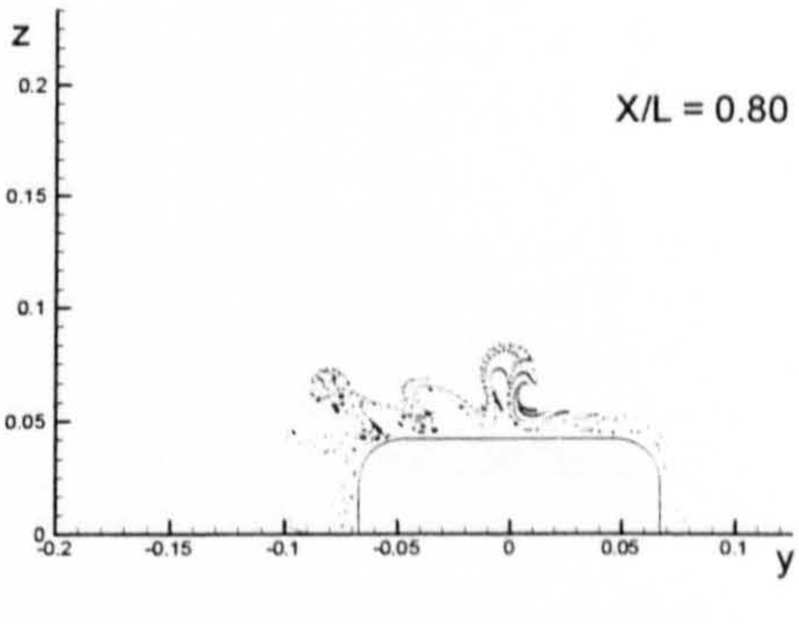

(British Bombardier with a pram stern)

Figure B.7: Comparison of vortex fields for the six ship hulls at $X/L = 0.80$ due to 5 degrees of drift motion.

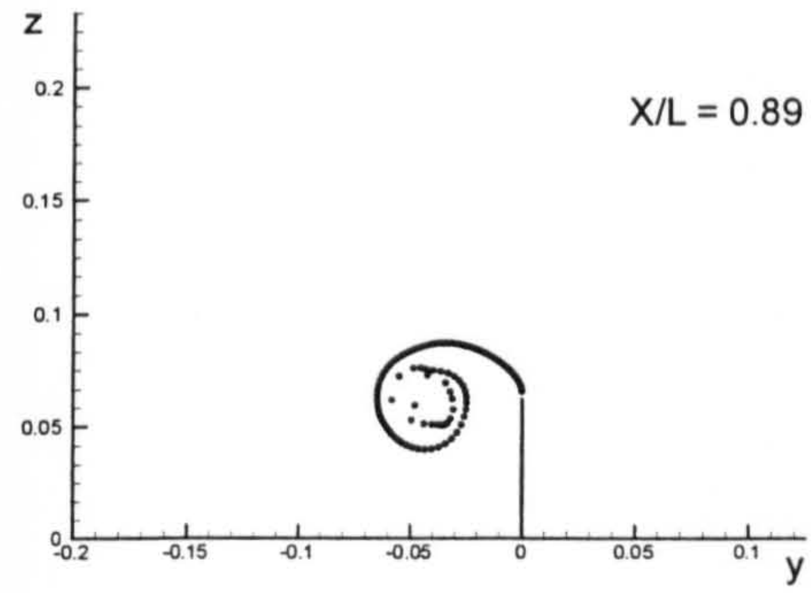

(Flat Plate)

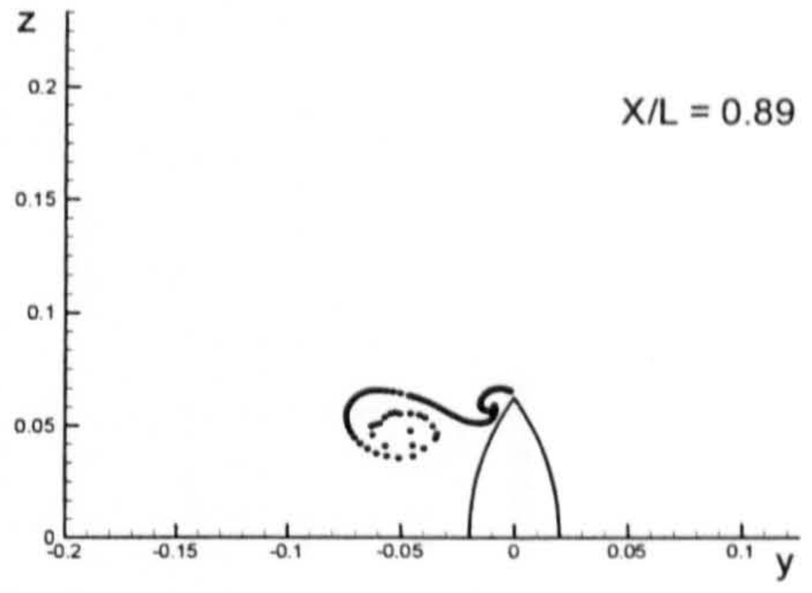

(Wigley Hull)

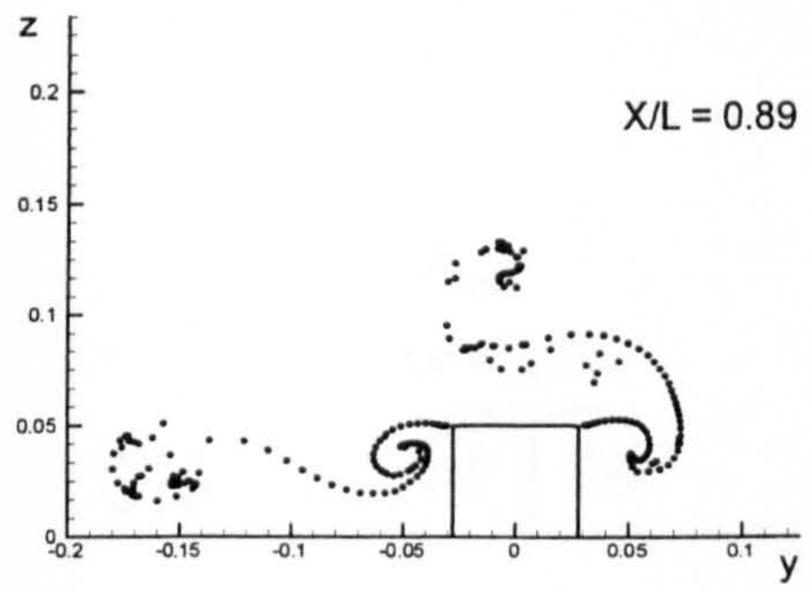

(Block Hull)

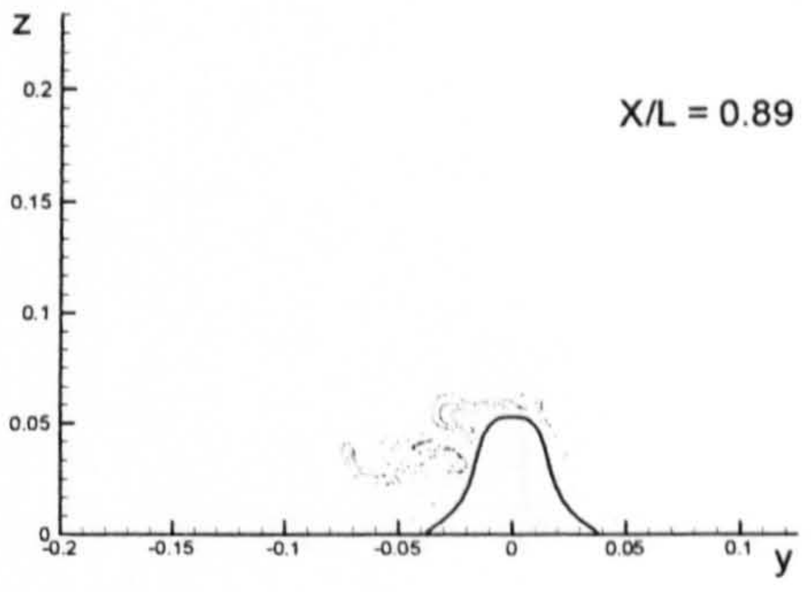

(Series 60 Hull)

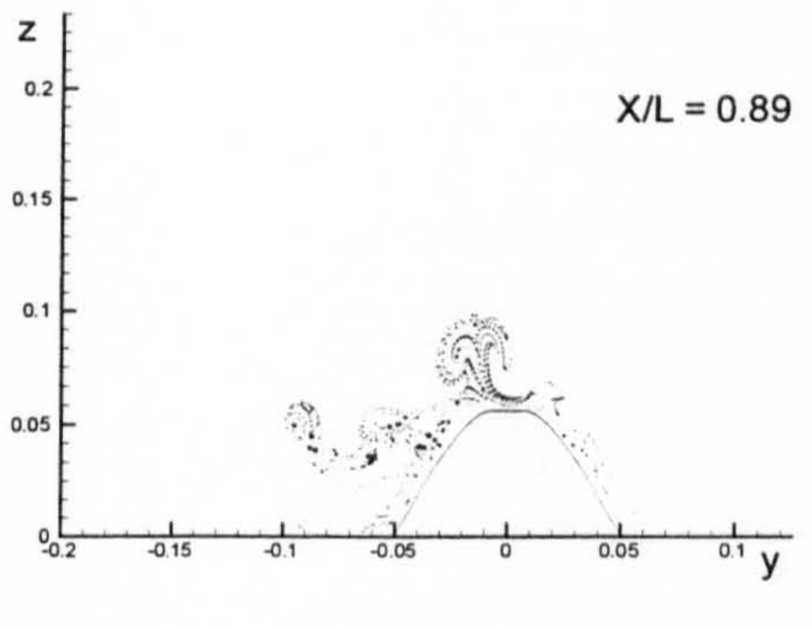

(British Bombardier)

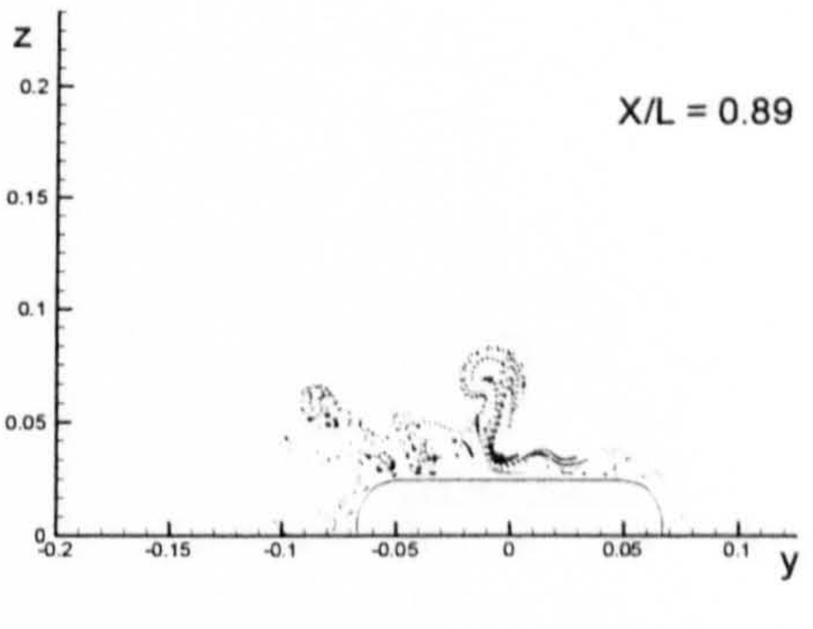

(British Bombardier with a pram stern)

Figure B.7: Comparison of vortex fields for the six ship hulls at $X/L = 0.89$ due to 5 degrees of drift motion.

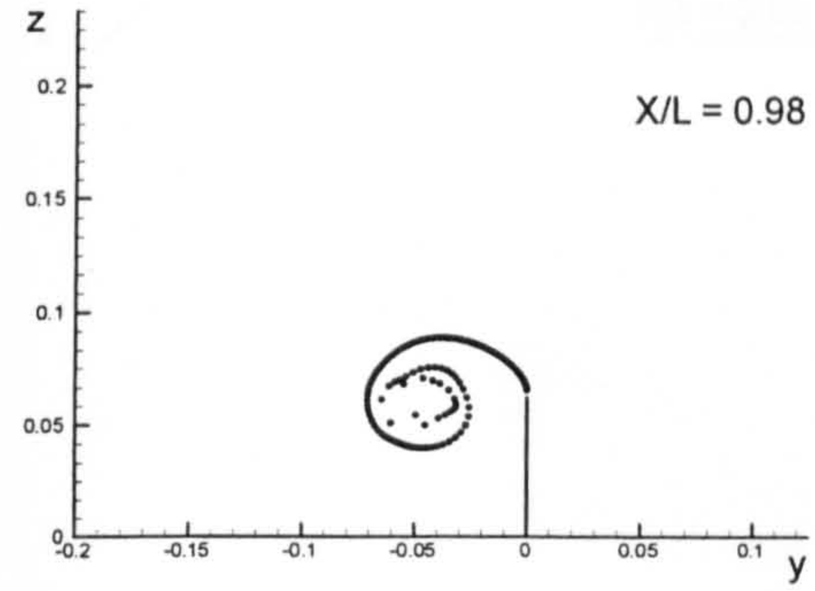

(Flat Plate)

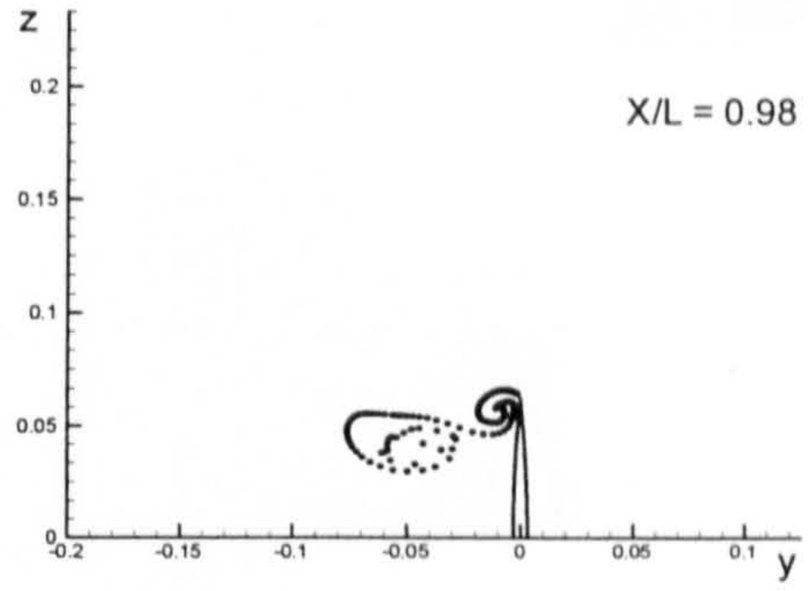

(Wigley Hull)

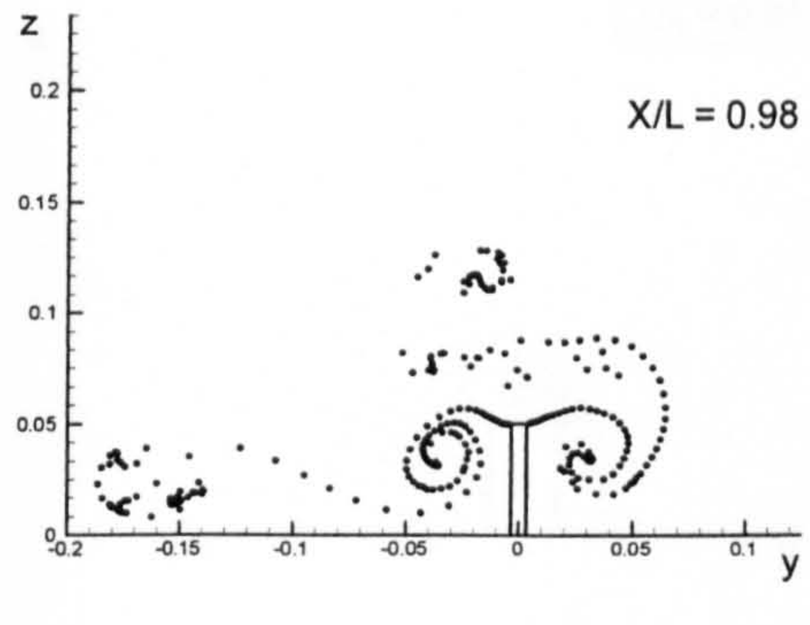

(Block Hull)

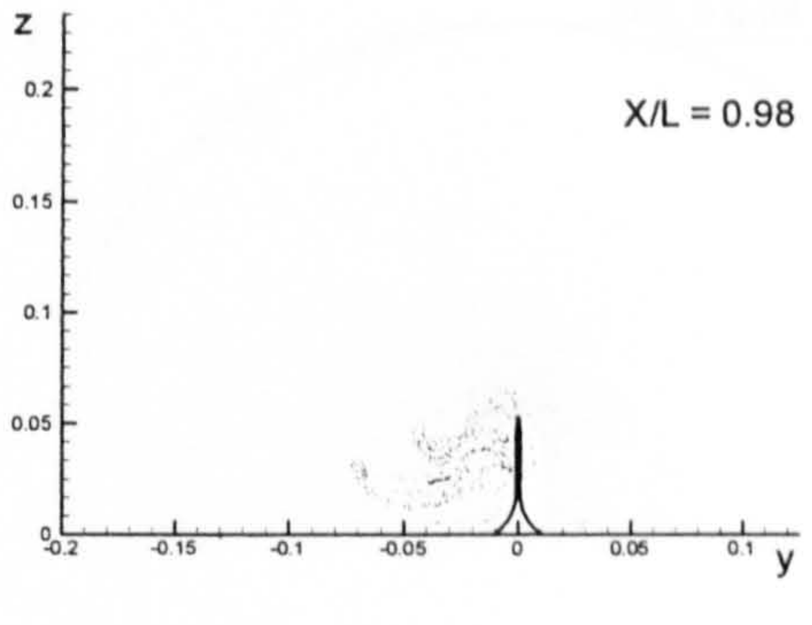

(Series 60 Hull)

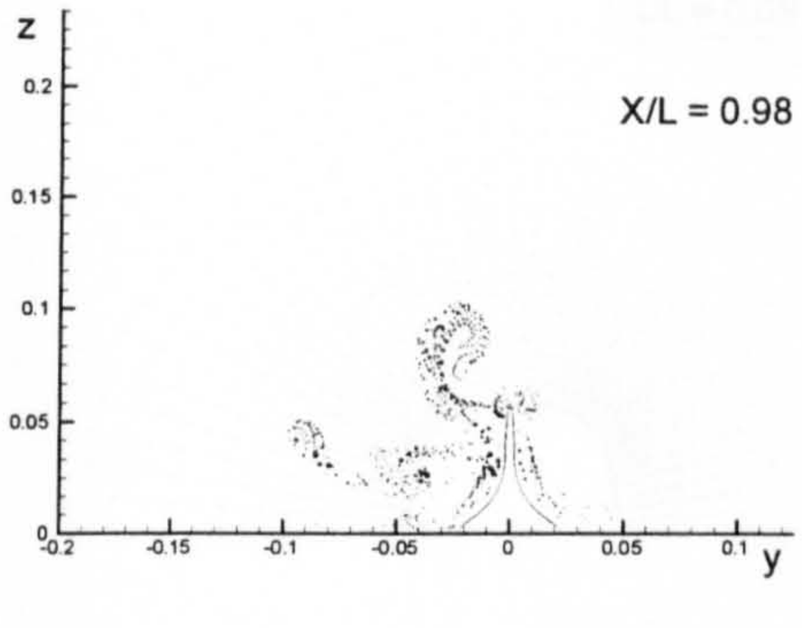

(British Bombardier)

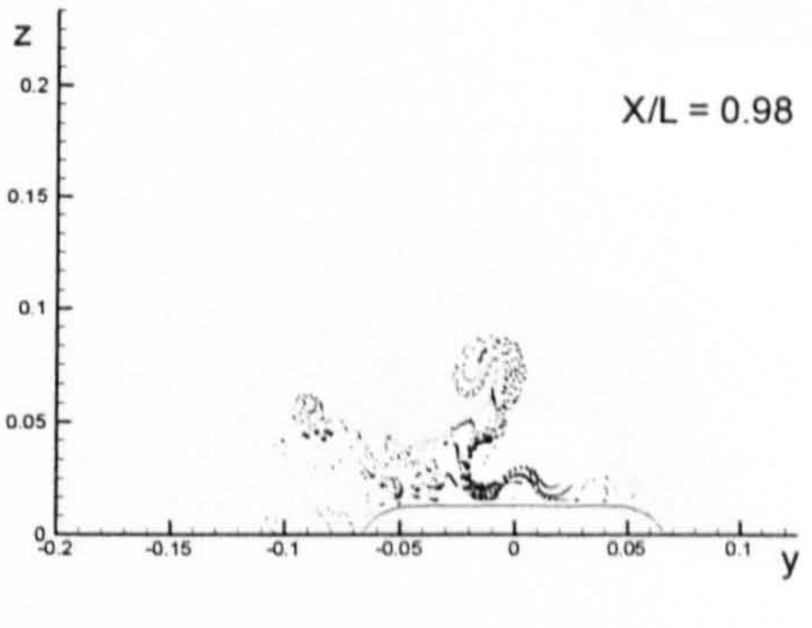

(British Bombardier with a pram stern)

Figure B.7: Comparison of vortex fields for the six ship hulls at $X/L = 0.98$ due to 5 degrees of drift motion.

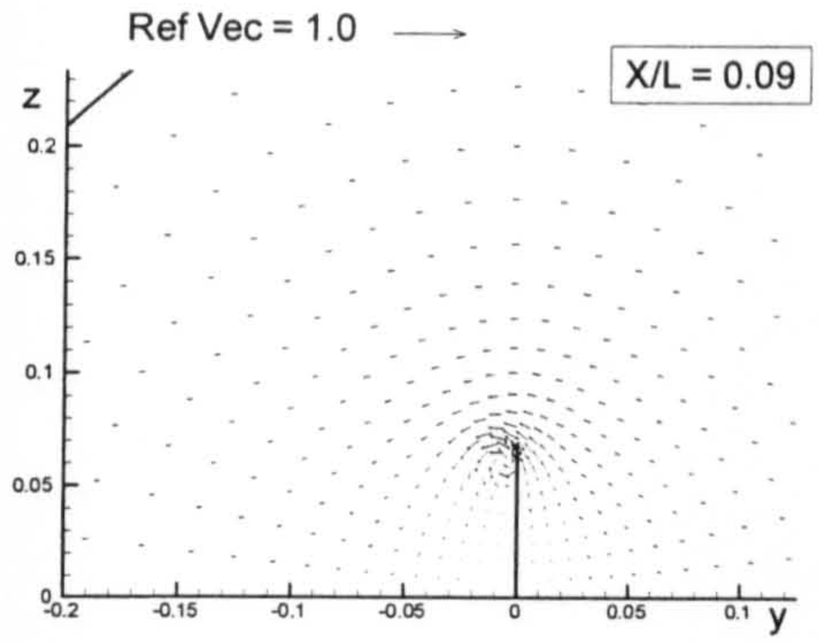

(Flat Plate)

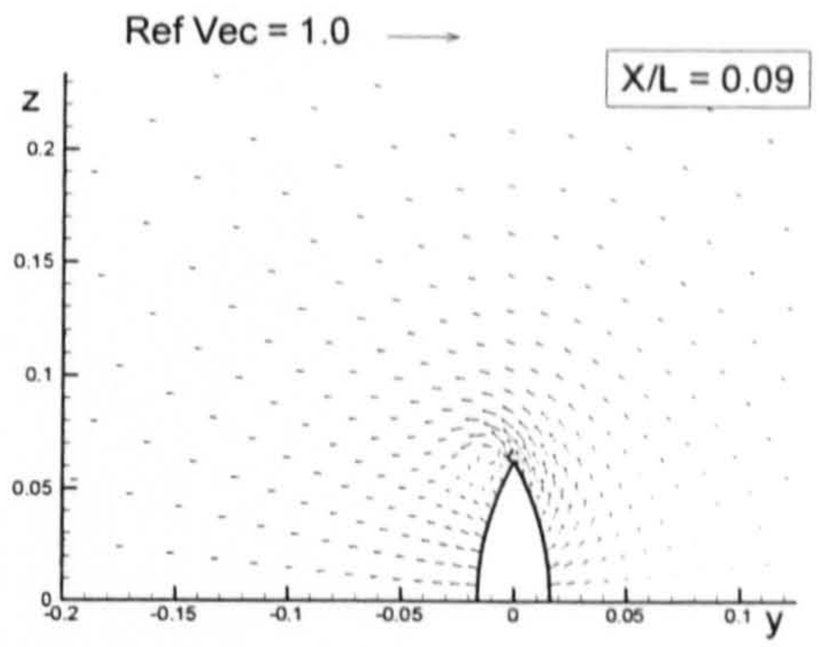

(Wigley Hull)

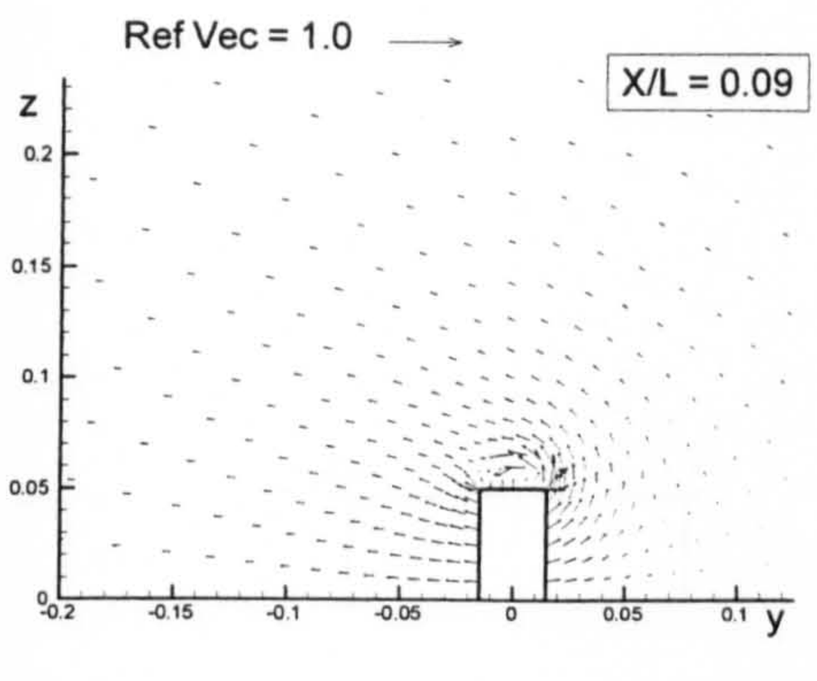

(Block Hull)

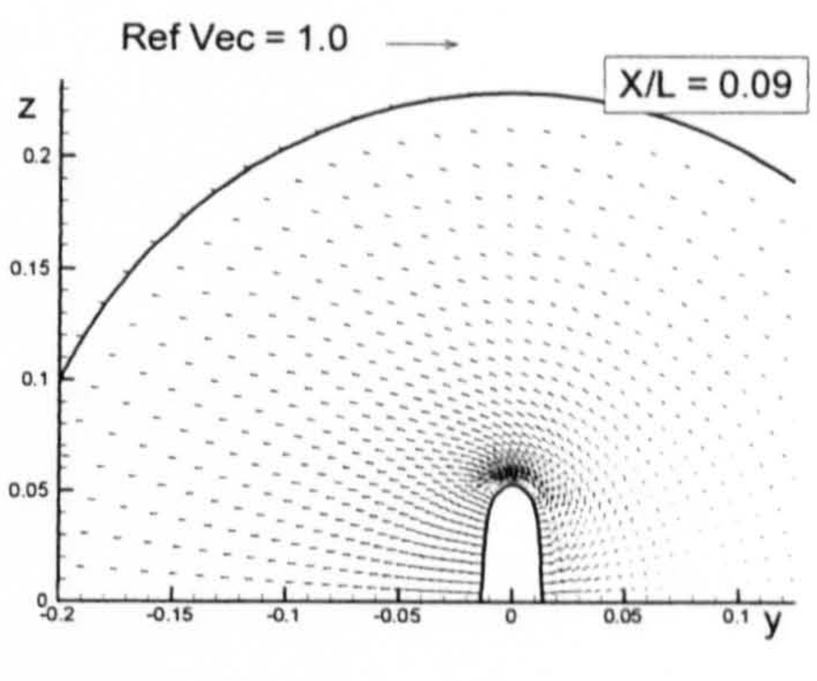

(Series 60 Hull)

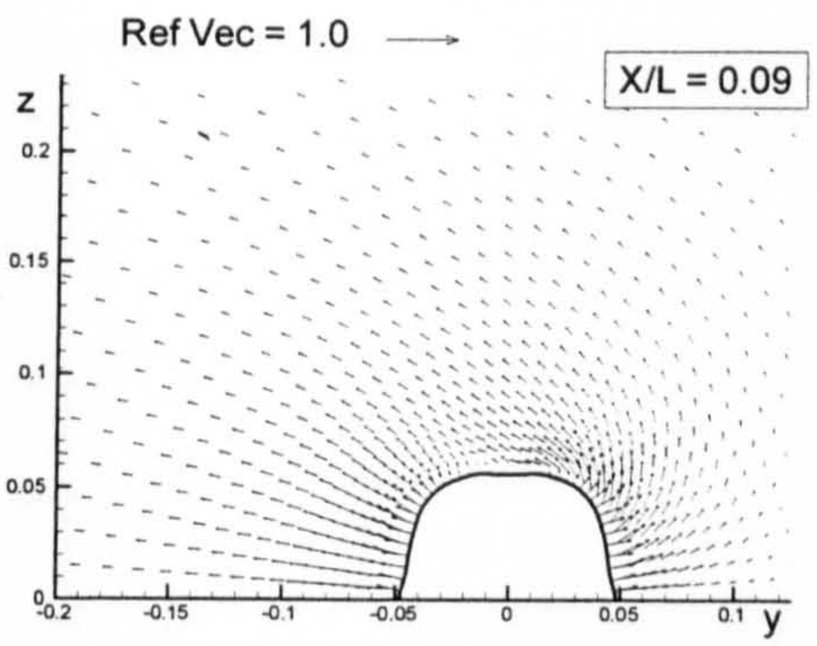

(British Bombardier)

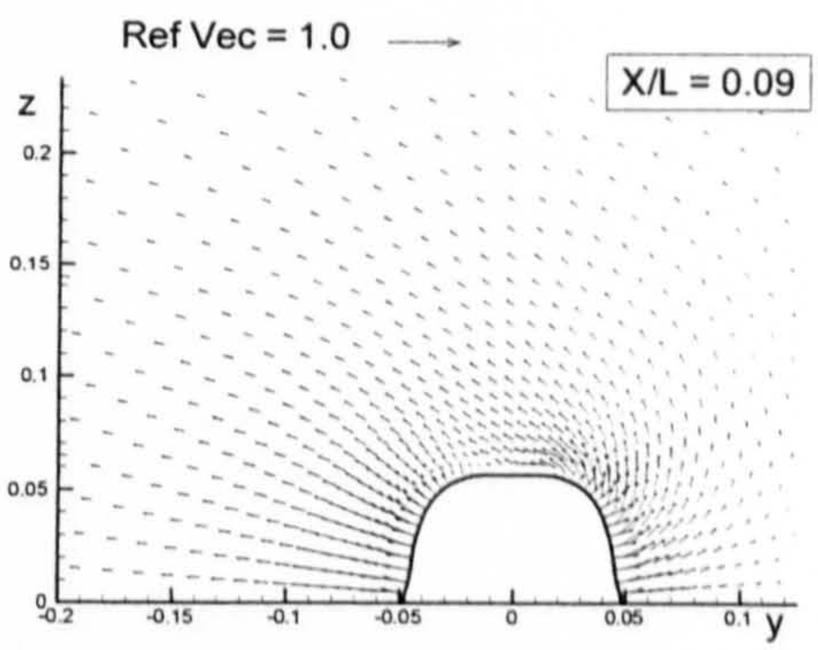

(British Bombardier with a pram stern)

Figure B.7: Comparison of velocity vectors for the six ship hulls at $X/L = 0.09$ due to 5 degrees of drift motion.

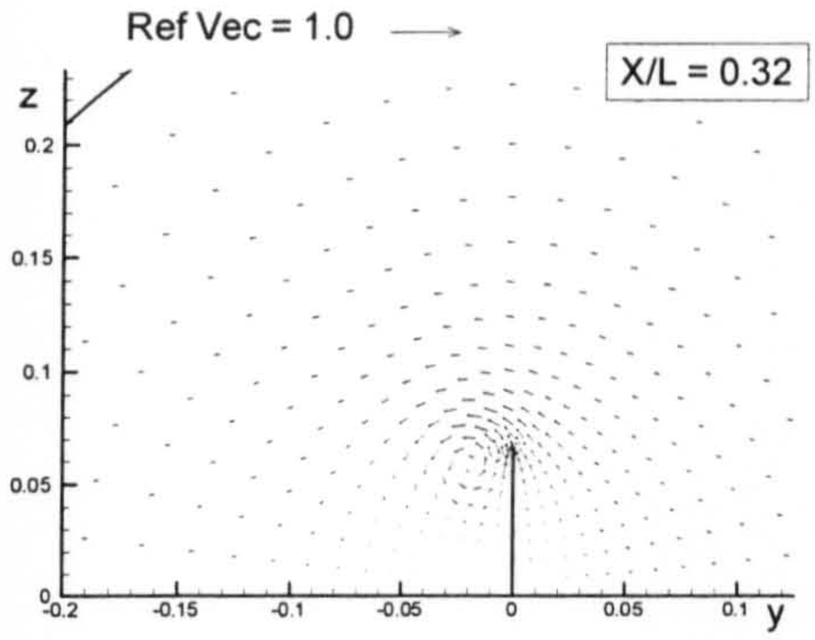

(Flat Plate)

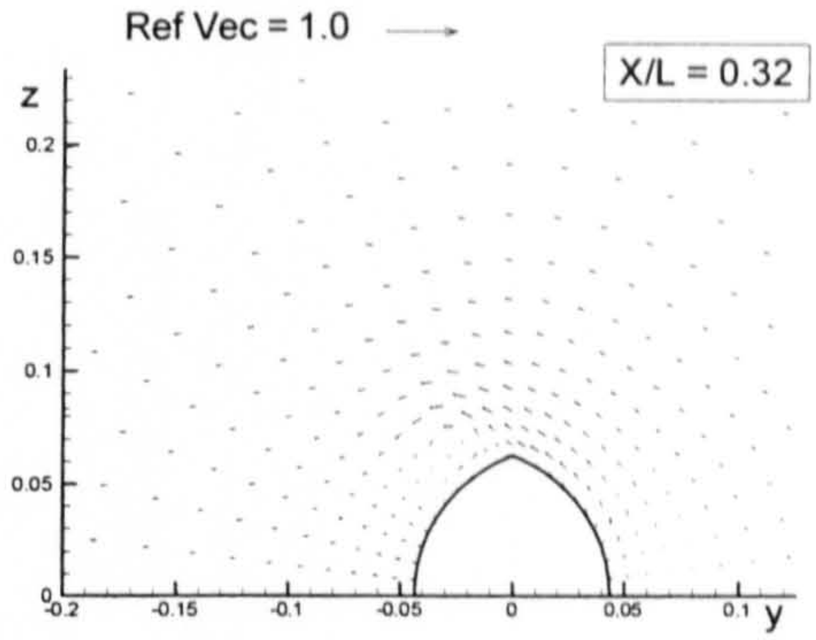

(Wigley Hull)

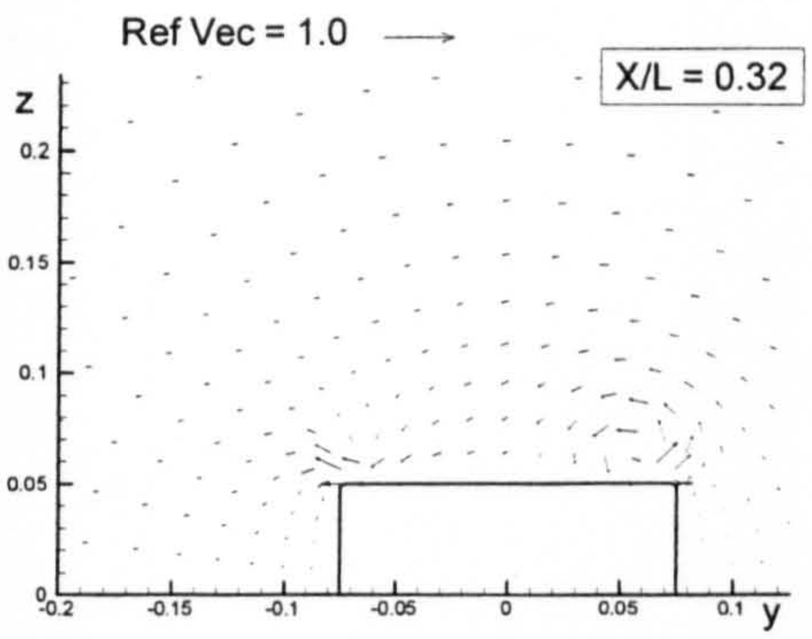

(Block Hull)

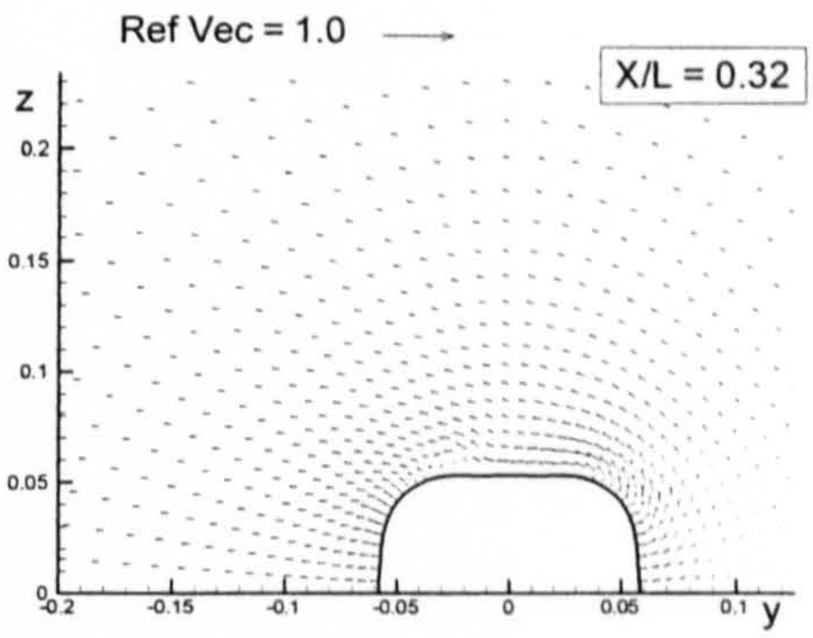

(Series 60 Hull)

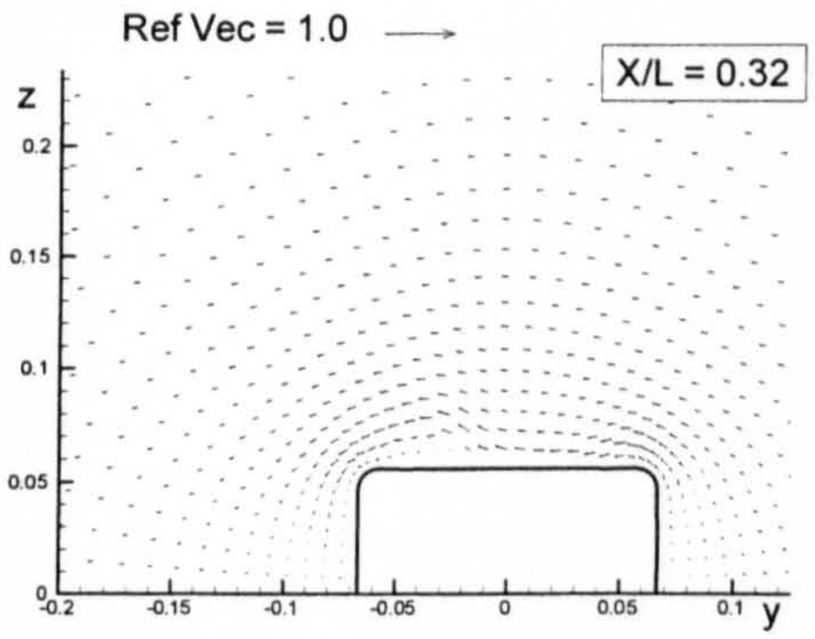

(British Bombardier)

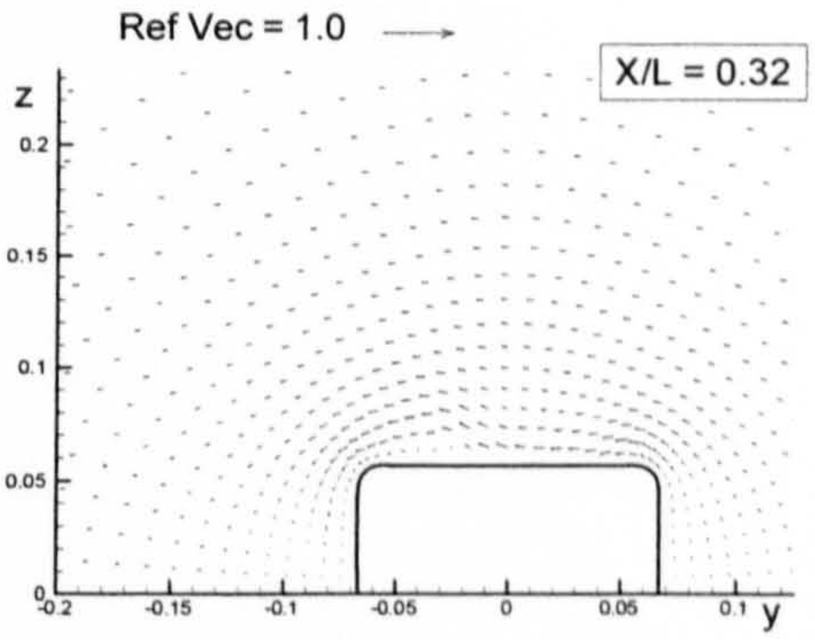

(British Bombardier with a pram stern)

Figure B.7: Comparison of velocity vectors for the six ship hulls at $X/L = 0.32$ due to 5 degrees of drift motion.

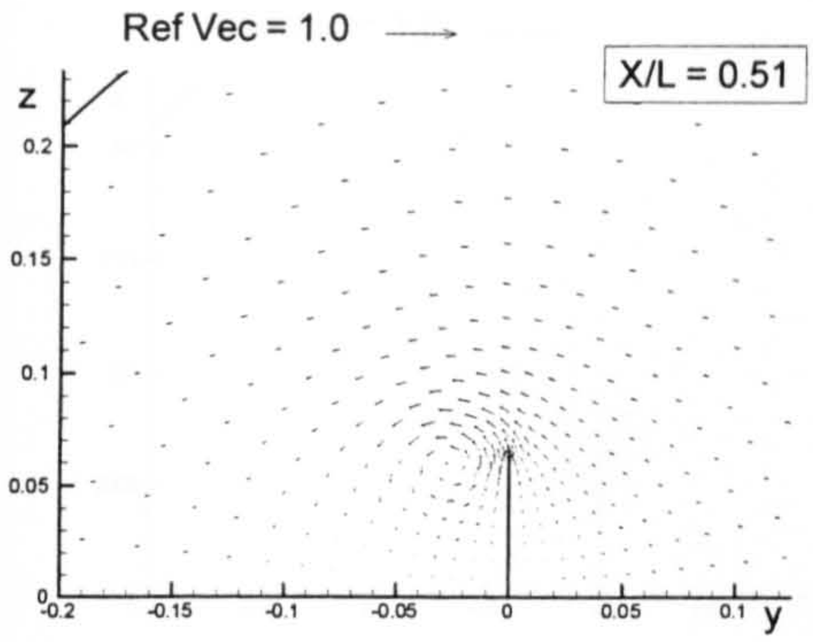

(Flat Plate)

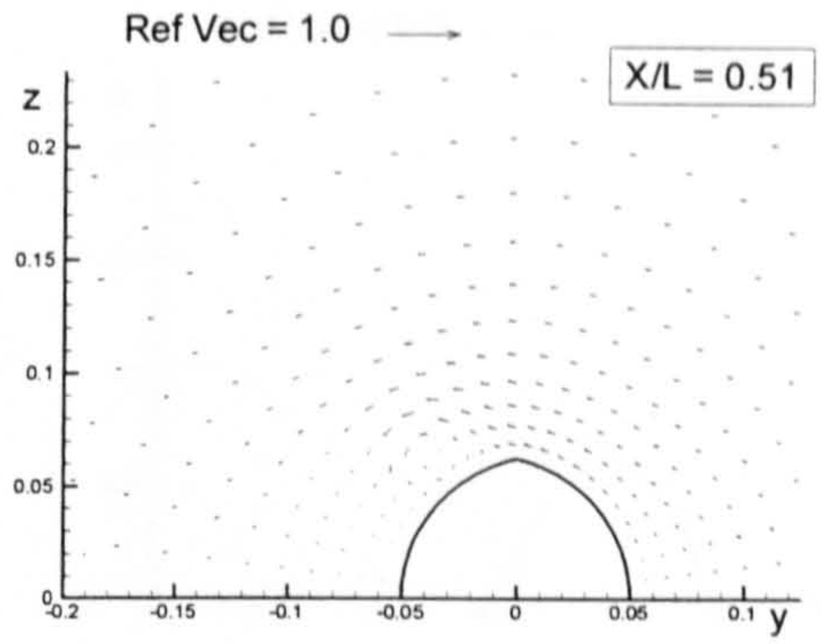

(Wigley Hull)

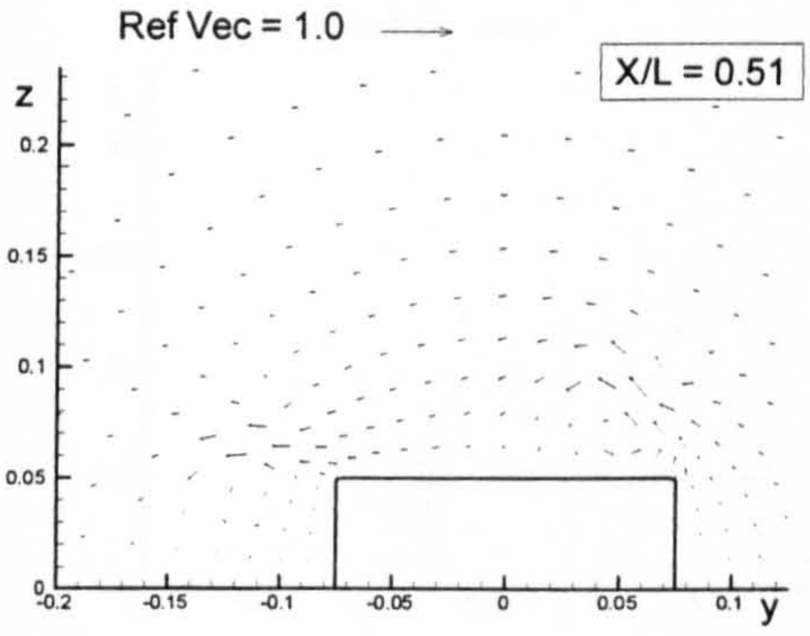

(Block Hull)

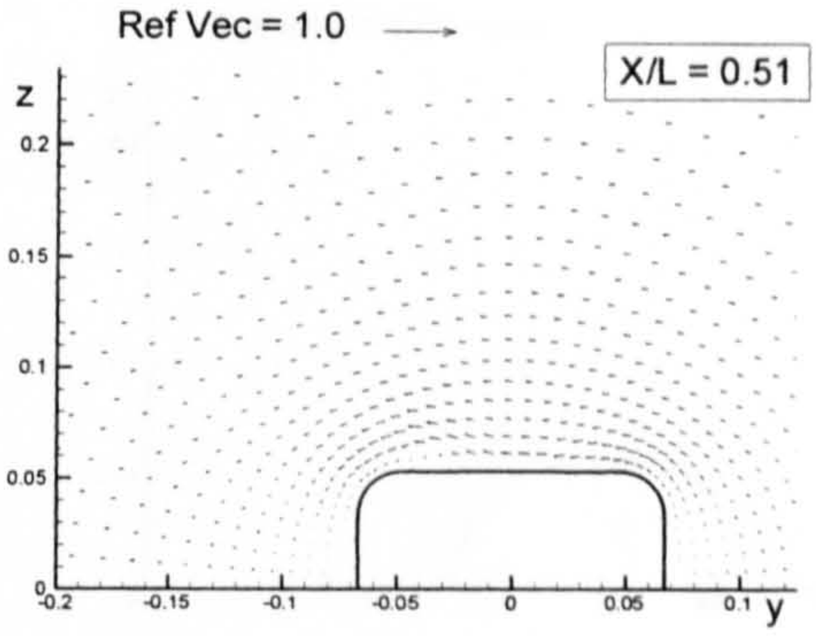

(Series 60 Hull)

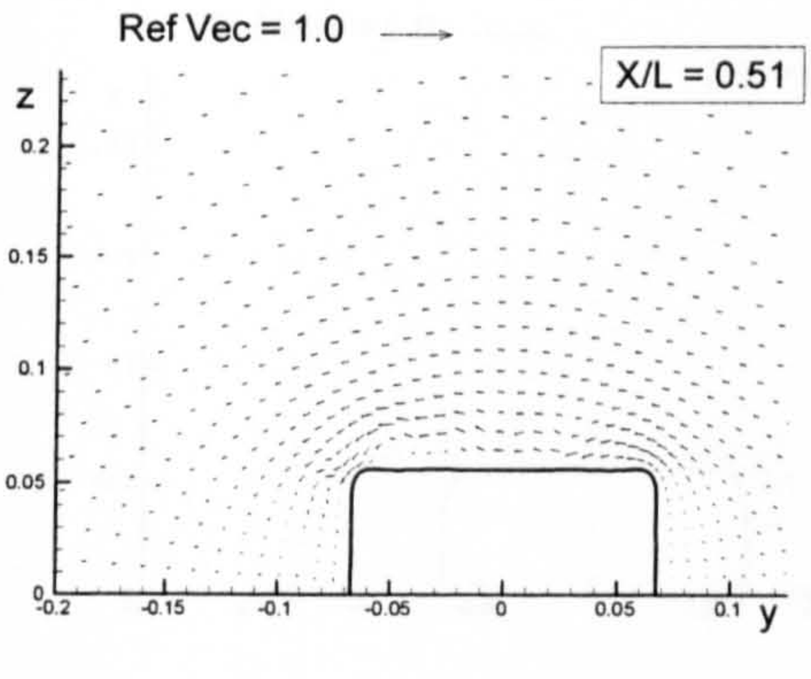

(British Bombardier)

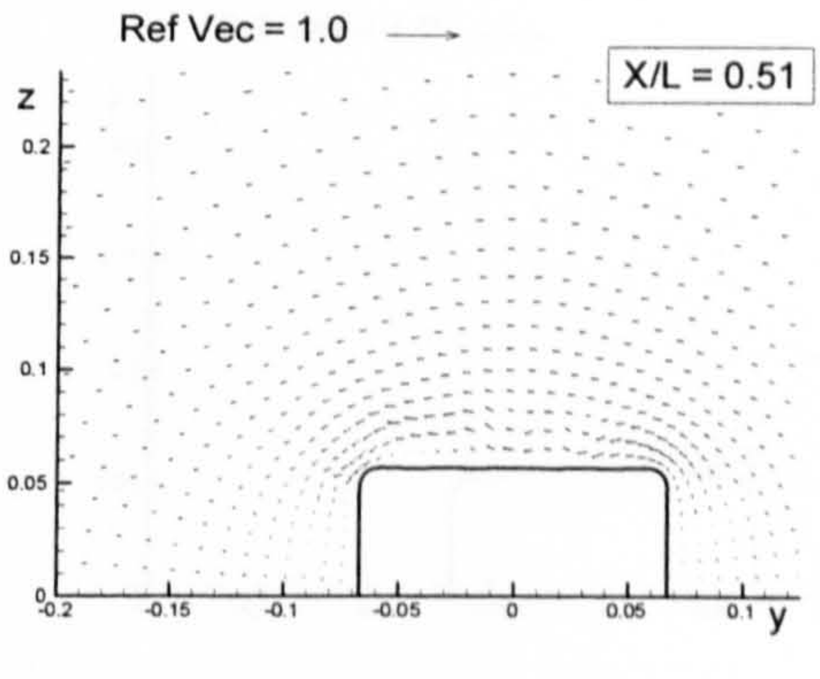

(British Bombardier with a pram stern)

Figure B.7: Comparison of velocity vectors for the six ship hulls at $X/L = 0.51$ due to 5 degrees of drift motion.

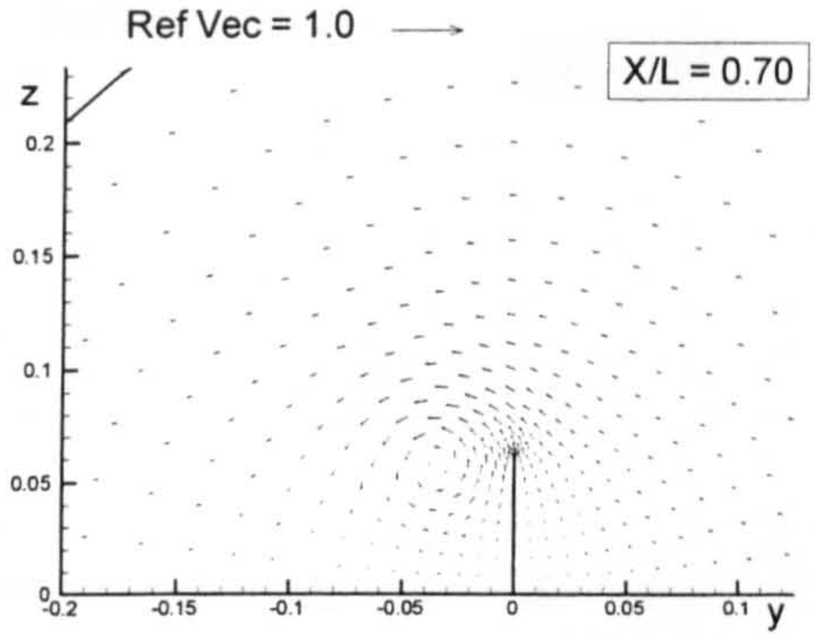

(Flat Plate)

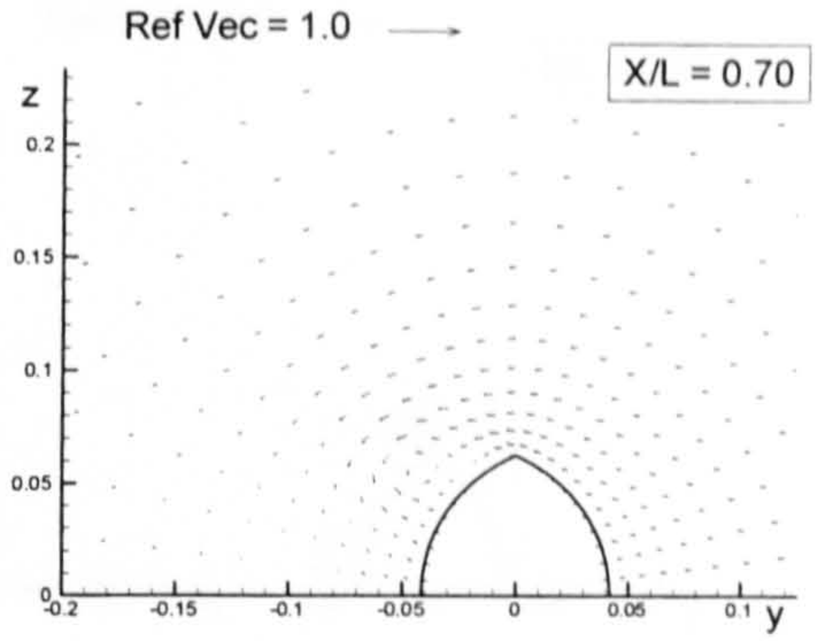

(Wigley Hull)

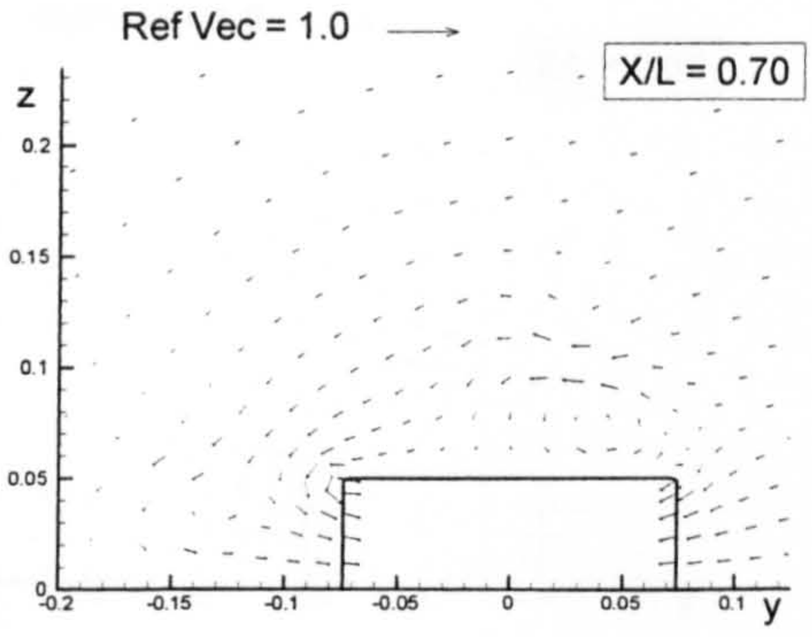

(Block Hull)

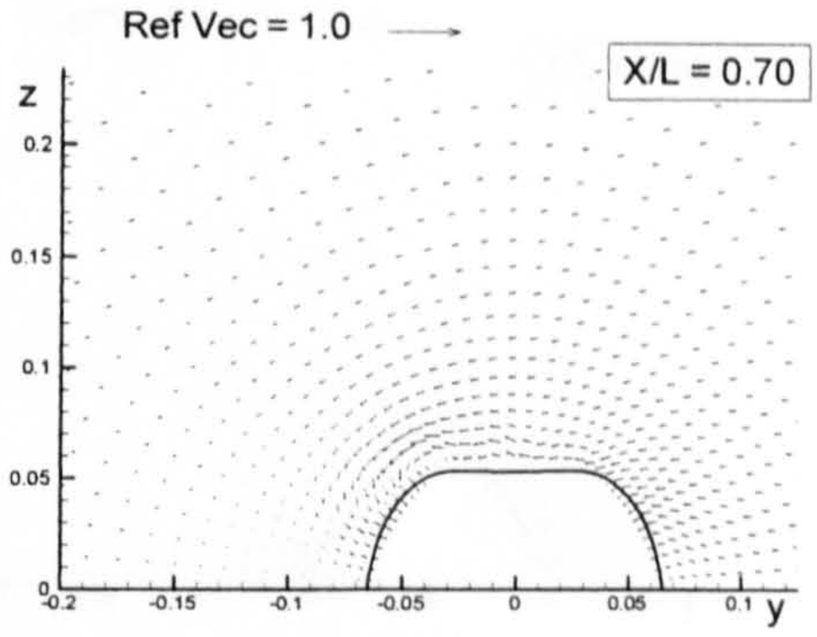

(Series 60 Hull)

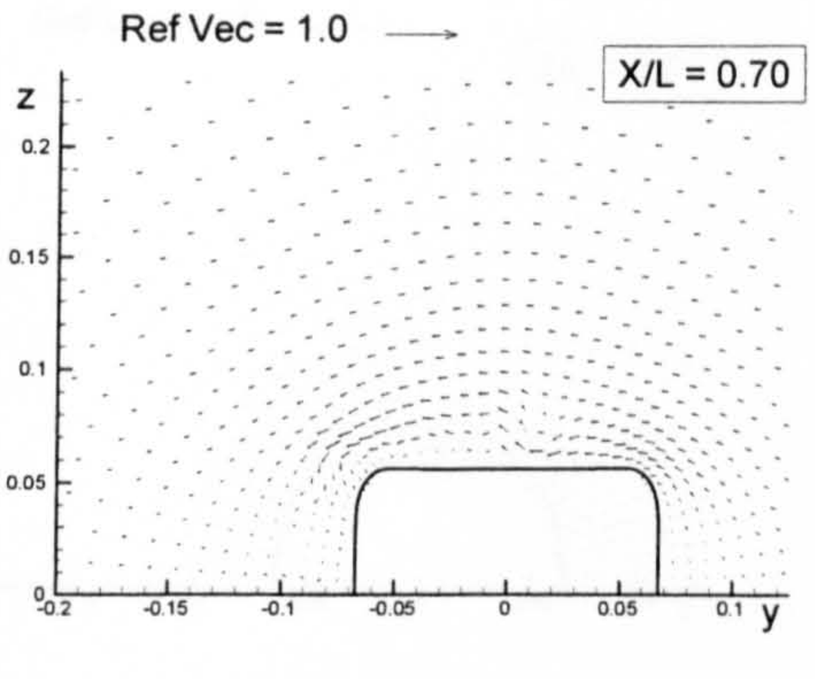

(British Bombardier)

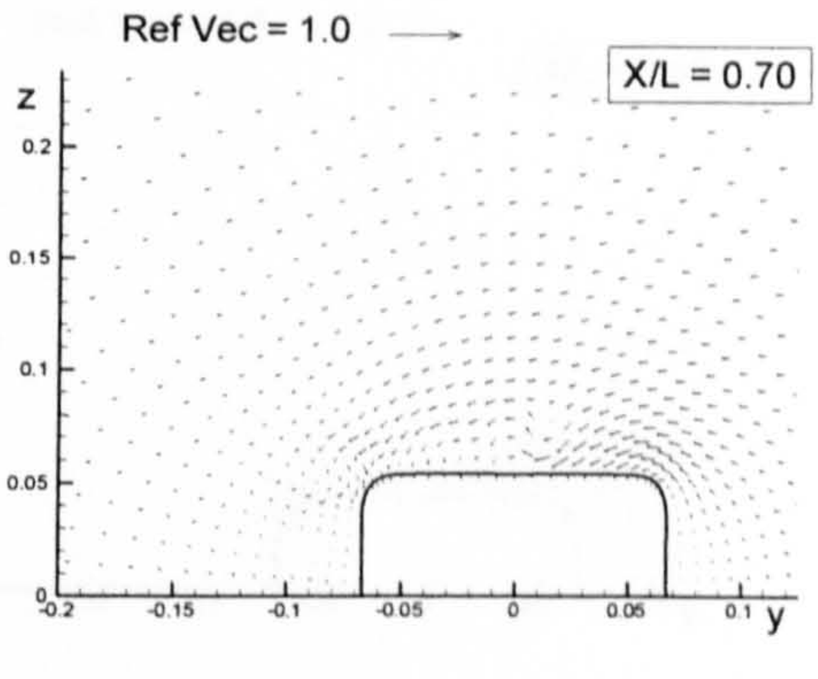

(British Bombardier with a pram stern)

Figure B.7: Comparison of velocity vectors for the six ship hulls at $X/L = 0.70$ due to 5 degrees of drift motion.

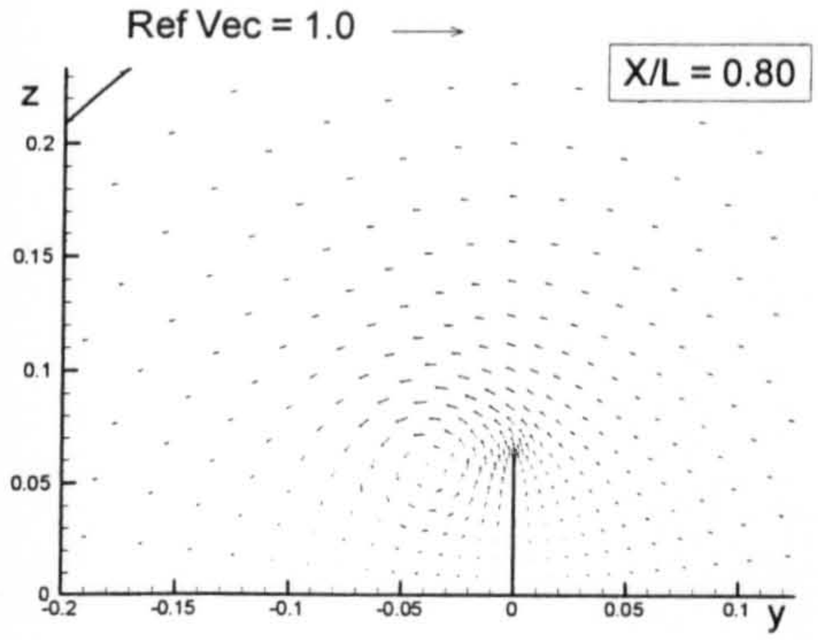

(Flat Plate)

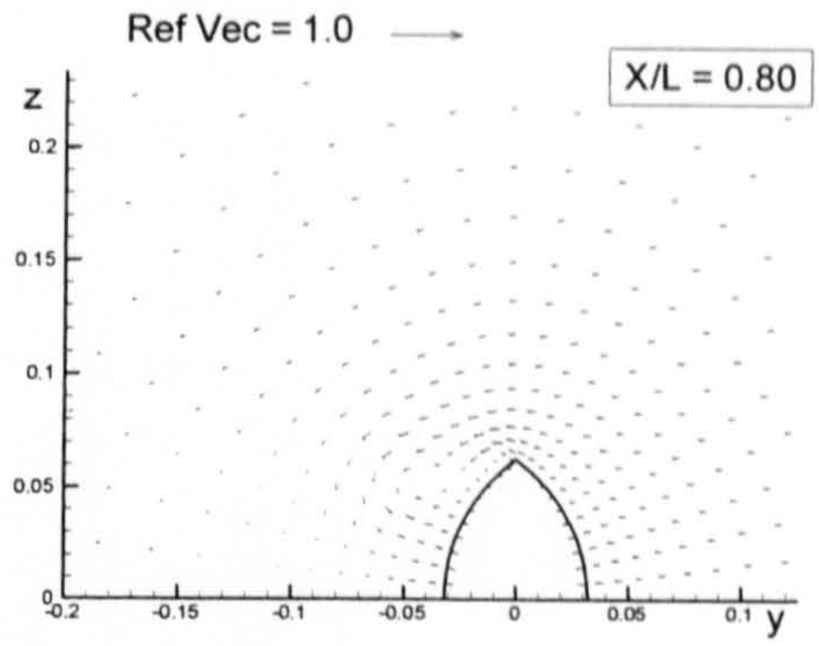

(Wigley Hull)

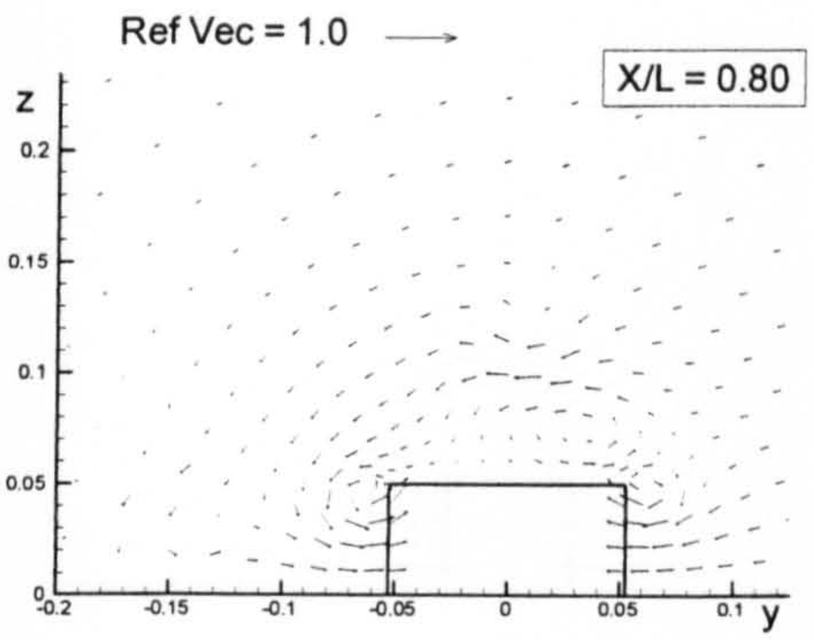

(Block Hull)

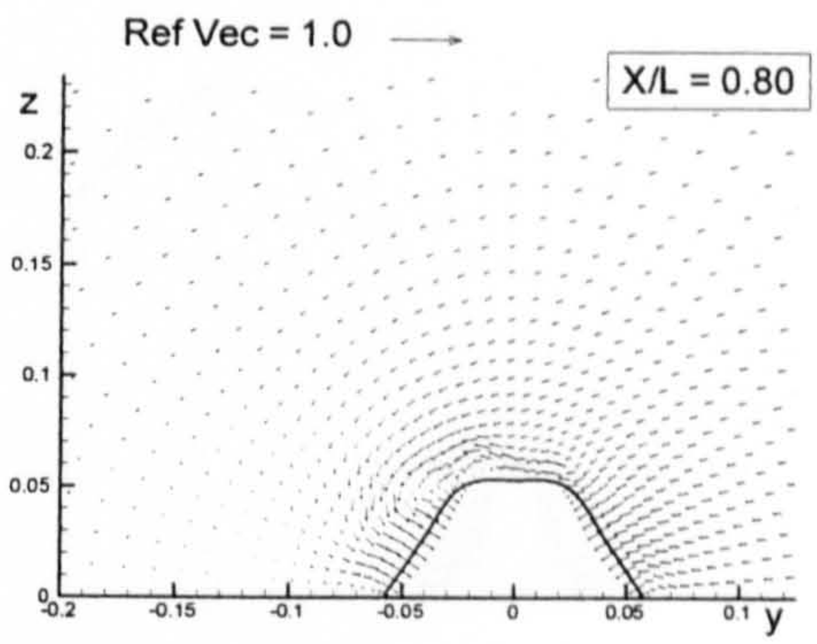

(Series 60 Hull)

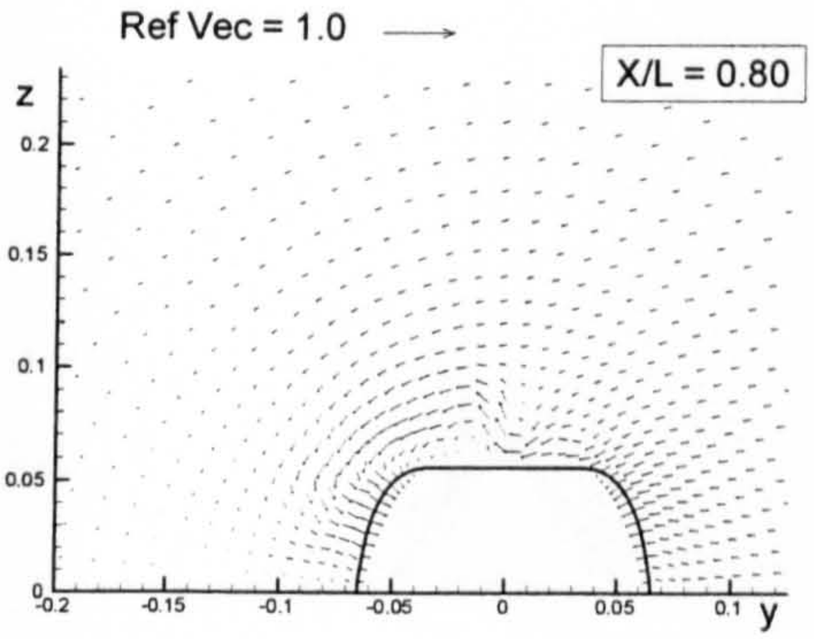

(British Bombardier)

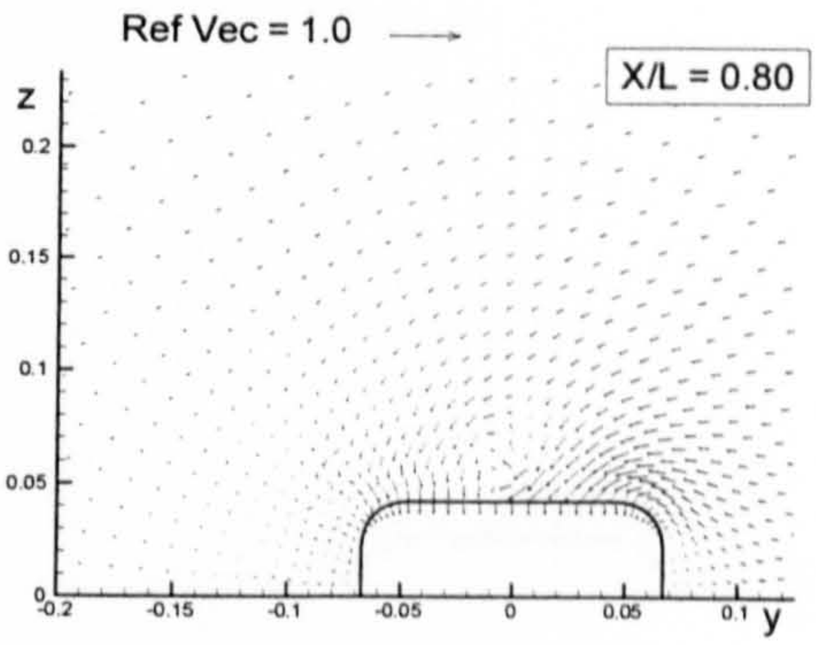

(British Bombardier with a pram stern)

Figure B.7: Comparison of velocity vectors for the six ship hulls at $X/L = 0.80$ due to 5 degrees of drift motion.

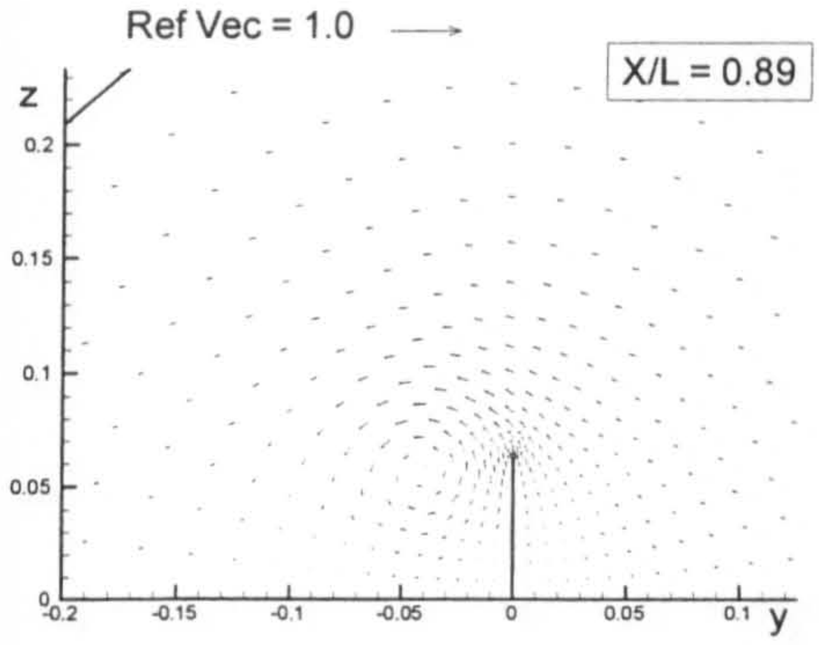

(Flat Plate)

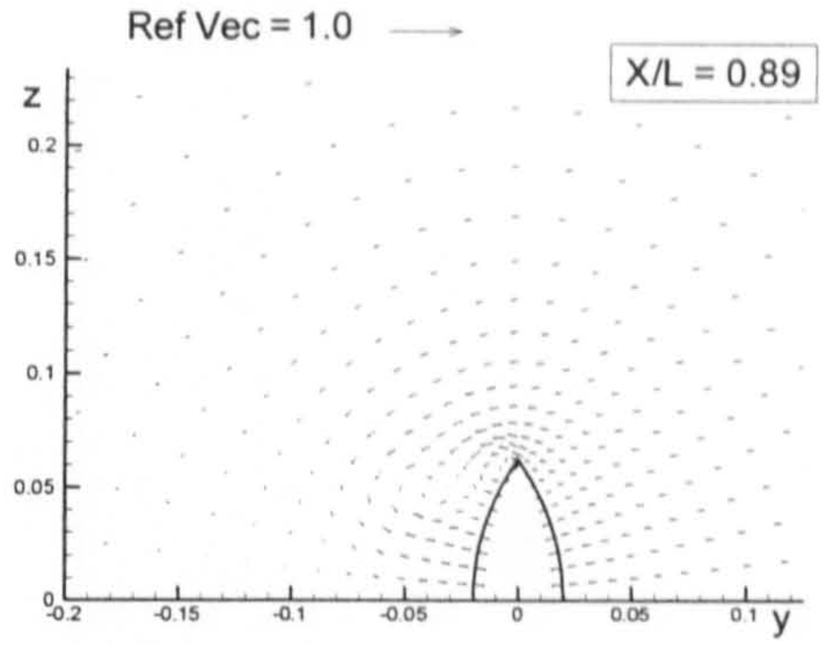

(Wigley Hull)

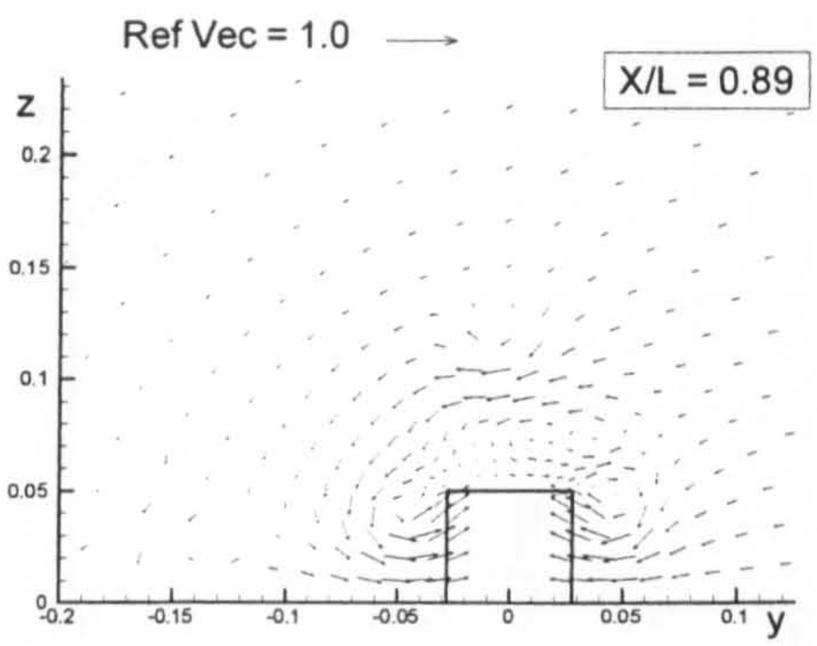

(Block Hull)

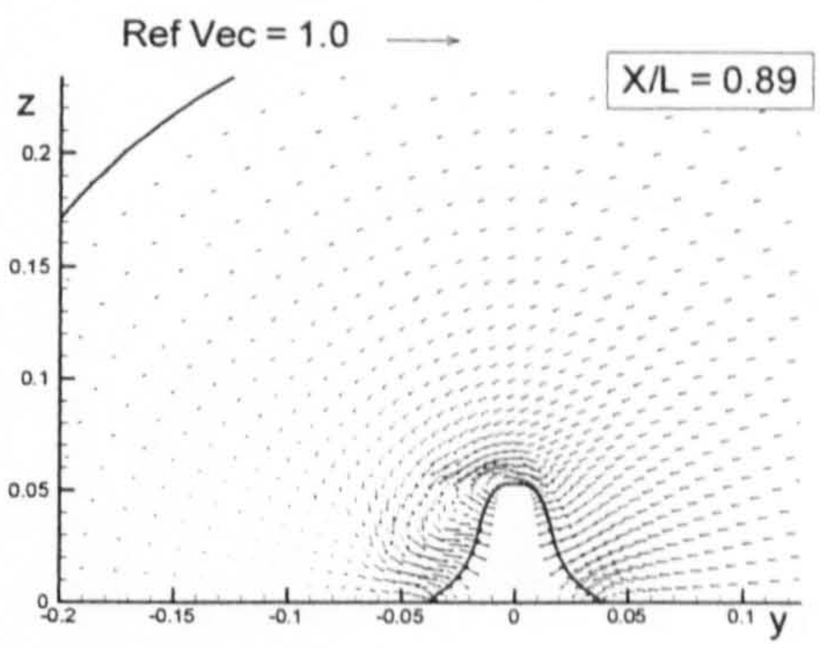

(Series 60 Hull)

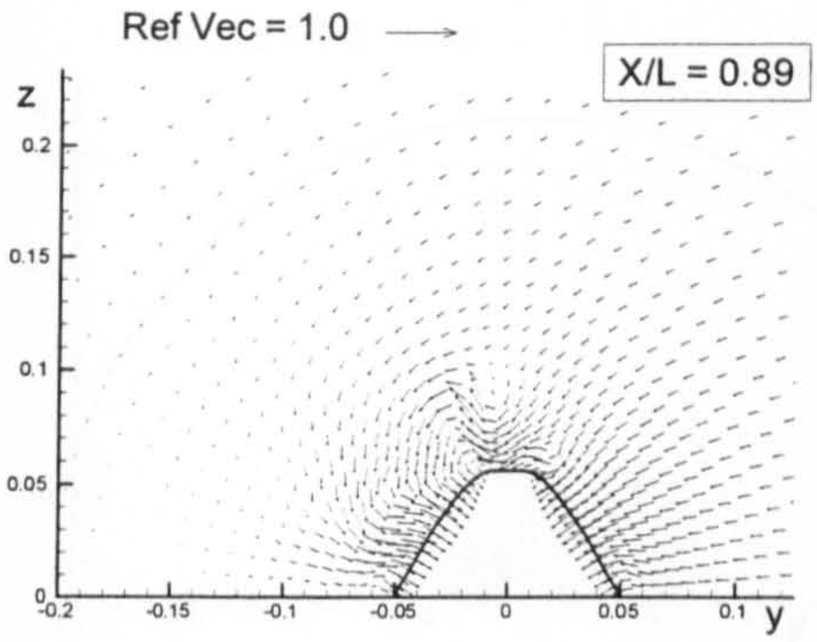

(British Bombardier)

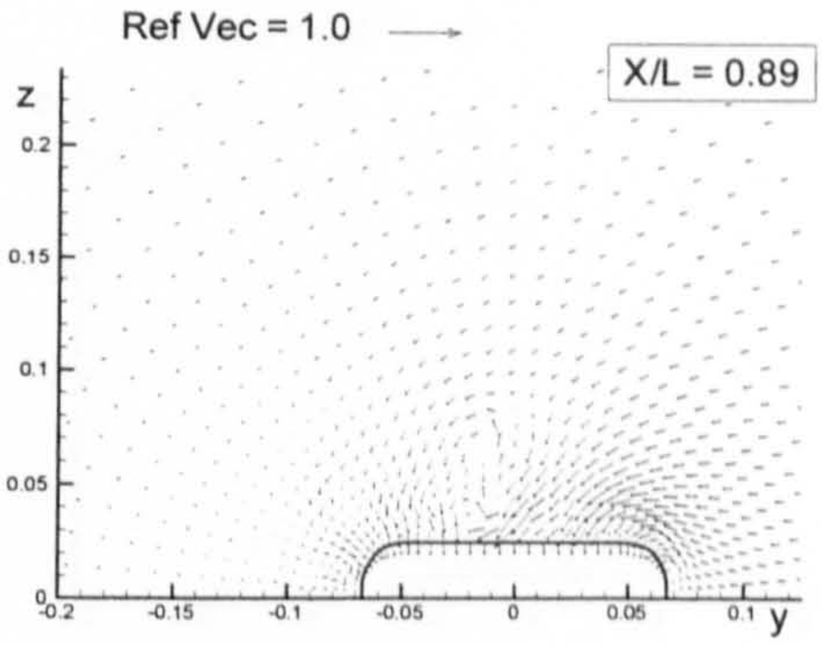

(British Bombardier with a pram stern)

Figure B.7: Comparison of velocity vectors for the six ship hulls at $X/L = 0.89$ due to 5 degrees of drift motion.

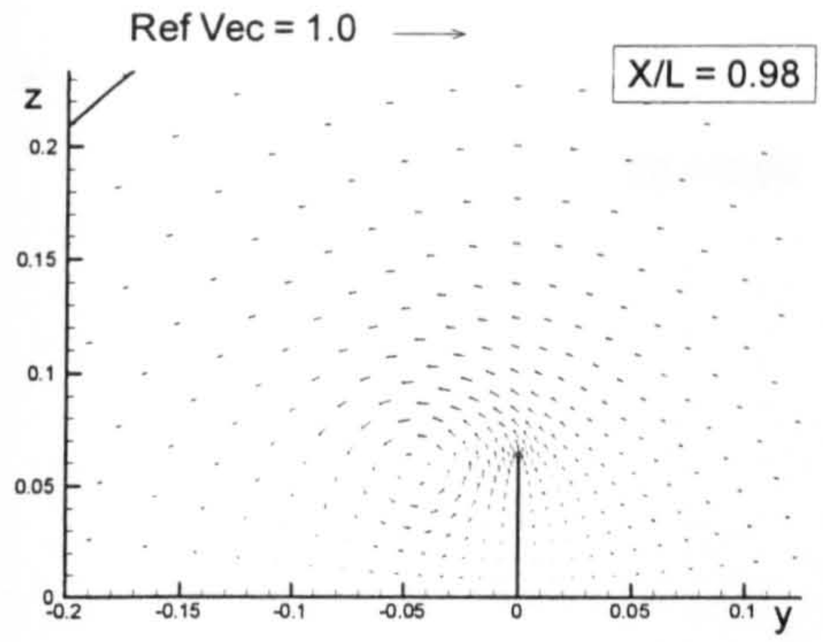

(Flat Plate)

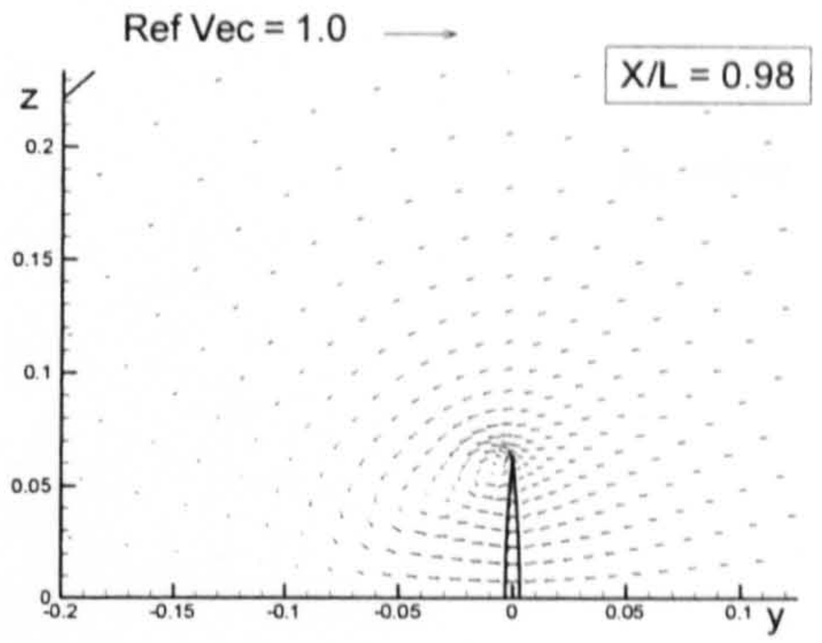

(Wigley Hull)

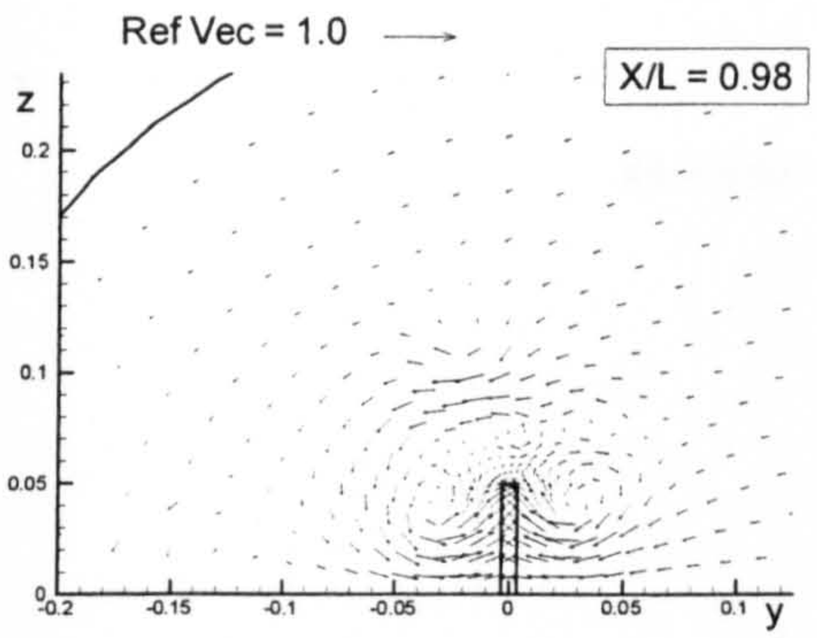

(Block Hull)

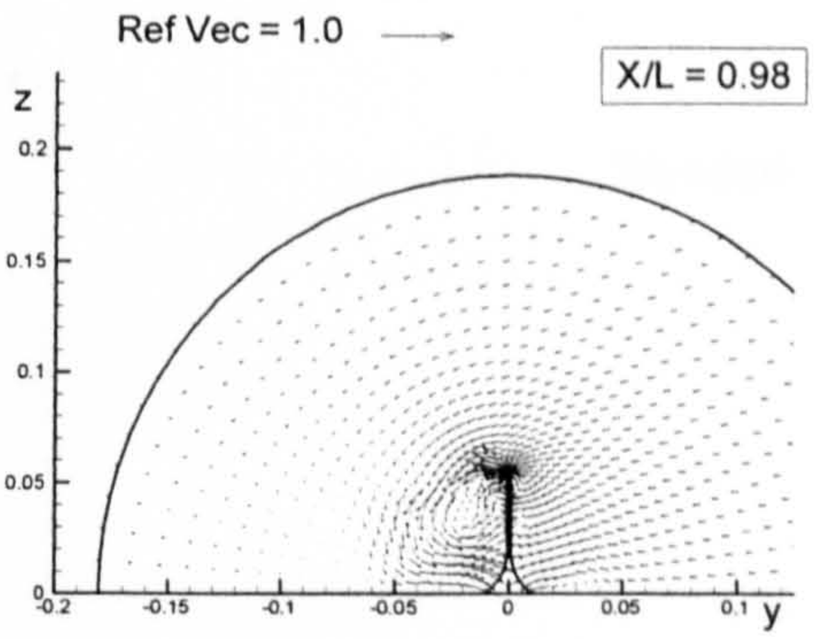

(Series 60 Hull)

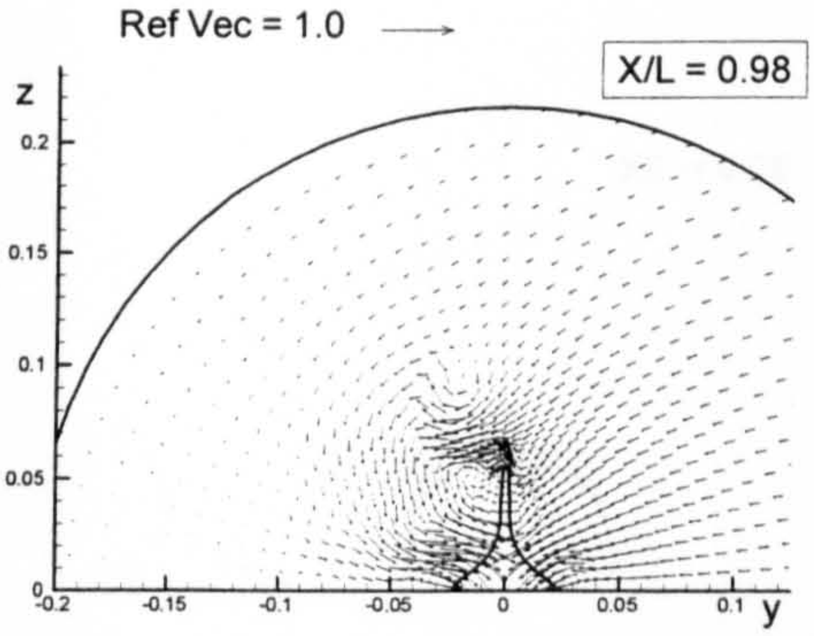

(British Bombardier)

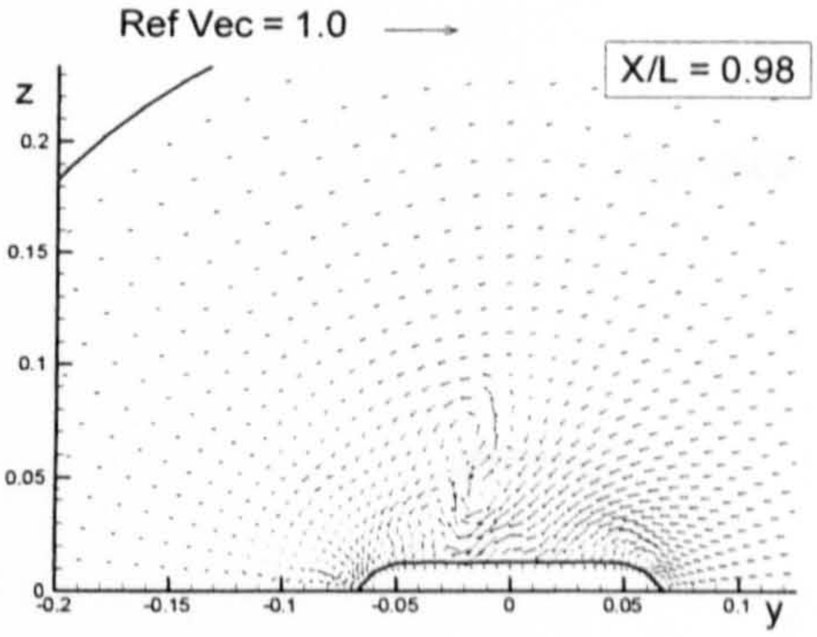

(British Bombardier with a pram stern)

Figure B.7: Comparison of velocity vectors for the six ship hulls at $X/L = 0.98$ due to 5 degrees of drift motion.

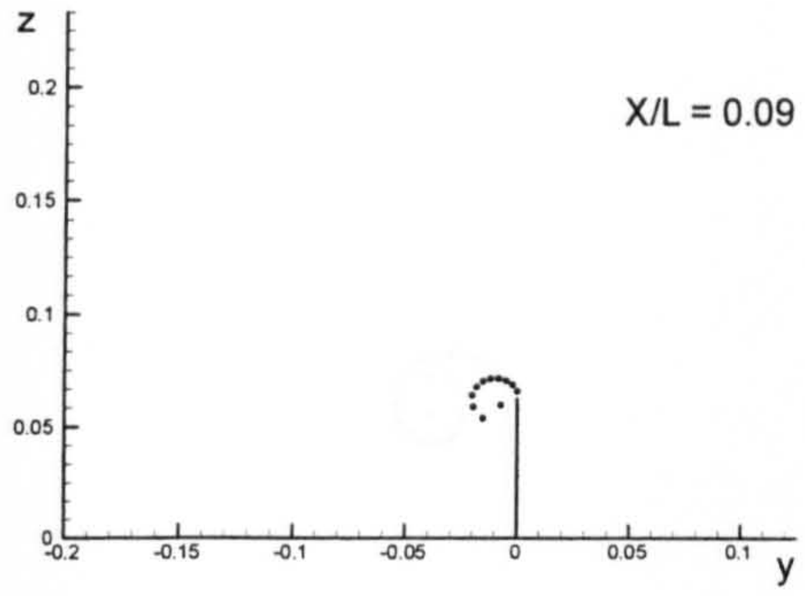

(Flat Plate)

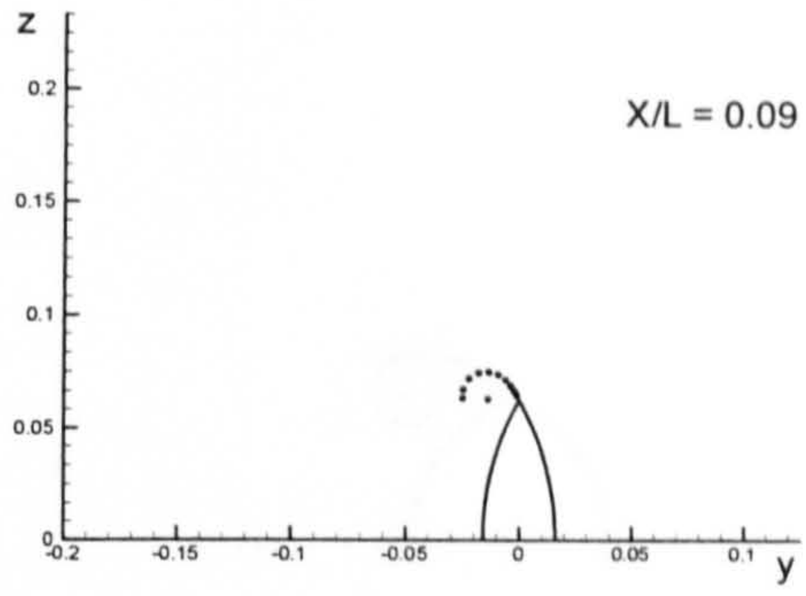

(Wigley Hull)

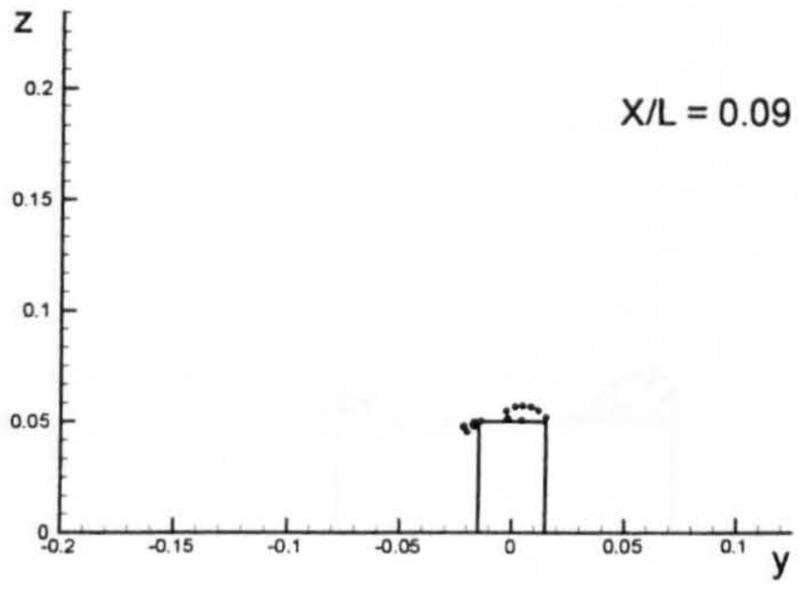

(Block Hull)

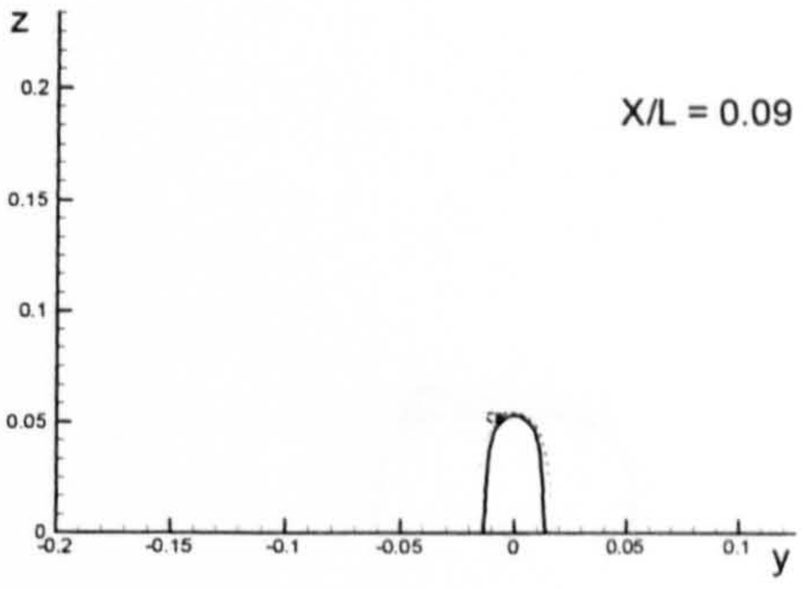

(Series 60 Hull)

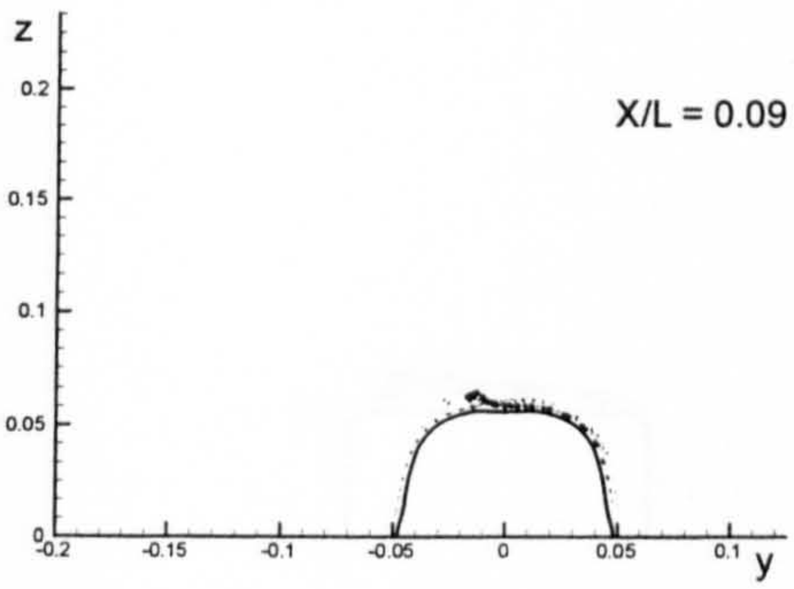

(British Bombardier)

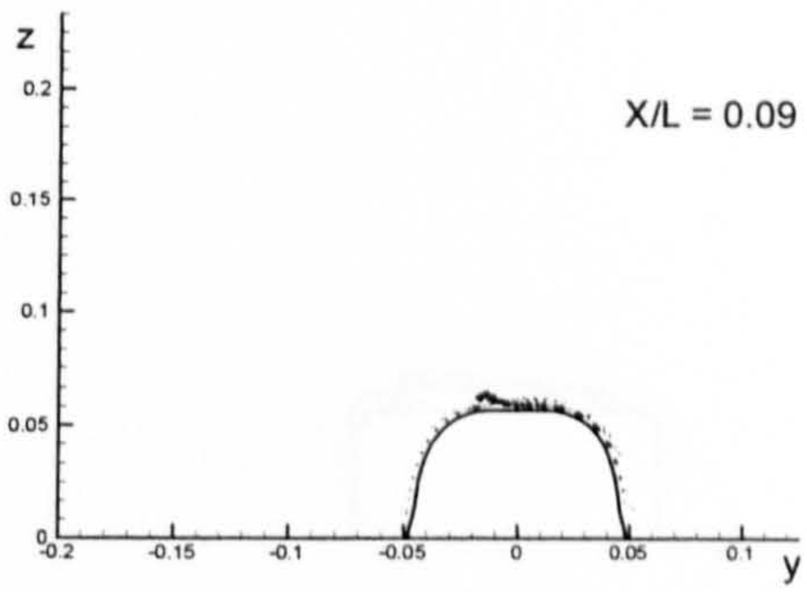

(British Bombardier with a pram stern)

Figure B.1: Comparison of vortex fields for the six ship hulls at $X/L = 0.09$ due to 10 degrees of drift motion.

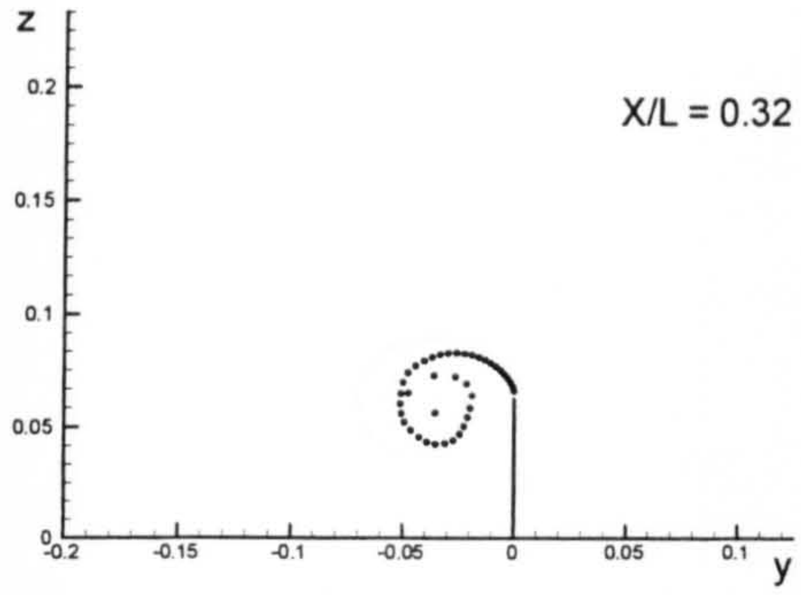

(Flat Plate)

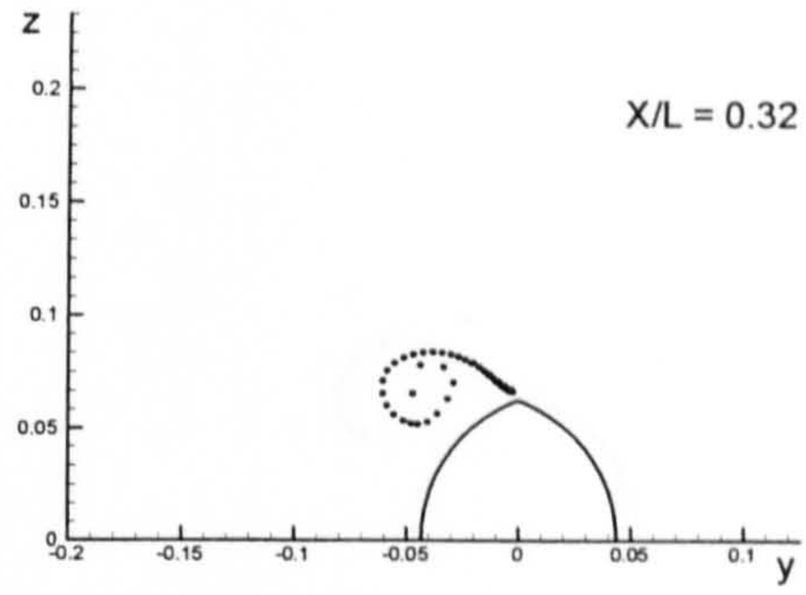

(Wigley Hull)

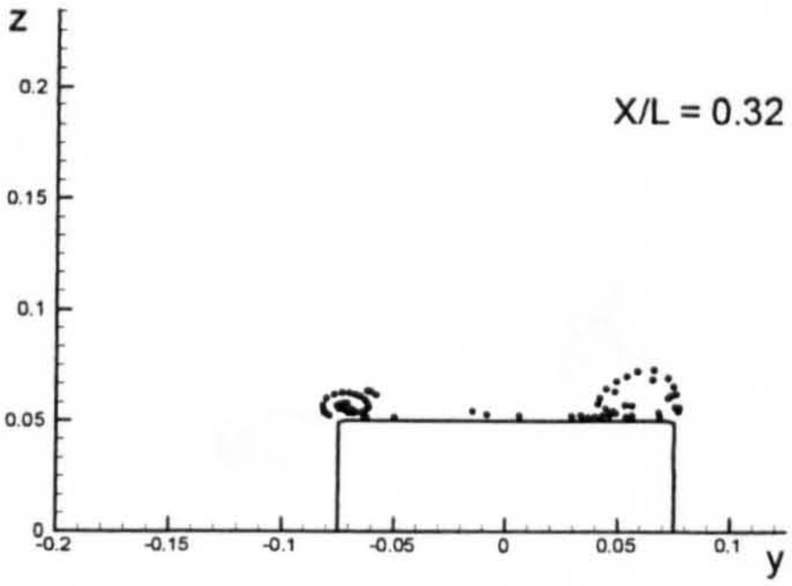

(Block Hull)

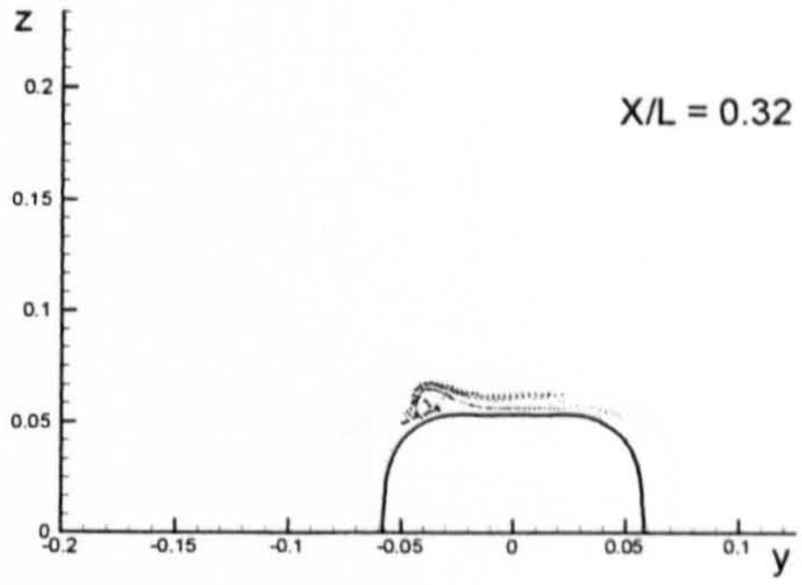

(Series 60 Hull)

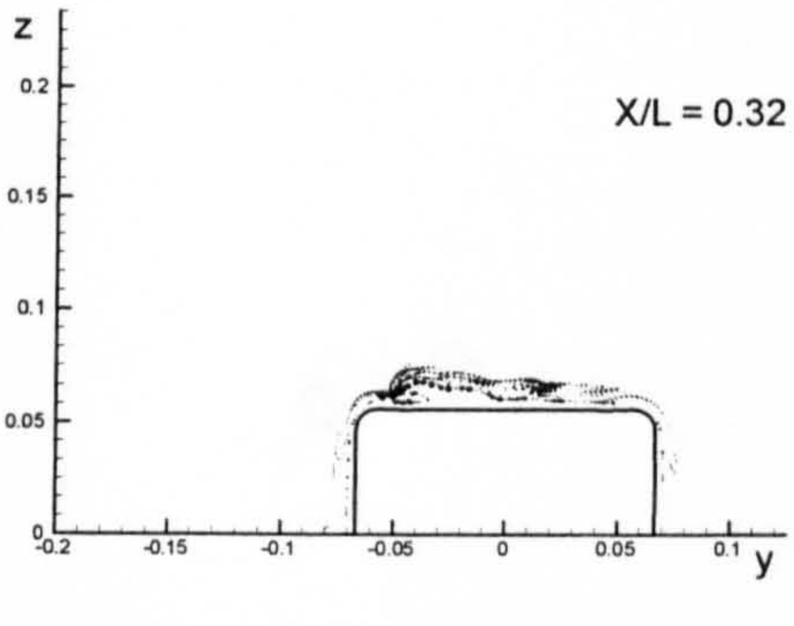

(British Bombardier)

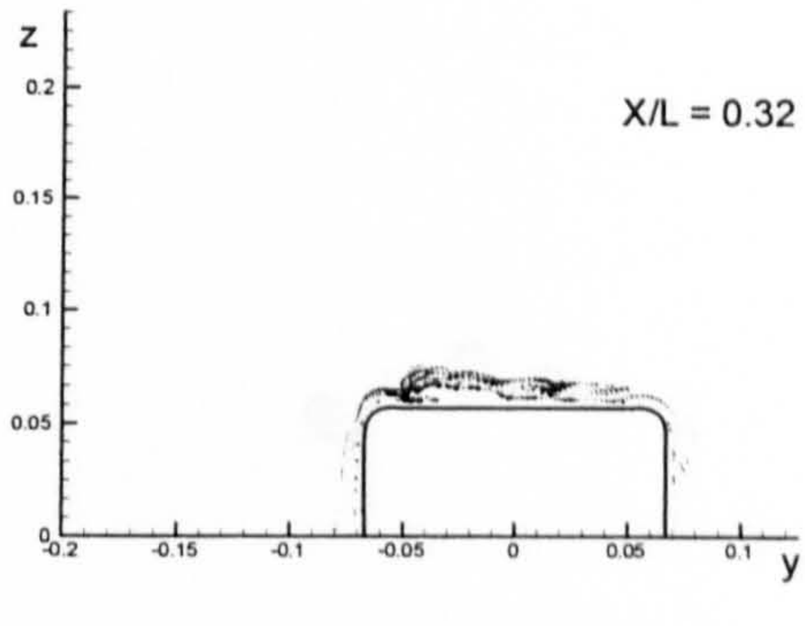

(British Bombardier with a pram stern)

Figure B.2: Comparison of vortex fields for the six ship hulls at $X/L = 0.32$ due to 10 degrees of drift motion.

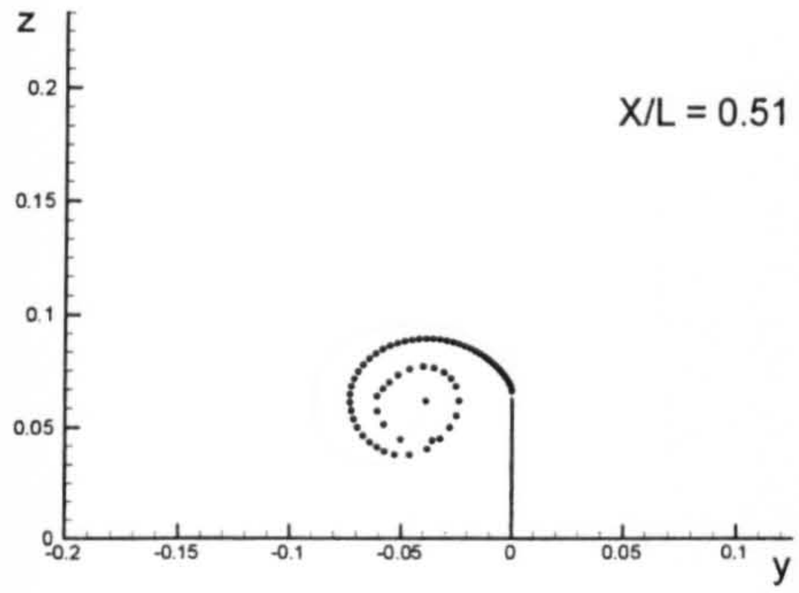

(Flat Plate)

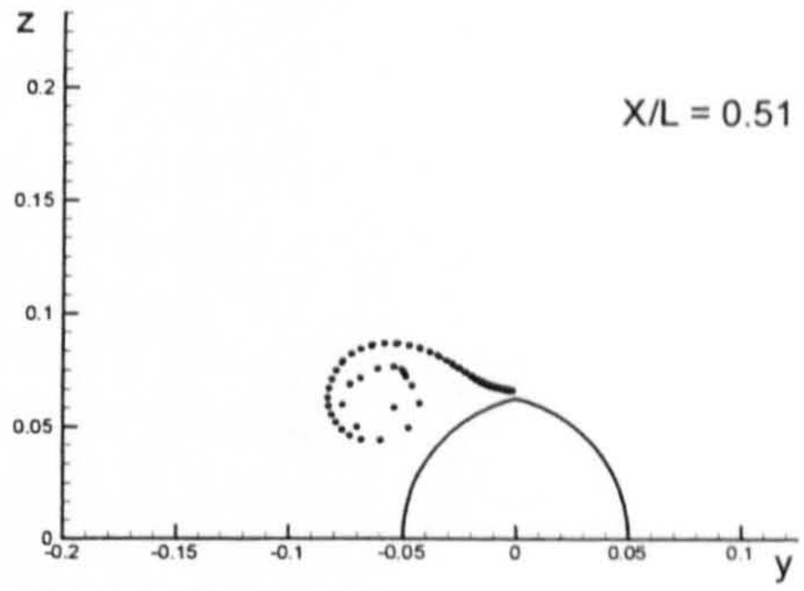

(Wigley Hull)

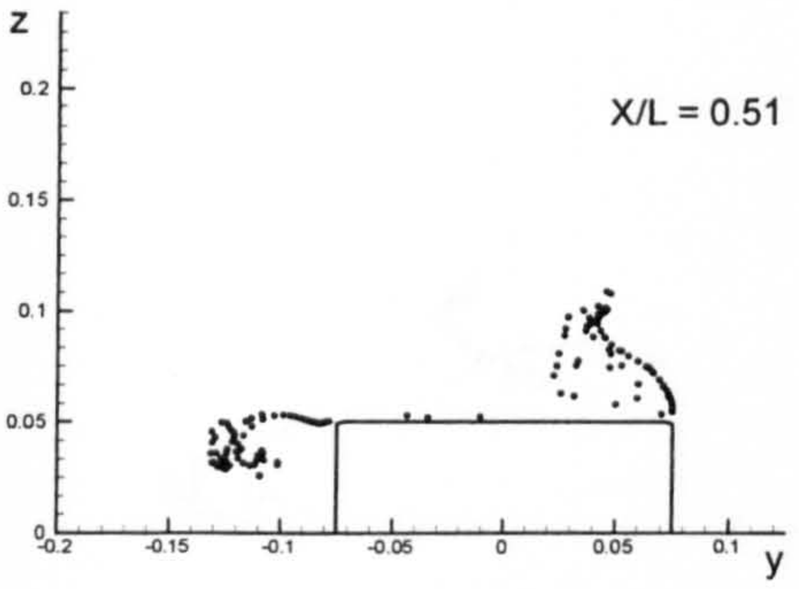

(Block Hull)

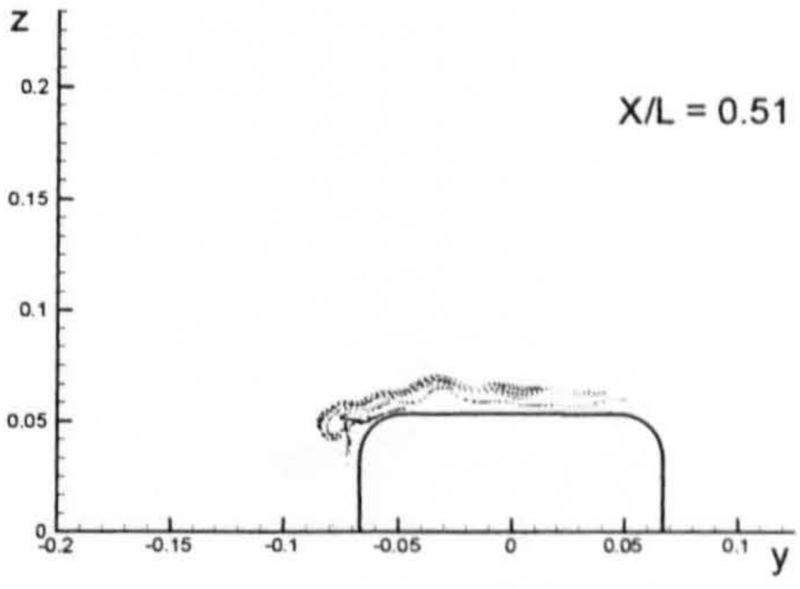

(Series 60 Hull)

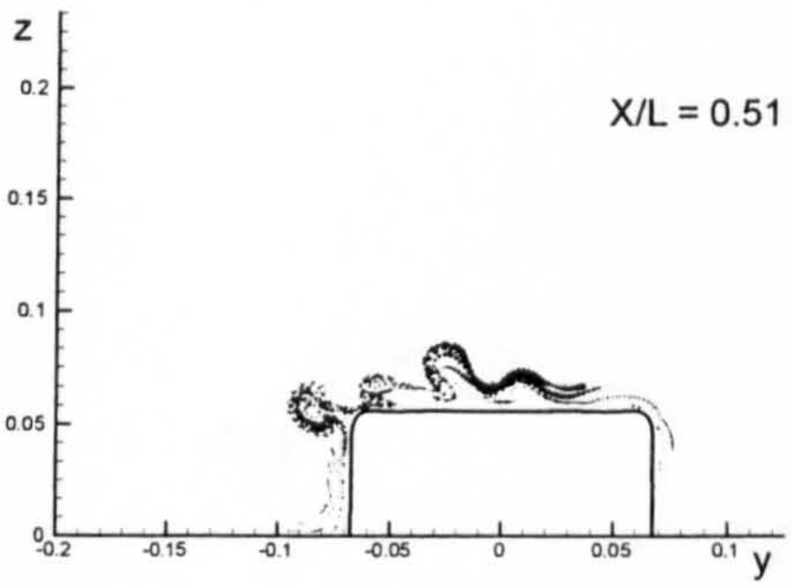

(British Bombardier)

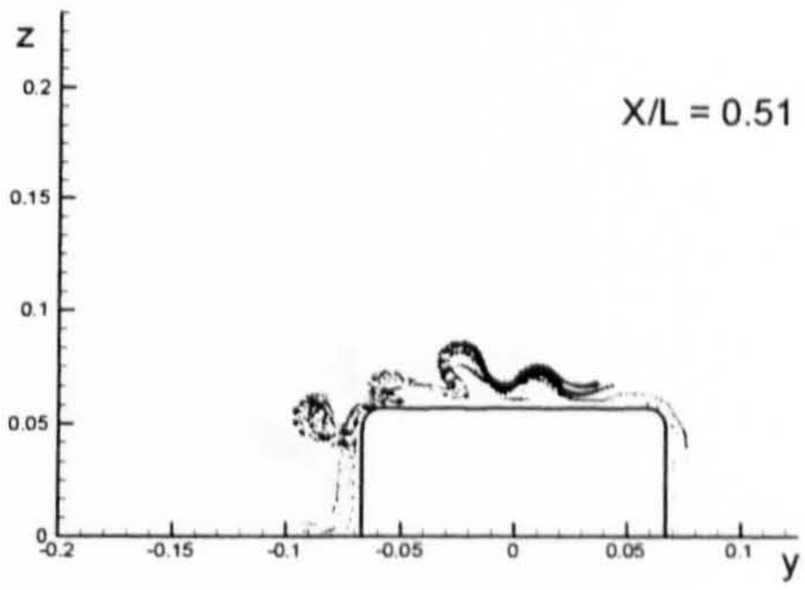

(British Bombardier with a pram stern)

Figure B.3: Comparison of vortex fields for the six ship hulls at $X/L = 0.51$ due to 10 degrees of drift motion.

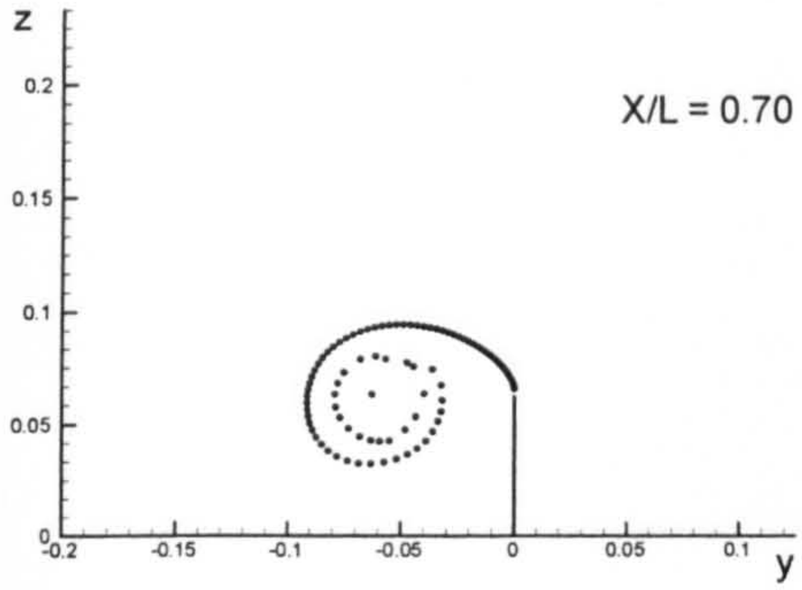

(Flat Plate)

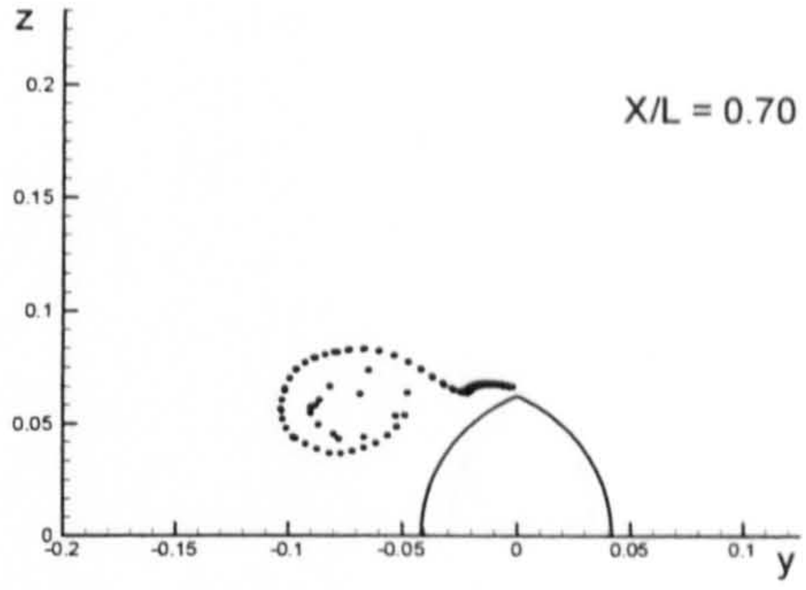

(Wigley Hull)

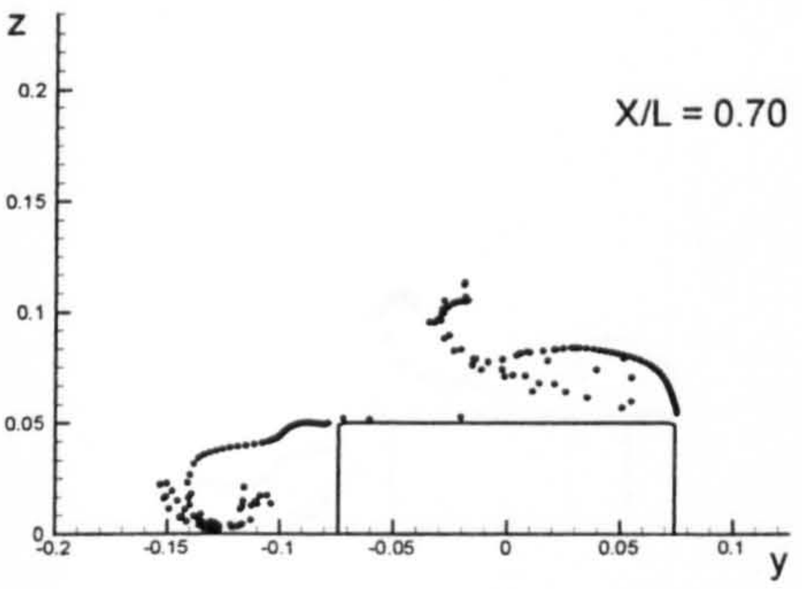

(Block Hull)

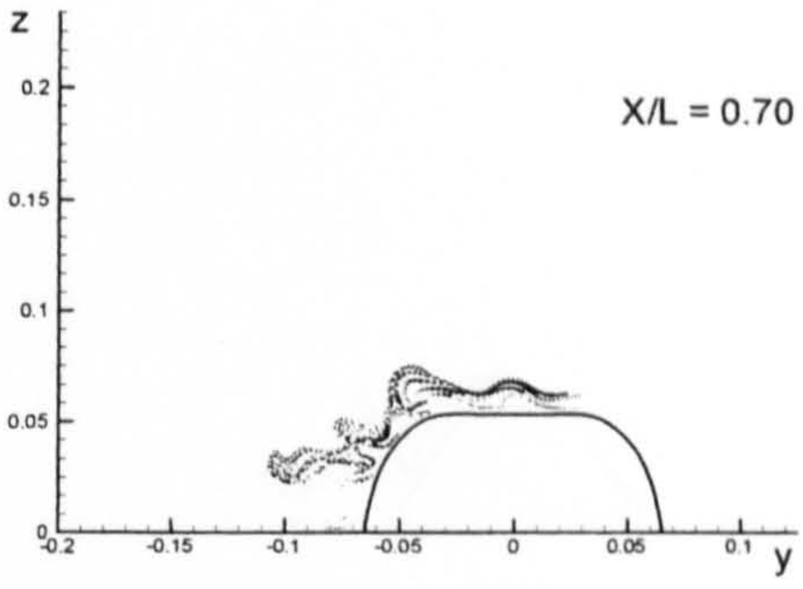

(Series 60 Hull)

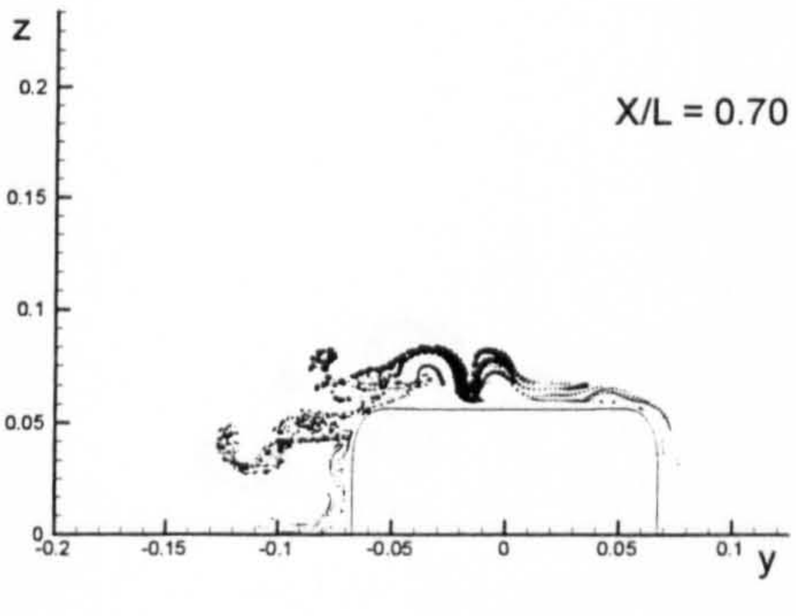

(British Bombardier)

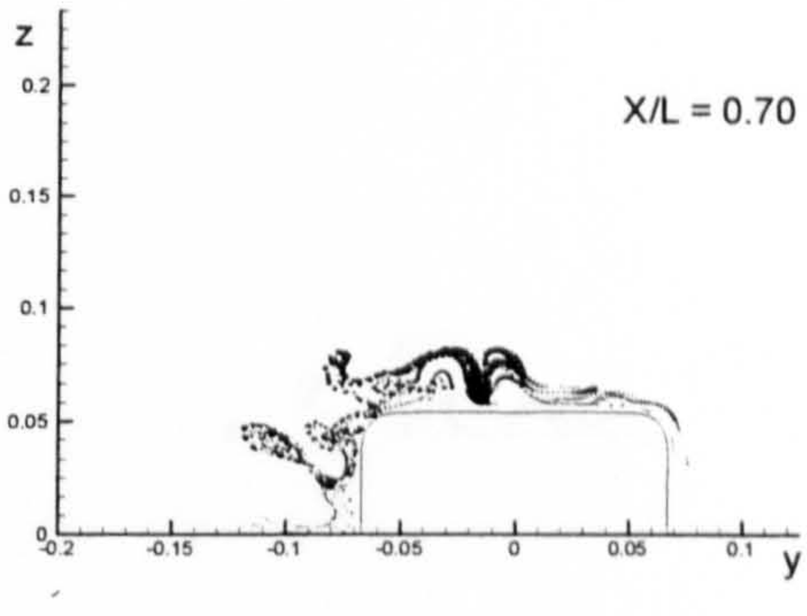

(British Bombardier with a pram stern)

Figure B.4: Comparison of vortex fields for the six ship hulls at $X/L = 0.70$ due to 10 degrees of drift motion.

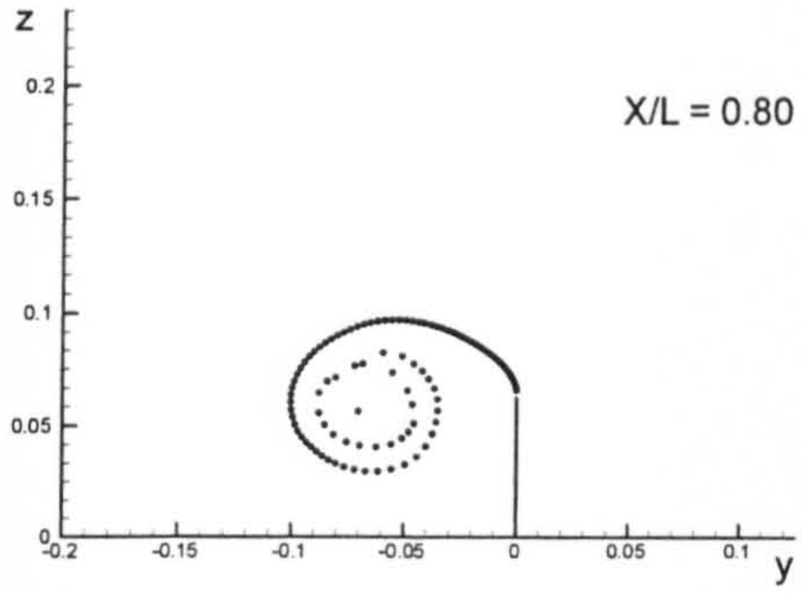

(Flat Plate)

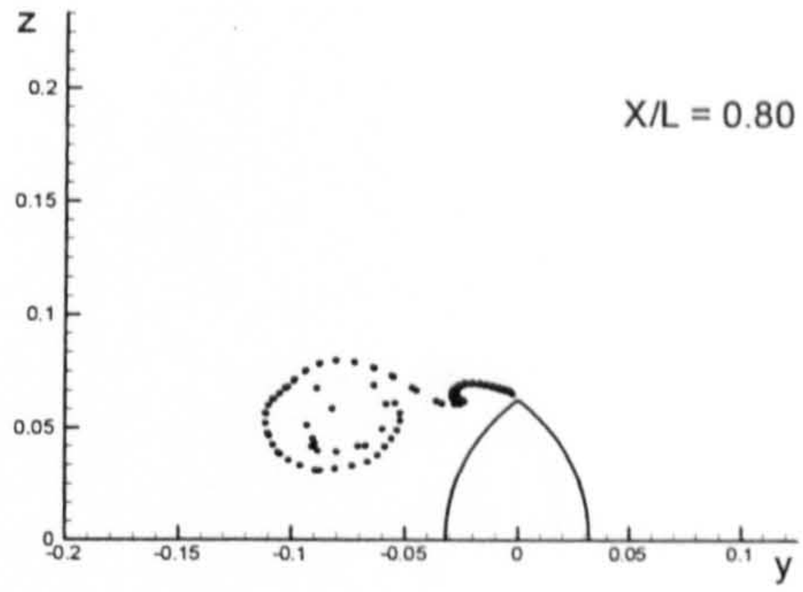

(Wigley Hull)

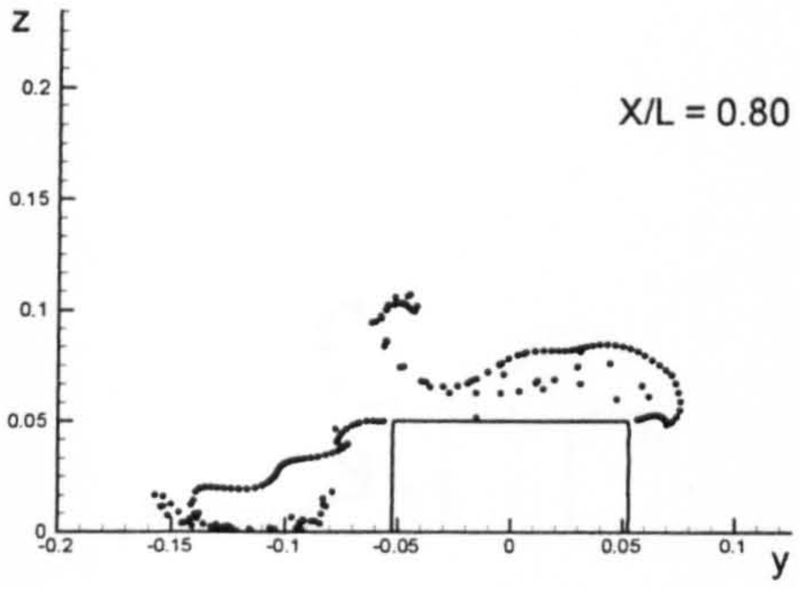

(Block Hull)

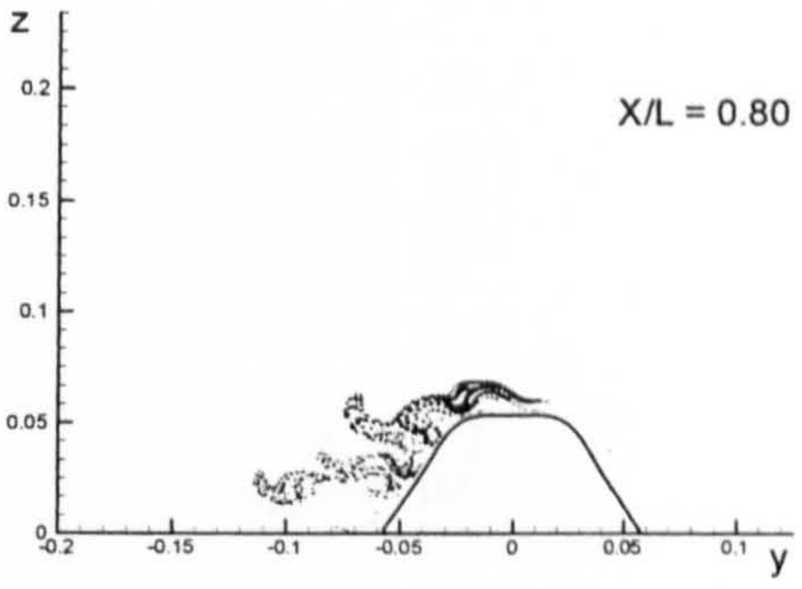

(Series 60 Hull)

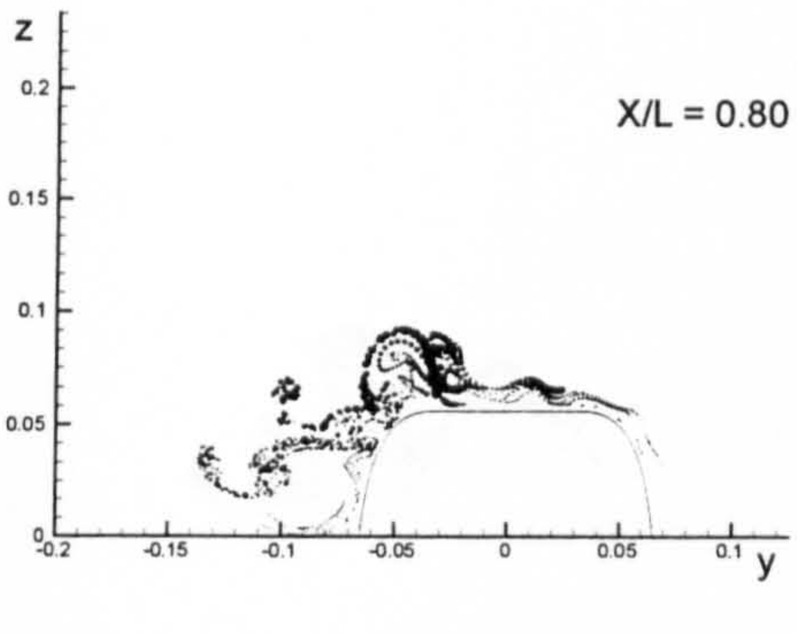

(British Bombardier)

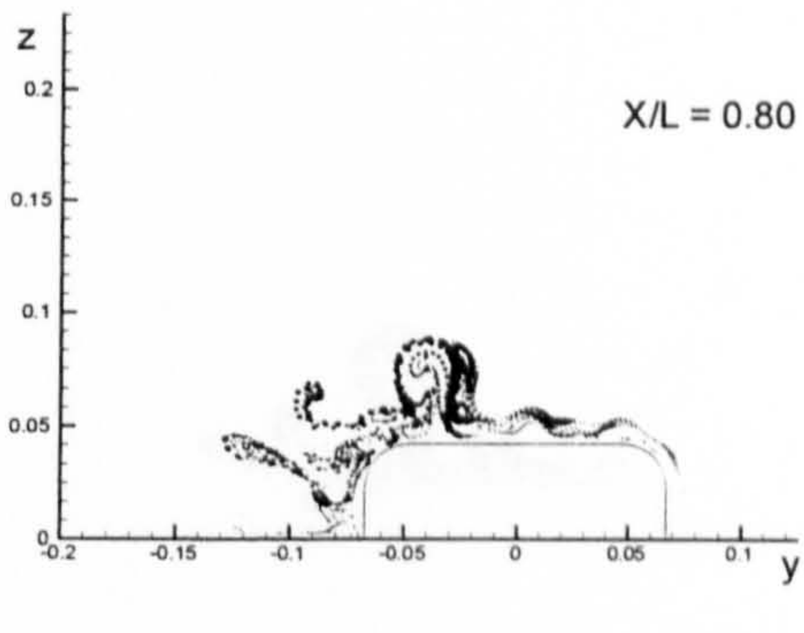

(British Bombardier with a pram stern)

Figure B.5: Comparison of vortex fields for the six ship hulls at $X/L = 0.80$ due to 10 degrees of drift motion.

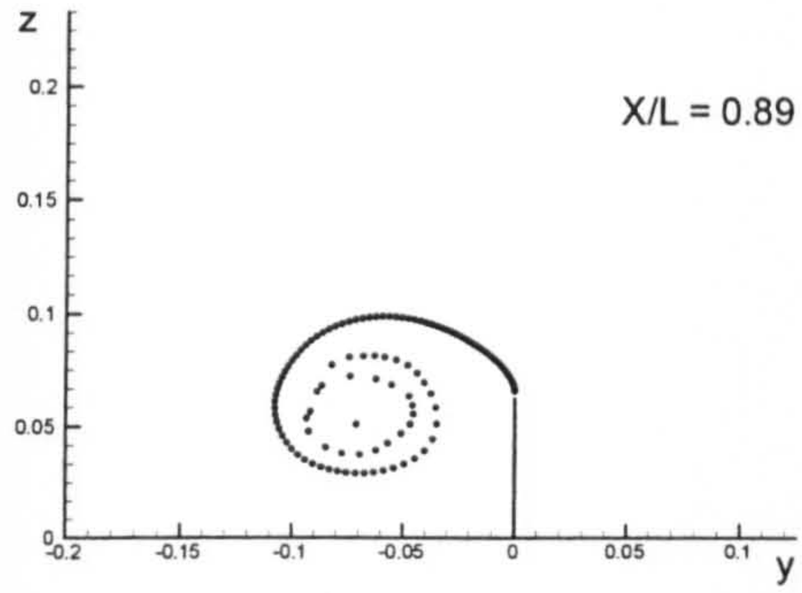

(Flat Plate)

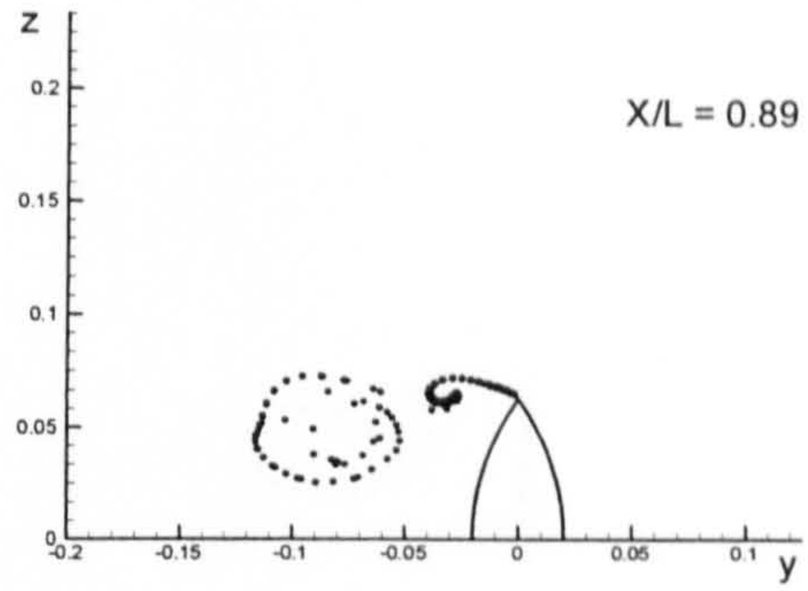

(Wigley Hull)

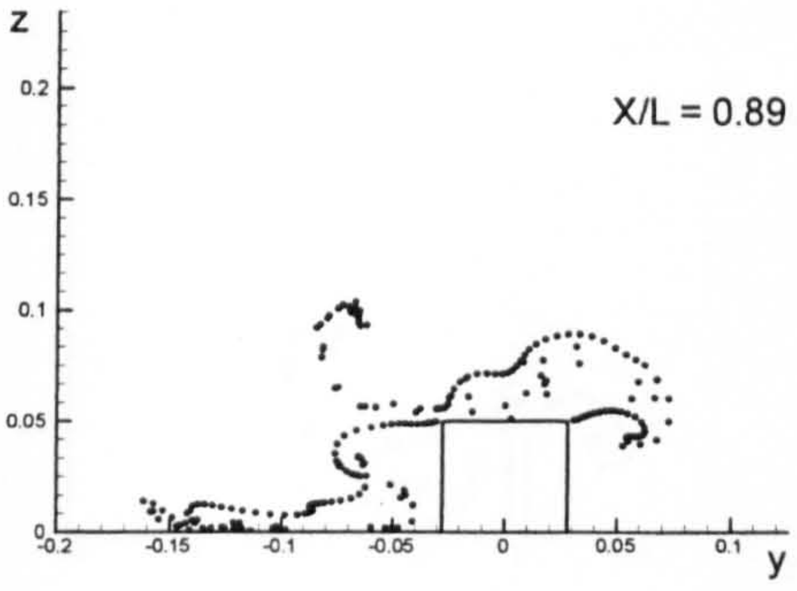

(Block Hull)

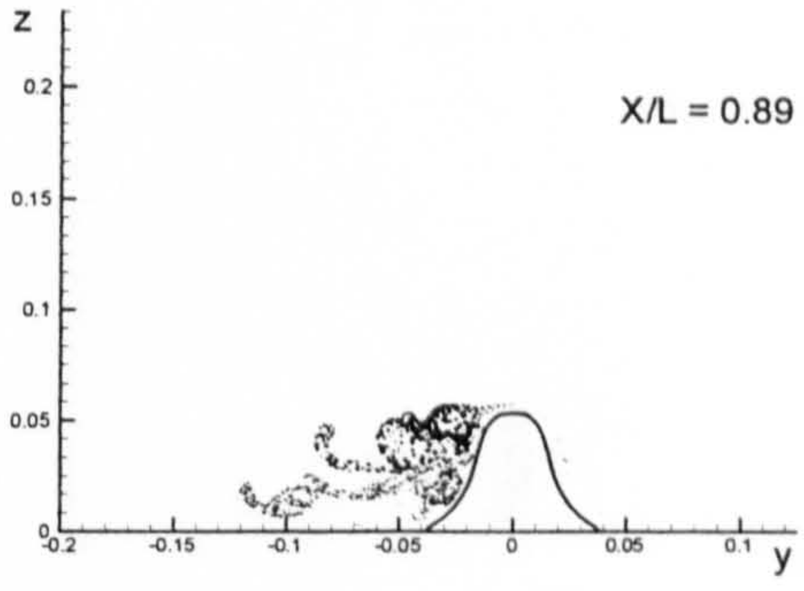

(Series 60 Hull)

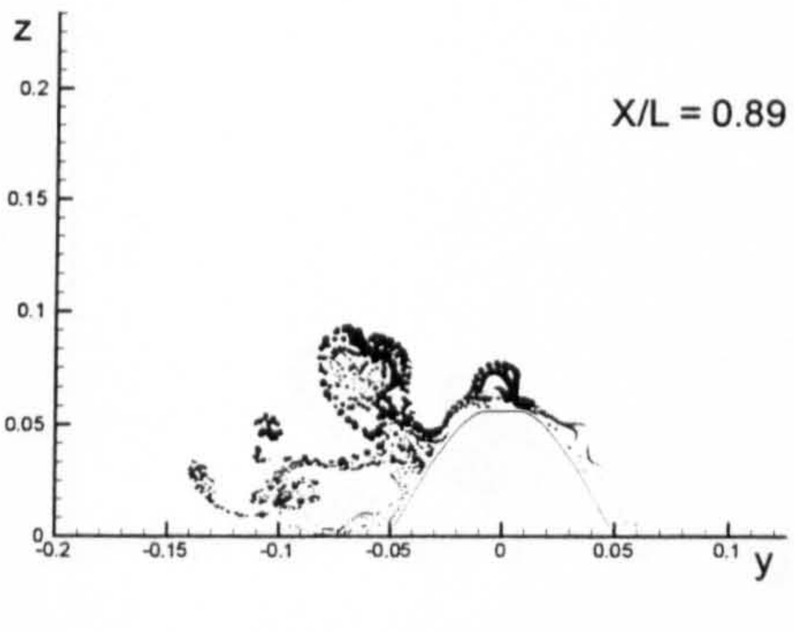

(British Bombardier)

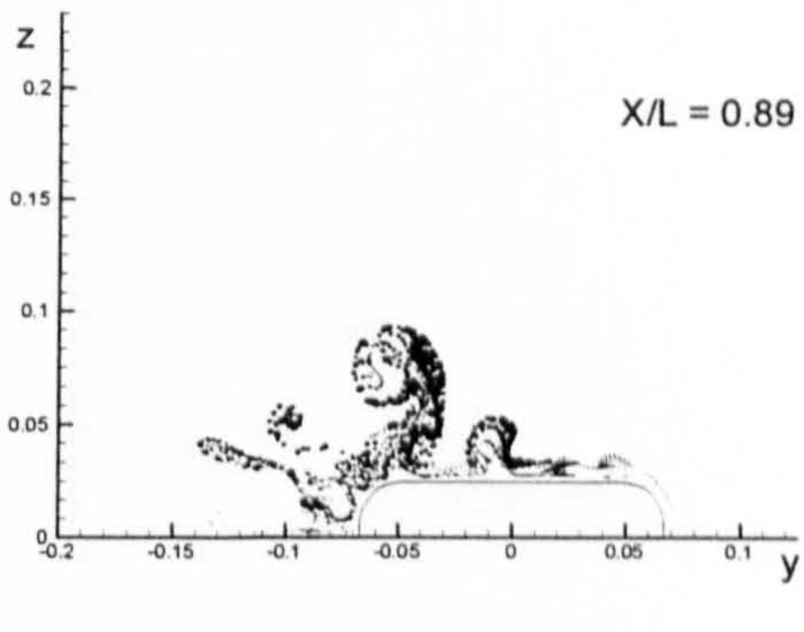

(British Bombardier with a pram stern)

Figure B.6: Comparison of vortex fields for the six ship hulls at $X/L = 0.89$ due to 10 degrees of drift motion.

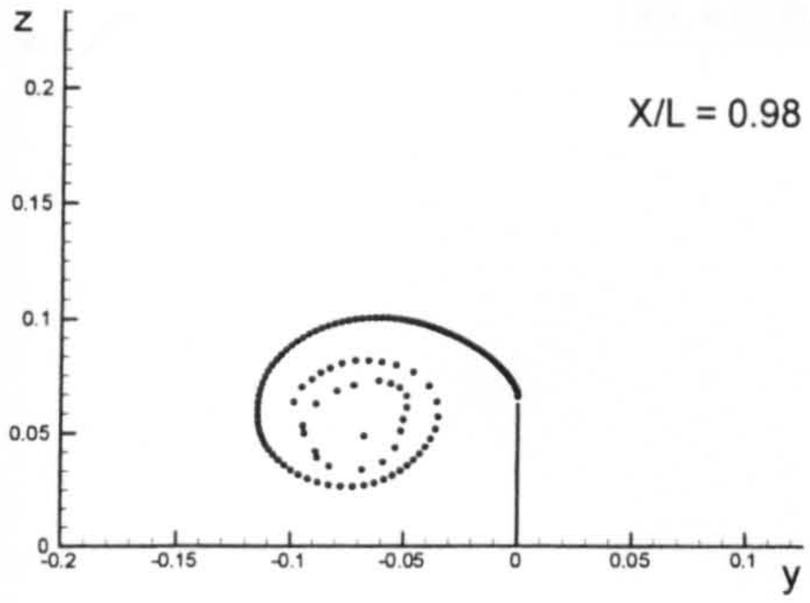

(Flat Plate)

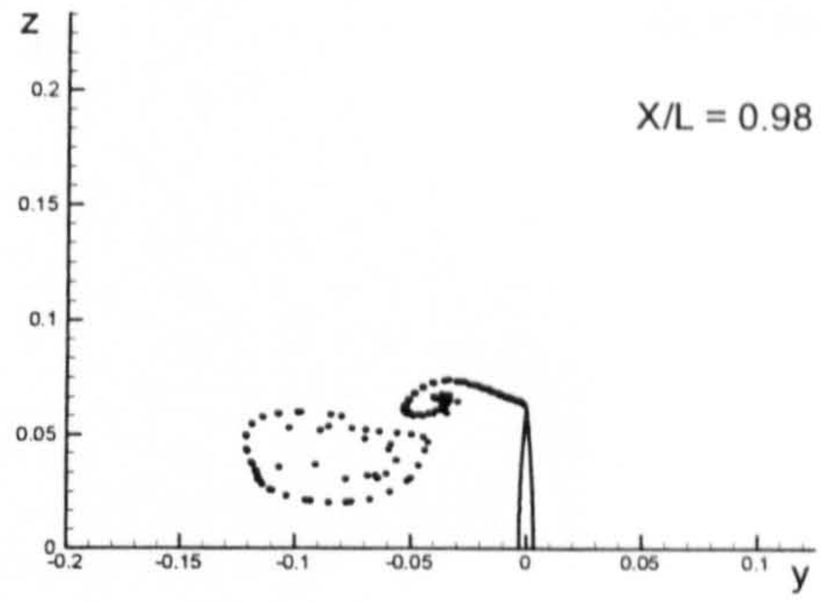

(Wigley Hull)

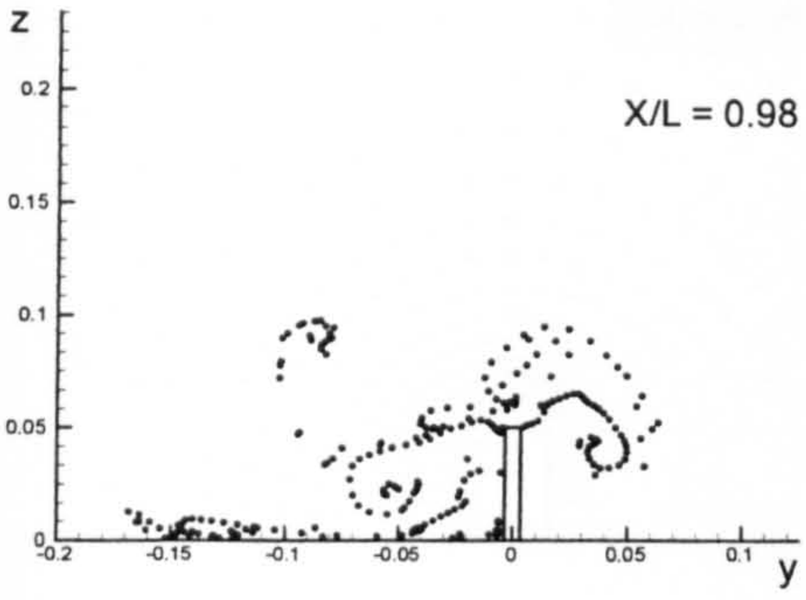

(Block Hull)

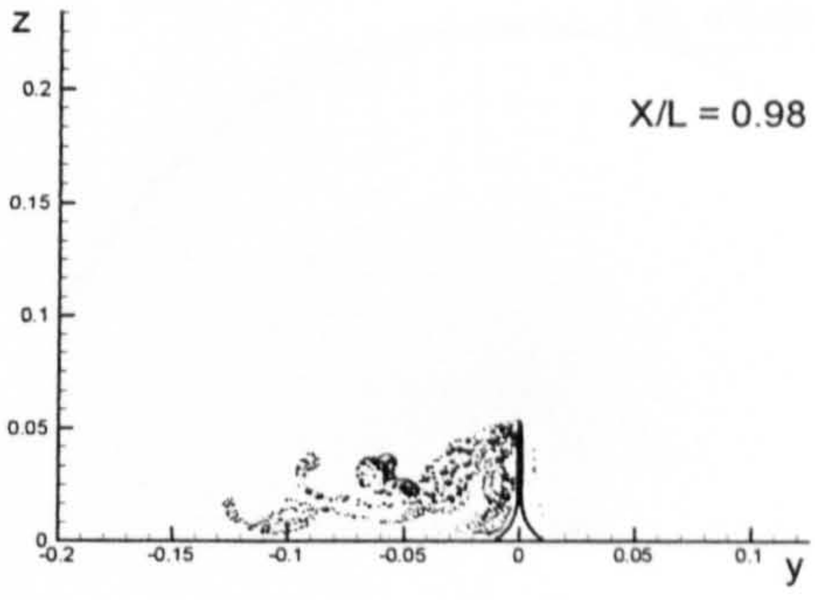

(Series 60 Hull)

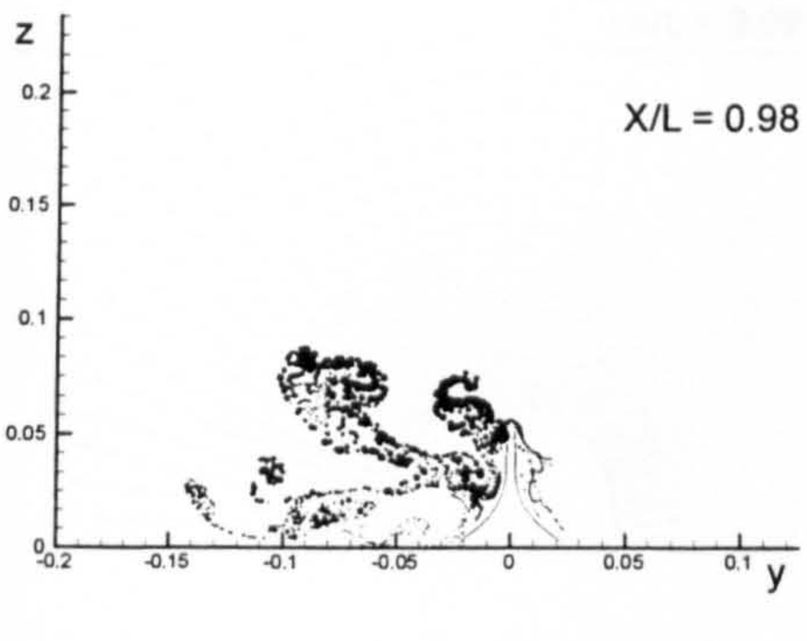

(British Bombardier)

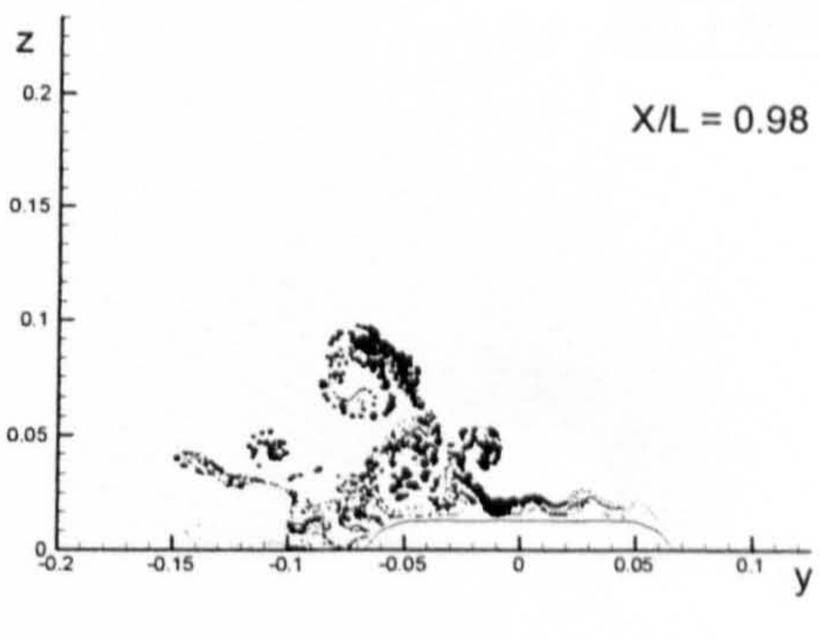

(British Bombardier with a pram stern)

Figure B.7: Comparison of vortex fields for the six ship hulls at $X/L = 0.98$ due to 10 degrees of drift motion.

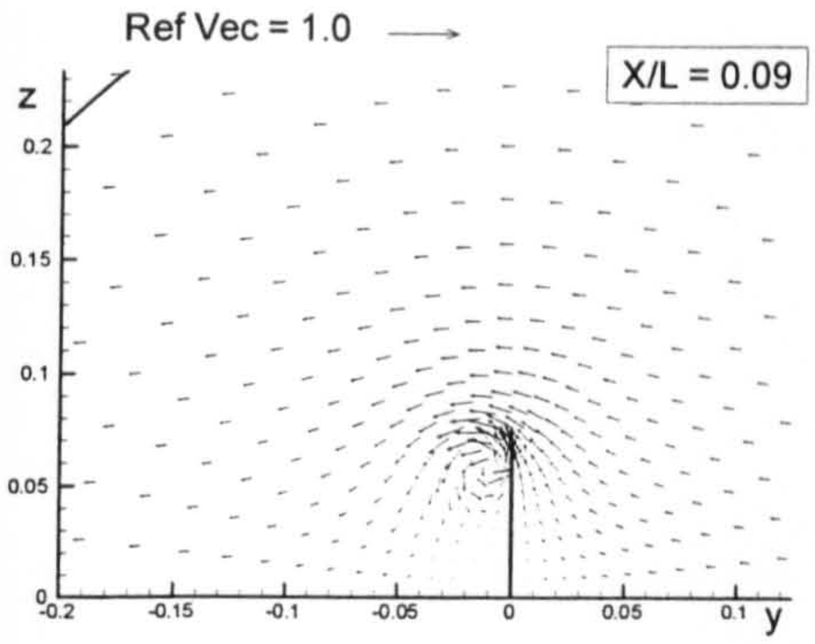

(Flat Plate)

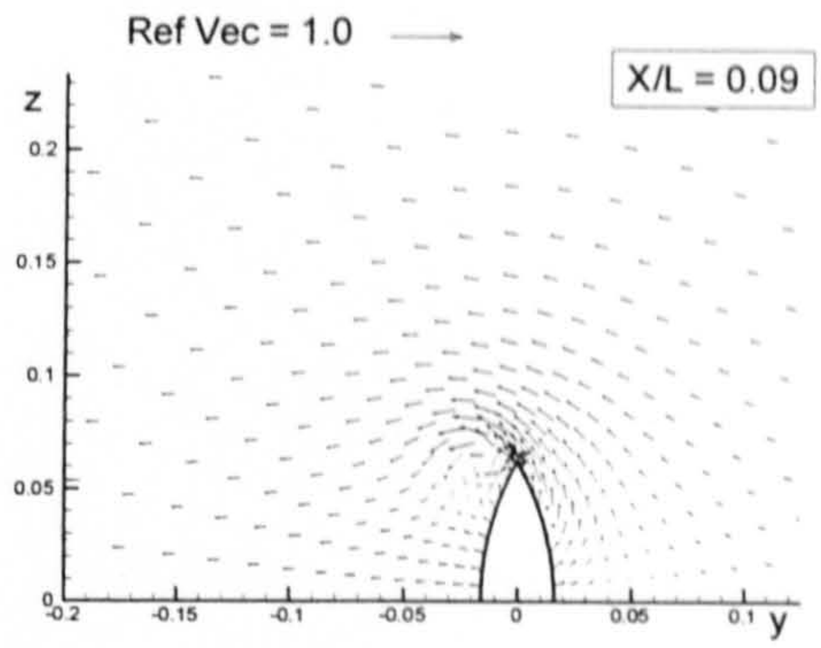

(Wigley Hull)

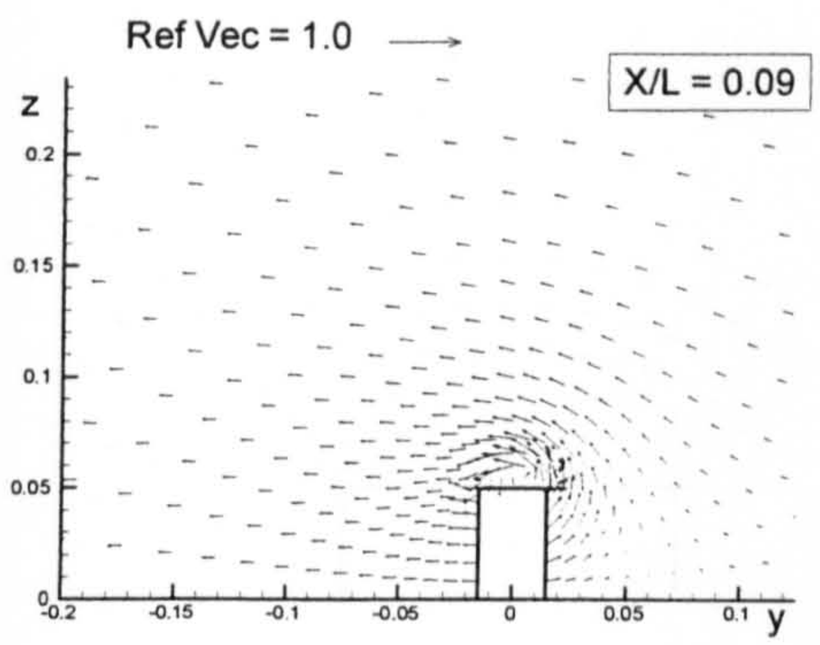

(Block Hull)

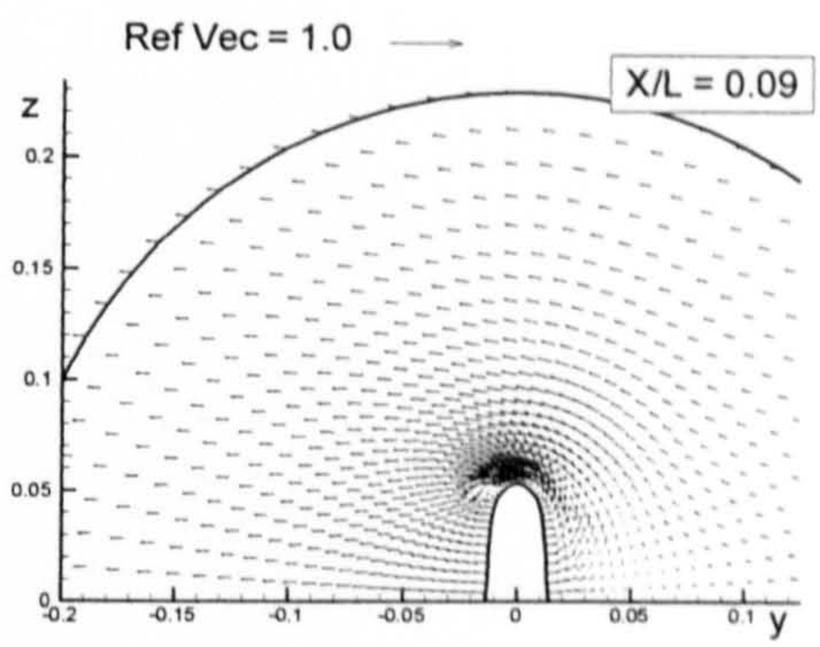

(Series 60 Hull)

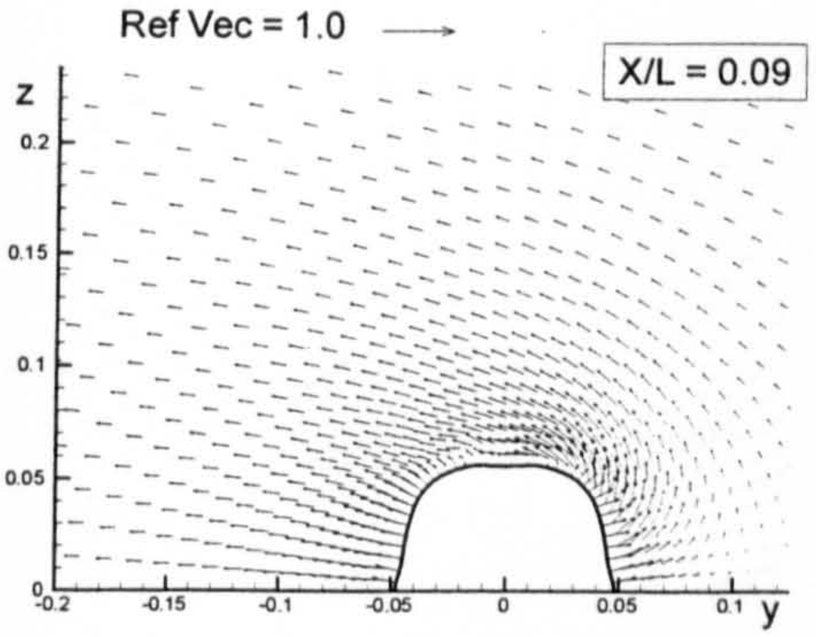

(British Bombardier)

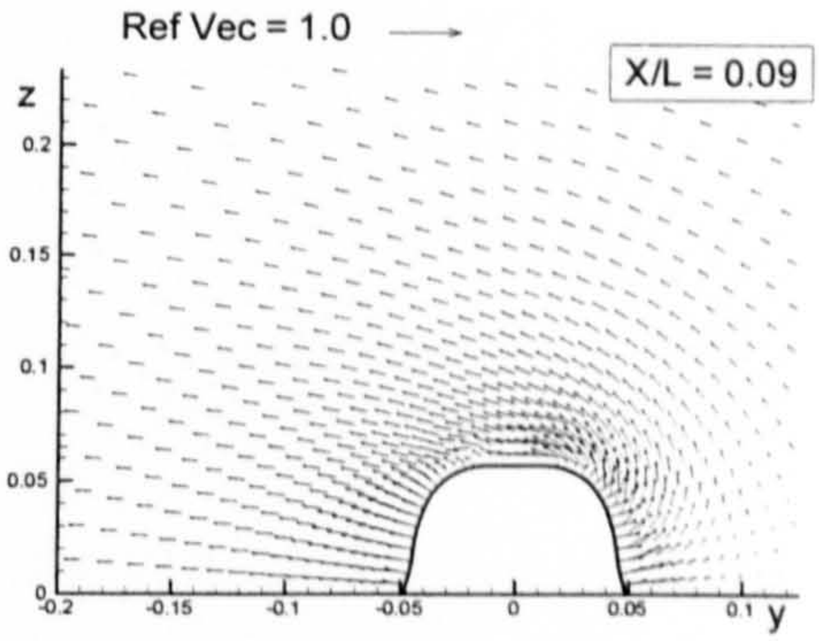

(British Bombardier with a pram stern)

Figure B.8: Comparison of velocity vectors for the six ship hulls at $X/L = 0.09$ due to 10 degrees of drift motion.

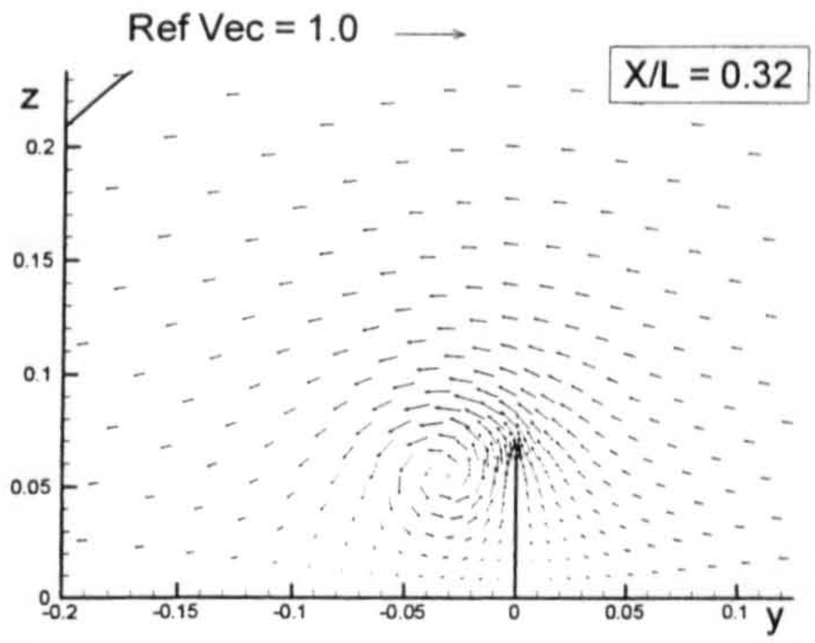

(Flat Plate)

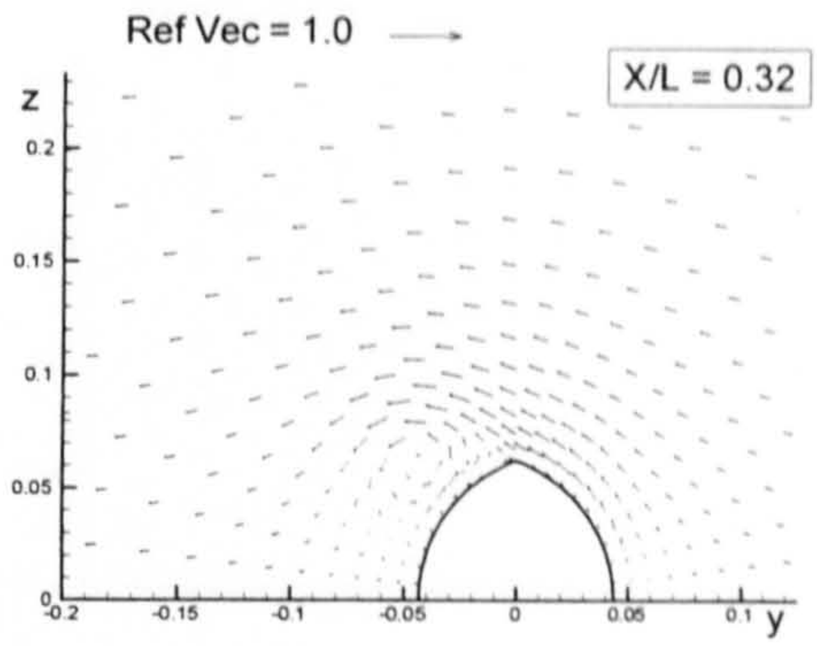

(Wigley Hull)

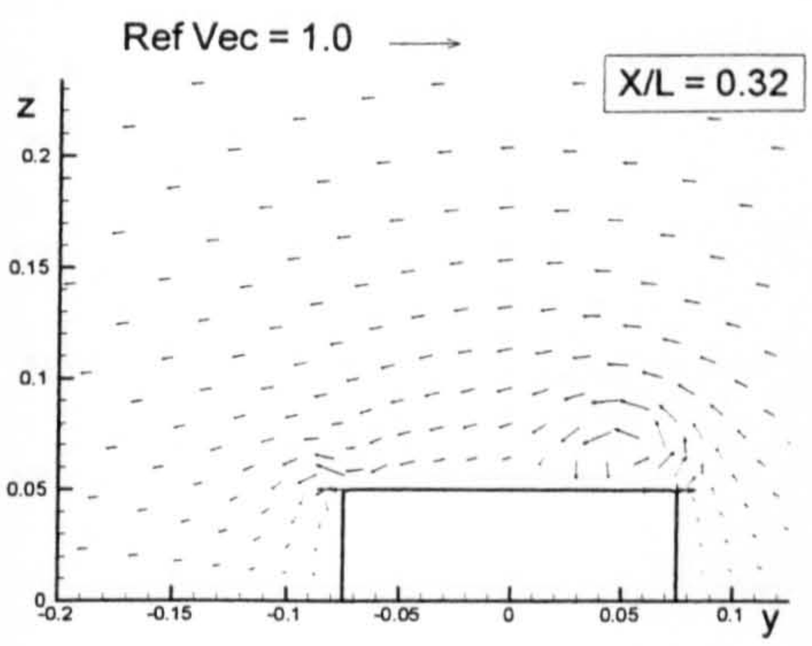

(Block Hull)

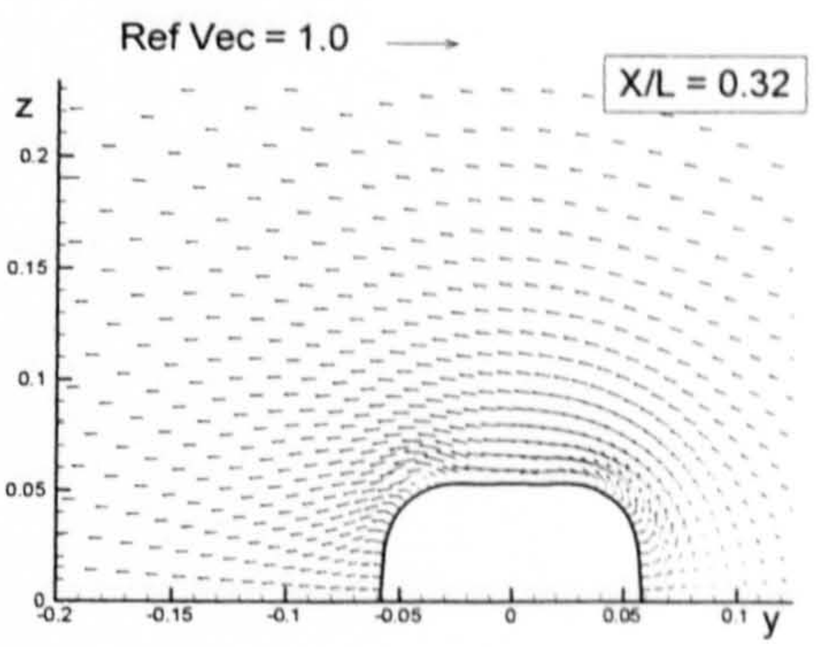

(Series 60 Hull)

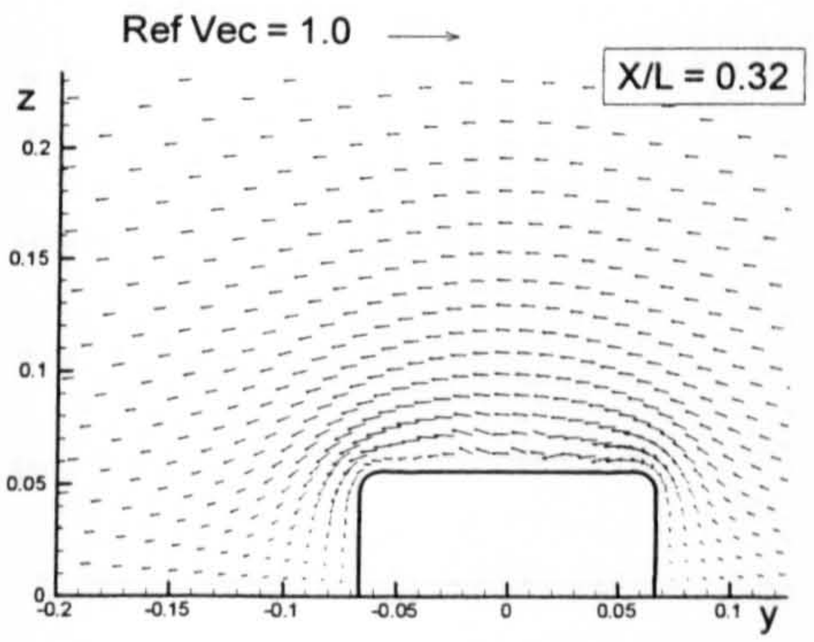

(British Bombardier)

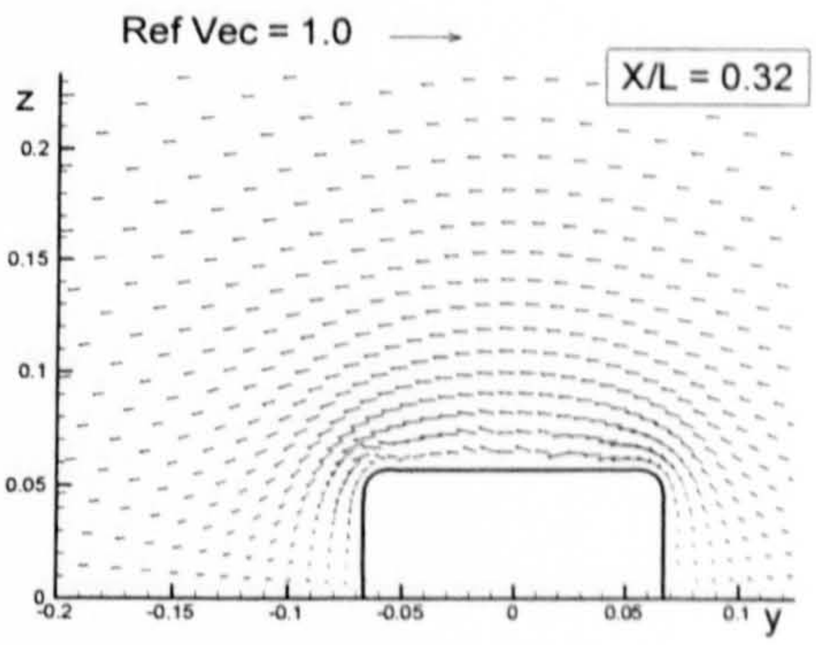

(British Bombardier with a pram stern)

Figure B.9: Comparison of velocity vectors for the six ship hulls at $X/L = 0.32$ due to 10 degrees of drift motion.

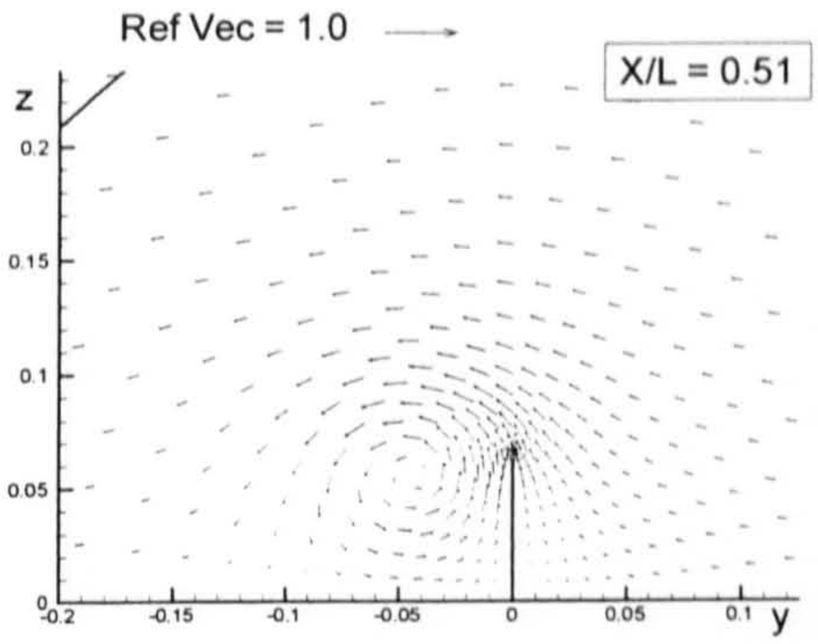

(Flat Plate)

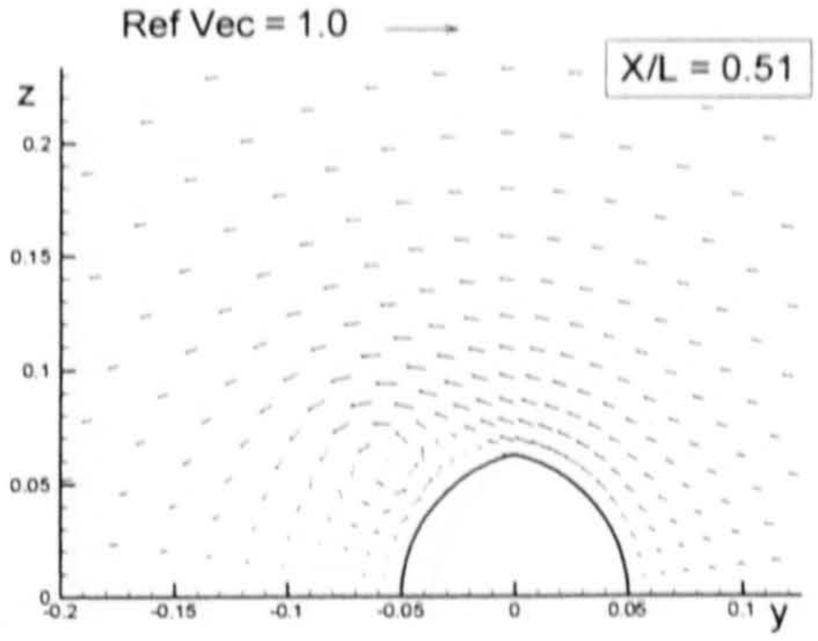

(Wigley Hull)

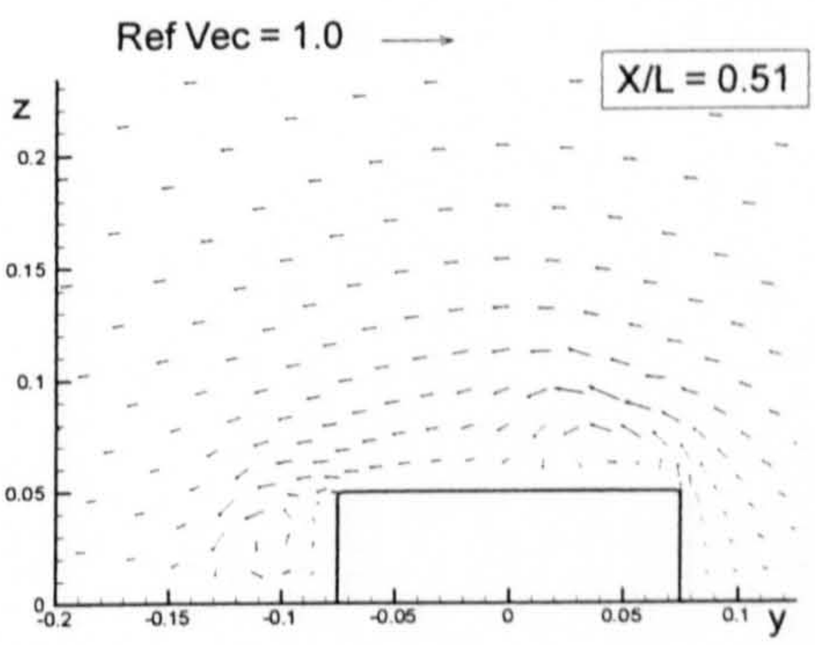

(Block Hull)

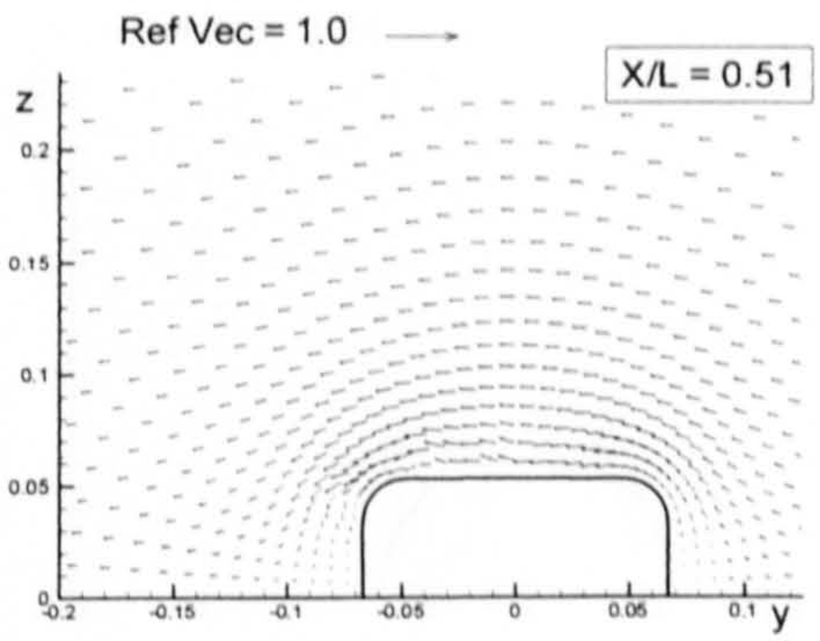

(Series 60 Hull)

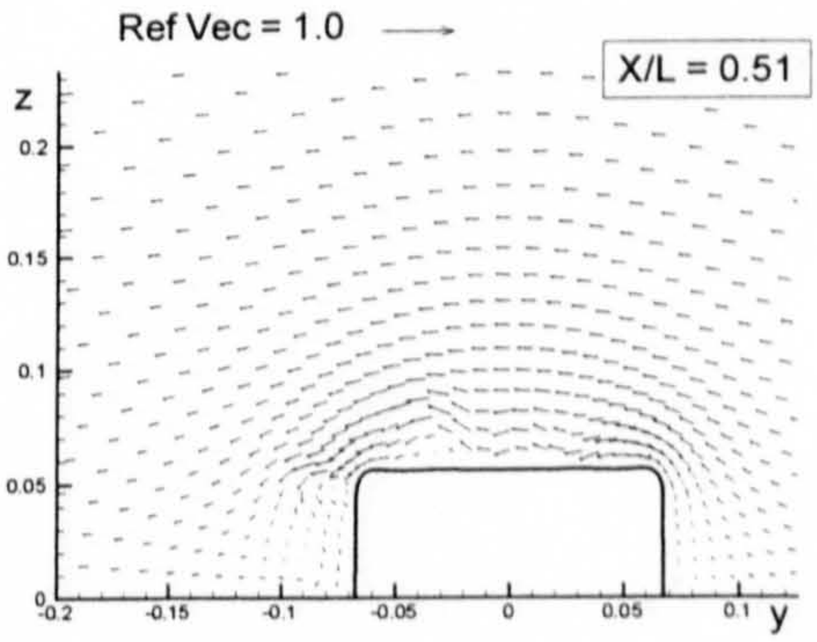

(British Bombardier)

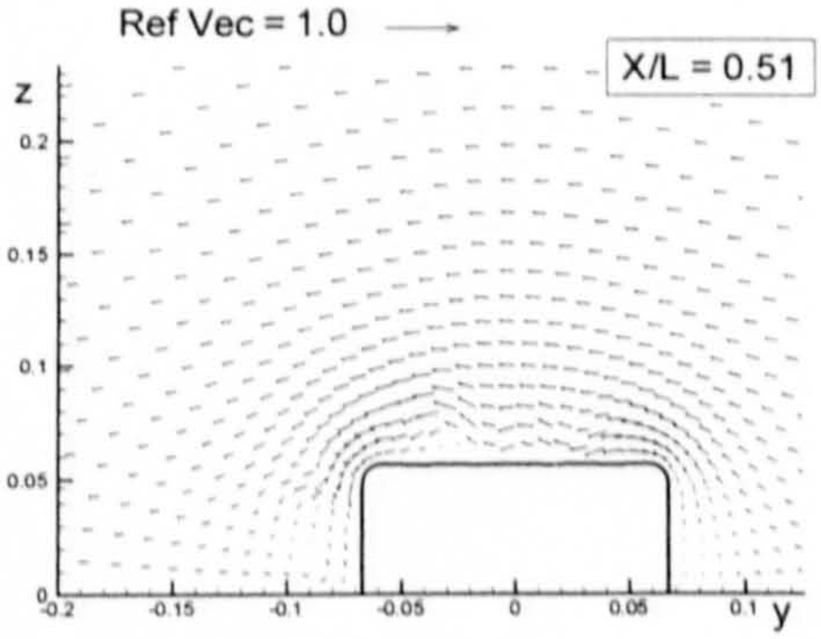

(British Bombardier with a pram stern)

Figure B.10: Comparison of velocity vectors for the six ship hulls at $X/L = 0.51$ due to 10 degrees of drift motion.

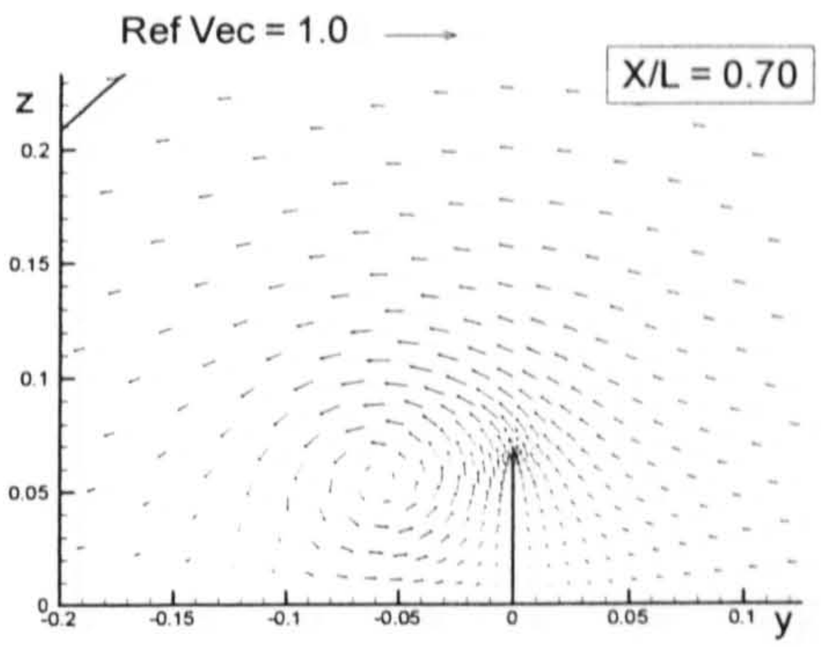

(Flat Plate)

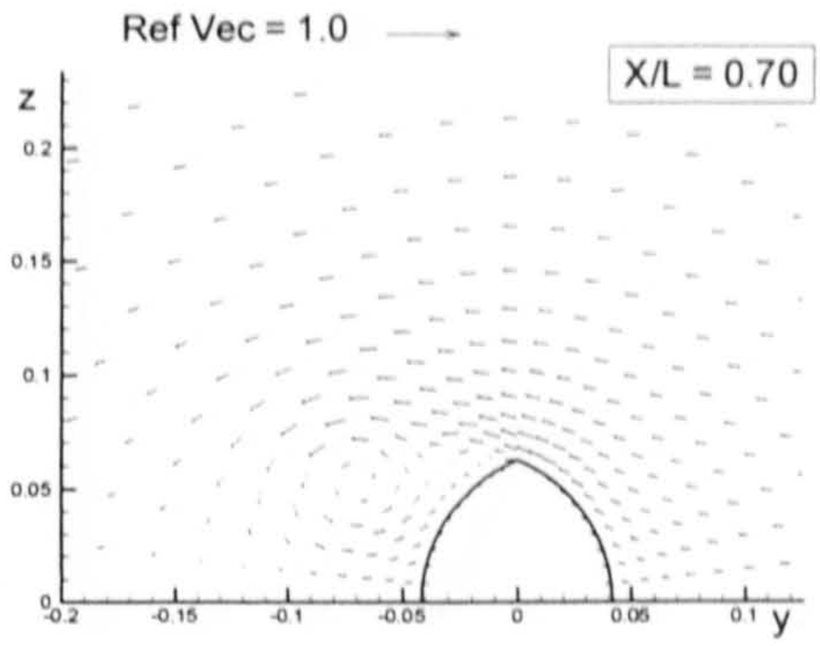

(Wigley Hull)

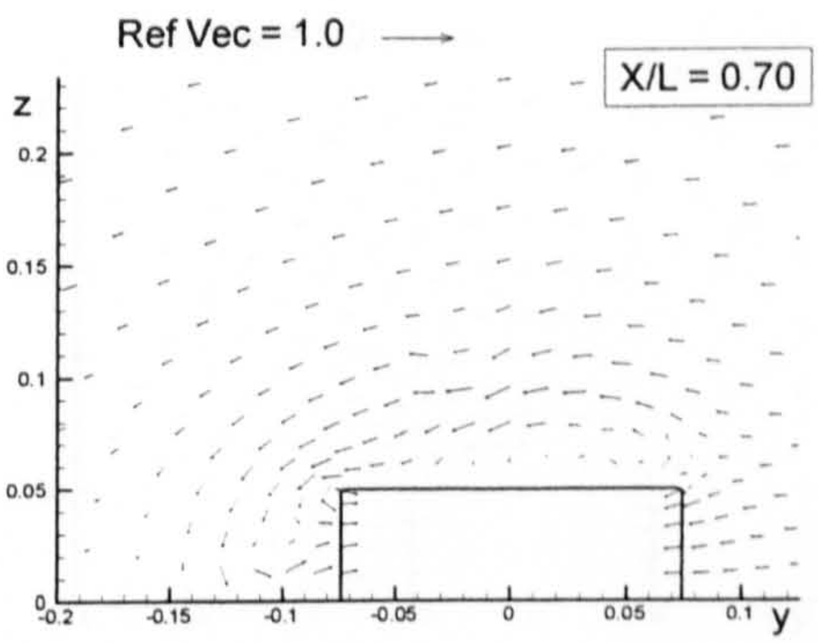

(Block Hull)

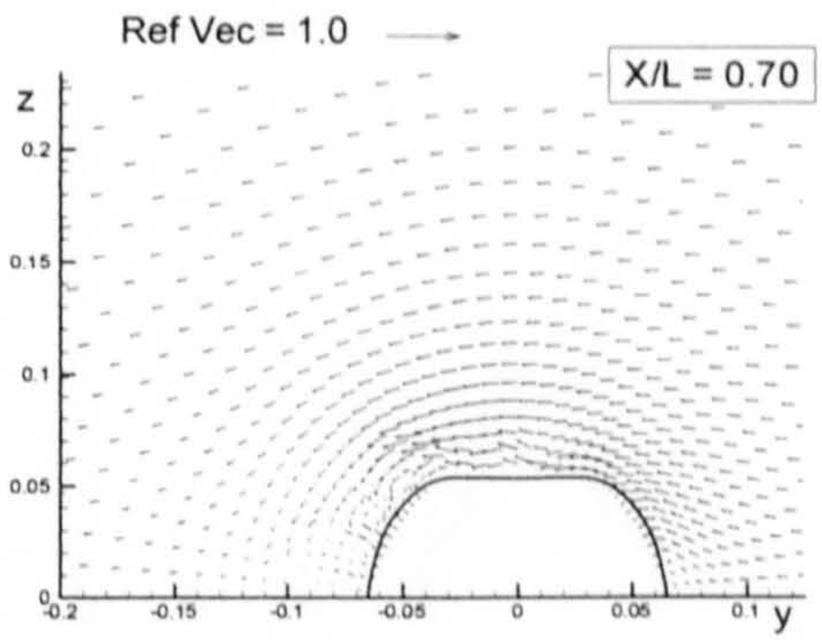

(Series 60 Hull)

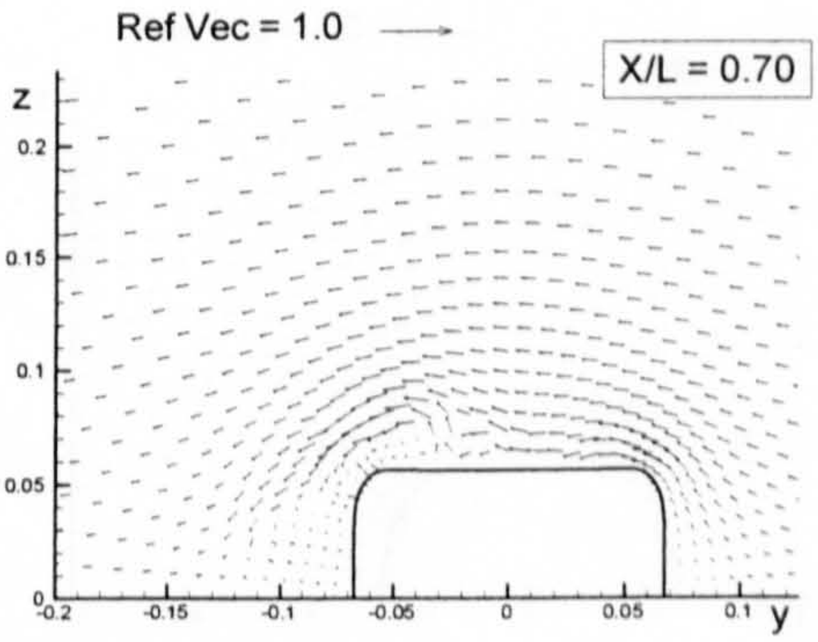

(British Bombardier)

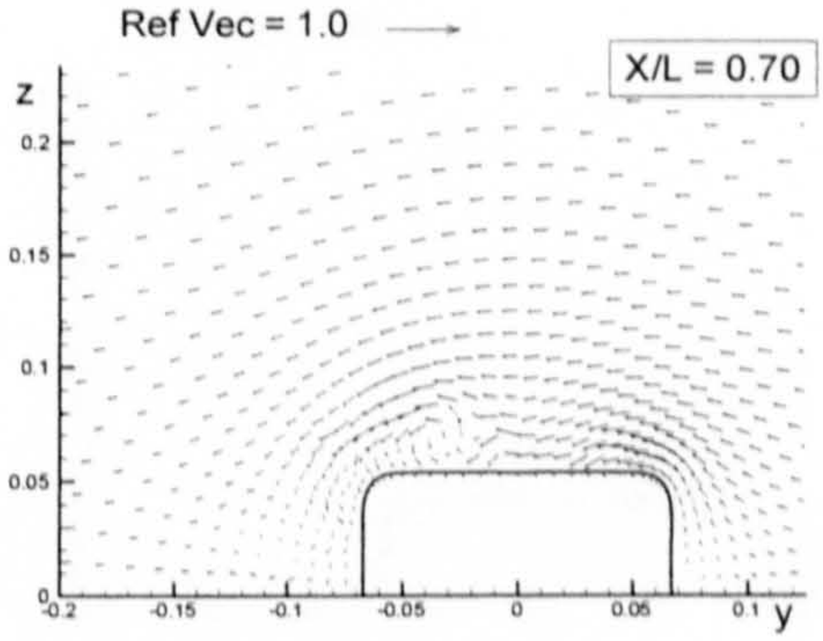

(British Bombardier with a pram stern)

Figure B.11: Comparison of velocity vectors for the six ship hulls at $X/L = 0.70$ due to 10 degrees of drift motion.

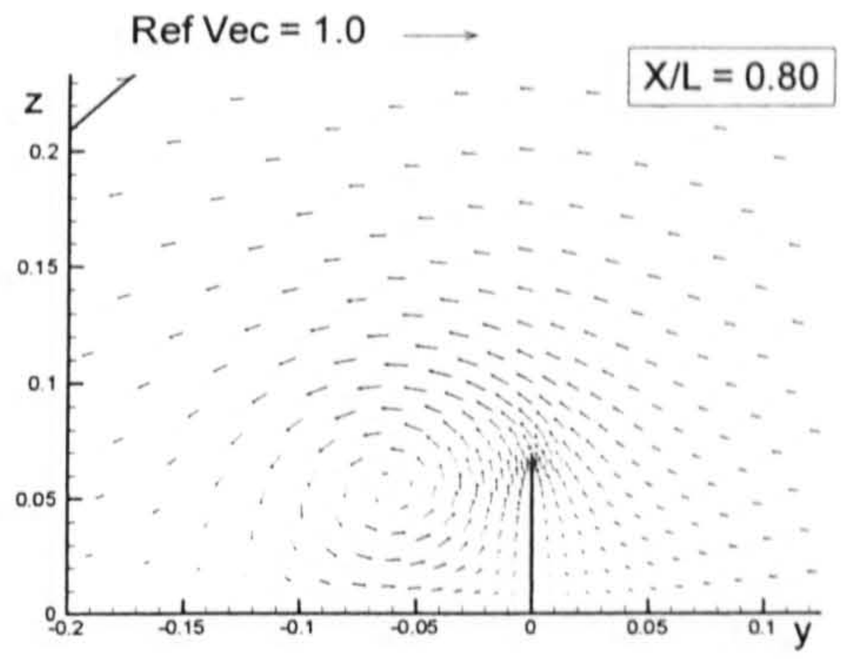

(Flat Plate)

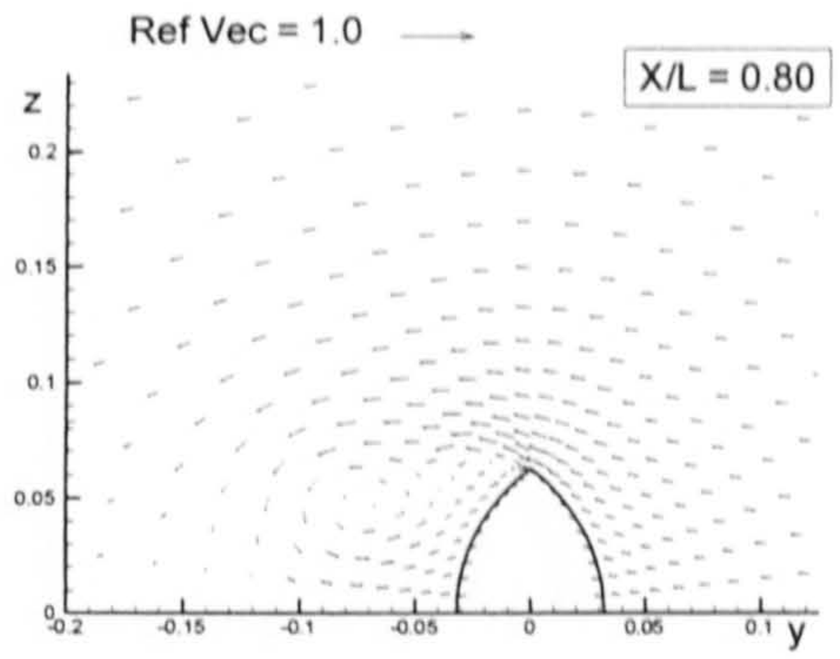

(Wigley Hull)

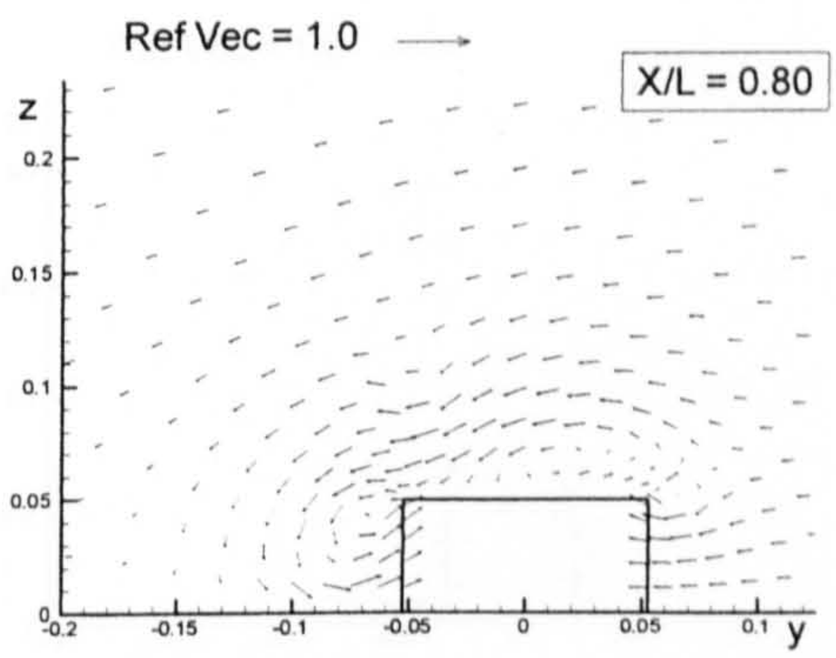

(Block Hull)

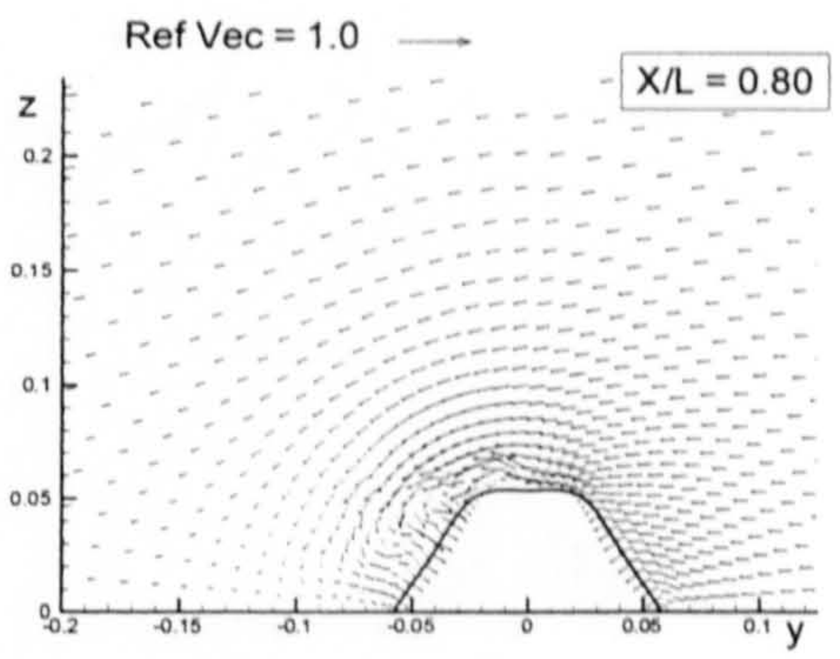

(Series 60 Hull)

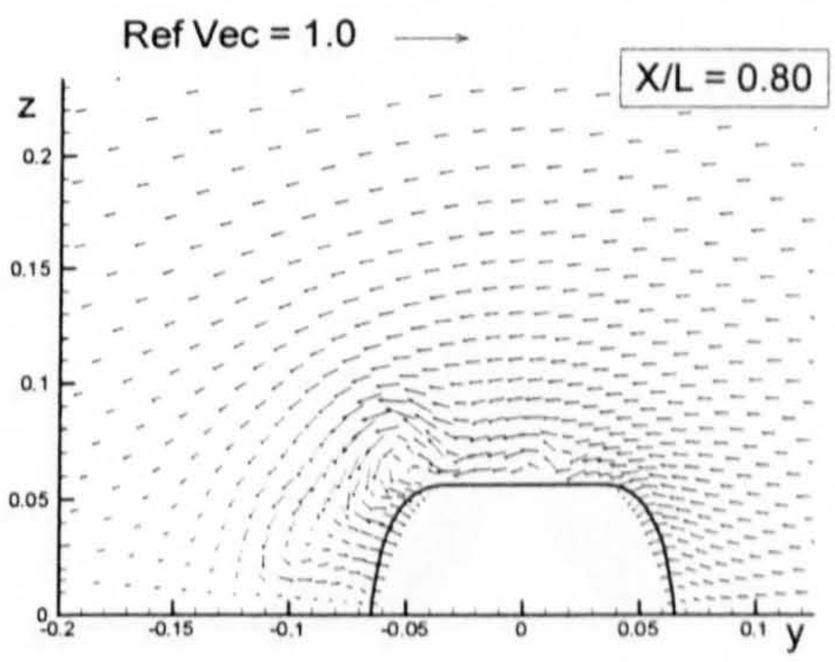

(British Bombardier)

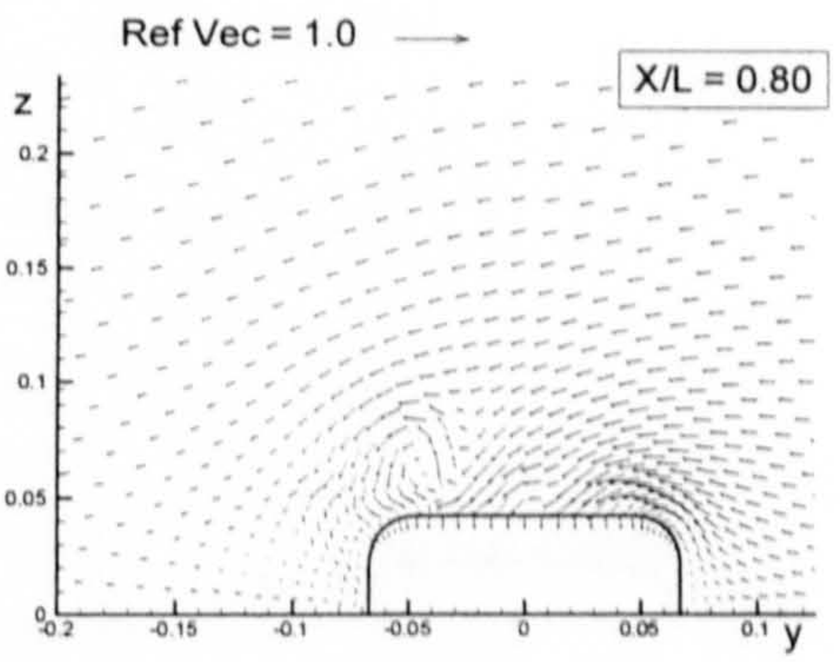

(British Bombardier with a pram stern)

Figure B.12: Comparison of velocity vectors for the six ship hulls at $X/L = 0.80$ due to 10 degrees of drift motion.

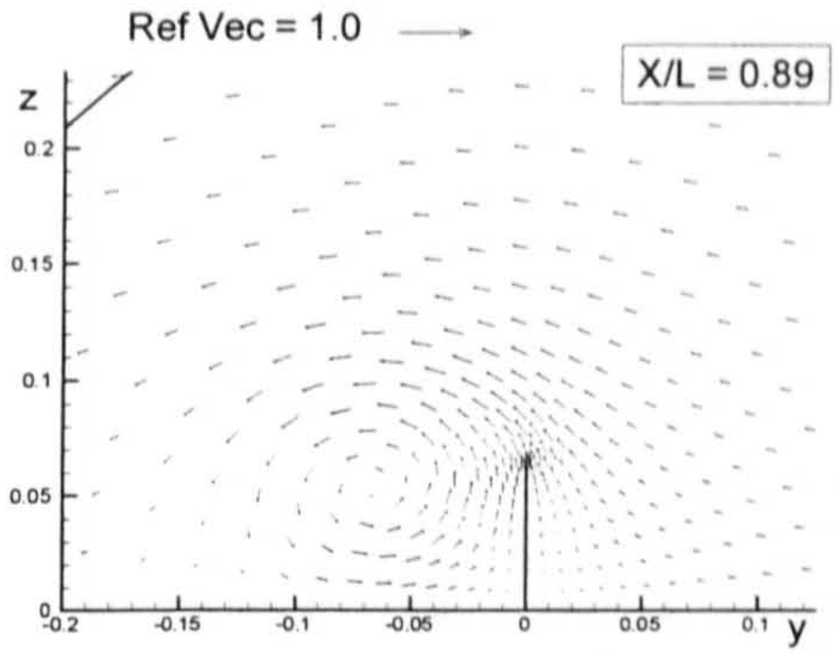

(Flat Plate)

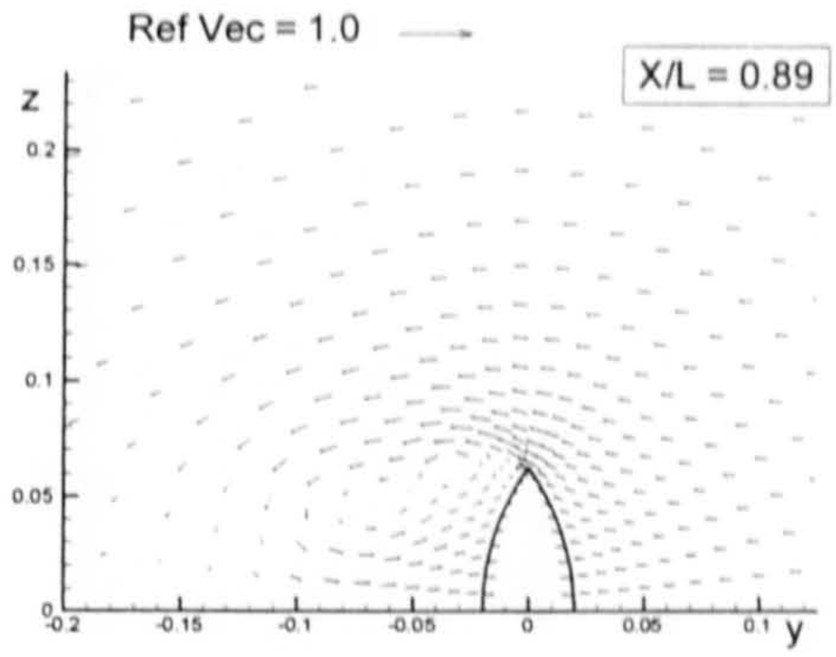

(Wigley Hull)

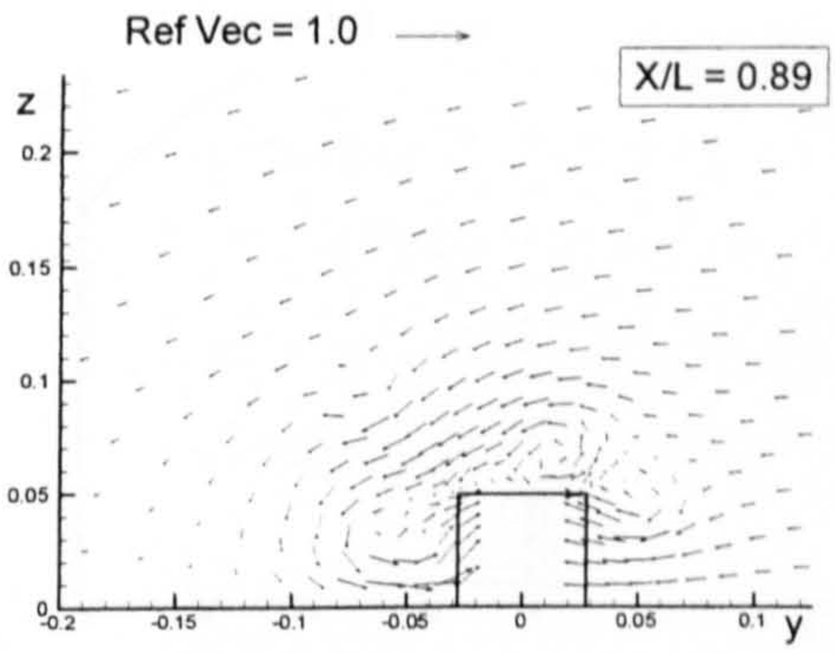

(Block Hull)

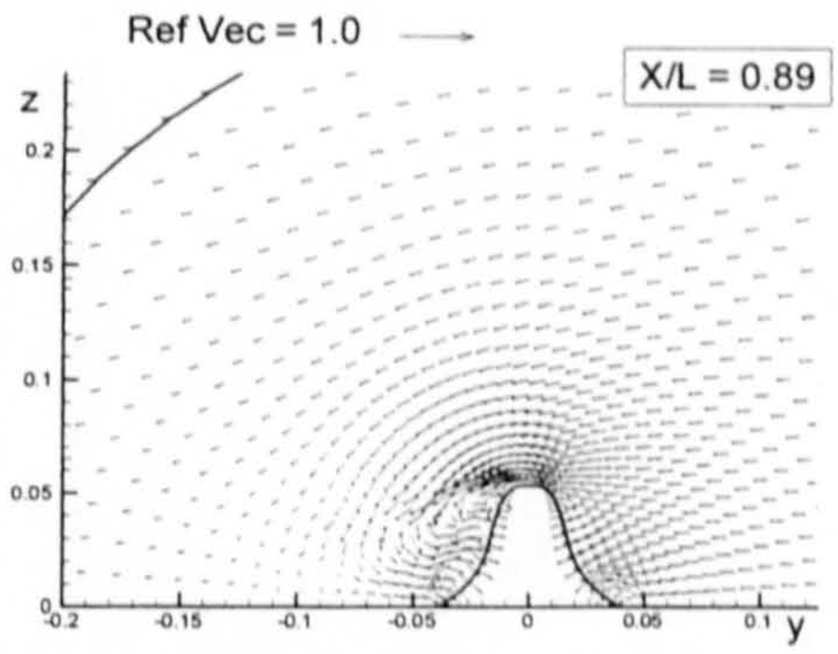

(Series 60 Hull)

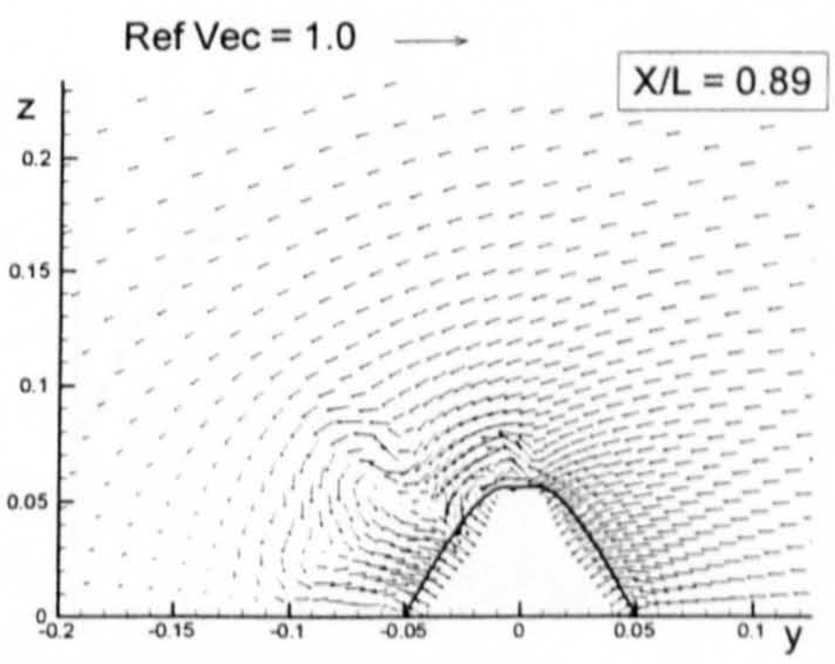

(British Bombardier)

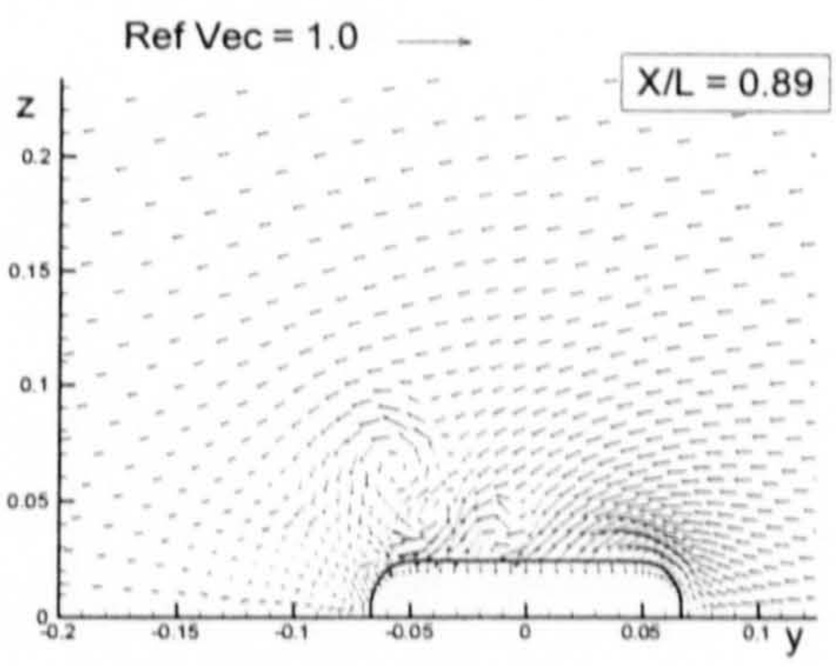

(British Bombardier with a pram stern)

Figure B.13: Comparison of velocity vectors for the six ship hulls at $X/L = 0.89$ due to 10 degrees of drift motion.

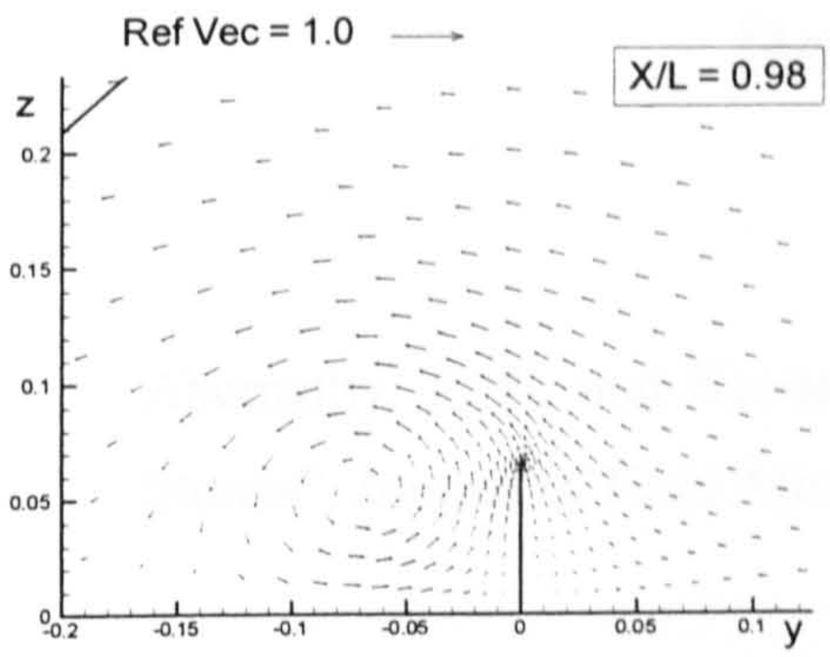

(Flat Plate)

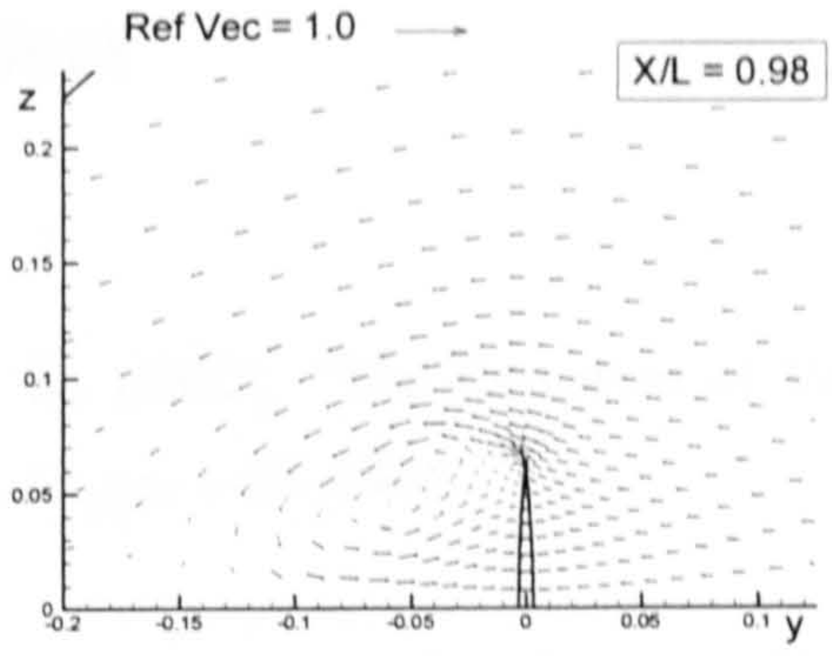

(Wigley Hull)

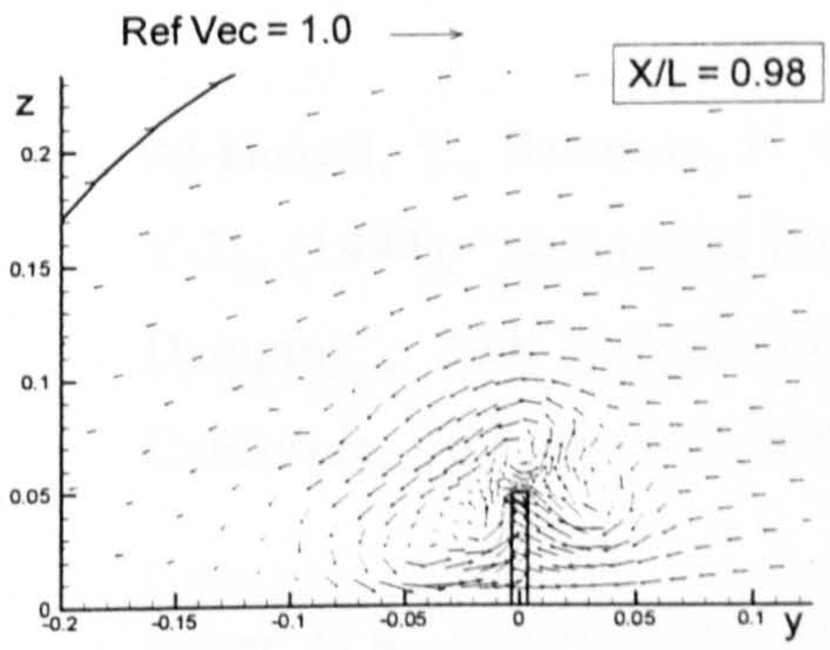

(Block Hull)

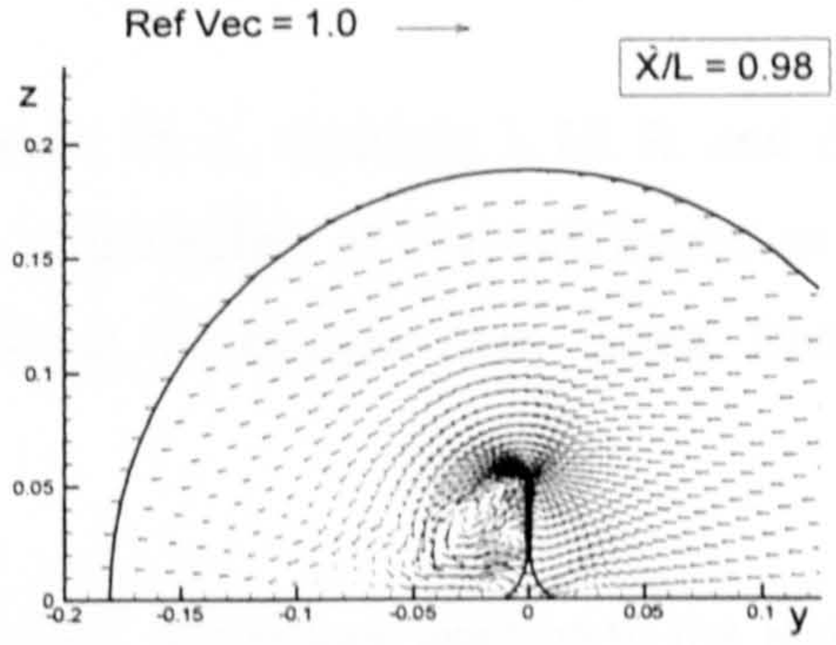

(Series 60 Hull)

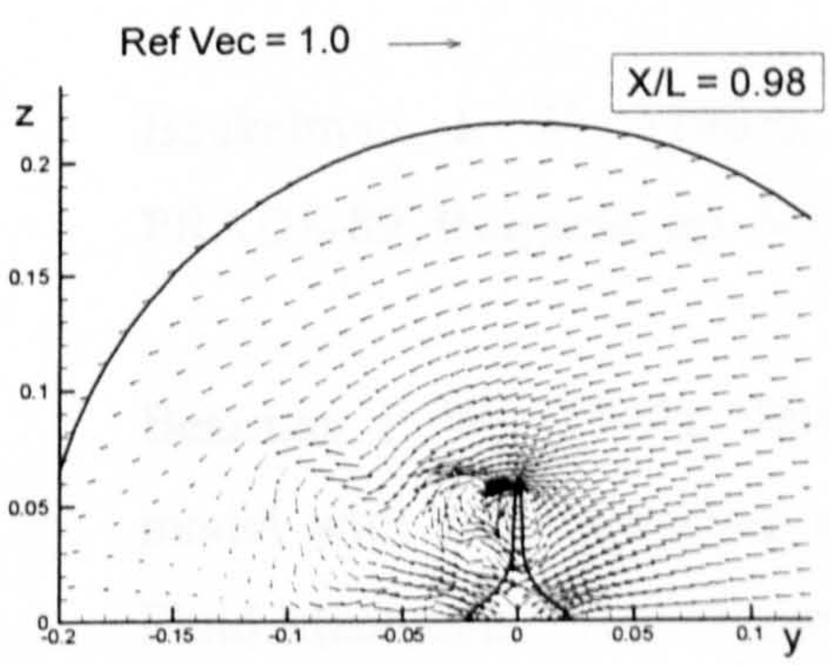

(British Bombardier)

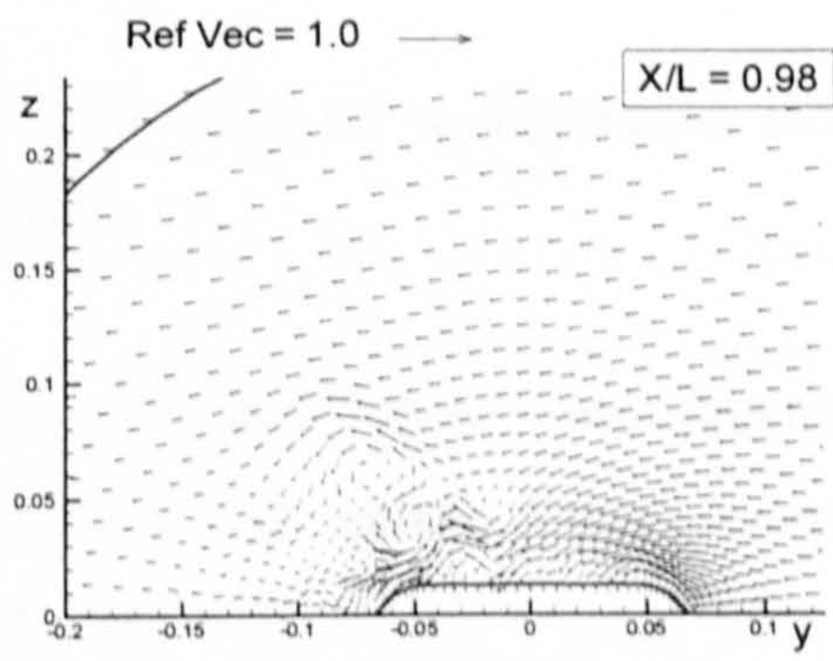

(British Bombardier with a pram stern)

Figure B.14: Comparison of velocity vectors for the six ship hulls at $X/L = 0.98$ due to 10 degrees of drift motion.

References

[1] Abernathy, F. H. and Kronauer, R. E., (1962), "The formation of Vortex Streets", Journal of Fluid Mechanics, 13, pp. 1-20, 1962.

[2] Al-Hukail, Y., (1992), "Roll Damping due to Vortex Shedding from Slender Ship Hull in Forward Motion", PhD Thesis, Aero Dept, Imperial College, London, 1992.

[3] Al-Hukail, Y., Bearman, P. W., Downie, M. J., Graham, J. M. R. and Zhao, Y-D., (1994), "Numerical Prediction of the Effect of Forward Speed on Roll Damping", 20th Symposium on Naval Hydrodynamics, Santa Barbara, California, USA, pp. 657-668, 1994.

[4] Baker, G.R., (1979), "The 'Cloud In Cell' Technique applied to the Roll Up of Vortex Sheets", Journal of Computational Physics, Vol. 31, pp.76-95, 1979.

[5] Beukelman, I. W., (1989), "Cross flow drag on a segmented model", PRADS-89, Bulgaria, pp. 5-1-5-11, 1989.

[6] Bearman, P. W., (1965), "Investigation of the flow behind a two-dimensional model with a blunt trailing edge and fitted with splitter plates", Journal of Fluid Mechanics, Vol. 21, pp.241-255, 1965.

[7] Birkhoff, G. and Fisher, J., (1959), "Do Vortex Sheets Roll up", Rendi. Circ. Mat. Palermo, Ser. 2, 8, pp. 77-80, 1959.

[8] Bradbury, W. M. S., (1983), "Large Sailing Ships – A Fluid Dynamic Investigation", PhD Thesis, Aero Dept, Imperial College, London, 1983.

[9] Bradbury, W. M. S., (1987), "A Bilge Vortex Calculation", Trans. RINA, Vol.129, pp.189-198, 1987.

[10] Bradshaw, P., Cebeci, T. and Whitelaw, J. H., (1981), "Engineering Calculation Methods for Turbulent Flow ", Academic Press, 1981.

[11] Brown, C. E. and Michael, W. H., (1954), "Effect of Leading Edge Separation on the Lift of Delta Wing", Journal of Aeronautical Science, Vol. 21, p690, 1954.

[12] Brown, C. E. and Michael, W. H., (1955), "On Slender Delta Wings with Leading-edge Separation", N.A.S.A. Technical Note 3430, 1955.

[13] Bruzzone, D., (1994), "Numerical Evaluation of the Steady Free Surface Waves", Proceedings of CFD Workshop, Tokyo, pp. 126-134, 1994.

[14] Burcher, R. K., (1972), "Developments in Ship Manoeuvrability", Trans. RINA, Vol.114, pp.1-32, 1972.

[15] Campana, E., Esposito, P. and Penna, R. (1994), "Numerical Simulation of the Drift Motion of a Ship", 20th Symposium on Naval Hydrodynamics, Santa Barbara, California, USA, pp. 856-869, 1994.

[16] CFD Workshop Tokyo, (1994), Proceedings of Vol.1 and Vol. 2, Ship Research Institute Ministry of Transport Ship & Ocean Foundation, 1994.

[17] CFX 4.1 Flow Solver User Guide, (1995), Computational Fluid Dynamics Services, U.K, 1995.

[18] Chan, H. S., Varyani, K. S. and Incecik, A., (1993),"Experimental Investigation of the Hydrodynamics of a Ship Moving at Drift Angle", Technical Report, NAOE 93-25, University of Glasgow, 1993.

[19] Chapman, R. B., (1976a), "Free-Surface Effects for Yawed Surface-Piercing Plates", Journal of Ship Research, Vol. 20, No. 3, pp. 125-136, 1976.

[20] Chapman, R. B., (1976b), "Prediction of Free-Surface Effects on Ship Manoeuvring", 11th Symposium on Naval Hydrodynamics, London, UK, pp. 533-543, 1976.

[21] Christiansen, J.P. (1973), "Numerical Simulation of Hydrodynamics by the method of Point Vortices", Journal of Computational Physics, Vol. 13, pp. 363-379, 1973.

[22] Clarke, D., (1972), "A Two-dimensional Strip Method for Surface Ship Hull Derivatives: Comparison of Theory with Experiments on a Segmented Tanker Model", Journal of Mechanical Engineering Science, Vol. 14, No. 7, Supplementary Issue, pp. 53-61, 1972.

[23] Clarke, D., (1992), "The Effect of Skegs and Stern Shape on the Dynamic Stability of Ships", Proceedings of Second International Conference on Manoeuvring and Control of Marine Craft, University of Southampton, 1992.

[24] Clarke, D., Downie, M. J. and Park, J. J., (2001), "Modelling Trailing Vortices for Manoeuvring Calculations", Trans. RINA, Vol.142, pp.259-267, 2001.

[25] Clarke, D., Gedling, P. and Hine, G., (1983), "The Application of Manoeuvring Criteria in Hull Design using Linear Theory", Trans. RINA, Vol.125, pp.45-68, 1983.

[26] Clarke, D. and Hearn, G.E., (1992), " A Re-analysis of the Segmented Model Data for the British Bombardier and Mariner Hullforms", Technical Memo No1, Department of Marine Technology, University of Newcastle upon Tyne, 1992.

[27] Clarke, D. and Horn, J R., (1997), "The Estimation of Hydrodynamic Derivatives", Proc. 11th Ship Control Symposium, Vol. 2, pp. 275-289, 1997.

[28] Clarke, D. and Horn, J. R., (1997), The Effect of Trailing Vortices and Stern Design on Ship Manoeuvring", Proc. 6th International Marine Design Conference (IMDC'97), Newcastle, UK, Vol. 1, pp. 595-608, 1997.

[29] Clement, R. R., (1973), "An inviscid model of two-dimensional vortex shedding", Journal of Fluid Mechanics, Vol. 57, pp. 321-336, 1973.

[30] Curry, I. G., (1993), "Fundamental Mechanics of Fluids", McGraw-Hill, Inc., ISBN 0-07-113242-2, 1993.

[31] Deng, G. and Visonneau, M., (1996), "Evaluation of Eddy Viscosity and Second-Moment Turbulence Closures for Steady Flows around Ships", 21st Symposium on Naval Hydrodynamics, Trondheim, Norway, pp. 453-469, 1996

[32] Di Mascio, A., Landrini, M. and Campana, E., (1996), "On the Modelling of the Flow Past a Free-Surface-Piercing Flat Plate", 21st Symposium on Naval Hydrodynamics, Trondheim, Norway, pp. 470-477, 1996.

[33] Downie, M. J., (1981), "An Inviscid Model for the Fluid Forces Induced by Vortex Shedding from a Circular Cylinder", Ph.D. Thesis, Royal Military College of Science, 1981.

[34] Downie, M. J., Murry, B. A. and Bettess, P., (1989), "Calculation of Force Coefficients of a Tubular Jacket Structural Member with an Appurtenance by Discrete Vortex Method", Int. J. for Numerical Method in Eng., Vol. 27, pp. 153-167, 1989.

[35] Fage, A. and Johanson, F. C., (1927) "On the flow of air behind an inclined flat plate of infinite span", Proc. Roy. Soc., Series A. 116, pp.170-179, 1927.

[36] Fage, A. and Johanson, F. C., (1928) "The Structure of the Vortex Sheet", Philosophical Magazine, Vol. 7, pp. 417-436, 1928.

[37] Fink, P. T. and Soh, W. K., (1974), "Calculation of vortex sheets in unsteady flow and applications in ship hydrodynamics", 10th Symposium on Naval Hydrodynamics, Cambridge, Massachusetts, USA, pp. 463-487, 1974.

[38] Fletcher, C. A. J., (1991), "Computational Techniques for Fluid Dynamics", Springer-Verlag, Heidelberg, 1991.

[39] Freitas, C. J., (1995), "Perspective: Selected Benchmarks From Commercial CFD Codes", Journal of Fluids Engineering, Vol. 117, pp.208-218, 1995.

[40] Gertler, A., (1959), "The DTMB planar motion mechanism system", Symposium of Towing Tank Facilities, Zagreb, Yugoslavia, paper 6, 1959.

[41] Gill, A. D. and Price, W. G., (1977), "Determination of Manoeuvring Derivatives of a Ship Model using a Horizontal Planar Motion Mechanism in a Circulating Water Channel", Trans. RINA, Vol. 119, pp.161-176, 1977.

[42] Goodman, A., (1960), Experimental techniques and Methods of analysis used in submerged body research", 3rd Symposium on Naval Hydrodynamics, Scheveningen, Netherlands, pp.379-449, 1960.

[43] Graham, J. M. R., (1977), "Vortex Shedding from Sharp Edges", Imperial College Aero. Report 77-06, 1977.

[44] Grigoropoulos, G. J. and Athanassoulis, G. A., (1997), "Investigation of an Extended-Lewis Form Family of Ship Sections and its Application to Seakeeping Optimisation", Trans. RINA, Vol. 139, pp.131-144, 1997.

[45] Hearn, G. E., Clarke, D., Chan, H. S., Incecik, A. and Varyani, K. S., (1994), "The Influence of Vorticity upon Estimation of Manoeuvring Derivatives", 20th Symposium on Naval Hydrodynamics, Santa Barbara, California, USA, pp. 669-681, 1994.

[46] IMO, (1993), International Maritime Organisation, Assembly Resolution A.751 (18), Adopted November 1993.

[47] ITTC, (1996), "Report of the Resistance and Flow Committee", 21th International Towing Tank Conference, Bergen, Norway, pp. 439-513, 1996.

[48] Inoue, S., Hirano, M. and Kijima, K., (1981), "Hydrodynamic Derivatives on Ship Manoeuvring", International Shipbuilding Progress, Vol. 23, No. 321, pp. 112-125, 1981.

[49] Ikeda, Y. and Himeno, Y., (1981), "Calculation of vortex-shedding flow around oscillating circular and Lewis-form cylinders", Proceeding of 3rd International Conference on Numerical Ship Hydrodynamics, Paris, pp. 335-346, 1981.

[50] Jensen, G., Soding, H. and Mi, Z. X., (1986), "Rankine Source Methods for Numerical Solutions of the Steady Wave Resistance problem", 16th Symposium on Naval Hydrodynamics, Berkely, California, USA, pp. 575-582, 1986.

[51] Jones, R. T., (1946), "Properties of Low-Aspect-Ratio Pointed Wings at Speeds Below and Above the Speed of Sound", N.A.C.A. Report 1032, 1946.

[52] Kamamoto, K. and Bearman, P. W., (1978), "The Importance of Time Step Size and Initial Vortex Position in Modelling Flow with Discrete Vortices", Imperial College Aero. Tech. Note 78-108, 1978.

[53] Kijima, K. and Furukawa, Y., (1996), "On a Prediction Method of Hydrodynamic Forces acting on Ship Hull including the Effect of Hull Form", Proceeding of MARSIM'96, Rotterdam, pp.411-418, 1996.

[54] Kim, S. E, and Choudhury, D., (1994), "A Computational Study of Turbulent Flows around Two Double-Body Ship Models", CFD Workshop, Tokyo, pp.201-210, 1994.

[55] Kiya, M. and Are, M., (1977), "A contribution to an inviscid vortex-shedding model for an inclined flat plate in uniform flow", Journal of Fluid Mechanics, Vol. 82, pp. 223-240, 1977.

[56] Kiya, M. and Are, M., (1977), "An inviscid numerical simulation of vortex shedding from an inclined flat plate in shear flow", Journal of Fluid Mechanics, Vol. 82, pp. 241-253, 1977.

[57] Kose, K., Xiong, X. and Misiag, W. A., (1997), "A New Prediction Approach for Ship Manoeuvring Hydrodynamics", Trans. of the West-Japan Society of Naval Architecture, No.93, pp.47-61, 1997.

[58] Kuiper, G., (1994), "Resistance and Propulsion of Ships", Report 847-K. TU Delft, 1994.

[59] Lamb, H., (1993), "Hydrodynamics", Cambridge University Press, ISBN 0-521-05515-6, 1993.

[60] Landrini, M., (1993), "A Nonlinear Hydrodynamic Mode for Ship Manoeuvrability", Proceeding of MARSIM'93, Newfoundland, Canada, pp. 351-358, 1993.

[61] Landrini, M., Casciola, C. M. and Coppola, C., (1992), "Numerical Modelling of Hydrodynamical Aspects in Ship Manoeuvrability", Proceeding. Workshop on Prediction of Ship Manoeuvrability, Fukuoka, Japan, pp. 123-131, 1992

[62] Landrini, M. and Campana, E. F., (1996), "Steady Waves and Forces About a Yawing Flat Plat", Journal of Ship Research, Vol. 40, No. 3, pp. 179-192, 1996.

[63] Larsson, L., (1997), "CFD in Ship Design-Prospects and Limitations", Schiffstechnik Bd. 44 / Ship Technology Research, Vol. 44, pp. 133-154, 1997.

[64] Leonard, B. P., (1979), " A stable and Accurate Convective Modelling Procedure Based Quardratic Upstream Interpolation", Computational Methods Appl. Mech. Eng., Vol.19, pp.59-98, 1979.

[65] Lewies, F. M., (1929), "The inertia of the water surrounding a vibration ship", Trans. SNAME, Vol. 37, pp.1-20, 1929.

[66] Liu, H. and Kodama, Y., (1993), "Computation of Waves Generated by a Ship Using an NS Solver with Global Conservation", Journal or the Society of Naval Architects of Japan, Vol. 173, pp. 1-8, 1993.

[67] Longo, J. and Stern, F., (1996), "Yaw Effects on Model-Scale Ship Flows", 21st Symposium on Naval Hydrodynamics, Trondheim, Norway, pp. 312-327, 1996.

[68] Longo, J., (1996), "Yaw Effect on Model-Scale Ship Flows", PhD Thesis, The Department of Mechanical Engineering, The University of Iowa, Iowa City, USA, 1996.

[69] Mangler, K. W. and Smith, J. H. B., (1959), A theory of the flow past a slender delta wing with leading edge separation", Proc. Roy. Soc., Vol. 251A, pp.201-217, 1959.

[70] Maruo, H. and Ikehata, M., (1966), "Observation of the Flow Pattern Around Ship Models", 11th International Towing Tank Conference, Tokyo, 1966.

[71] Maruo, H. and Song, W. S., (1990), "Numerical Appraisal of the New Slender Ship Formulation in Steady Motion", 18th Symposium on Naval Hydrodynamics, Ann Arbor, Michigan, USA, pp. 239-257, 1990.

[72] Matheson, N. and Joubert, P. N, (1973), " Experimental Determination of the Components Resistance of a Small 0.80 C_B Tanker Model", Journal of Ship Research, Vol. 17, No. 3, pp. 162-180, 1973.

[73] Meng J. C. S. and Thomson J. A. L., (1978), "Numerical Studies of some Non-linear Hydrodynamic Problems by Discrete Vortex Element Methods", Journal of Fluid Mechanics, Vol. 84, pp. 433-453, 1978.

[74] Milne-Thomson, L. M., (1960), "Theoretical hydrodynamics", St Martin's Press, 1960.

[75] Miyazaki, H., Honaka, K., Hino, T., Hirata, N., Nimura, T. and Ueno, M., (2000), "Computation of Hydrodynamic Forces acting on a Ship in

Manoeuvring Motion", Journal of the Society of Naval Architects of Japan, Vol. 187, pp. 121-130, 2000.

[76] Moore, D. W., and Saffman, P. G., (1973), "Axial Flow in Laminar Trailing Vortices", Proc. Roy. Soc., Series A, Vol. 333, pp. 491-508, 1973.

[77] Munk, M. M., (1924), "The Aerodynamic Forces on Airship Hulls", N.A.C.A. Report 184, 1924.

[78] Murray, B. A., (1992), "Hydrodynamic Loading due to Appurtenances on Jacket Structures", PhD Thesis, Dept. of Marine Technology, University of Newcastle upon Tyne, 1992.

[79] Nakatake, K., Ando, J., Maita, S. and Yamamoto, T., (1998), "Prediction of Forces acting on Ship with Different Afterbody Shapes in Oblique Towing", Int. Symposium and Workshop on Force Acting on a Manoeuvring Vessel, Val de Reuil, France, pp.1T-6T, 1998.

[80] Naylor, P. J., (1982), "A Discrete Vortex Model For Bluff Bodies in Oscillatory Flow", PhD Thesis, Aero Dept, Imperial College, London, 1982

[81] Newman, J. N., (1977), "Marine Hydrodynamics", MIT Press, ISSBN 0-262-14026-8, 1977.

[82] Nonaka, K., Nimura, T., Haraguchi, T. and Ueno, M. (1996), "Measurements of Stern Flow Field of a Ship in Oblique Towing Motion", Proceeding of MARSIM'96, pp389-398, 1996.

[83] Park, J. J., (1996), "A Numerical Computation of Free Surface Flow around a Hull with Appendages", Msc Thesis, Dept of Naval Architecture, Inha University, Korea, 1996.

[84] Park, J. J. and Downie, M. J., (1999), "The Computation of Trailing Vortices from a Slender Ship Hull", 7th Annual Conference of ACME, University of Durham, pp. 179-182, 1999.

[85] Patankar, S. V., (1980), "Numerical Heat Transfer and Fluid Flow", Hemisphere, New York, 1980.

[86] Patel, M. H. and Brown, D. T., (1986), " On Prediction of Resonant Roll Motions for Flat-Bottomed Barges", Trans. RINA, Vol.128, pp.173-187, 1986.

[87] Patel, V. C., Ju, S. and Lew, J. M., (1990), "Viscous Flow Past a Ship in a Cross Current", 18th Symposium on Naval Hydrodynamics, Ann Arbor, Michigan, USA, pp. 721-726, 1990.

[88] Reed, A. M. and Nowacki, H., (1974), "Interactive Creation of Fair Ship Lines", Journal of Ship Research, Vol. 18, No. 2, pp. 96-112, 1974.

[89] Rodi, W., (1980), "Turbulence Models and their Application in Hydraulics", I. H. A. R., Delft, 1980.

[90] Rosenhead, L., (1931), "The Formation of Vortices from a Surface of Discontinuity", Pro. Roy. Soc. Series A., 134, pp.170-192, 1931.

[91] Rogers, R. H., (1978), "Fluid Mechanics", Routlege & Kegan Paul Ltd, ISSBN 0-7100-8681-4, 1978.

[92] Rottman J. W., Simpson J. E. and Stansby P. K., (1987), "The Motion of a Cylinder of Fluid Released from Rest in a Cross Flow", Journal of Fluid Mechanics, Vol. 177, pp.307-337, 1987.

[93] Russo, V. L. and Sullivan, E.K., (1953), "Design of the Mariner-Type Ship", Transaction of SNAME, Vol.61, pp.98-166, 1953.

[94] Sarpkaya, T., (1968), "An Analytical study of Separated Flow About Circular Cylinders", Transaction of the ASME, J. Basic Engineering, pp. 511-520, 1968.

[95] Sarpkaya, T., (1975), "An inviscid model of two-dimensional vortex shedding for transient and asymptotically steady separated flow over an inclined plate", Journal of Fluid Mechanics, Vol. 68, pp. 109-128, 1975.

[96] Sarpkaya, T., (1989), "Computational Methods with Vortices – The 1988 Freeman Scholar Lecture", Journal of Fluids Engineering, Vol. 111, pp. 5-52, 1989.

[97] Sarpkaya, T. and Schoaff, R. L., (1979), "Inviscid Model of Two-Dimensional Vortex Shedding by a Circular Cylinder", AIAA Journal, Vol. 17, No. 11, pp. 1193-1200, 1979.

[98] Smith, J. H. B., (1968), "Improved calculation of Leading-edge separation from slender, thin, delta wings", Pro. Roy. Soc., Series A., Vol. 306, pp. 67-90, 1968.

[99] Sotiropoulos, F. and Patel, V. C., (1995), "Application of Reynolds-Stress Transport Models to Stern and Wake Flows", Journal of Ship Research, Vol.39, pp.263-283, 1995.

[100] Stansby, P. K., (1977), "Inviscid Model of Vortex Shedding in Steady and Oscillatory Far Flows", Proc. Inst. Civil Engineering, Vol.63, Part 2, pp.865-880, 1977.

[101] Tagori, T., (1966), "Investigations on vortices generated at the bilge", 11th International Towing Tank Conference, Tokyo, pp. 54-57, 1966.

[102] Tahara, Y., Stern, F. and Rosen, B., (1990), "An inter active approach for Calculating Ship Boundary Layers and Wakes for Numerical Froude Number", 18th Symposium on Naval Hydrodynamics, Ann Arbor, Michigan, USA, pp. 699-721, 1990.

[103] Tanaka, H., Kawakami, Y., Ueda, T., Takahashi, K., and Yahagihara, T. Y., (1983), "Experimental Studies on Trailing Vortices of Ships", Proceedings of 2nd Internesional Symposium PRADS 83, Tokyo and Seoul, pp. 295-302, 1983.

[104] Telionis, D. P., (1979), "Review-Unsteady Boundary Layers, Separated and Attached", ASME Journal of Fluid Engineering, Vol. 101, pp. 29-43, 1979.

[105] Turk, E. O., (1964), "Some Methods for Flows past Blunt Slender Bodies", Journal of Fluid Mechanics, Vol. 18, pp. 619-635, 1964.

[106] Turk, E. O. and von Kerczek, C., (1968), "Streamlines and Pressure Distribution on Arbitrary Ship Hulls at Zero Froude Number", Journal of Ship Research, Vol. 12, Pt 3, pp. 231-236, 1968.

[107] von Kerczek, C. and Turk, E. O., (1969), "The Representation of Ship Hulls by Conformal Mapping Functions", Journal of Ship Research, Vol. 13, Pt 4, pp. 284-298, 1969.

[108] Wagner Smitt, L., (1970), Steering and Manoeuvring of Ships-Full Scale and Model Tests", European Shipbuilding, No. 6, pp.86-96, 1970.

[109] Wagner Smitt, L., (1971), Steering and Manoeuvring of Ships-Full Scale and Model Tests, Part II", European Shipbuilding, No. 1, pp.8-17, 1971.

[110] Wardhana, W., (1995), "Prediction of Two Dimensional Separated Flows about a Circular Cylinder in the Presence of Boundaries", PhD Thesis, Dept. of Marine Technology, University of Newcastle upon Tyne, 1995.

[111] Wardlaw, A. B., (1974), "Prediction of Yawing Force at High Angle of Attack", AIAA Journal, Vol. 12, pp. 1142-1144, 1974.

[112] Westlake, P. C. and Wilson, P. A., (2000), "A New Conformal Mapping Technique for Ship Sections", Int. Shipbuild. Progr., 47, No. 448, pp. 2-22, 2000.

[113] Wong, H. L., (1994), "Slender Ship Procedures That Include the Effects of Yaw, Vortex Shedding and Density Stratification", Phd Thesis, Dept. of Mechanical Engineering, University of British Columbia, Canada, 1994..

[114] Wong, H. L. and Calisal, S. M., (1996), "Numerical algorithms for slender bodies with vortex shedding and density stratification", Journal of Ship Research, Vol. 40, No. 1, pp. 11-21, 1996.

[115] Wellicome, J.F, Wilson, P. A. and Cheng, X., (1995), "Prediction of Sway Force and Yaw Moment on Slender Ships", International Shipbuilding Progress, Vol. 42, pp. 259-275, 1995.

[116] Wellicome, J. F., Wilson, P. A. and Cheng, X., (1997), "Experimental and Numerical Studies of the Manoeuvring Forces on Slender Ships", Trans. RINA, Vol. 139, pp. 147-156, 1997.

[117] Xiong, X., and Kose, K., (1996), "A study on Numerical Methods for the Manoeuvring Hydrodynamics Based on the Slender Body Theory", Trans. of the West-Japan Society of Naval Architecture, No.91, pp.61-70, 1996.

[118] Zou, Z. and Soding, H., (1994), "A Panel Method for Lifting Potential Flows around Three-dimensional Surface-Piercing Bodies", 20th Symposium on Naval Hydrodynamics, Santa Barbara, California, USA, pp. 810-821, 1994.

[119] Zou, Z. J., (1996), "Hydrodynamic Force on a Surface-Piercing Plate in Steady Manoeuvring Motion", 21st Symposium on Naval Hydrodynamics, Trondheim, Norway, pp. 986-995, 1996.